Sea surface and energy dissipation

Pedro Veras Guimaraes

UNIVERSITE BRETAGNE LOIRE

CENTRALE NANTES

Thèse de Doctorat

Pedro VERAS GUIMARÃES

Mémoire présenté en vue de l'obtention
du grade de Docteur de l'Ecole Centrale de Nantes
Sous le label de l'UNIVERSITÉ BRETAGNE LOIRE

École doctorale: SPIGA

Discipline: Mécanique des fluides
Unité de recherche: LHEEA

Soutenue le 17 Janvier 2018

Surfaces de mer et dissipation d'énergie

JURY

Rapporteurs :	**Bertin Xavier**, Directeur de Recherche CNRS, Université de La Rochelle **Benetazzo Alvise**, Chercheur, ISMAR - CNRS
Examinateurs:	**Menéndez Melisa**, Chercheur, IH Cantábria **Hauser Daniele** Directrice de Recherche, IPSL-CNRS
Directeur de thèse :	**Ferrant Pierre**, Professeur, École Centrale de Nantes
Co-directeur de thèse : Co-encadrant de thèse :	**Ardhuin Fabrice**, Directeur de Recherche CNRS, Ifremer **Perignon Yves**, Ingénieur de Recherche, École Centrale de Nantes

Live as If You Were to Die Tomorrow
Learn as If You Were to Live Forever

Mahatma Gandhi

Résumé

Les formulations et modèles de vagues stochastiques sont les outils les plus traditionnels pour l'évaluation et la prévision des états de mer. Cependant, la prise en compte de nombreux processus physiques essentiels à l'évolution des vagues reste souvent lacunaire dans ces types d'approches. Une des raisons possible est notamment que peu d'observations viennent documenter ces processus. La dissipation des ondes est ainsi mal quantifiée par les méthodes d'observation traditionnelles dans tout l'éventail des conditions océaniques.

Dans ce contexte, le travail présenté dans cette thèse explore plus avant les conditions menant au déferlement à travers la modulation de l'énergie des ondes courtes par de fort courants de marée et par des ondes plus longues. Dans cette étude, nous avons profité des campagnes de mesure BBWAVES, spécialement conçues pour acquérir de la donnée dans des zones d'interactions vagues-courants. Ces campagnes ont notamment permis de tester une nouvelle bouée dérivante conçue pour la mesure des vagues dans des zones à forts courants de marées. Grâce à des mesures simultanées en zones de forts courants, il a été possible de mettre en évidence des lacunes dans la modélisation des états de mer, et l'influence vraisemblable des erreurs dans la modélisation atmosphérique pour ces conditions.

Cette thèse a également tiré parti d'une campagne de mesure stéréo-vidéo d'états de mer en Mer Noire afin d'étudier différents aspects du déferlement des vagues dans une grande variété de conditions d'état de mer bimodales. Ces mesures ont permis de mettre en évidence une modulation des ondes courtes par des longues et une incidence sur les propriétés de déferlement.

Mots-clés: Vagues; stéréo-vidéo; bouée dérivante; modélisation; interaction vague-courant; modulation; déferlement

Abstract

Stochastic wave formulations and models are the most common tools for the assessment and forecast of sea surface conditions. Their ability to account for some of the processes encountered by waves during their evolution remains however a central question.

Among other processes, the wave dissipation is for instance still poorly quantified and traditional methods for wave measurements fail to proper insight into its physics in a wide range of conditions. In this context, the work presented in this PhD aims to explore available observation techniques for their application to several quantitative aspects of the dissipation of wave energy, and particularly for short wave modulated by strong tidal currents, for short wave modulated by longer waves.

This work takes advantage of the BBWAVES oceanic campaigns, especially planned to explore questions related to wave and current interactions. Data from a large variety of sensors are analyzed. The campaign provides the ground for the test of a new design of drifting buoy aimed at measuring waves in areas of strong tidal current. Its performances are verified and the description it provides of the area is explored. From simultaneous measurements, it was possible to highlight the actual inaccuracies in wave model capabilities as well as the contribution of the error contained in the atmospheric modeling over strong tidal currents to the mis-evaluation of sea states.

This work also used an extensive dataset from a stereo video experiment in the Black Sea to investigate wave breaking in bimodal sea state conditions. These measurements have revealed the influence of long wave modulation over short wave breaking.

Key words: Ocean waves; stereo video; drifting buoy; wave modeling; wave-current interaction; modulation; breaking

Acknowledgment

Firstly, I would express my sincere gratitude to my advisors Fabrice Ardhuin, Yves Perignon and Pierre Ferrant to give the opportunity to research such important and captivating topic. Also for all their advices, meetings, discussions, motivation and engagement with my supervision. My acknowledgment also goes to the jury of this thesis for their constructive contribution. Besides my mentors, I also owe special thanks to Mickael Accensi for all the help in my arrival in France, for the support with WaveWatch III, stereo video and buoy experiments. I also would like to thank Fabien Leckler for the contributions and support with the stereo video, Arthur Lemoine for the help in the ship motion correction and Peter Sutherland for the ship-mounted stereo video system, for all the support during BBWAVES experiment and profitable scientific discussions.

My sincere thanks also go to Alvise Benetazzo and Filippo Bergamasco from the Institute of Marine Sciences, Italian National Research Council (ISMAR-CNR), Italy. I would like to thank you for all the help with the stereo video observations and discussions. Also to Jim Thompson from the Applied Physics Lab, University of Washington, US, for the support with SWIFT buoys and scientific discussions.

For the stimulating discussions, I would like to thank my fellow laboratory mates at Laboratoire, d'Océanographie Physique et Spatiale (LOPS), Charles Peureux, Justin Stopa, Marie-Noëlle Bouin, Valérie Garnier, Louis Marie, Jean-Luc Redelsperger, Antoine Grouazel, Bertrand Chapron, Nicolas Rascle, Aurélien Ponte, Sebastien Prigent and Michel Hamon. From LHEEA lab, École Centrale de Nantes, Guillaume Ducrozet, for the support during the Fluid Mechanics classes, and to all "*Team Tupperware*" group for the healthy lunch company. From the Groupe littoral, Université de Bretagne Occidentale, I would like to thank France Floch and Charles Caulet for the collaboration during the stereo video beach experiments. Thanks for all the secretaries and technical support at Ifremer and École Central de Nantes to make our work possible. Besides the personal, I am grateful for Ifremer and École Centrale de Nantes for the PhD. scholarship.

Last but not the least, I would like to thank my wife Fabiane Alves Farias Guimarães for all the commitment and spiritual support throughout this journey. To my parents Francisco and Nara Guimarães, my brother Miguel and sister Clara, I miss you so much.

Thesis structure

This thesis is written in English, but each chapter is introduced by a *Résumé* in French language, summarizing the main information presented in the chapters. The main research findings are presented in Chapter 4 about short **wind waves modulation by tidal currents** and in Chapter 5 about **short wave modulation by longer waves**. The first scientific publication arising from this work is presented in Chapter 3 to be submitted to Ocean Science. To sustain the main scientific findings presented in this work, this thesis organization comprises the following main parts:

Chapter 1: Consists in a brief introduction about ocean waves, their importance and the motivations for research underlying this work. To synthesize the thesis structure, the theoretical background is limited to the main research topics presented here and those are included directly in the main research chapters (4 and 5).

Chapter 2: This chapter presents a short literature review about waves sensing techniques, focusing on wave buoys analysis, stereo video system and breaking detection. These observation techniques comprise the main methods used in Chapters 4 and 5.

Chapter 3: Complementary to Chapter 2, more detailed information are presented here about the Surface KInematics Buoy (SKIB), the drifting buoy especially developed for studying wave-current interactions. This chapter includes the validation of this equipment and an investigation about its capability to measure current-induced wave variations.

Chapter 4: Explores the impact of tidal current on the dynamics of short waves. Our primary observation under moderate wind conditions and strong currents have shown a significant increment of energy in the local wind sea that could not be reproduced by the numerical model. After extensive numerical tests we have identifed that the main source off error was in the wind forcing, causing a significant underestimation of short waves growth.

Chapter 5: Focuses on the observation of the modulation by longer waves on the breaking of shorter waves by stereo video system, which possibly provides the first direct field observation of this phenomenon. Furthermore, based on the frequency-wavenumber spectra it is discussed the possibility of modifying the saturation-based parameterizations, by including the modulation transfer function on the short wave spectrum.

Chapter 6: Presents a short summary and some final considerations.

Contents

List of Figures

List of Tables

1. Introduction

Résumé

Les ondes de l'océan sont très importantes pour les prévisions météorologiques et la modélisation climatique, ainsi que pour l'évaluation des risques côtiers, la définition des routes d'expédition et la planification des opérations offshore. Les ondes peuvent être responsables de différentes contributions aux risques côtiers, induire des courants de la côte, des changements morphodynamiques et l'érosion des plages. Associés aux ondes de tempête, elles peuvent causer des surcotes et des submersions côtières.

Au cours de leur évolution, les vagues de l'océan peuvent se briser à leur surface et elles constituent alors le principal flux de gaz dans les systèmes environnementaux marin. Cela contribue de manière significative à l'activité et à la production biologiques marines, à la biogéochimie, à la physique des nuages, aux radiations atmosphériques et à la thermodynamique des ouragans et à la formation d'écume, qui modifie les propriétés optiques de la surface de l'océan et, par conséquent, l'interprétation de la couleur de l'océan. Les ondes de surface peuvent contribuer à modifier les températures de la surface de la mer, la rugosité de la surface et le frottement des vents, et l'impactde leur action est directement sensible dans les prévisions météorologiques, et a fortiori celles des évènements extrêmes tels que les ondes de tempête et les ouragans.

Malgré l'importance de l'étude des vagues océaniques, une compréhension complète de la dynamique des ondes passe par des méthodes d'observation de terrain relativement limitées. Ce chapitre présente une courte introduction de l'étude des ondes océaniques, des motivations et des défis scientifiques et présente les principaux sujets d'étude abordés dans cette thèse. Ce travail vise à explorer la répartition d'énergie des états de mer et la dissipation des ondes de surface à partir de plusieurs expériences de terrain et de techniques de détection modernes pour améliorer la compréhension de la dynamique des ondes.

Ocean wind waves are one of the main sources of energy conservation in the ocean. The winds shear transfer energy to the oceanic-atmospheric boundary layer, creating and growing surface waves. Once created, the ocean waves propagate at the ocean surface, growing, grouping, transporting and exchanging energy, occasionally dissipating during wave breaking. However, the comprehension of the energy balance between the wind input, dissipation and nonlinear wave transformations is still partially empirical. New field observations of wave breaking, waves and ice, wave and current interactions are still revealing important informations about the sea surface dynamics (e.g. Melville and Matusov, 2002; Campbell et al., 2014; Rascle et al., 2014, and others).

Ocean waves are very important for weather forecasting, climate modeling as well as for coastal hazard assessment, shipping routes definition and planning of offshore operations. From surf forecast and recreational applications to marine energy converters, wave modeling and forecasting are an economics businesses, where they are a key for several coastal projects.

Waves can contribute to diverse forms of coastal hazards. For example, they can induce coastal currents (Visser, 1991) and morphodynamic changes (Baldock et al., 2010). In some storm conditions, waves can also cause coastal flooding, extreme wave runup, overtopping, beach erosion and property loss (Guimarães et al., 2015).

Waves can also be an important source of gas flux in the marine environment systems. When waves break, the air injected in sea surface can significantly contribute to the marine biological activity and production, biogeochemistry, cloud physics, atmospheric radiation balances and hurricane thermodynamics. The entrainment of bubbles in the ocean can also modify the optical properties of the ocean surface and therefore the interpretation of ocean colour (Melville and Matusov, 2002). Also, the spray, bubbles, turbulence, vortical structures, buoyant plumes, surface and internal waves are important fluid dynamical processes that populate the air-sea boundary layers and can influence the vertical wind transport of momentum and scalars (Sullivan and Mcwilliams, 2010).

Recent studies on the coupled atmosphere-ocean-wave have shown the importance of ocean waves on the sea surface temperatures in climate models (Sullivan and Mcwilliams, 2010). On meso-scale process, waves can modulate the surface roughness and the surface friction (Mastenbroek et al., 1993; Bertin et al., 2012) directly impacting in weather forecasting, storm surge and hurricane models. As ocean waves conditions are permanently evolving with the atmospheric boundary layer, the knowledge of how ocean waves will behave facing climate changes will be of great interest to decision makers for coastal communities and marine industry.

Figure 1.1: Why study ocean waves? Ocean waves can: a) be the cause of property loss, as example, 2016 savage storm in Sydney, AU report by Beers and Tran (2016), photo: Damian Shaw; b) create risk for conditions of navigation (e.g., ship DELAWARE II from NOAA); c) be a recreational activity and tourist attraction; d) provide an energy source (e.g., Retzler, 2006, Pelamis projects for marine energy converters).

Despite the importance in studying ocean waves, field observations are still very limited to few moored buoys installed in specific regions in the world or to large scale observations of wave conditions from satellites altimeters. Our understanding of the energy balance in ocean waves during storm conditions is still limited by non-existent measurements of the full directional spectrum in these conditions. Wave observations under strong current conditions are still mainly studied in laboratory experiments with limited field monitoring. Also, large scale breaking detection is not feasible by high-resolution SAR images, so field detection still restrict to a few video observations.

Wave buoys and satellite altimeters have been providing substantial informations of significant wave heights for the validation of local and global scale model. However, a global observation of shorter wave components is usually limited by the satellite resolution and wave buoys only provide single point measurements.

The hydrodynamic response of large buoy limits their range of effective measurement to wavelengths that are above a few times the buoy diameter. For this reason, smaller buoys are needed to better measure shorter waves at higher frequencies. The comprehension of short waves dynamics is extremely important for remote sensing applications because it directly interfere in the sea surface backscattered signal, where the short wave modulation by longer waves creates a non-linear short-long wave interaction that must be corrected in the satellite analyses (Alpers and Hasselmann, 1978).

In this context, the Katsiveli 2013 experiment in the Black Sea was developed to observe short surface waves and wave breaking in a broad range of meteorological conditions. The sea surface observations in this experiment were mainly done by stereo video system, that is a quite powerful tool to measure short waves, wave breaking and non-linear wave interactions (Leckler, 2013; Leckler et al., 2015). However, this experiment in the Black Sea does not cover situations of waves propagating over strong current conditions.

To supplement that, we took advantage of the BroadBand WAVES and currents (BBWAVES) sea campaigns which were specifically planned to address questions related to the interactions between long, intermediate and short gravity waves, in the presence of surface current gradients. For that purpose, this experiment used simultaneous acquisitions made by an array of drifting buoys and a ship-mounted stereo video system around gradients of strong tidal currents in Northwest of France.

With the deployment and analysis of modern wave sensing techniques applied in the Katsiveli 2013 stereo video campaign and in the BBWAVES 2015 and 2016 experiments, this work aims to explore the repartition of the energy among waves at the sea surface and its dissipation in order to improve the comprehension of the waves dynamics. More specifically, this work intends to explore aspects of the modulation of

short wave energy by strong tidal currents, short wave modulation by longer waves and wave energy dissipated by breaking.

To explore it, we first start by presenting a short literature review about waves sensing techniques, focusing on main methods used in this work: wave buoys analysis, stereo video system and breaking detection (Chap.2). We complement this methodology in Chapter 3, by introducing a new set of drifting buoys, the Surface KInematics Buoy (SKIB). This drifting buoy was especially developed for studying wave-current interactions and essential in the investigation present in Chapter 4, about the tidal current impact on the short waves dynamics.

The wind, wave and current informations archived during the BBWAVES campaigns are compared against the current impact on short waves propagation theory and compared with several numerical simulations, considering different wind forcing, source packages and parametrization (Chap.4).

The short wave modulation by longer waves and its impact on the short wave breaking is explored using a stereo video system (Chap.5). This method provided a unique observation of this phenomenon and the results leads to a discussion about how to introduce the longer waves modulation effect on the short waves breaking probability, where we propose to include the modulation transfer function in the saturation-based parameterizations.

In this work we intend to present uniques observations of non-linear sea surface phenomenons and discuss its impacts in stochastic waves modeling.

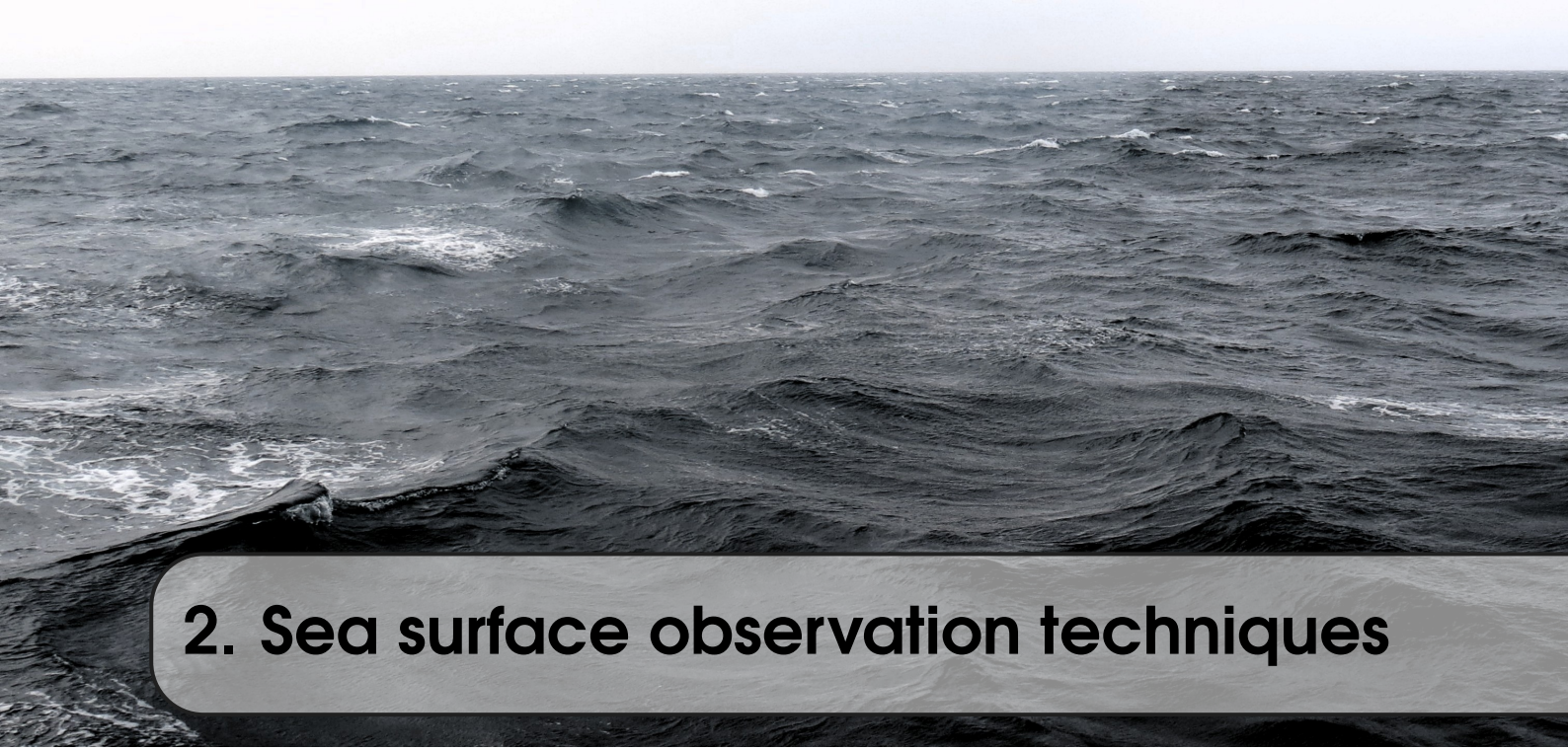

2. Sea surface observation techniques

Résumé

Les vagues dans l'océan peuvent être mesurées par différentes méthodes et instruments, chacun avec son but et ses limites propres. Ce chapitre présente les principales techniques d'observation utilisées dans les autres chapitres de cette thèse. Une attention particulière est portée sur les techniques développées au cours de cette thèse, en particulier l'utilisation de bouées dérivantes, et la stéréo-vidéo pour la reconstuction de la forme de la surface et la détection du déferlement.

Les bouées houlographes mesurent généralement les positions de la surface de la mer (x, y, z) déduites d'une double intégration de mesures d'accélération, ou la vitesse horizontale (u, v) en utilisant le système de positionnement global (GPS), la vitesse verticale étant généralement trop peu précise. Une bouée dérivante mesure donc les mêmes paramètres, mais elles se déplace librement à de la surface de l'océan sans aucune ligne amarrée. Dans des conditions avec des courants forts, près de 1 m/s ou plus, il est généralement impossible de mesurer des vagues avec une bouée de surface amarrée, en raison de la tension sur la ligne d'ancrage et de la perturbation induite sur la dynamique du flotter. Ce problème peut être évité en utilisant des bouées dérivantes, mais la nature de la mesure est différente. Les bouées dérivantes ne mesureront pas de longues séries temporelles au même endroit, mais elles peuvent fournir des transects uniques des ondes rencontrées lors de leur dérive dans le courant. En ce sens, l'application d'une technique Lagrangienne est particulièrement précieuse car les bouées dérivantes actuelles peuvent observer la structure spatiale du champ de vagues dans l'écoulement et donner un aperçu différent de la dynamique qui peut être obtenue à partir des données de bouées fixes. Les méthodes de reconstruction de spectrale pour les deux bouées sont relativement similaires et sont détaillées dans la Section 2.2 et 2.5, mais la quantité océanique est différente puisque l'un des cadres de référence est Eulerian et l'autre Lagrangien.

Le principe général de la reconstruction de la surface 3D par un système de stréréo-vidéo consiste lui à trouver le meilleur pixel de corrélation: à partir de l'image de gauche, $I(iL, jL)$, chaque pixel est associé à un pixel dans l'image de droite, $I(iR, jR)$. Cette association est basée sur la corrélation maximale entre deux fenêtres de l'image entourant les pixels à associer. Pour chaque paire de points correspondants, la géométrie de la vue donne la position (x_c, y_c, z_c) de l'élévation de la surface de la mer dans les coordonnées centrées sur le centre optique de la caméra gauche. Le système stéréo monté sur le navire fonctionne de manière similaire, mais il est nécessaire d'utiliser une centrale inertielle synchronisée avec les caméras vidéo pour obtenir la matrice de rotation (quaternion) et corriger l'observation des mouvements du navire. À partir des mesures de surface de la mer $\zeta(x,y,t)$, il est possible d'obtenir les spectres en nombres d'onde et en fréquence. Ceci est détaillé dans la Section 2.3.2. A la différence des bouées dérivantes, le spectre issu du système stéréo-vidéo monté sur le navire est mesuré directement dans un référentiel eulérien lié au bateau. Du fait de la dérive lagrangienne du bateau, la mesure spectrale est corrigée du déplacement, afin de l'exprimer dans un référentiel fixe par la suite.

La méthode de détection de déferlement est une combinaison de mesures stéréo-vidéo et de détection des moutons à partir d'une technique de traitement d'images. L'application de ces méthodes permet une observation spatio-temporelle des déferlements.

2.1 Introduction

Many devices have been developed to measure ocean waves, from in situ moored or drifting sensors, to remote sensing systems using optical or radar devices (COST Action 714 Working Group 3, 2005). Each measurement system has a specific range of applications defined by the required space and time resolution and coverage, water depth, or current speed. These have been very useful in studying upper ocean processes or monitoring sea states for various applications.

2.1.1 Measurements at the sea surface

The most simple methods for measuring the surface elevation $\zeta(x,y,t)$ at or near a fixed point (x_0, y_0) use wave gauges in the laboratory and surface buoys in the field.

Wave gauges, as example, measure ζ through the electrical resistance or capacity of a conducting wires forming a loop closed by the sea surface. In order to measure wave direction, a network of several synchronized wave gauges can be used (Cavaleri et al., 1981). Wave gauges can be mounted on ocean platforms (e.g. Donelan et al., 1985; Long and Resio, 2007) or floating buoys (Graber et al., 2000), in which case the

elevation must be corrected for the buoy motion.

Floating buoys are a more common alternative because they do not require an expensive platform. Buoy measurements are different from wave gauges because of the horizontal motion. Some buoys estimate sea surface positions (x, y, z) from measured accelerations, other estimate the elevation and slopes, and yet others use the horizontal velocities (u, v) using Global Positioning System (GPS). In all these cases, the horizontal position (x, y) oscillates around a mean position (x_0, y_0), which gives slightly different wave elevation time series $\zeta(t)$, closer to what is given by linear wave theory. Estimates of the wave direction is provided by the phase relationship between the different measured time series, be it (x, y, ζ) for Datawell waveriders, or $(\partial\zeta/\partial x, \partial\zeta/\partial y, \zeta$ for pitch-and-roll buoys. An electronic compass is usually used to determine the orientation of the buoy axis.

In conditions with strong currents, close to 1 m/s or higher, it is usually impossible to measure waves with a moored surface buoy, due to the tension in the mooring line. This problem can be avoided by using drifting buoys, but the nature of the measurement is different. Drifting buoys will not measure long time series at the same location, but they can provide a unique cross-section of waves following the current. In this sense, the application of a Lagrangian technique is particularly valuable, because current-following buoys or 'drifters' can observe the spatial structure of the sea states in the flow field and provide different insight into the flow dynamics that is hardly obtainable from fixed buoy data.

2.1.2 Measurements in the water column

An alternative method can be performed through the measurement of the associated orbital velocity. One example of sensor that allow that is a PUV sensor. As the name already suggests, a PUV measures the pressure p (by a piezo-electric sensor) and the two horizontal components of the velocity, u and v by a current meter (acoustic, electromagnetic). This instrument is particularly designed to be installed on the sea bottom and is mostly used to measure the agitation at the bottom. In this situation, the closer to the surface, the more reliable will be the measurement. To measure the wave heights it may use a transfer functions between pressure, velocities, elevation (see note in Sec.2.2).

Another alternative water column sensor is the Acoustic Doppler Current Profiler (ADCP). This is the most widely used instrument for observing ocean currents, but it is also useful for measuring the surface wave spectrum via wave orbital flow field (Herbers and Lentz, 2010). The time series of ADCP velocity, collected at a large number of positions spanning the aperture of three or more acoustic beams, contain detailed

two-dimensional phase information of the surface wave field. These multicomponent observations can be analyzed using cross-spectral array processing techniques to infer the frequency directional surface wave spectrum (Terray et al., 1999; Herbers and Lentz, 2010). When compared with PUV, the main benefit of ADCPs is the possibility to get measurements close to the sea surface, where the wave motion is less attenuated than at the bottom.

2.1.3 Video techniques

A three dimensional map of the sea surface $\zeta(\boldsymbol{x},\boldsymbol{y},t)$ can also be obtained by stereo-photography. This method use a pair of video records of the sea surface, taken at the exact same time. Correlation methods then provide pairs of matching points, one in each image. Knowing the camera properties allows to recover the physical position $(x,y,z=\zeta(x,y))$ of each point. Combining all these points provides a 3D map of the sea surface (Chase et al., 1957; Holthuijsen, 1983) and it can be converted in a sea surface spectrum as demonstrated by Gallego et al. (2008). Alternatively, the use of more expensive infrared cameras is a very interesting extension for overcoming the variability of lighting conditions and the lack of texture at small scale for a correlation analysis (Sutherland and Melville, 2013). With optical imagery and using only correlations, it is possible to resolve wavelengths of about 20 cm with cameras located about 5 m from the sea surface (Banner et al., 1989), or of about 1 m with a larger field of view Leckler et al. (2015). Using also the radiance of the images, it is possible to convert radiance into slopes (Gallego et al., 2008; Kosnik and Dulov, 2011) and extend the measurement range to wavelengths around 1 cm. A similar slope measurement can be provided also by using the polarization of the light reflected by the sea surface (Zappa et al., 2008; Laxague et al., 2015). The great advantage of having the full surface $\zeta(\boldsymbol{x},\boldsymbol{y},t)$, is that we can now measure a 3D spectrum, without the need to use linear wave theory. This is most important for the short wave components, for which nonlinear contributions are important (Banner et al., 1989; Leckler et al., 2015).

From space, the processing of optical imagery can be used to obtain the 2D spectrum using a relation between radiance and slope. With pairs of images acquired within a small interval, as is the case of the different color channels on Sentinel 2, the 180° ambiguity in wave propagation direction can be lifted, and the surface current vector can be derived from the measured dispersion relation (Kudryavtsev et al., 2017a,b).

2.1.4 Radar remote sensing

Radars are also widely used for ocean measurements. Their versatility comes from their all-weather capability, retrieving ocean information through clouds, at day or night.

Satellite altimeters

The most commonly used radars are nadir-pointing altimeters. Analysis of the time history of returned power provides a direct estimate of the significant wave height H_s (e.g. Gower, 1979). Altimeter data has been available routinely with the satellite missions ERS-1, Topex-Poseidon, ERS-2, Geosat Follow On, Jason-1, Envisat, Jason-2, Cryosat, SARAL-AltiKa, HY-2, Jason-3 (e.g. Queffeulou, 2004; Sepulveda et al., 2015). Initially, the main application of the altimeters were for mapping the geoid, then the dynamic sea surface anomalies associated to ocean currents and tides. Waves play an important role in the estimation of the mean sea level, because of a range bias induced by wave non-linearities (Minster et al., 1991).

Airborne scanning radars

More details on the wave properties can be obtained from airplanes, in which case it is possible to have a footprint smaller than the wavelength of the waves of interest and obtain $\zeta(x,y)$ with a resolution of a few meters (Walsh et al., 1985; Hwang et al., 2000).

LiDAR scanning

Recent investigations of Blenkinsopp et al. (2012) and Martins et al. (2017) attempt to uses a LiDAR (Light Detection And Ranging) to measure the free-surface in shallow waters and surf zone. This is also an optical remotesensing technology which uses a scanning laser to provide accurate two or three-dimensional measurements of surface profiles at a horizontal spatial resolution O(10 mm) and with a comparable vertical accuracy. This equipment is able to measure the entire wave field at high resolution, providing a detailed evaluation of wave transformation throughout the experimental domain.

SAR imagery

From space it is not possible to focus a radar beam on a few meters, and high resolution radar imagery uses synthetic aperture radar (SAR) processing. SAR processing

uses the relative motion of the radar antenna and the target to interpret the measured Doppler shift in the radar signal as a position along the flight track (azimuth direction). In the presence of ocean waves, the motion due to waves blurs the image along the azimuth direction and the detailed shape of the sea surface cannot be recovered. Only the part of the wave spectrum that corresponds to swells can be measured (Hasselmann and Hasselmann, 1991; Hauser et al., 1992; Chapron et al., 2001; Caudal et al., 2014).

Rotating real aperture radars

For a radar pointing away from the vertical, the resolution along the range direction is provided by the travel time, which can be resolved to within a meter or less depending on the bandwitdh of the radar signal. The footprint dimension in the azimuth is much larger, only limited by the radar aperture and frequency, typically a few kilometers at least. Hence the returned power and phase recorded by a radar for one range gate combines echoes from a narrow strip of a few meters by a few kilometers. The fluctuations of radar power and phase as a function of range contain information about the wave field. In fact, the radar can measure the wave spectrum $E(k, \theta_0)$ for all k but only in the direction θ_0 where the radar is pointing (Jackson et al., 1985; Nouguier et al., 2017). Rotating the radar antenna allows to cover all directions θ_0. This principle will be used by the SWIM instrument (Hauser et al., 2017) on the China France Ocean Satellite (CFOSAT) due for launch in August 2018. With the addition of Doppler capability it has also been proposed for the Sea surface KInematics Multiscale mission (SKIM Ardhuin et al., 2017a), which is one of the two proposals retained for phase A studies by the European Space Agency for an Earth Explorer 9 launch in 2025.

2.1.5 Summary

These different sensing techniques have different benefits for investigating the properties of sea surface waves at different scales. In this thesis we focus on the behavior of dominant waves, with wavelengths around 100 m, and their possible interactions with shorter waves, as short as 1 m, and currents. In particular, only the video-based methods and small drifting wave buoys have the potential to measure these short wave properties.

We will now describe in more details the techniques we have used and further developed. In Sections 2.2 we present a short review about wave buoys measurement techniques and in Section 2.3 about stereo video and breaking detection technique. Section 2.4 and 2.5 is dedicated to present two Lagrangian observation techniques using ship-mounted stereo video and drifting buoys. Complementary to Sections 2.5, Chapter

3 presents the Surface KInematics Buoy (SKIB), especially developed for studies of wave-current interactions.

2.2 Wave buoys

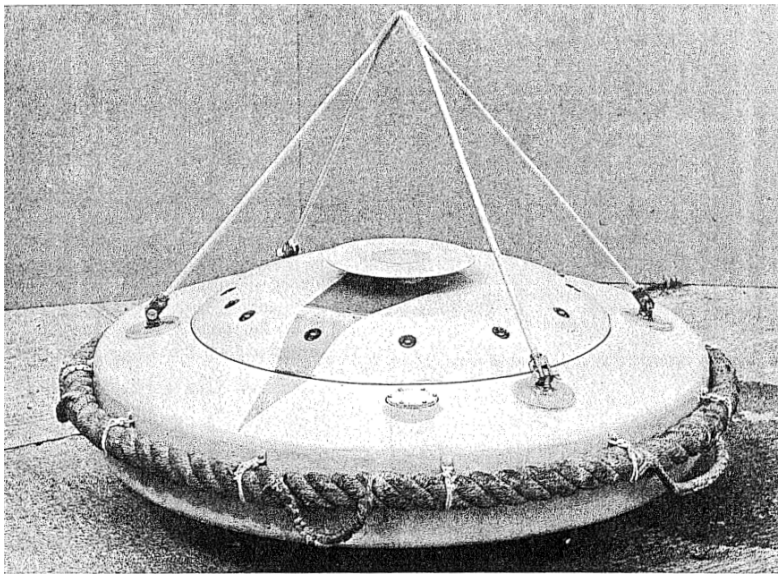

Figure 2.1: Longuet-Higgins et al. (1963) floating buoy.

Longuet-Higgins et al. (1963) presented the basis of the estimation of the directional wave spectrum using floating buoys. In his original design, the buoy measures the vertical acceleration from which displacement (heave) is estimated, and the pitch and roll angles. This combination of heave, pitch and roll is still use in the 3-m discus buoys deployed around the coasts of the United States (e.g. O'Reilly et al., 1996).

Alternatively, the measurement of pitch and roll can be replaced by the measurement of horizontal accelerations as done in Waverider buoy from Datawell. Waveriders have been updated with smaller hulls, new sensors and software packages over the past 40 years (Gerritzen, 1993; Rademakers, 1993; Vries et al., 2003; Jeans et al., 2003; van Weeren et al., 2005; de Vries and Haarlem, 2007).

One very important evolution is the design and production of buoys based on satellite navigation systems, such as GPS, instead of accelerometers Vries et al. (2003). global navigation satellite system or vertical acceleration (and than, double integrated to get the elevation signal).

For all buoy types, the most common method to represent the random nature of wind waves from buoys is spectral analysis (here presented following Longuet-Higgins et al., 1963). This method is based on the Fourier Transform that decompose a wave elevation record into a superposition of several cosine waves, each with a particular period, wavelength, propagation direction with a random phase.

The sea surface representation in terms of the waves spectrum is slightly different if the sensor moves with the waves. Wave buoys do not measure the same as a

Eulerian fixed (x,y) position sensor. The linear Lagrangian motion of a buoy contains some of sea surface nonlinearities like Stokes and harmonics, as a result, the buoy measurements are "more linear" than fixed position sensors. However, for simplicity we will approximate the buoy measurements as estimates of the surface elevation (ζ) at a fixed (x,y) position. In the case of linear waves the frequency is uniquely related to the wavenumber and we can write

$$\zeta(x,y,t) = \sum_{i,j} A_{i,j} \cos(k_i x \cos\theta_j + k_i y \sin\theta_j - 2\pi f_i t + \phi_{i,j}) \tag{2.1}$$

with amplitude $A_{i,j}$, wavenumber $k_{i,j}$, direction θ_j, frequency f_i and a random phase $\phi_{i,j}$, i and j are frequency and direction indexes.

The horizontal positions in the x and y directions are

$$\xi_1(x,y,t) = -\sum_{i,j} \frac{A_{i,j}\cos\theta_j}{\tanh(kD)} \cos(k_i x \cos\theta_j + k_i y \sin\theta_j - 2\pi f_i t + \phi_{i,j}) \tag{2.2}$$

$$\xi_2(x,y,t) = -\sum_{i,j} \frac{A_{i,j}\sin\theta_j}{\tanh(kD)} \cos(k_i x \cos\theta_j + k_i y \sin\theta_j - 2\pi f_i t + \phi_{i,j}) \tag{2.3}$$

For waves sufficient long compared with the diameter of the buoy, the horizontal velocity follows the orbital velocity of a water parcel $u = \partial\xi_1/\partial t$, $v = \partial\xi_2/\partial t$. To correct for possible buoy spin, the motion sensor package in the buoys is usually connect to an electronic compass that converts the motion relative to the hull into a motion relative to a fixed heading. Where in a fixed reference frame, the dispersion relation is write as

$$\omega = \sigma + \boldsymbol{k}\cdot\boldsymbol{U} \tag{2.4}$$

where $\omega = 2\pi f$ and $\sigma^2 = gk\tanh kD$,

The elevation spectrum can be obtained taking the average of the records by the discrete Fourier transform $E(f) = \langle\zeta(f_i)^2\rangle$ with is the sum of the variance over all the directions i, j.

$$E(f,\theta) = \frac{\overline{d\boldsymbol{A}d\boldsymbol{A}^*}}{2df d\theta} \tag{2.5}$$

where $*$ denotes the complex conjugate.

The covariance functions between ζ and u,v can be calculated by taking cross products among this three variables. In the limit of long time records, the discrete

Fourier transform can be replaced by a Fourier-Stieltjes integral and we have

$$\zeta(x,t) = \Re \iint \mathrm{e}^{\mathrm{i}(\boldsymbol{k}\cdot\boldsymbol{x}-\omega t)} d\boldsymbol{A} \tag{2.6}$$

$$u(x,t) = \Re \iint \frac{\sigma \cos\theta_j}{\tanh(kD)} \mathrm{e}^{\mathrm{i}(\boldsymbol{k}\cdot\boldsymbol{x}-\omega t)} d\boldsymbol{A} \tag{2.7}$$

$$v(x,t) = \Re \iint \frac{\sigma \sin\theta_j}{\tanh(kD)} \mathrm{e}^{\mathrm{i}(\boldsymbol{k}\cdot\boldsymbol{x}-\omega t)} d\boldsymbol{A} \tag{2.8}$$

Here are the spectra for these quantities

$$C_{11}(f) = \int_0^{2\pi} E(f,\theta) d\theta \tag{2.9}$$

$$C_{22}(f) = \int_0^{2\pi} \frac{\sigma^2 \cos^2\theta}{\tanh^2(kD)} E(f,\theta) d\theta \tag{2.10}$$

$$C_{33}(f) = \int_0^{2\pi} k^2 \frac{\sigma^2 \sin^2\theta}{\tanh^2(kD)} E(f,\theta) d\theta \tag{2.11}$$

and the co-spectra

$$C_{23}(f) = \int_0^{2\pi} \frac{\sigma^2 \cos\theta \sin\theta}{\tanh^2(kD)} E(f,\theta) d\theta \tag{2.12}$$

$$C_{12}(f) = \int_0^{2\pi} \frac{\sigma \cos\theta}{\tanh(kD)} E(f,\theta) d\theta \tag{2.13}$$

$$C_{13}(f) = \int_0^{2\pi} \frac{\sigma \sin\theta}{\tanh(kD)} E(f,\theta) d\theta \tag{2.14}$$

These spectra C_{xx} and co-spectra C_{xy} are related to the Fourier coefficients of the directional distribution

$$a_n + i b_n = \int_0^{2\pi} e^{ni\theta} E(f,\theta) d\theta. \tag{2.15}$$

One has,

$$a_0(f) = C_{11} \tag{2.16}$$

$$a_1(f) = \tanh(kD) C_{12}/\sigma, \qquad b_1(f) = \tanh(kD) C_{13}/\sigma \tag{2.17}$$

$$a_2(f) = \tanh^2(kD)(C_{22} - C_{33})/\sigma^2, \qquad b_2(f) = \tanh^2(kD) C_{23}/\sigma^2 \tag{2.18}$$

Finally the last parameter that can be obtained from the measurements is,

$$c(f) = C_{11}(f)/(C_{22}(f) + C_{33}(f)) = \tanh^2(kD)/\sigma^2 \tag{2.19}$$

which is not a function of the wave spectrum. As a result, the combination of 3 time series from a single instrument can only provide 5 directional moments.

Similar relations can be obtained for other triplets of variables such as (ζ, ξ_1, ξ_3) provided by directional Waveriders, or (p,u,v) measured by bottom-mounted instruments. In case of a PUV sensor, as example, this sensor measures the pressure p and

the two horizontal components of the velocity, u and v. In this case a transfer function is required to relate any variable Ψ to the surface elevation ζ through a linear relation established by M, where

$$\Psi = M\zeta \tag{2.20}$$

For the bottom pressure, $M = \rho g/\cosh(kD)$ (Ardhuin and Filipot, 2016). From that, we get the spectrum of the x-component of the bottom velocity.

From the first moments it is customary to define a mean direction $\theta_1(f)$ and directional spread $\sigma_1(f)$ following Kuik et al. (1988),

$$\theta_1(f) = \tan^{-1}(b_1/a_1), \tag{2.21}$$

$$\sigma_1(f) = \sqrt{2\left(1-\sqrt{a_1^2+b_1^2}\right)}. \tag{2.22}$$

A very crude approximation of the directional distribution $E(f,\theta)$ can be obtained from these first moments

$$E(f,\theta) \simeq a_0(f) + (a_1(f)\cos\theta + b_1(f)\sin\theta) + (a_2(f)\cos 2\theta + b_2(f)\sin 2\theta). \tag{2.23}$$

This approximation is very bad as it tends to make a much broader spectrum than the real one: if one re-computes a_1 and b_1 from this estimated spectrum $E(f,\theta)$ using Equation 2.15, the value of σ_1 obtain is much larger than the one from the original values of a_1 and b_1. Instead of this approximation, it is better to use a statistical method that produces a spectrum $E(f,\theta)$ which does have the correct moments. One good example is the Maximum Entropy Method of Lygre and Krogstad (1986).

When only velocity measurement are available, one can only estimate $E(f)$, $a_2(f)$ and $b_2(f)$, which gives the two following parameters,

$$\theta_2(f) = \frac{1}{2}\tan^{-1}(b_2/a_2), \tag{2.24}$$

$$\sigma_2(f) = \sqrt{0.5\left(1-\sqrt{a_2^2+b_2^2}\right)}. \tag{2.25}$$

with a 180° ambiguity on the direction of propagation.

Main waves parameters

From the integration of the sea surface variance $E(f,\theta)$, or $E(f)$, we get the elevation variance E of the spectrum. This is related to the scale of the wave amplitudes by Equation 2.5 ($E(f) = \langle \zeta(f_i)^2 \rangle$ of waves amplitude). So $\sqrt{2E}$ is an equivalent to the root mean square (rms) waves amplitude and in therms of waves hight it is $2\times$ the amplitude

$$H^{rms} = 2\sqrt{2E} \tag{2.26}$$

However, in terms of waves application the most widely wave parameter is the "significant wave height" H_s or H_{m0},

$$H_s = 4\sqrt{\int_0^{\inf}\int_0^{2\pi} E(f,\theta)dfd\theta} = \frac{\sqrt{2}}{2}H^{rms} \tag{2.27}$$

The peak of waves energy in the waves spectrum is associated around a frequency defined as f_p, where $E(f_p)$ is maximum. This frequency point corresponds to the peak period of the wave spectrum $T_p = 1/f_p$. The mean wave period can be characterized from the spectral moments

$$T_{m_0,p} = \left[\frac{\int_0^{\inf}\int_0^{2\pi} f^p E(f,\theta)d\theta df}{\int_0^{\inf}\int_0^{2\pi} E(f,\theta)d\theta df}\right]^{-1/p} \tag{2.28}$$

where m_0 index indicates that it is based on the zeroth moment of the spectrum (a_0) and the p index indicate the p-th moment of the spectrum, where the most used p-th correspond to the periods $T_{m0,-1}$,$T_{m0,1}$ and $T_{m0,2}$, that is very close to the mean wave period given by wave-by-wave analysis.

The directional properties of the dominant waves can also be characterized with the mean direction $\theta_1(f_p)$ and directional spreading $\sigma_1(f_p)$ of the spectral peak (Eqs. 2.21 and 2.22), while the mean direction would rather be an average over the entire spectrum:

$$\theta_m(f) = \tan^{-1}\left(\frac{\int_0^{\inf} b_1(f)E(f)df}{\int_0^{\inf} a_1(f)E(f)df}\right) \tag{2.29}$$

In practice, there are an upper and a lower frequency limit for the integration, that vary according the equipment capability. The definition of these limits sometimes are important and can impact the estimation of the integrated variables, depending of the energy level at the frequencies limits.

2.3 Stereo video

Figure 2.2: 2013 stereo video experiment on the Marine Hydrophysical research platform, next to Katsiveli in the Black Sea.

Similar to wave buoys, stereo video also measure the sea surface elevation. However, it allows to cover an area of dozens of meters of the ocean surface. The system is based on snap shots or video records of the sea surface captured by a pair of synchronized cameras. The first projects to proposed stereo photography to measure sea surface topography was presented by Chase et al. in 1957. However, the efforts required to extract the three dimensional (3D) elevation maps from a pair of images have limited the use of this technique until late 70s and early 80s (with the works of Sugimori, 1975; Holthuijsen, 1983). A directional measurement of short-scale ocean waves applying stereography was proposed Shemdin et al. (1988), on their experiment were used a pair of cameras mounted on an oceanographic offshore tower to measure the 3D sea surface elevation. Later on, Banner et al. (1989) applied similar stereographic measurement techniques to study the wavenumber spectra of short gravity waves.

More recently, Klette et al. (1998), used a stereo vision technique to measure the water surface topography. They used a conventional stereographic technique algorithms to survey geodetical surfaces and static objects. In 2006, Benetazzo proposed a technique to estimate the shape of water waves using video image analysis that is inexpensive and partially automated with high spatial and temporal resolutions. Based on the same Benetazzo (2006) stereo video technique and the breaking identification method developed by Mironov and Dulov (2008), Leckler (2013) explored the surface

elevation around breaking events and its statistical properties. Nowadays, this stereo video technique is widely used for different investigation proposes on ocean waves (for example the works of Romero et al., 2012a; Fedele et al., 2013; Banner et al., 2014; Leckler et al., 2015; Benetazzo et al., 2016, 2017), with recent efforts of Bergamasco et al. (2017) in publishing a first open source version of WASS (Wave Acquisition Stereo System).

One of the main advantage of this technique is its space and time high resolution. This system is also particularly interesting to investigate breaking conditions because its footprint in the surface reflection can be easily identified in the video records. This observation technique is very important because it fills the gap between large to small-scale ocean observations (for example, 10 m pixel resolution by SAR images) or a single point high frequency observation (wave gauge, moored buoys, PUV, ADCP and others). In this section it is intended to present a short review of the main stereo video principles, 3D wavenumber and frequency spectrum reconstruction and the main principles for breaking detection. The stereo video method present in this section is used in Chapters 3, 4 and 5. The breaking detection method has a especial importance in Chapter 5 and it essential to investigate the longer waves modulation effect on short wave breaking.

2.3.1 3D surface reconstruction principles

The general principle of 3D surface reconstruction presented here are a short compilation of the works developed by Benetazzo (2006) and Leckler (2013) using the WASS system. The main bases of the 3D surface reconstruction consist in finding, given a point in the first image, the same corresponding point in the second image. Usually it uses two fixed and pre-calibrated cameras (Zhang, 2000), and the search of correspondences assumes that the point is over an epipolar lines (Leckler, 2013). This method is optimized using a pinhole camera (Jahne, 2004), which relates a point of the scene to its projection on the image plane. It assumes a rectilinear projection in which the straight lines in a scene are projected into straight lines in the image, where all rays from the 3D scene straightly crosses the image plane and focus on the projection center, at a distance f_c.

A metric coordinate system is fixed to the camera optical axis, with origin in the projection center O_c. The image plane I is defined by the vectors $I(\boldsymbol{i}, \boldsymbol{j})$ orthogonal and parallel to the image plane. The axis Z_c is collinear to the optical axis and the vectors X_c and Y_c are respectively collinear to $\boldsymbol{i}$ and $\boldsymbol{j}$. Therefore, the point $P(X_c, Y_c, Z_c)$ of the scene is related to its projection point $I(i, j)$ on image plane by the pinhole approxima-

tion

$$\begin{bmatrix} i \\ j \end{bmatrix} = \frac{f_c}{Z_c} \begin{bmatrix} X_c \\ Y_c \end{bmatrix} \tag{2.30}$$

The link between the image point $I(i, j)$ and the 3D point $P(X_c, Y_c, Z_c)$ in the 3D world coordinate system depends on its projection in the in the undistorted image and minimal two knows references systems defined by the two or more camera (with a center of projection at the points C_1 and C_2). However, the coordinates P are unknown in the camera reference system $C(O_c, x_c, y_c, z_c)$, so it is defined an external reference system (O', X_o, Y_o, Z_o) called world coordinate system. Assuming that both the camera axes and the world axes are orthogonal and isotropic, the unique Euclidean 3D transformation between the two coordinate systems can be defined by a 3×3 rotation matrix R that transforms axes (X_c, Y_c, Z_c) into axes (X_o, Y_o, Z_o). A 3-dimensional translation vector $\boldsymbol{T}$ can also be used to move the origin from O' to O_c, such that:

$$\begin{bmatrix} X_c \\ Y_c \\ Z_c \end{bmatrix} = R \times \begin{bmatrix} X_o \\ Y_o \\ Z_o \end{bmatrix} + \boldsymbol{T} \tag{2.31}$$

The orientation between the camera and world coordinate systems is given by three successive rotations (ϕ, azimuth; ϑ, tilt; ρ, roll). The complete transformation from world coordinate to camera coordinates (and vice versa) is expressed by the rigid-body motion $g = [R, \boldsymbol{T}]$.

Note, here we present the method considering a pinhole camera, where the image plane is already rectified. But in the reality, the camera lens cause some distortion in the image and must be rectified. Here we simplify this part of the methodology and consider that the lens distortions are already corrected. A detailed explanation of the images calibration and rectification can be obtained in Leckler (2013, section 3.4) and we follow the same method here.

Epipolar geometry

For a two (or more) cameras system with distinct projection centers, the epipolar geometry describes geometric constraints existing between the cameras. This geometry is exemplified at Figure 2.3 and 2.4. The cameras system is based on the pinhole camera model, where the cameras distortion must be previously corrected. The world coordinate system is a priori unknown, so the reference coordinate system is set coincident with the left camera coordinate system where the external parameters $g = [R_1, T_1]$

for left cameras (C_1) is defined by $R_1 = I_3$ and $T_1 = [0,0,0]T$, and $[R_2, T_2]$ describe the relative positions of the left and right cameras. Figure 2.3 from Benetazzo (2006) exemplify relation.

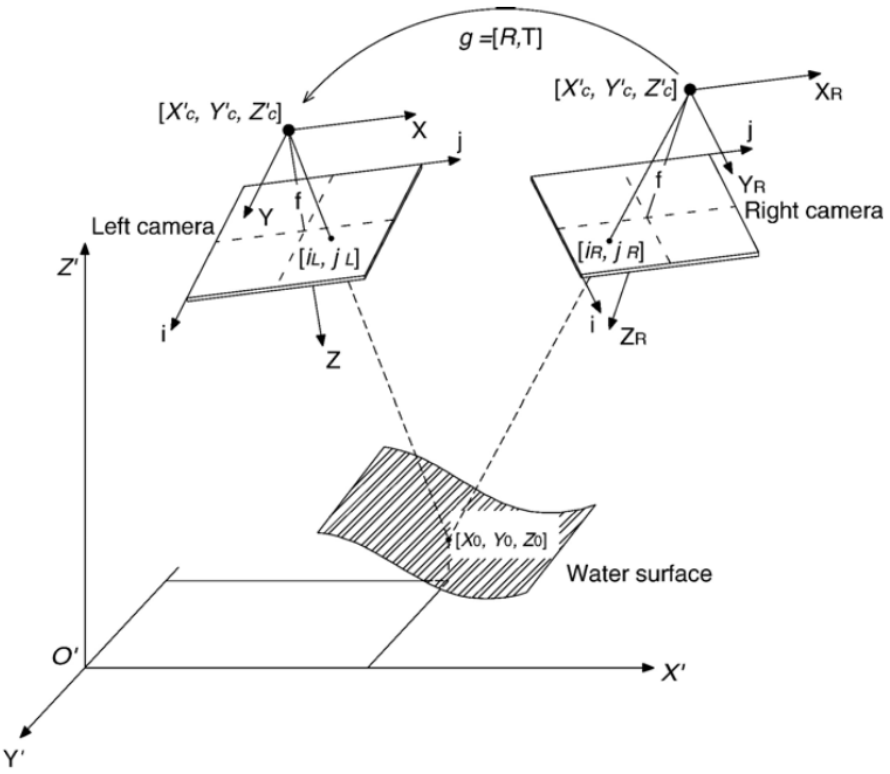

Figure 2.3: Set-up of two camera, Left (C_1) and Right (C_2), stereometric intersection which allows to determinate the three dimensions of a water surface point $[X_0, Y_0, Z_0]$. $[i_L, j_L]$ and $[i_R, j_R]$ are the Left and Right pixel coordinates of the point $[X_0, Y_0, Z_0]$. $g = [R, \boldsymbol{T}]$ is the rigid transformation between Right $[X_R, Y_R, Z_R]$ and Left $[X, Y, Z]$ camera coordinate systems (Image get from Benetazzo, 2006).

This plane that intersects the left and right image planes in lines is called epipolar lines (see Fig2.4). The epipolar points (e_1, e_2) are defined as the intersection of the line (C_1C_2) with the image planes. The projection of the first image plane (I_1) onto $p_1(i_L, j_L)$ corresponds to the point P in the scene and it must be on the ray (C_1, I_1). Therefore, its projection on the second image must be on the epipolar line, which corresponds to the projection of the ray. This relation is exemplified in Figure 2.4 from Leckler (2013).

Best matching corresponding points

This property is used to match the two images corresponding points in the reconstruction processing, with a significant reduction of the search area. The stereo-matching algorithm is proposed by (Benetazzo, 2006) and is based in a pixel-correlation

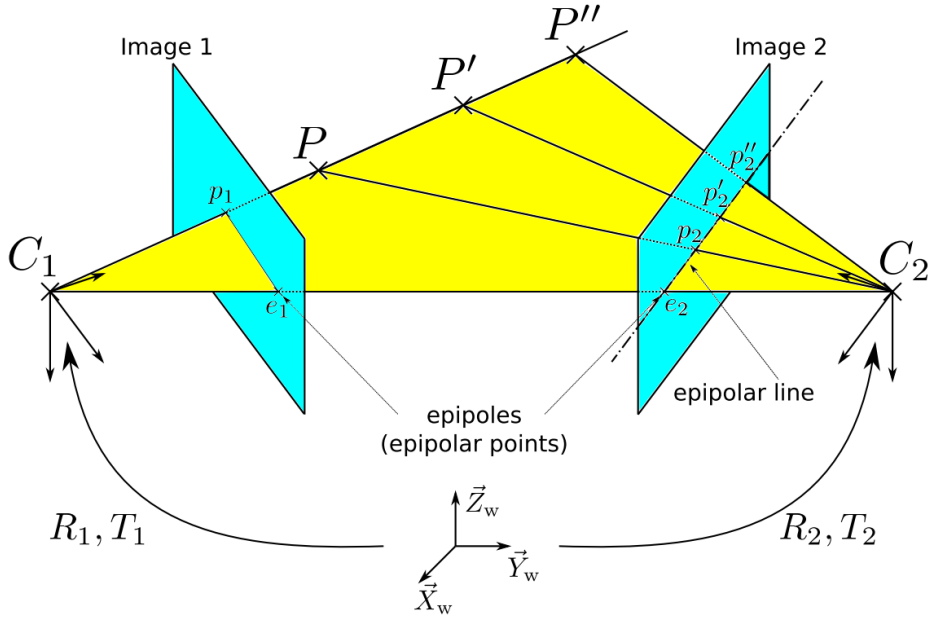

Figure 2.4: Illustration of epipolar geometry for a pair of cameras. The points C_1 and C_2 are the center of projection. The image points e_1 and e_2 are epipolar points. The epipolar plane corresponding to scene point P is represented in yellow. The intersection between the epipolar plane and the image planes defined the epipolar line (Image get from Leckler, 2013, where X_w, Y_w, Z_w correspondent to our world coordinate system X_0, Y_0, Z_0).

between right and left image. A rectangular area is defined around the point in right image to automatically find the corresponding pixel in the other images. This principles of epipolar geometry to find the best matching points were adapted from Ma et al. (2004) by Benetazzo et al. (2012), reducing some the discontinuous transitions in disparity map, and later improved by Leckler (2013) by including best matching corresponding points.

3D triangulation

The determination of the 3D coordinates of a point from its projections onto two images is called stereo triangulation. The homogeneous 3D points coordinates in world reference system are given by vector $[X_o, Y_o, Z_0, 1]^T$ and respectively in camera reference system by $[X_c, Y_c, Z_c, 1]^T$. So the projection of a scene points into the bitmapped image can be represented with a 3×4 matrix C (neglecting the distortion) is

given by

$$Z_c \begin{bmatrix} i \\ j \\ 1 \end{bmatrix} = C \begin{bmatrix} X_o \\ Y_o \\ Z_o \\ 1 \end{bmatrix} = A \begin{bmatrix} R & T \end{bmatrix} \begin{bmatrix} X_o \\ Y_o \\ Z_o \\ 1 \end{bmatrix} \tag{2.32}$$

where R and T are the external parameters and A is the matrix containing the intrinsic cameras parameters from the individual cameras calibration (see Leckler, 2013, Sections 3.4.2 and 3.4.3 for more informations), such that

$$Z_c \begin{bmatrix} i \\ j \\ 1 \end{bmatrix} = A \begin{bmatrix} X_c \\ Y_c \\ Z_c \end{bmatrix} \tag{2.33}$$

R and T can be obtained from the extrinsic calibration (Leckler, 2013)

So, the triangulation process uses the intersection of rays corresponding to left and right corresponding points by a given coordinates of its projection, given by

$$\begin{bmatrix} X_c \\ Y_c \\ Z_c \end{bmatrix} = \alpha C^{-1} \begin{bmatrix} i \\ j \\ 1 \end{bmatrix} \tag{2.34}$$

The ray where are all the possible positions of the point is then given by varying α, and coordinates of the 3D point are given by $\alpha = Z_c$, which is initially unknown.

$$\begin{bmatrix} X_c \\ Y_c \\ Z_c \end{bmatrix} = \alpha_L C_L^{-1} \begin{bmatrix} i_L \\ j_L \\ 1 \end{bmatrix} = \alpha_R C_R^{-1} \begin{bmatrix} i_R \\ j_R \\ 1 \end{bmatrix} \tag{2.35}$$

For a known relative cameras position and the intrinsic camera matrix, triangulation searches for α_L and α_R, which are solution of

$$\begin{bmatrix} X_c \\ Y_c \\ Z_c \end{bmatrix} = \alpha_L A_L^{-1} \begin{bmatrix} i_L \\ j_L \\ 1 \end{bmatrix} = \alpha_R R A_R^{-1} \begin{bmatrix} i_R \\ j_R \\ 1 \end{bmatrix} + T \tag{2.36}$$

When left and right rays intersect, these two points are directly linked by rigid transformation between camera. In general case, the two different points are expressed

in the same reference system (here left camera) where

$$\begin{bmatrix} X_R \\ Y_R \\ Z_R \end{bmatrix} = R \begin{bmatrix} X_L \\ Y_L \\ Z_L \end{bmatrix} + T \tag{2.37}$$

So for each stereo pair (left and right image), the final triangulation returns a scattered set of 3D coordinates points in conformity with the 3D water surface shape and the distribution of the matched pixels (i, j)

Mean plane correction

After the triangulation process, the positions of the 3D water surface points in space and time still in the left camera coordinate system, that is usually tilted in relation to earth plane, with Z' parallel to the gravity acceleration. For a given sequence Benetazzo (2006), explored the hypothesis that the mean water surface elevation time is zero. This is used to define a mean plane, representing the water surface without waves, orthogonal to gravity direction. In fact, it is fair to assume that over a long period of time (say, at least ten times the dominant period of the waves), the time–mean water surface elevation on a single point on the surface will be zero (if no long period waves are observed).

So a rigid transformation can be used to rotate and translate the results from the cameras plane to a mean plane, where the rotation matrix, R_m, and a translation vector T_m are used to define the rigid transformation such that $\boldsymbol{X'} = R_m \boldsymbol{X_L} + \boldsymbol{T}_m$.

In the camera coordinate system, the equation of the mean plane $(aX + bY + cZ + d = 0)$ is obtained through a least square solution. For each point, the water elevation (in the world coordinate is calculated as the distance from the mean plane. Then, the last row of the rotation matrix, R, is given by

$$R = \begin{bmatrix} r_1 \\ r_2 \\ r_3 \end{bmatrix} \tag{2.38}$$

From the mean plane equation parameters a, b, c and d it gives:

$$r_1 = \frac{[a, -(1+a^2)/b, -1]^T}{\sqrt{a^2 + (1+a^2)^2/b^2 + 1}}, \; r_2 = \frac{[b, 0, ab]^T}{\sqrt{a^2 b^2 + b^2}}, \; r_3 = \frac{[a, b, -1]^T}{\sqrt{a^2 + b^2 + 1}} \tag{2.39}$$

So, for a given $[X, Y, Z]^T$ point, the water surface elevation evaluated from the

horizontal mean plane can then be expressed as:

$$Z' = r_3 \begin{bmatrix} X \\ Y \\ Z \end{bmatrix} + \frac{d}{\sqrt{a^2+b^2+1}} \tag{2.40}$$

Thus, the transformation between camera and world coordinate systems is given by:

$$\begin{bmatrix} X' \\ Y' \\ Z' \end{bmatrix} = R \begin{bmatrix} X \\ Y \\ Z \end{bmatrix} + \begin{bmatrix} 0 \\ 0 \\ \frac{d}{\sqrt{a^2+b^2+1}} \end{bmatrix} \tag{2.41}$$

Surface grid

Then all $O'[X',Y',Z']$ scatter cloud of point representing sea surface are gridded at each time frame, producing a discretized surface elevation map $\zeta(x,y,t)$. Here it is usually using a 10 cm grid resolution to cover an area of $\sim$15 to 20 m of sea surface. Due to the strong heterogeneity of the density in the cloud of points, which is denser closer to the cameras, the average distance of matched points tends to be 10 cm for the last part of the construction. The final result is a $\sim$ 30 min evolution of the wavy sea surface with a covered area of about 11 by 20 m. One example of an image and its corresponding reconstructed surface from a stereo video experiment is presented in Figures 2.5 and 2.6.

2.3.2 The wavenumber and frequency spectrum

From the time and space surface elevation map $\zeta(x,y,t)$ it is possible to represent the sea surface in terms of the wavenumber and frequency spectrum. This kind of spectrum was already shown by Dugan et al. (2001), for light intensity spectra. This concept was later appropriated for sea surface elevation by Gallego et al. (2008); Fedele (2012); Fedele et al. (2013), using the similar stereo video system.

The basic ideas of wavenumber and frequency spectrum is to apply a Fast Fourier Transform (FFT) to converts the physical space (x,y,t) into a three dimensional spectral (3D) space $E(k_x,k_y,f)$. For example, for the stereo video acquisitions used in this work it was applied a Fourier transform over the time intervals of 1024 frames and averaging the modulus squared of the three-dimensional Fourier transform over all of overlapping time intervals. Usually, for approximately 29 minutes acquisition at 15 Hz results in 39 overlapping time intervals. The number of degrees of freedom for each spectrum

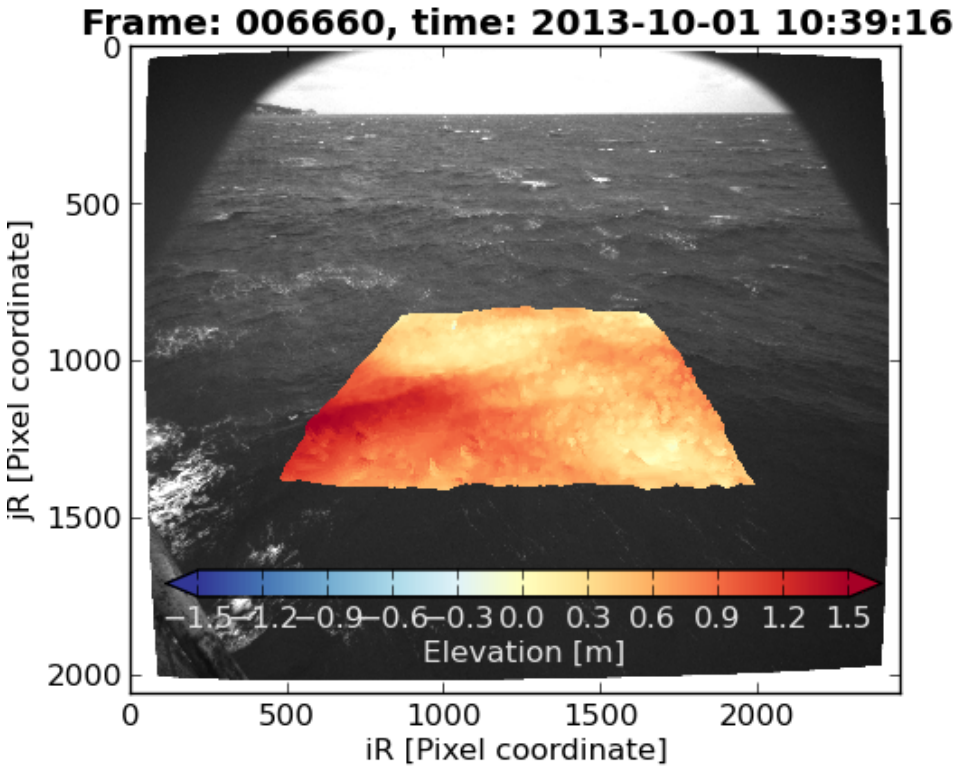

Figure 2.5: Example of stereo video elevation map $\zeta(x,y,t)$ over the associated right camera picture using a wide angle lens.

is $2\times$ the number of FFT without the overlap. But it depends on the duration of each acquisition and number of frames per second (fps), i.e. 20 independent intervals giving 40 degrees of freedom for each spectral density in (k_x,k_y,f)-space.

For this kind of two-dimensional data, windowing is especially important before FFT application, because a rectangular window results in a star-like pattern in the spectra along the principal axes. In this work, the spectrum $E(k_x,k_y,f)$ is obtained after applying a Hamming window in all three dimensions ($h_3(n)$) to the elevation maps $\zeta(x,y,t)$.

$$h(n) = 0.54 - (1-0.54)\cos\left(\frac{2\pi n}{W-1}\right) \tag{2.42}$$

where n is the interval and W is representing the window width. The width of the main lobe of Hamming window in k_x direction is approximately $8\pi dx/\Delta x$ and the side-lobe attenuation is down by 43 dB. It is expected that the Hamming window application can reduce the bounds of Fourier transform noise at approximately 30 dB, causing low loss

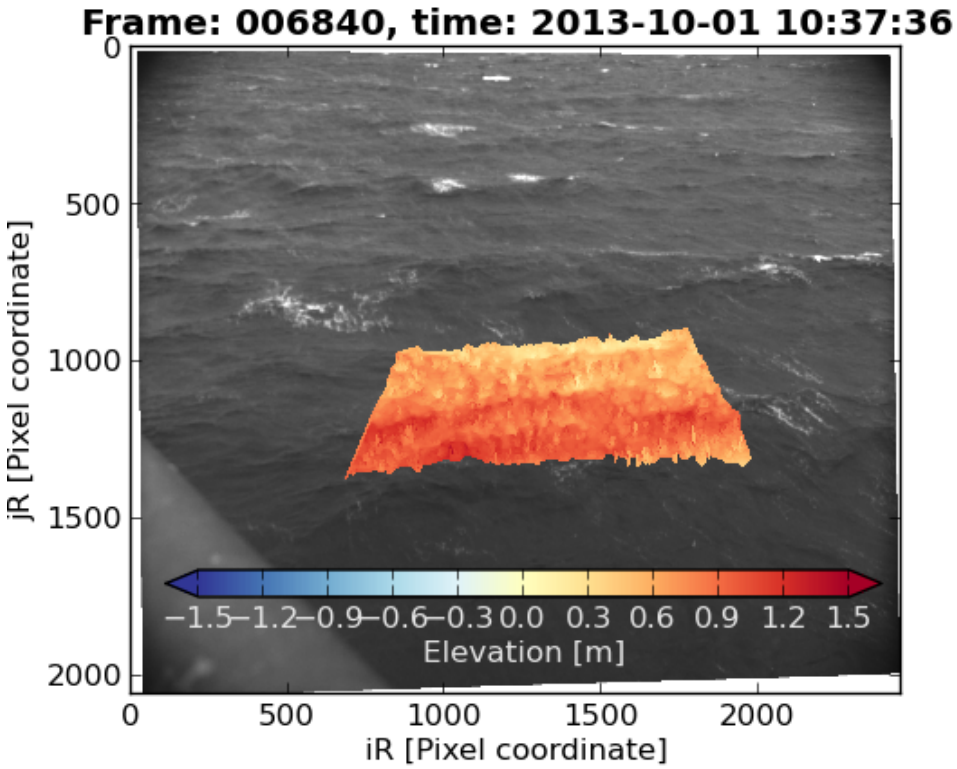

Figure 2.6: Example of stereo video elevation map $\zeta(x,y,t)$ over the associated right camera picture a) using 5 mm zoom lens and 5 cm grid interpolation resolution.

in the narrow-band of the spectrum and small impact in frequency lower than 1.6 Hz.

After the definition of the 3D Hamming window h_3, the energy can be obtained from the complex Fourier amplitude $A(k_x,k_y,f)$ of the three dimensional matrix as (Young, 1999):

$$\zeta_h = \zeta(x,y,t) \times h_3 \tag{2.43}$$

$$\boldsymbol{A}(k_x,k_y,f) = \mathrm{FFT}\left(\frac{\zeta_h}{n_{x,y,t}}\right) \tag{2.44}$$

$$E(k_x,k_y,f) = \frac{1}{h_3^2}\frac{\overline{\boldsymbol{A}\boldsymbol{A}^*}}{dk_x dk_y df} \tag{2.45}$$

The wavenumber spectrum is limited by $L < \frac{1}{2}\Delta x$ and the time frequencies by $T \leqslant \frac{1}{2}\Delta T$. So by combining the space and time spectral analysis, it is reasonable to expect an appropriate wave representation inside the frequency interval 0.07 to 1.6 Hz.

The most traditional spectral representations are usually expressed in terms of $E(f)$ or $E(f,\theta)$, measured by directional buoys or satellite images. However, the works of Leckler (2013); Leckler et al. (2015) and Peureux et al. (2017) explore interesting short wind waves properties from this three dimensions wavenumber and frequency spectrum and dispersion relation. Figure 2.7 exemplifies the aspect of a $\sim$ 30 min 3D spectrum volume for a stereo video measurement started at 2013/09/21 12:16:45 in the research platform of the Marine Hydrophysical Institute in the Black Sea.

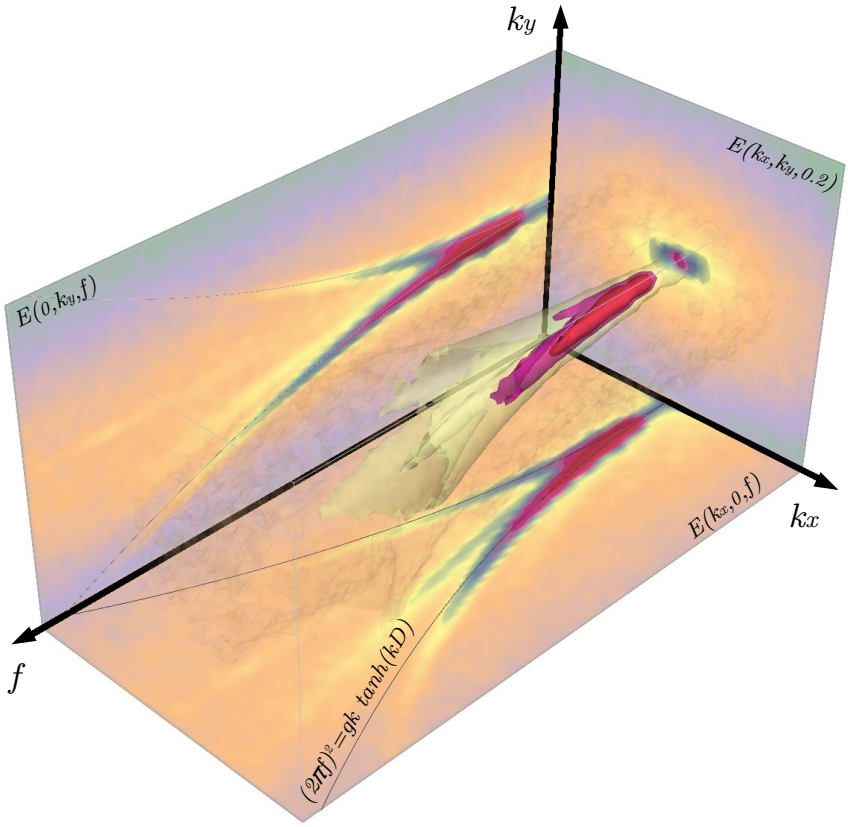

Figure 2.7: Schematic representation of the 3D wave spectrum $E(k_x,k_y,f)$. The volume contours represent the wave energy in logarithmic scale $log(E)$. Projected on three orthogonal planes of the reference frame are three slices in the spectrum (at $k_x = 0$, $k_y = 0$ and $f = 0.2$). The dashed curves plotted over the planes projection represents the linear dispersion relation ($(2\pi f)^2 = gk\tanh(kD)$).

At Figure 2.7 it is expected that the wave energy is mostly concentrated around the linear dispersion relation $(2\pi f)^2 = gk\tanh(kD)$ or shifted by $\boldsymbol{k}\cdot\boldsymbol{C}$ in the presence of uniform current as showed by Leckler et al. (2015) where $D \sim 30m$ is the water depth, g is the acceleration of gravity, $\boldsymbol{C}$ is the current velocity.

2.3.3 Stereo video validation

To evaluate the ability of stereo video to represent the sea surface elevation spectrum, the results are compared here with data from a wave gauge system. The stereo video and wave gauge observations were acquired at a location approximately 30 m deep, during a stereo video experiment on the Marine Hydrophysical research platform, located 500 meters off the coast next to Katsiveli in the Black Sea, near the southern tip of Crimea coast.

The wave gauge was measuring the sea surface elevation at a 10 Hz sampling frequency. The direct application of a FFT, over the wave gauge elevation time series allows to represent the dimensional spectrum $E(f)$ for the same times as the stereo video acquisitions. To compare with the stereo video spectrum, the 3D spectrum $E(k_x, k_y, f)$ was integrated along k_x and k_y direction, resulting in a $E(f)$ dimensional spectrum. The stereo video results were linearly interpolated for the same frequency space and a the comparison between this two sources of data are presented at Figure 2.8.

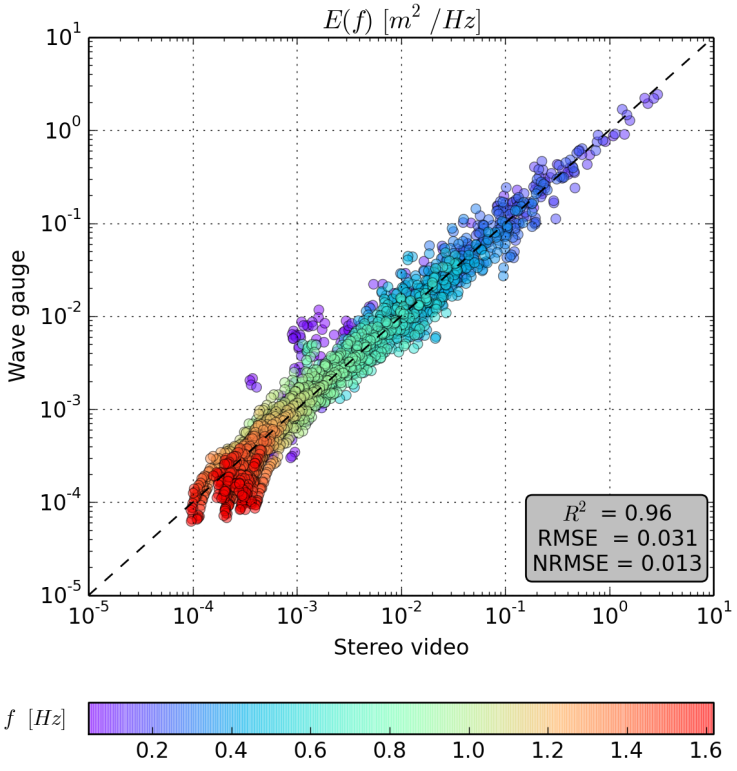

Figure 2.8: Comparison between the wave frequency spectrum $E(f)$ measured by wave gauge installed in the same the Marine Research platform and stereo video system in m^2/Hz. The color scale represents the wave frequency of that sampled data. In the gray box are shown the squared Pearson correlation coefficient (R^2), the Root Mean Square Error (RMSE) and the Normalized Root Mean Square Error (NRMSE).

The statistical parameters used to compare the wave gauge (E_{wg}) and the stereo video (E_{sv}) were the Pearson's linear correlation coefficient (R^2), the Root Mean Square Error (RMSE) and the Normalized Root Mean Square Error (NRMSE)

$$R^2 = \frac{\sum_n (E_{\mathrm{wg}} - \overline{E_{\mathrm{wg}}})(E_{\mathrm{sv}} - \overline{E_{\mathrm{sv}}})}{\sqrt{\sum_n (E_{\mathrm{wg}} - \overline{E_{\mathrm{wg}}})^2 (E_{\mathrm{sv}} - \overline{E_{\mathrm{sv}}})^2}} \tag{2.46}$$

$$\mathrm{RMSE} = \sqrt{\frac{\sum_n (E_{\mathrm{wg}} - E_{\mathrm{sv}})^2}{n}} \tag{2.47}$$

$$\mathrm{NRMSE} = \sqrt{\frac{\sum (E_{\mathrm{wg}} - E_{\mathrm{sv}})^2}{\sum E_{\mathrm{wg}}^2}} \tag{2.48}$$

where the overbar denotes the arithmetic average.

The analysis of Figure 2.8 shows that this processing is consistent in terms of spectral level with the data from the wave gauges, considering a significance level of 95%. It is possible identify an overestimation of the data for some acquisitions at higher frequencies, over 1.4 Hz. According to Leckler (2013), two main sources of error may hinder the accuracy of stereo reconstruction when applied to the sea surface. First, specular sun reflections can give high correlation (one bright spot correlates well with any other bright spot) without corresponding to the same point of the sea surface because the two cameras have different view angles and thus do not see the same specular points. This effect can be removed by choosing both, the position of the cameras and the time of acquisition as a function of the sun position. The second, is given by whitecaps. The foam at the surface makes it difficult to find the best correspondent point in the two cameras because it introduces such a strong inhomogeneity in the brightness that they bias the window-based matching process. To mitigate that effect, Leckler (2013) introduced a histogram equalization combined with a pyramidal search algorithm in three steps, starting from large windows and refining to smaller windows. This procedure reduced considerably the error in matching points around whitecaps. Another source of error can also come from the linear interpolation over the grid. Because the stereo results are not uniformly distributed over the surface and the stereo resolution decreases with the distance from the cameras, the linear interpolation over the grid may include some bias at high frequency. To minimize this error it is possible to increase the number of correlation points in the stereo process. However, to improve the results at higher frequencies, the number of correlation points needed would significantly increase the

computation time during the correlation process.

2.3.4 Waves breaking detection

Recently several authors have been using video processing field observations of wave breaking (e.g. Melville and Matusov, 2002; Mironov and Dulov, 2008; Romero et al., 2012a; Thomson, 2012; Leckler, 2013; Sutherland and Melville, 2013, 2015, and others). The breaking detection method used for this study combines the automatic foam identification (using video records from Mironov and Dulov, 2008) and the surface elevation information captured by stereo video (from Leckler, 2013). The basis of the image processing algorithm proposed by Mironov and Dulov (2008) eliminates human influence in the foam detection by defining a fixed pixel threshold for the whitecapping identification. This method has two main steps (e.g. Mironov and Dulov, 2008) 1) binarization of raw video data and 2) data grouping and dynamic filtration. A third step implemented by Leckler (2013) aim to obtaining the breaking elevation and speed from the stereo video processing. This three steps are briefly summarized here:

Binarization of raw video data

The image brightness varying with several parameters, like the sun position, sea surface slope and clouds, this hinders the definition of an single brightness threshold for whitecapping detection. So the first step of breaking detection consists in removing all unnecessary information not connected with breaking wave properties. For that purpose, the brightness variance at a fixed point of sea surface the image $I(i,j)$ is decomposed into two time scales, $\overline{I}$, that is the averaging sequence of consecutive images and $\widetilde{I}$ that is the instant brightness, where $\widetilde{I}$ must only correspond to the variation of the surface brightness due to the variation of the sea surface $\zeta(x,y)$. So $I = \overline{I} + \widetilde{I}$ and $\overline{I}$ is averaged over 2000 images (e.g. Leckler, 2013).

$$\widetilde{I} = I - \frac{1}{2000}\sum_{t=1}^{2000} I \tag{2.49}$$

Fore example, for 2000 images acquired at 12 Hz, this averaging corresponds to approximately 2.7 min. This process is exemplified in Figure 2.9.a, b and c.

Mironov and Dulov (2008) assumed that the whitecap footprint on the normalized image $\widetilde{I}$ is much more intense than the brightness variation from the sea surface slopes. In other words, from a Gaussian probability distribution $p(\widetilde{I})$ the brightness variations caused by breaking waves are much higher than the σ_I^2 variance. The breaking positions on $\widetilde{I}(i,j)$ image can be obtained from the probability function $F(\widetilde{I})$ of excess the

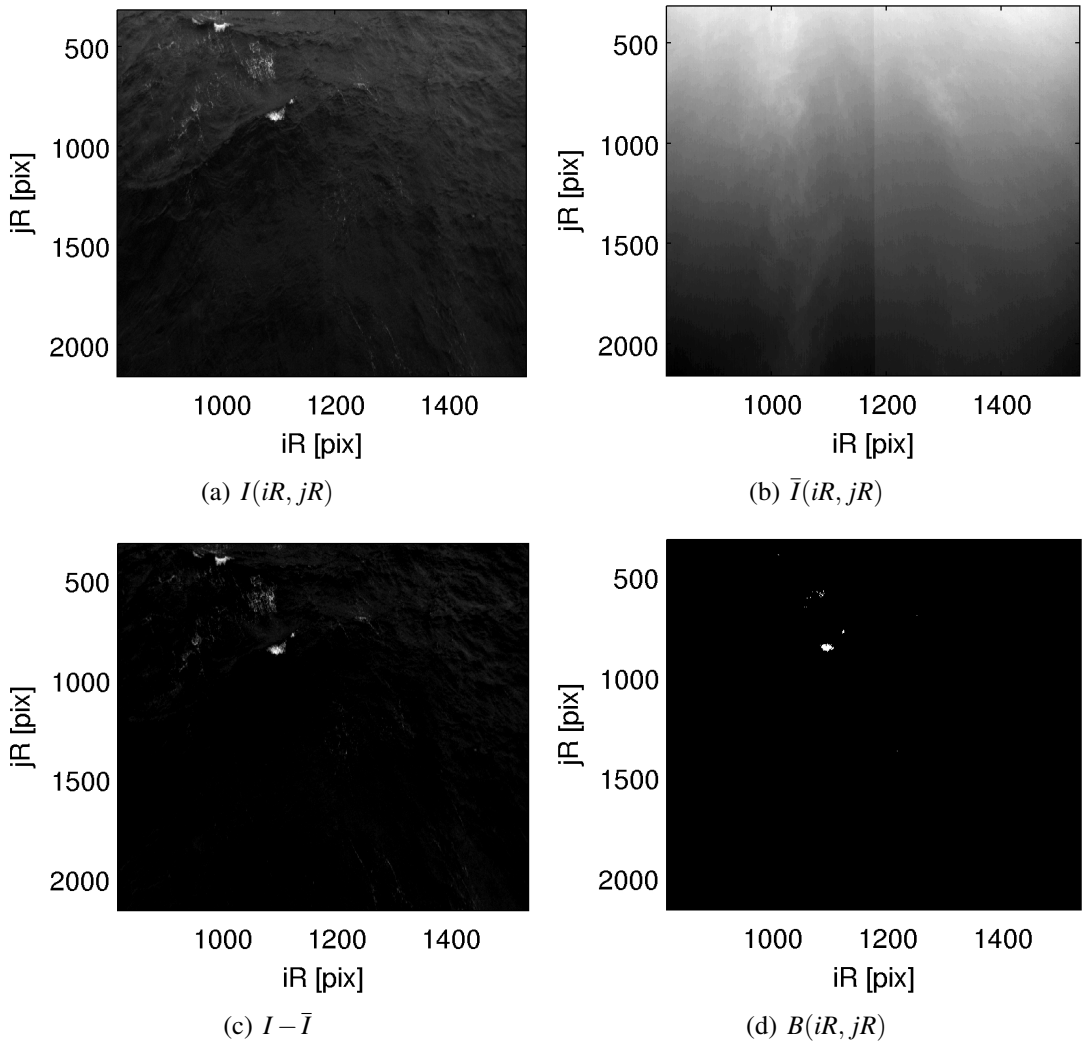

(a) $I(iR, jR)$ (b) $\bar{I}(iR, jR)$

(c) $I - \bar{I}$ (d) $B(iR, jR)$

Figure 2.9: Example of binarization in the video processing for breaking detection as proposed by Mironov and Dulov (2008) and Leckler (2013). a) bitmap gray scale image; b) average image; c) sunlight reduction; d) binary image.

brightness $\widetilde{I}$. For a normal Gaussian function it is:

$$F(I) = \frac{1 - \frac{I - \bar{I}}{\sqrt{2}\sigma_I}}{2} \tag{2.50}$$

Finally the brightness threshold for waves breaking is defined by I_T

$$F_0(I_T) = \frac{F(I_T)}{\varepsilon} \tag{2.51}$$

where $\varepsilon = 10$ is a constant which is adjusted to a threshold level in the $F(I_T)$ distribution. If ε is larger than all pixels highlighted by whitecaps, than it will pass the threshold but the level of errors caused by wave slopes will be too high. Otherwise, if

ε is reduced to a minimum, then we will not detect most of the whitecap information (Mironov and Dulov, 2008). All pixel values above the threshold were then marked as 1 and all others as 0 resulting in a binary matrix $B(i,j)$ (Fig.2.9.c)

$$B(i,j) = \begin{cases} 1, \text{ if } \widetilde{I}(i,j) \geq I_T \\ 0, \text{ if } \widetilde{I}(i,j) < I_T \end{cases} \tag{2.52}$$

Data grouping and dynamic filtration

After a wave breaking event some parts of the whitecaps still remain at the surface. However, this remaining foam condition has very different kinematic characteristics than the active breaking events at the surface. So this second step of Mironov and Dulov (2008) methodology aims to connect the space and time variation of active breaking events only.

Firstly all whitecaps groups which contain less than 200 white points, or whose duration is less than 0.4 seconds are removed. After that the waves were classified as active or passive breaking events. For that purpose, each group of foam points marked with 1 is analyzed separately. The time evolution of the number of foam points $N(t)$ is first computed with

$$N(t) = \sum_i \sum_j B(i,j,t) \tag{2.53}$$

During the breaking, the foam pixels in a same group stretch on a small and localized image part. So, the time evolution of the pixel number $N(t)$ for active breaking can be related to the production of new bubbles, at a faster rate than passive foam disappearance. Typically, $N(t)$ increases to a maximum during active wave breaking and then decreases as a function of the foam lifetime.

If two active breaking events occur in the same image, they are splitted according to their proximity between the foam patches. Each breaking group is split into independent events, such that an event ends when its number of foam points N becomes smaller than 25% of its maximum. A new event starts further if N becomes higher than 25% of the previous minimum of N, and so on.

Breaking elevation and velocity

This third part of the methodology is incorporated by Leckler (2013). As the stereo video processing carries the $I(i_R, j_R)$ transform to $\zeta(x,y,t)$, it is possible obtain a pixel point $P_n(x,y,z,t)$, in world coordinates, for each binarized pixel where $B_n(i,j) \equiv 1$ and $N = n_1, n_2, n_3, \ldots$ corresponds to the total number of of pixels. So, for each

separated active breaking event, the foam points are then projected on the 3D surfaces to obtain the set of N points on a $P_n(x,y,z,t)$ cloud of foam point.

Therefore, speed in each direction of the point set is computed as the least square solution of

$$V_{x,n}(t-\bar{t}) = x_n - \bar{x} \tag{2.54}$$

$$V_{y,n}(t-\bar{t}) = y_n - \bar{y} \tag{2.55}$$

This returns an instantaneous breaking velocity V_n for each n element of the breaking group, where mean foam distribution is given by $\bar{x}$ and $\bar{y}$,

$$\bar{x} = \frac{1}{N}\sum_{n=1}^{N} x_n \qquad \text{and} \qquad \bar{y} = \frac{1}{N}\sum_{n=1}^{N} y_n. \tag{2.56}$$

The breaking velocities are used afterward to identify active breaking from the passive foam drift (where foam moves with rather slow speed, modulated by wave orbital velocity). In this case, all events with breaking speed lower than 1 m/s were considered to be small breaking events or passive foam, so they were removed. If the breaking velocity is consider equal to the phase velocity, this also must filter any wave breaking for waves shorter than 1.5 Hz. Figure 2.10 shows the time evolution of a breaking event, the red dots contour the active breaking foam and the blue dots represent small breaking conditions or passive foam, removed from the statistics. Figure 2.11 shows the same active breaking event projected over the surface elevation from stereo video detection.

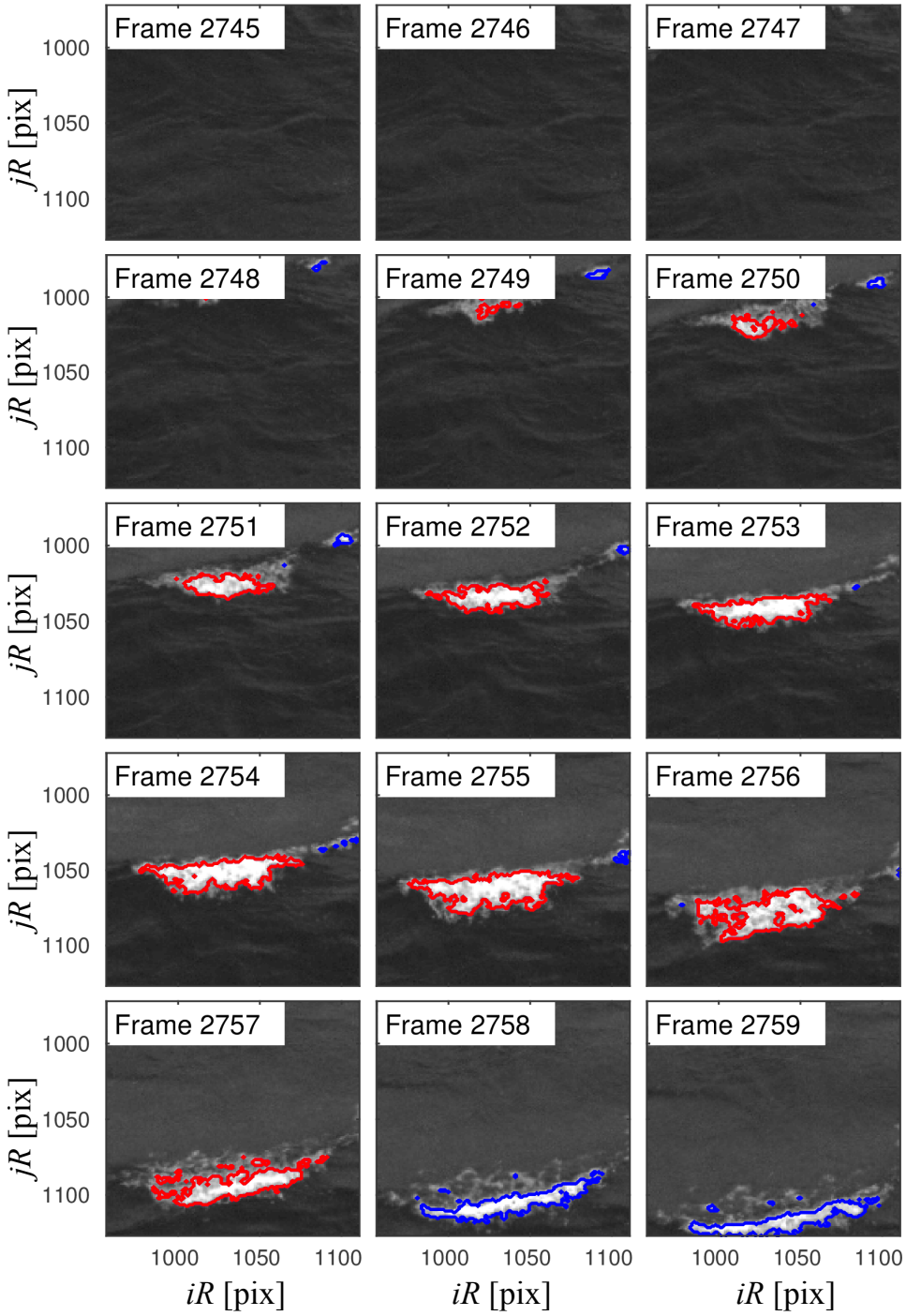

Figure 2.10: Example of active breaking event detection for a 12 Hz stereo video acquisition starting at 2013/10/01 10:30:01Z. The figure shows the $I(iR, jR, nt)$ matrix for $nt = [2745 : 2759]$. The blue contours white patches are detected by threshold method, which represent the none active breaking. The red contour is the filtered active breaking.

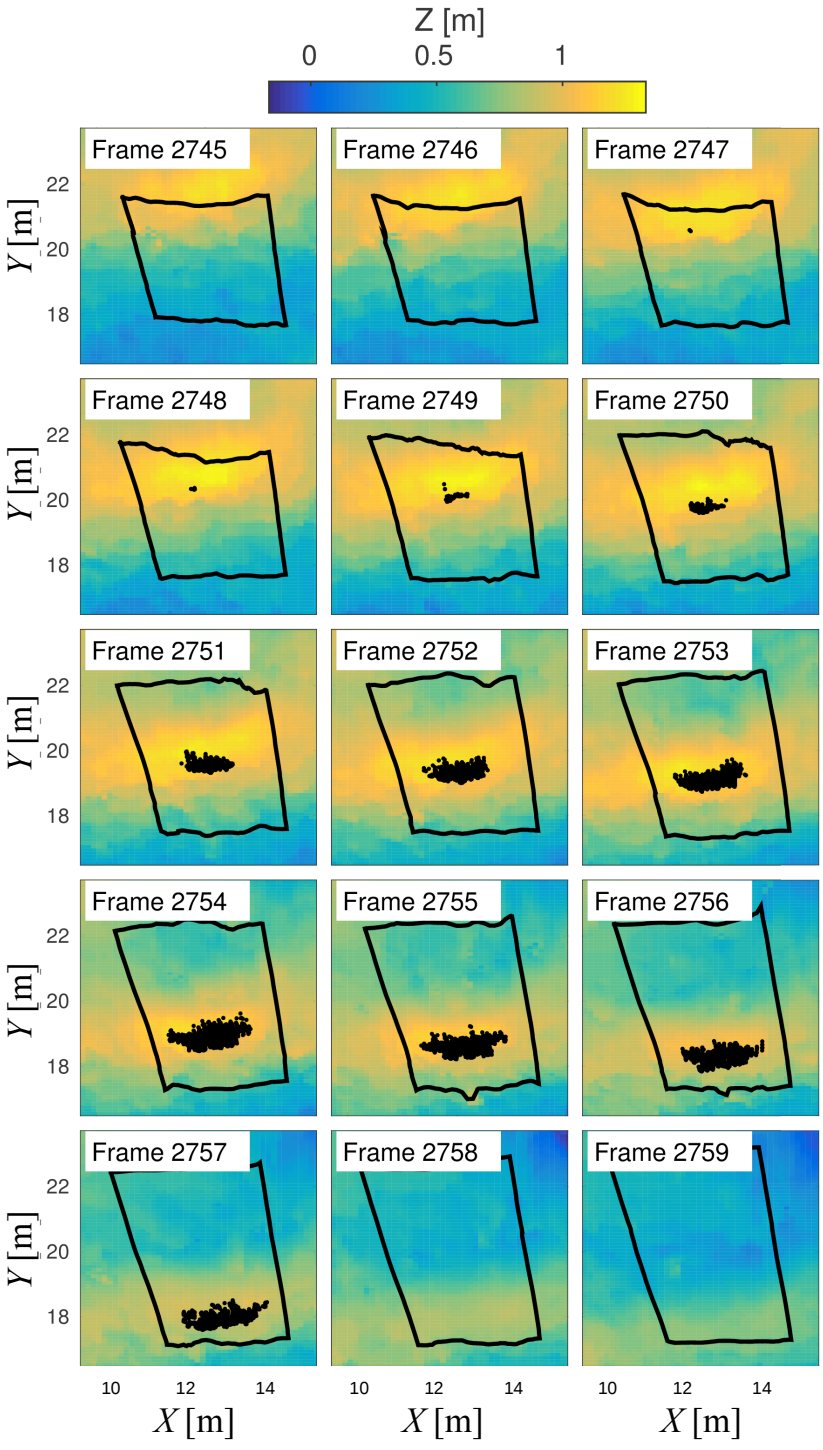

Figure 2.11: Example of active breaking event detection for a 12Hz stereo video acquisition starting at 2013/10/01 10:30:01Z. The figure shows the $\zeta(x,y,t)$ elevation map, the black dots correspond to the *iR* and *jR* pixels points inside the red contour showed on 2.10.

2.4 Ship-mounted stereo video

A ship-mounted stereo video wave system was proposed by Benetazzo et al. (2016). On their system the plane orientation and position were relative to the mean sea plane correction accounted at each single frame, without complementary data sources for the compensation of ship motion. The system described here, and used in the Chapters 4 and 3, is just a little bit different. In our case, the pair of video cameras were synchronized with a Motion Unit to correct the ship movements and with a GPS system to get the geographical cameras position (Fig2.12).

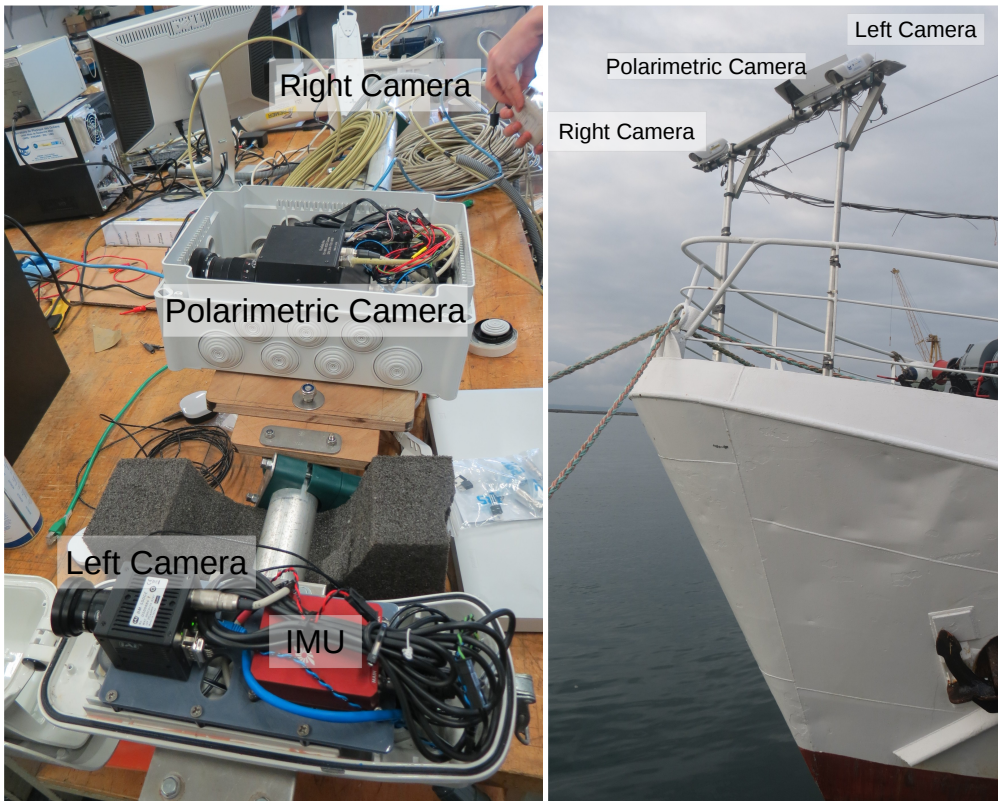

Figure 2.12: Ship-mounted stereo video system

To correct the reference frame of the image on a moving platform a compact Inertial Navigation System with integrated Dual-antenna GNSS (Global Navigation Satellite System) receiver Ellipse2-D was used. This includes a MEMS-based Inertial Measurement Unit (IMU) and runs an enhanced Extended Kalman Filter (EKF) which fuses inertial and GNSS data. It provides the Roll, Pitch, Heading, Heave, and Navigation data at 50Hz. The EKF output, using the Kalman filter, returns the device 3D orientation represented with a normalized quaternion $(q_0; q_1; q_2; q_3)$ or there equivalent in Eulerian angles in radian with roll, pitch and yaw.

The triangulation process is exactly the same as in a fixed platform and it converts

the 3D pixel coordinates over a moving reference frame (X_c, Y_c, Z_c) with an origin in the left camera. A solid transform is used to translate the origin to the IMU reference system, obtained from a previous laboratory measurements of the relative positions. So, from the normalized quaternion measured by the IMU it is possible to obtain the quaternion-derived rotation matrix $R = R_{Q_1} R_{Q_2} R_{Q_3}$, in which

$$
\begin{aligned}
R_{Q_1} &= \begin{bmatrix} q_0^2 + q_1^2 - q_2^2 - q_3^2 \\ 2(q_1 q_2 + q_0 q_3) \\ 2(q_1 q_3 + q_0 q_2) \end{bmatrix}, \\
R_{Q_2} &= \begin{bmatrix} 2(q_1 q_2 + q_0 q_3) \\ q_0^2 + q_1^2 - q_2^2 - q_3^2 \\ 2(q_2 q_3 + q_0 q_1) \end{bmatrix}, \\
R_{Q_3} &= \begin{bmatrix} 2(q_1 q_3 + q_0 q_2) \\ 2(q_2 q_3 + q_0 q_1) \\ q_0^2 + q_1^2 - q_2^2 - q_3^2 \end{bmatrix}
\end{aligned}
\tag{2.57}
$$

and from the GPS coordinates it is possible to translate the reference system to the earth reference coordinate system (X_e, Y_e, Z_e) in meters. The earth reference coordinate system has an arbitrary origin, with $Z_e = 0$ corresponding to the mean sea surface height, and X_e and Y_e directed toward the east and north, respectively.

$$
\begin{bmatrix} X_e \\ Y_e \\ Z_e \end{bmatrix} = R \begin{bmatrix} X_c \\ Y_c \\ Z_c \end{bmatrix} + \boldsymbol{T}
$$

where $\boldsymbol{T}$, the translation vector is here simplified to directly transform from left camera optical center to the earth reference system. This includes the translations from image to camera and camera to IMU references. Additionally, X_e and Y_e are translated to the Universal Transverse Mercator (UTM) conformal projection (Fig.2.13). Once the stereo video data are expressed in UTM reference system, the results are gridded to produce a discretized surface elevation map $\zeta(y,x,t)$. The $\sim$30 min results were gridded over a 10×10 m square surface with 0.1 m resolution (black square in Fig.2.13.b), where X, Y represent the longitude and latitude in UTM. Because the boat is moving, the central grid position is adjusted to move at the same speed.

The 3D spectrum $E(k_x, k_y, f)$ were obtained afterwards, similarly as described in Section 2.3.2, applying a Hamming window in all three dimensions to the elevation maps over time intervals of 85.33 seconds (1024 frames), with 50% overlapping as well, resulting on 41 windows and 40 degrees of freedom. However, the energy over frequency and waves number are now in a Lagrangian reference frame moving at the

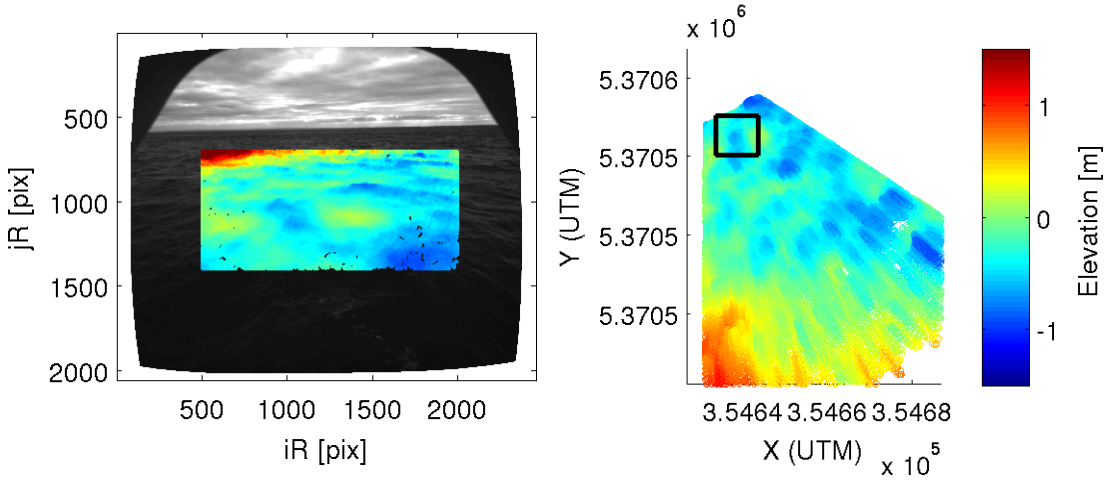

(a) (b)

Figure 2.13: Results from the ship-mounted stereo video. a) sample of the resulting surface elevation $\zeta(iR, jR, 100)$ from the stereo video over the right bitmap image. b) sample of the stereo video surface elevation $\zeta(X_e, Y_e, 100)$ in UTM coordinate system, with limits of the grid surface used for the the FFT in black.

same speed as the boat. So the Doppler shift in σ must be corrected by the mean boat velocity ($\boldsymbol{U_b}$) over the 1024 time windows. Thus, the apparent frequency is corrected by $\sigma_c = \sigma - \boldsymbol{k} \cdot \boldsymbol{U_b}$. Consequently, the heave frequency spectrum $E(f)$ is obtained by integration of the 3D spectrum and it is expressed in terms of the absolute frequency $\omega = \sigma_c + \boldsymbol{k} \cdot \boldsymbol{U} = 2\pi f_a$.

This kind of ship-mounted stereo video system has some advantages over Eulerian stereo video because it allows to follow some oceanic structures and to observe different scales of oceanic processes interacting with the waves system, like thermohaline front or tidal current. A field observation of wave and current interactions by this equipment is presented in Chapter 4 and a spectral comparison between this the ship-mounted stereo video system and a moored Waverider buoy is presented on Section 3.3.

2.5 Drifting buoys

Figure 2.14: Drifting buoys during BBWAVES 2016 experiment, also see Chapter 3.

As an alternative to the ship-mounted stereo video system, drifting buoys can be also quite efficient to measure the transformations of waves traveling across varying current conditions. Drifters or Lagrangian free-floating buoys follow the surface currents and measure the wave conditions across their path. This kind of buoys can measure a quite broad range of ocean conditions. When placed in arrays and synchronized, they can cover a wide ocean area where they measure the wave transformations.

The basis of sea surface reconstruction for a Lagrangian free-floating buoys is already described by Longuet-Higgins (1986). The spectral measurement of the sea surface is very similar to what was described in Section 2.2, but this time over a Lagrangian frame, moving at speed $\boldsymbol{U}$, the spectra and co-spectra of these time series provide moments of the directional distribution of the spectrum $E(f_r, \theta)$, in terms of the relative frequency, that are the first terms in a Fourier expansion of the directional distribution, $E(f_r)$, $a_1(f_r)$, $b_1(f_r)$, $a_2(f_r)$, $b_2(f_r)$. From those quantities it is possible to obtain the mean direction and the directional spreading such as the one presented on Equations 2.25 and 2.25.

The energy quantities measured by drifting buoys are indeed different from the one from moored buoys. So a special attention must be paid to compare current-following buoys with other Eulerian sensors or numerical simulations. Eulerian sensors measure $E(f_a)$ while drifters measure $E(f_r)$. In order compare the two systems we must correct the wave energy to the same inertial frame, where $E(f_a)df_a = E(f_r)df_r$,

so

$$E(f_a) = E(f_r)\frac{df_r}{df_a} \tag{2.58}$$

In terms of applicability, moored buoys can usually not be placed in current conditions because the tension in the moored line can interfere in the measurement. So in practice, in low current conditions $f_r \approx f_a$ and $E(f_a) \approx E(f_r)$ (also see, Sec.2.4).

Because of this limitation for moored buoys measuring wave conditions over strong tidal current conditions, we developed and tested a new design of drifting buoy as part of this work. The "surface kinematic buoy" (SKIB), was indeed particularly optimized for the measurement of wave-current interactions. A technical paper introducing SKIB and its applicability is being prepared and a preliminary version is presented in Chapter 3.

2.6 Final considerations

In summary, this chapter presents a short review of the most common sea surface observation techniques, like PUV, ADCP, radar, satellite and focused on the main instruments used in this work, wave buoys, stereo video and wave breaking detection.

Each of the these equipments have their owns pros and cons. So the observation of certain phenomenons at the ocean may have been limited by the choice of the most appropriate technique for each condition.

The stereo video techniques (Sec.2.3), for example, can provide a unique space and time measurement of the sea surface elevation, including all the wave non-linearities. However, this method is still limited to a few meters of sea surface reconstruction inside of the cameras view and to a short time series acquisitions. When combined the stereo video with the breaking detection, these methods can provide deterministic properties of breaking waves, usually only observed in laboratory conditions. These tools are mainly explored in Chapter 5 to investigate long wave modulation on short waves breaking. Some primary results for stereo video experiments in shallow water and surf zone are also presented in Appendix A.

In Chapter 4 the ship-mounted stereo video system (Sec.2.4) is used to explore waves and current interactions and in Chapter 4 it is compared with Waverider buoy in Chapter 3.

Because of its long term reliability, in this work, the Datawell waverider buoy (Sec.2.2) is mostly used to validate other sensors. However, because of the tension that current creates in the mooring line, this equipment is not suitable to be placed in

strong current environments. In this sense, drifting buoys (Sec.2.5) were very essential to observe the transformation under strong tidal current gradients, that will be deeper explored in Chapter 4. Because this buoys importance in this work, a deeper exploration of this equipment limitations and advantages will explored in next chapter, that is mainly dedicated to introduce and validate a new design of drifting buoys especially developed for measuring wave-current interaction.

3. Surface KInematics Buoy (SKIB)

Résumé

Les systèmes mondiaux de navigation par satellite (Global Navigation Satellite Systems, GNSS) et les ensembles de capteurs de mouvement modernes permettent de mesurer les vagues de surface de l'océan à l'aide de bouées dérivantes à faible coût. La dérive le long ou à travers les gradients de courant fournit des mesures uniques des interactions vagues-courant. Dans cette étude, nous étudions la réponse de plusieurs combinaisons de récepteur GNSS, de capteurs de mouvements et de coques pour définir un prototype de bouée appelé SKIB (Surface Kinematic Buoy), particulièrement optimisé pour mesurer les interactions vagues-courant, y compris les composantes d'ondes relativement courtes (fréquence relative autour de 1 Hz) qui sont importantes pour les interactions air-mer et applications de télédétection. La comparaison avec les bouées existantes, Waverider Datawell et SWIFT, ainsi que l'imagerie stéréo-vidéo, démontre la précision de SKIB. L'utilisation d'accéléromètres à faible coût intégrés dans une coque sphérique nervurée et à jupe fournit des spectres de pilonnement acceptables, tandis que les estimations de vitesse des récepteurs GNSS donnent une direction moyenne de courant et une donnée de directionnalité de l'état de mer. L'utilisation d'une carte d'acquisition basse consommation permet des déploiements autonomes sur plusieurs mois avec des données transmises par satellite. La capacité à mesurer les variations dans le champ de vagues induites par le courant est illustrée par des données acquises dans un environnement côtier macrotidal.

A Surface KInematics Buoy (SKIB) for wave-current interactions studies

Pedro Veras Guimarães, Peter Sutherland, Fabrice Ardhuin, Michel Hamon and Mickael Accensi

Ifremer, Laboratoire, d'Océanographie Physique et Spatiale (LOPS), IUEM, Brest, France.

Alvise Benetazzo

Institute of Marine Sciences, Italian National Research Council (ISMAR-CNR), Venice, 30122, Italy.

Jim Thomson

Applied Physics Lab, University of Washington, US

Yves Pérignon and Pierre Ferrant

LHEEA lab - UMR6598, Ecole Centrale de Nantes

Abstract

Global Navigation Satellite Systems (GNSS) and modern motion-sensor packages allow the measurement of ocean surface waves with low-cost drifters. Drifting along or across current gradients provides unique measurements of wave-current interactions. In this study, we investigate the response of several combinations of GNSS receiver, motion-sensor package and hull design in order to define a prototype "surface kinematic buoy" (SKIB) that is particularly optimized for measuring wave-current interactions, including relatively short wave components (relative frequency around 1 Hz) that are important for air-sea interactions and remote sensing applications. The comparison with existing Datawell Directional Waverider and SWIFT buoys, as well as stereo-video imagery demonstrates the accuracy of SKIB. The use of low-cost accelerometers and a spherical ribbed and skirted hull design provide acceptable heave spectra, while velocity estimates from GNSS receivers yield a mean direction and directional spread. Using a low-power acquisition board allows autonomous deployments over several months with data transmitted by satellite. The capability to measure current-induced wave variations is illustrated with data acquired in a macro-tidal coastal environment.

Submitted to Ocean Science

3.1 Introduction

Many devices have been developed to measure ocean waves, from in situ moored or drifting sensors, to remote sensing systems using optical or radar devices (COST Action 714 Working Group 3, 2005). Each measurement system has a specific range of applications defined by the required space and time resolution and coverage, water depth, current speed. These have been very useful in studying upper ocean processes or monitoring sea states for various applications.

Among all these, surface buoys such as the Datawell directional Waverider has been a reference instrument for the estimation of the surface elevation spectrum in frequency from measurements of vertical acceleration. The horizontal accelerations combined with vertical give the first five moments of the directional spectrum that can be used to estimate the directional wave spectrum (e.g. Benoit et al., 1997). In conditions with strong currents, say more than 1 m/s, it is usually impossible to measure waves with a moored surface buoy, due to the tension on the mooring line. This problem is avoided with drifting buoys, but the nature of the measurement is different. Drifting buoys will not measure long time series at the same location, but they can provide a unique cross-section of waves following the current (Pearman et al., 2014).

Several such drifting buoys have been developed recently for different applications (Herbers et al., 2012; Thomson, 2012; Reverdin et al., 2013). With our focus on relatively short gravity waves, with wavelenghts between 1 and 30 m, there is a trade-off between the size and the response of the device to the waves.

Herbers et al. (2012) proposed a compact and low-cost 45-cm diameter GPS-Tracked drifting buoys. This buoy uses a GPS receiver for absolute position tracking. Compared with Datawell this authors find that the horizontal wave orbital displacements are accurately resolved, although, the vertical sea surface displacements were not well resolved by standard GPS measurements, requiring to attach an external high precision antenna to the drifter.

Thomson (2012) developed the Surface Wave Instrument Float with Tracking (SWIFT), a multi-sensor drifter buoy. This short instrumented spar buoy has a 0.3 m diameter and 2.15-m height, and has been designed to measure wind, waves, whitecap properties and underwater turbulence and current profiles. Wave measurements are derived from the phase-resolving GPS, that contain the wave orbital motions relative to the earth reference frame. The relatively large size of the buoy is needed for the other measurements, and it results in a very weak response for wave frequencies above 0.4 Hz. Obviously, the SWIFT buoy design has other benefits, such as the use of an acoustic Doppler current profiler that allows to investigate the effect of the vertical

current shear on the waves (Zippel and Thomson, 2017).

Reverdin et al. (2013) developed a surface wave rider (called “Surpact") to measure sea state and atmospheric sea level pressure as well as temperature and salinity at a small fixed depth from the surface. Surpacts use a floating annular ring (28 cm diameter) with a rotating axis across it to which the instrumented tag is attached and uses the vertical acceleration to obtain the power spectrum between 0.2 Hz and 2.2 Hz.

Within limitations, the changing position of drifting buoys can also be used to estimate near surface currents, with buoy trajectories representing the result of the integral of wind and current forcing over the entire buoy.

Our intention is to capture the response of surface gravity waves to horizontal current gradients, in order to better interpret airborne and satellite imagery of waves and current features (e.g. Kudryavtsev, 2005; Rascle et al., 2014, 2017), and improve on the parameterizations of numerical wave models (e.g. Ardhuin et al., 2009; van der Westhuysen et al., 2012).

The paper is organized as follows. Section 3.2 presents the relations between parameters recorded by the various devices used in our study and the wave spectrum. Section 3.3 explains the design of SKIB and validation in the laboratory and in situ. Section 3.4 describes an example application to measurements of waves and currents, and conclusions follow in Section 3.5.

3.2 measurable parameters and processing

For irregular wind waves, variance of the sea surface is described using variance density spectra $E(f_r,\theta)$, or the action density spectrum $N(k,\theta)$, where $N(k,\theta) = E(f_r,\theta)/\sigma$, $f_r = 2\pi/\sigma$ is the intrinsic wave frequency, θ is the wave direction.

The wavenumber k is related to the intrinsic wave frequency, the frequency measured by a drifting buoy following the current,

$$\sigma^2 = gk\tanh(kD). \tag{3.1}$$

This frequency differs from the absolute frequency $f_a = \omega/(2\pi)$ observed in a reference frame attached to the solid Earth. Assuming a current vector $\boldsymbol{U}$ that is uniform over the vertical, these two frequencies are related by a Doppler shift,

$$\omega = \sigma + \boldsymbol{k}\cdot\boldsymbol{U}. \tag{3.2}$$

When drifting with the current vector $\boldsymbol{U}$, a surface buoy can measure the three components of the acceleration vector (a_x, a_y, a_z), the GPS horizontal Doppler velocities

(u,v) and positions (x,y,z). In practice the accelerations and horizontal velocities have relatively low noise and can be used to measure waves. In our SKIB acquisition system, the GPS data is sampled at 1 Hz while the accelerometer is sampled at 25 Hz and they are independent systems.

The spectra and co-spectra of these time series can provide the moments of the directional distribution of the spectrum $E(f_r,\theta)$, that are the first terms in a Fourier expansion of the directional distribution, $E(f_r)$, $a_1(f_r)$,$b_1(f_r)$,$a_2(f_r)$,$b_2(f_r)$ (Longuet-Higgins et al., 1963; Kuik et al., 1988).

From the first moments it is customary to define a mean direction $\theta_1(f_r)$ and directional spread $\sigma_1(f_r)$,

$$\theta_1(f_r) = \tan^{-1}(b_1/a_1), \tag{3.3}$$

$$\sigma_1(f_r) = \sqrt{2\left(1-\sqrt{a_1^2+b_1^2}\right)}. \tag{3.4}$$

When only velocity measurement are available, one can only access $E(f_r)$,$a_2(f_r)$,$b_2(f_r)$, which give the two following parameters,

$$\theta_2(f_r) = \tfrac{1}{2}\tan^{-1}(b_2/a_2), \tag{3.5}$$

$$\sigma_2(f_r) = \sqrt{0.5\left(1-\sqrt{a_2^2+b_2^2}\right)}. \tag{3.6}$$

For completeness, here are how the spectra of and co-spectra C_{xy} of two quantities x and y, with x or y replaced by h for heave, and u or v for the horizontal velocity components, are linked to the directional moments,

$$\begin{pmatrix} a_1(f_r) \\ b_1(f_r) \\ a_2(f_r) \\ b_2(f_r) \end{pmatrix} = \int_0^{2\pi} \begin{pmatrix} \cos\theta \\ \sin\theta \\ \cos 2\theta \\ \sin 2\theta \end{pmatrix} E(f_r,\theta)d\theta \Big/ \int_0^{2\pi} E(f_r,\theta)d\theta = \begin{pmatrix} C_{uh}/\sqrt{C_{hh}(C_{uu}+C_{vv})} \\ C_{vh}/\sqrt{C_{hh}(C_{uu}+C_{vv})} \\ (C_{uu}-C_{vv})/(C_{uu}+C_{vv}) \\ 2C_{uv}/(C_{uu}+C_{vv}) \end{pmatrix}. \tag{3.7}$$

We estimated the auto- and cross-spectra following Welch (1967), using Fourier transforms over time series of 5000 samples, with a 50% overlap, and using a Hann window. The resulting spectra have a frequency resolution of 0.005 Hz and 24 degrees of freedom (12 independent windows and 11 overlapped windows).

Because the GPS and accelerometer have different sampling frequencies, the buoy displacements are linearly interpolated on the accelerometer sampling time steps. This is only required for the co-spectrum of the horizontal displacements $C_{uv}(f)$, and quadrature-spectra of horizontal and vertical displacements $C_{uh}(f)$, $C_{vh}(f)$.

Here we will focus on frequencies between 0.06 to 0.80 Hz for our investigation of current gradients. We will also discuss the full frequency range for a validation of the buoy behavior.

3.3 Buoy design and validation

3.3.1 Hull shape and constraints of deployment at sea

We performed a first experiment in September 2014 using buoys provided by T. T. Janssen. These were early prototypes that evolved into the Spotter buoy (https://spoondrift.co/). They functioned very well, using GPS-derived orbital velocities giving estimates of $E(f_r)$, $\theta_2(f_r)$ and $\sigma_2(f_r)$ up to a frequency of 0.5 Hz. These buoys had a spherical plexiglass hull and were deployed with a lead weight attached to their bottom with a rope to provide some stability. This weight introduces a mass-spring resonance at a frequency of 0.8 Hz, making the measurement of wave properties in the frequency range 0.5 to 1 Hz difficult. A similar resonance exists for the short spar SWIFT buoys, due to their shape.

The hull shape is clearly important when resolving short wave components. The main drivers are the stability of the buoy, we typically want to have the top of the buoy stay above its bottom, in particular for radio transmission, we also wish to avoid rotation of the buoy relative to the water around it, and finally the buoy has to be big enough to be visible for recovery and small enough to be easily handled and to follow the motion of short waves. One final driver is the cost of the hull.

With all these constraints in mind we found that a nearly spherical shape with ribs and an additional skirt provided a good water-following behavior. Three-dimensional printing was tested without much success due to the porosity of the printed material. For the small number of buoys that we needed we finally settled on glass spheres, for which we had other oceanographic uses, encased in a plastic ribbed cage, as shown in Figures 3.1 and 3.2.a,b.

3.3.2 SKIB Electronics

The accelerometer and the GPS system are directly integrated in a general-purpose oceanographic "Advanced Low Energy Electronic System" (ALEES) board developed by Ifremer/RDT especially for applications which need very low power consumption. This generic board uses a micro-controller 32bits EFM32 cortex M3, working at 48MHz, 1Mb flash memory and 128Kb RAM. The data is stored in a SDHC micro memory card. The GPS and the accelerometer are not synchronized and and the

acquisition rates are 1Hz and 25Hz respectively.

The integrated accelerometer is a STMicroelectronics model LIS3DH (this is the SKIB STM buoy version), already incorporated in the ALEES board for other uses, namely the detection of strong motions for under-water sensors. This low-cost (less that 2 USD) component was chosen for its very low power use, between 2 and 6 μA at 2.5 V.

A specific board was designed to control the GPS acquisition and send the buoy position via the IRIDIUM board. We typically programmed the buoy to send position messages every 10 min, in order to be able to find the instruments at sea in highly variable currents. The ALEES board and Xbee module are plugged in a SYREDOMY board for an underwater wireless pop-up system. The ALEES and GPS boards can be controlled by a 802.15.4. Zigbee wireless link with an application layer. This wireless link also allow the user to setup the buoy and to recover the data without opening the glass spheres, allowing to powering on and off the system.

All the system, the electronic boards, battery pack and antennas (Xbee, GPS, Iridium) is mounted inside a 10-inch diameter glass sphere, which is vacuum-sealed. See Figure 3.1.

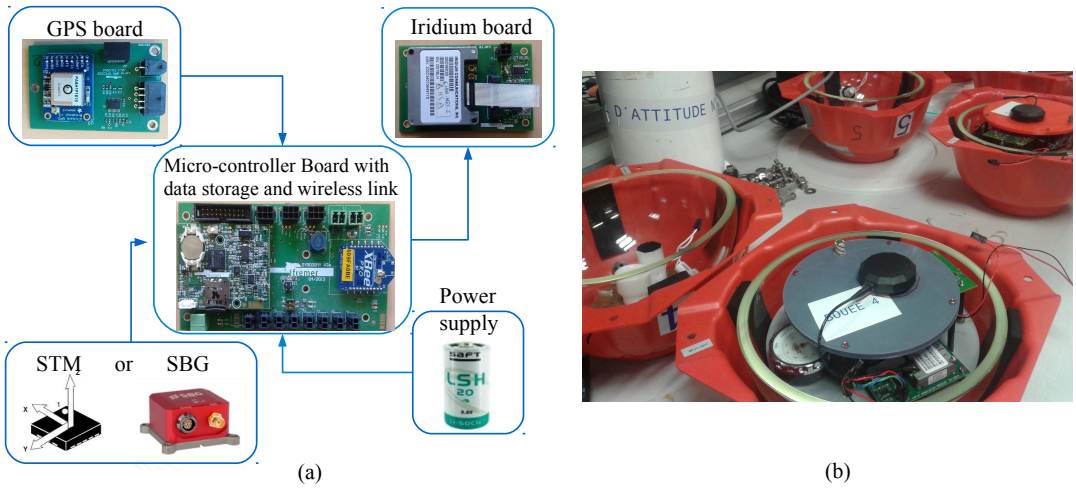

Figure 3.1: SKIB a) main electronics components b) SKIBs with top cover removed, showing the 10-inch diameter glass spheres.

For a detailed validation we have also integrated a more accurate sensor in two of the SKIB buoys (this is the SKIB SBG buoy version). In those buoys were used the IMU SBG Ellipse N, set with an acquisition rate of 50 Hz. However, this sensor significantly increases the equipments cost, with a unit price typically above 4000 USD.

3.3.3 Laboratory tests and in situ validation

Buoy testing started with verification of expected acceleration accuracy in a wave tank, followed by a comparison with in situ measurements with a reference wave buoy.

The Laboratory tests were very useful for testing various hull shapes, from spheres to short cylinders. These led to the addition of the plastic skirt that effectively removes rotations around the horizontal axes, with a limited impact on the water-following capacity for short wave components. This final design has a heave transfer function close to 1 up to 0.8 Hz, decreasing to 0.6 at 1 Hz, as established in wave basin tests(Thomas, 2015). This extends to high frequency the useful range of buoys such as Datawell waveriders or SWITFs.

For in situ validation, the SKIB buoy was deployed drifting within 200 m of a directional Mark III Datawel directional Waverider of 70 cm diameter, moored in a region of weak currents with a mean water depth of 60 m, at 48.2857°N, and 4.9684°W. This Waverider buoy is part of the permanent CEREMA wave buoy network, with the World Meteorological Organization number 62069 (Ardhuin et al., 2012). This buoy provides measurements of the first five moments for frequencies 0.025 to 0.580 Hz, based on accelerometer data.

Contrary to Herbers et al. (2012) who strapped their new acquisition system on a Waverider buoy, we wanted to validate the full system, including the hull response. As a result the different sensors do not measure the same waves (with the same phases) but should be measuring the same sea state, i.e. the same spectrum, moments, and derived parameters.

The test presented here was performed on 21 September 2016, from 10:44 to 11:56 UTC, following a similar test in 2015 with only a SKIB and a with a different GPS receiver but the same hull, and a Datawell. The results were very similar. In the 2016 experiment, we also deployed a SWIFT buoy (Thomson, 2012) and a ship-mounted stereo video wave system (Benetazzo et al., 2016). Pictures of all these systems are shown in figure 3.2, as used during the experiment.

The SWIFT model used is shown in the water in Figure 3.2.c. It uses a GPS receiver integrated with an IMU (Microstrain 3DM-GX3-35), a Doppler velocity profiler (Nortek AquadoppHR), an autonomous meteorological station ultrasonic anemometer (AirMar PB200), a digital video recorder system, and real time tracked radio frequency transmitter. The wave spectra for each 10-min burst are calculated as the ensemble average of the fast Fourier transform of 16 subwindows with 50% overlap, which results in 32 degrees of freedom and a frequency bandwidth $df = 0.0117$ Hz in the range $0.05 < f < 0.5$. The IMU data gives information of the tilt and horizontal rotation, as well as accelerations, of the SWIFT as it follows wave motions. Post-processing of the

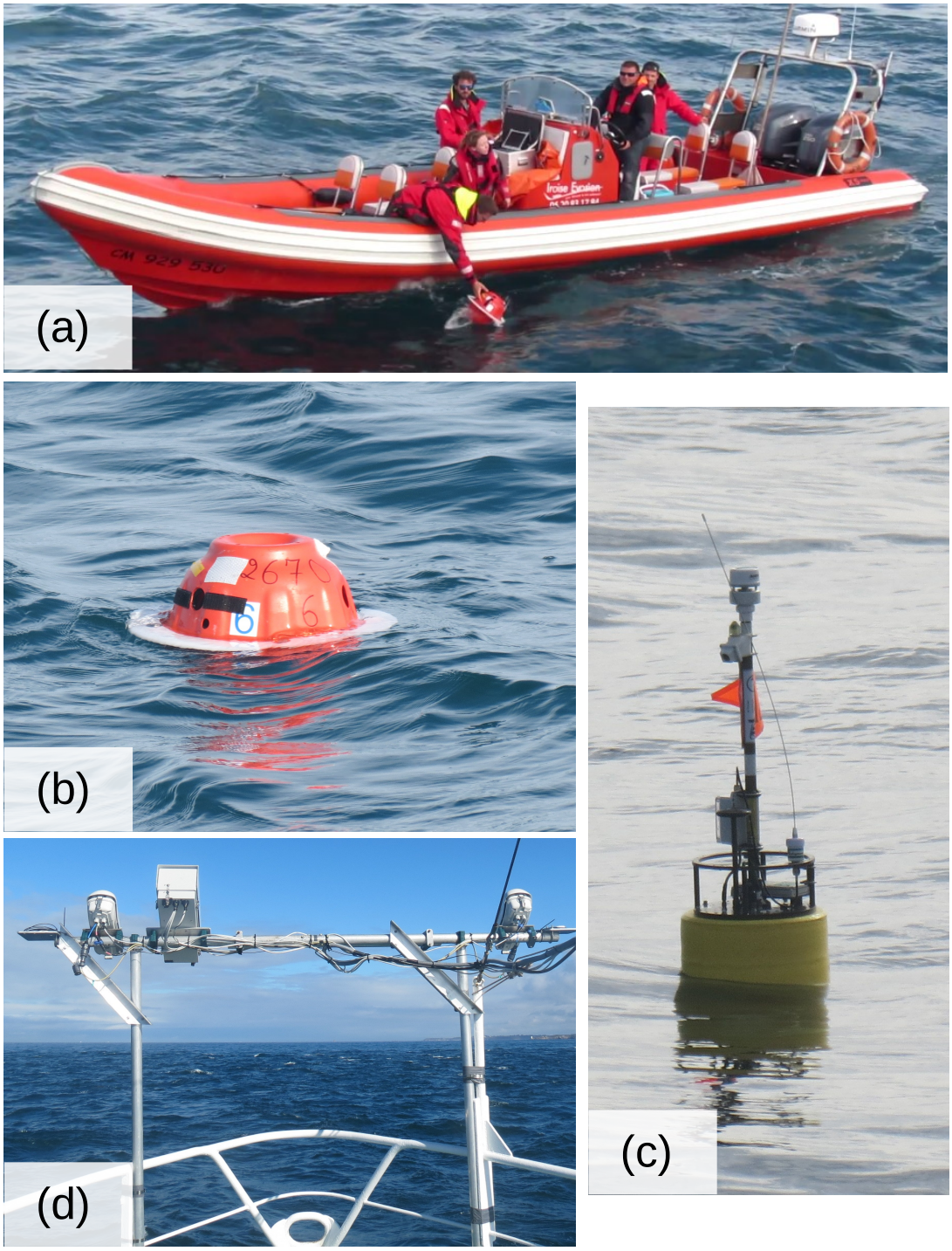

Figure 3.2: Sensors using during BBWAVES campaign for in situ validation. a) SKIB deployment; b) SKIB buoy; c) SWIFT buoy; d) Stereo video system

merged GPS and IMU data applies as classic RC filter to exclude signals at frequencies lower than $f < 0.04$ Hz.

The stereo video system is the same as used by Leckler et al. (2015), based on

a pair of synchronized video cameras (2048 $\times$ 2456 pixels) BM-500GE JAI, mounted with wide angle lenses. However, here the system was installed at the bow of R/V Thalia, a 24.5 m ship of the French coastal oceanographic fleet. The cameras are located approximatively 7 m above the sea level (fig.3.2.c), and an Ellipse-D Inertial Measurement Unit is fixed on the bar joining the cameras to correct for ship motion with 0.2° accuracy on all rotation angles. The video processing follows the methods of Benetazzo (2006), Leckler (2013) and Benetazzo et al. (2016). However, instead of use the mean surface plane correction, like in these earlier papers, here the rotation matrix is optimized by the quaternions of IMU data and translation obtained by the IMU and GPS data. The resulting surface elevation $\zeta(x,y,t)$ maps acquired over 30 minute records at 12 Hz are gridded in a 10 by 10 m square surface with 0.1 m resolution. This square is moving with the mean velocity U_m, relative to the solid Earth, as given by the GPS data. The 3D spectrum $E(k_x,k_y,f)$ were obtain after applying a Hann window in all three dimensions to the elevation maps over time intervals of 85.33 seconds (1024 frames), with 50% overlapping as well. As result, the energy over frequency and wavenumber are in a reference frame moving at the speed U_m, and the measured radian frequency of the waves σ_m must be corrected by the mean ship velocity ($\boldsymbol{U}_m$) over each time window. So the absolute frequency in an Earth reference frame is $\omega = \sigma_m - \boldsymbol{k}\cdot\boldsymbol{U}_m$. This procedure is particularly prone to errors for wave components longer than 20 m, that are not resolved in the field of view. These longer components can be treated separately using a slope array estimation of the directional spectrum (e.g. Leckler et al., 2015), but we focus here on the short waves. The stereo heave frequency spectrum $E(f)$ is obtained by integration over wavenumbers and it is expressed in terms of the absolute frequency $f = f_a$, with $\omega = 2\pi f_a = \sigma - \boldsymbol{k}\cdot\boldsymbol{U}$, where $\boldsymbol{U}$ is an unknown current field.

The comparison of the different sensors in terms of usual sea state parameters is shown in Table 3.1, with the significant wave height H_s, mean wave period $T_{m0,1}$ and peak wave period T_p. Since the only reliable directions are provided by the GPS data alone, we define the peak wave direction D_p and the peak wave direction $\theta_{m,2}$ from the second moments as $\theta_{m,2} = 0.5\tan^{-1}(B_2/A_2)$ with

$$A_2 = \int E(f)a_2(f)\mathrm{d}f \tag{3.8}$$

$$B_2 = \int E(f)b_2(f)\mathrm{d}f \tag{3.9}$$

For this comparison the records from each sensor have been synchronized over 10 minute intervals, and averaged over the 30 minutes of the Waverider records and a integration interval from 0.06 to 0.58 Hz. Figure 3.3.a shows the buoys drift trajectories

for the 1 hour of the acquisition, with one color symbol every 10 minute and the track of R/V Thalia. The stereo-video record is 20 minutes, starting at the same time as SKIB and SWIFT acquisitions. The Waverider data correspond to two acquisition of 28 minute each, ending at 10:30 and 11:00 UTC.

Table 3.1: Comparison of wave parameters, significant waves hight (H_s), mean absolute wave period (T_{m01}) and mean wave direction ($\theta_{m,2}$). The root mean square difference between Waverider and other sensors is given in a second column. The $[H_s^-, H_s^+]$ represents the maximum and minimum limits for 95% H_s confidence interval, considering a chi square distribution (according Young, 1995, eq.5 and 6), for two perfect devices measuring the same random wave field.

Sensor	H_s [m]	$[H_s^-, H_s^+]$	*RMSD*	T_{m01} [s]	*RMSD*	$\theta_{m,2}$ [°]	*RMSD*	ν
Datawell Mark III	2.55	[2.31,2.64]	–	10.49	–	238.1	–	193.4
SKIB STM	2.86	[2.63,2.94]	0.36	10.85	0.91	245.4	8.3	289.9
SKIB SBG	2.55	[2.29,2.65]	0.15	10.52	0.44	231.0	7.3	169.3
SWIFT	2.08	[1.88,2.16]	0.48	9.98	0.89	263.1	25.3	193.4
Stereo video	1.89	[1.73,1.94]	0.63	9.40	0.54	249.6	8.2	253.9

As reported in Table 3.1, SKIB results generally agree on H_s, T_{m01} and mean directions, with confidence intervals for H_s overlapping with the reference Waverider buoy.

The Largest differences are between the SKIB STM and SWIFT buoys are associated with the filtering of low frequency content in the SWIFT processing chain (fig.3.3.b), and unfiltered low frequency noise in the SKIB STM. However, for frequencies from 0.1 to 0.5 Hz, the spectra are consistent with the stereo-video and Datawell data. At higher frequencies, for which we do not have other validation data, the result follows the same trend and appears realistic up to at least 0.8 Hz, consistent with laboratory tests (Thomas, 2015).

A closer look at the heave spectra (Fig.3.3.b) shows a good correspondence by between Datawell and SKIB buoys at the peak of the spectrum.

The main source of error in the SWIFT data, around the peak of the spectrum, was associated to a high-pass filter applied to the IMU acceleration before each time integration. This part of the SWIFT processing, to obtain $E(f)$, were optimized by Thomson et al. (2016) to reduce the low frequency noisy and to have best agreement with a Datawell waverider at Ocean Station Papa. This uses a double time integration of the IMU acceleration, with a high-pass filter at each integration, to reconstruct a wave-resolved time series of sea surface elevations. This generally improves the estimation of the spectrum for $f > 0.1$ Hz, but it reduces the level of lower frequencies (as it is

also observed on Fig.3.3.b). For the SKIBs we have not filtered the acceleration data and the $E(f)$ was directly obtained form the twice in the time domain integration of the accelerometer data.

Other differences are found for the main direction, that is in better retrieved with the SBG IMU. The main benefit of the SBG IMU is the reduction of the noise floor at low frequencies compared to an estimation of the motion from GPS alone. This is most important for swells of long periods and low heights, but not critical for our investigation of wind-seas interacting with currents.

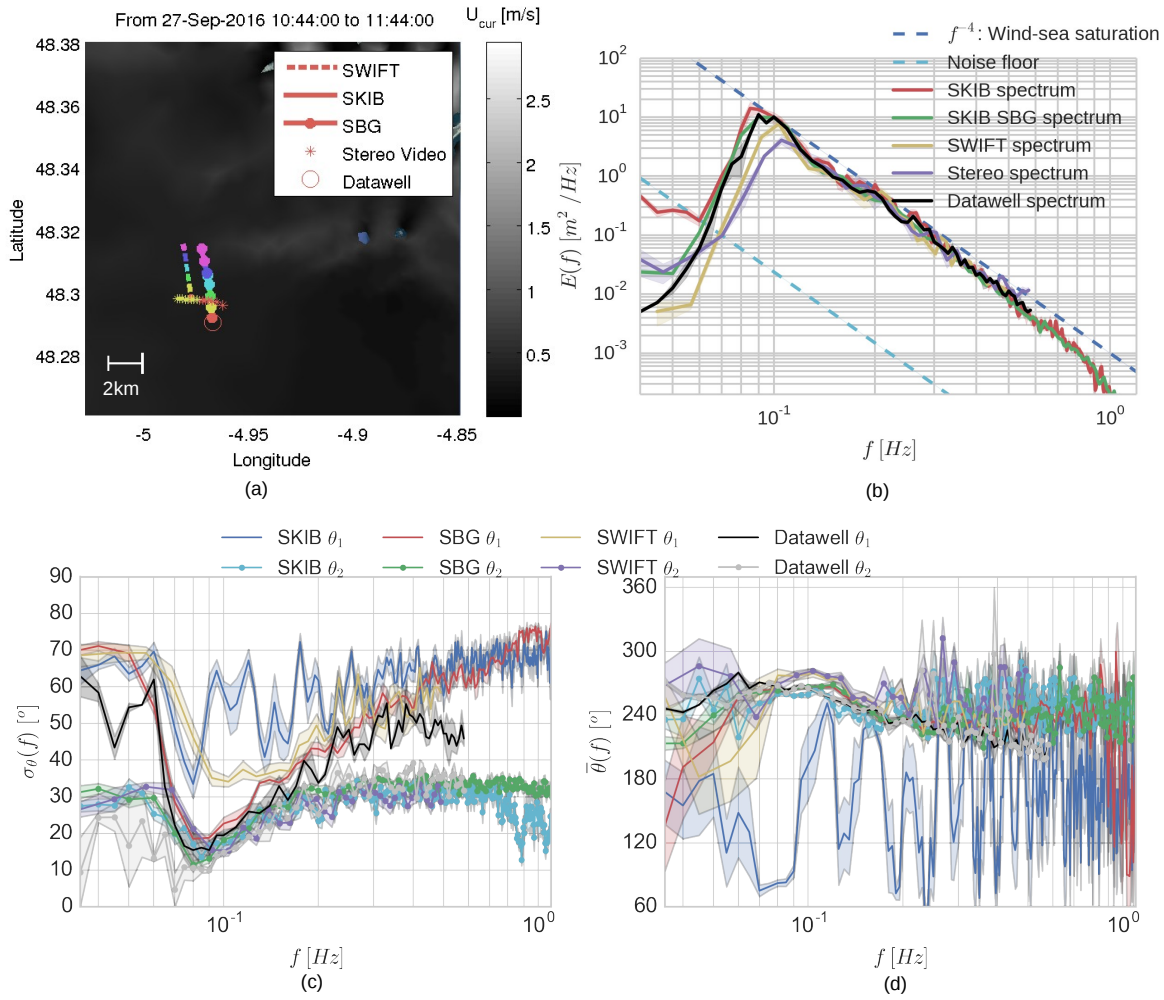

Figure 3.3: Comparison of wave spectra estimates from SKIB, SWIFT, Datawell and Stereo video. a) Wave sensors path, the colors represent 10-min displacement, starting in read b) $E(f)$ Sea surface variance spectral density; c) $\sigma_\theta(f)$ Directional spreading from first and second-order directional moments (θ_1 and θ_2); d) $\overline{\theta}(f)$ frequency-dependent mean wave direction from first and second-order directional moments (θ_1 and θ_2). The shadow in the lines represent the error for a 95% confidence interval.

Figure 3.3.c and 3.3.d present the estimates of σ_θ and $\overline{\theta}$ based on the first and second-order moments. We see a significant difference in the wave spread and mean

direction estimates, especially in the first-order estimation ($\sigma_{\theta 1}$ and $\overline{\theta_1}$). This occurs because the accelerometer is not internally synchronized with the GPS and because they have different characteristics errors. So, as the second-order moment depends only on horizontal displacements while the first-order depends of both horizontal and vertical displacements. The second-order moments are more accurate, because there is no cross products between different sensors. Although there are differences, the results suggest that the usage of the combination of GPS drifter displacement and vertical acceleration produces a good estimation of the spectrum directionality. These results are particularly important, as the drifter was not equipped with a compass and only used a low-cost GPS receiver. Because the GPS acquisition were limited to 1 Hz in the SKIB with STM accelerometer, the directional analysis are limited to 0.5 Hz (and 0.8 Hz for SBG which uses only accelerometer data).

In order to validate the SKIB buoys in different sea state conditions, others deployments were performed next to the buoy 62069, one at August 05, 2015 and other four between September 21 and 27 of 2016. For the 2016 experiment, we used two SKIB buoys equipped with SBG IMU and two others with the STM accelerometer. For the 2015 experiment we have only one buoy equipped with the STM accelerometer. Results for integral parameters are presented in Figure 3.4, and a selection of two spectra with different shapes is shown in Figure 3.5.

For most sea states H_s and D_p are measured correctly (Fig.3.4.a and d), with RMSD around 0.3 m and 5.3^o respectively. As expected, the SKIB-SBG agrees best with the Waverider for all the analyzed parameters, and the regression lines for the SBG data (Fig.3.4) are closer to the ideal correlation line (gray dash lines Fig.3.4) than those from the SKIB STM data. In general, the STM accelerometer has more energy at the lower frequencies and this can produce overestimations on H_s and T_{m01} measurements. These errors are confined to frequencies below 0.12 Hz. The main difference between the SKIB and Datawell was found at the peak wave period (T_p, Fig.3.4.c). Higher errors in the identification of the peak frequency are already expected as the buoys present different spectral resolutions and different numbers of degrees of freedom (Young, 1995). Again the SKIB-SBG performs better than SKIB-STM.

When the frequency range is restricted to $f > 0.1$ Hz the agreement with Datawell is much closer (Figure 3.4d and e). The buoys low frequency noise varies at each sea state conditions. The error associated to the low frequency limit and at the spectrum peak are illustrated in Figure 3.5.

In most sea states analyzed here, the SKIB buoy measured measured correctly the sea stare condition at frequencies higher than 0.07 Hz. In terms of H_s, the instrument usually presents a root mean square error within the statistical uncertainty expected

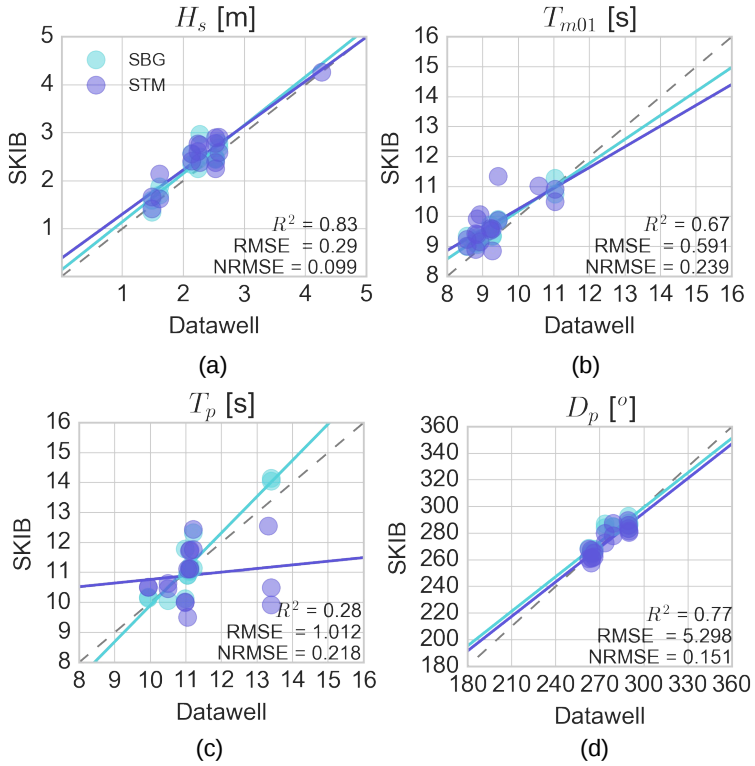

Figure 3.4: Comparison of the integrated wave parameters estimates from Datawell and SKIB with SBG (IMU sensor) and STM (accelerometer). a) Significant wave hight b) Mean waves period c) Peak waves period and d) Peak direction for a frequency interval between 0.06 to 0.6 Hz. The color regression lines are computed independently for SBG and STM data set. The gray dash line represent the ideal correlation regression line and the statistics coefficient wrote in the Figures are computed considered booth data sets, SBG and STM.

for two perfect devices measuring the same random wave field (Young, 1995, eq. 6). However, because of a significant low frequency noise in SKIM-STM we reduced the integration interval for this buoy. The low frequency noise was reduced by using the SBG IMU, that presented the best performance among the sensors tested here. In summary, we had a good performance of SKIB for $f > 0.07$ Hz, that makes it appropriate to use in the investigation of young wind-waves interacting with currents.

3.4 Example of wave evolution in current gradients

Wave properties are largely defined by the wind field and the geometry of the basin in which they develop, but currents can introduce large variations, particularly at small scales (e.g. Phillips, 1984; Masson, 1996; Ardhuin et al., 2017b). Current effects are generally strongest for the shortest wave components due to a larger ratio of current speed to phase speed, and can enhance the probability of wave breaking (e.g. Chawla

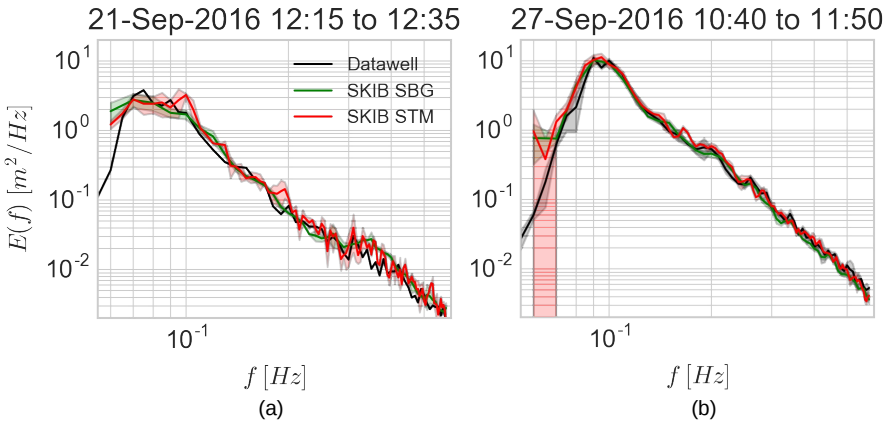

Figure 3.5: Comparison of Datawell and SKIB with SBG and STM for the sea surface variance spectral density $E(f)$ for two different field measurements around the Datawell buoy "Pierres Noires" (with World Meteorological Organization number 62069).

and Kirby, 2002; Zippel and Thomson, 2017).

Here we illustrate the capabilities of SKIB drifters with a deployment through a current gradient that opposes the waves, following the method of Pearman et al. (2014). We deployed buoys in the current upstream of a large gradient area and recorded the evolution of the wave field as the buoys drifted across the current gradient .

The selected area for this study is at the southern end of the Chenal du Four, a passage oriented north-south surrounded by shallow rocks, with Beniguet island to the west, and the mainland to the east (see Fig.3.6 and Fig.3.8). The water depth in this region ranges from 10 to 13 m relative to chart datum, and increases to 25 m at the southern end near latitude 48.32° N. At the time of our measurements, the water depth was the depth relative to chart datum plus 6 m. The tidal flow in this area is stronger in the shallower part of the channel, resulting in a current gradient at the channel mouth that often enhances wave breaking and can lead to hazardous navigation conditions.

On October, 23 from 13:40 to 14:40 UTC of 2015, six drifters buoys were deployed from a small boat (see Fig.3.2a.). Winds were approximately 6.2 m/s from the south, blowing against a tidal current of approximately 1.4 m/s (see Fig.3.8). The offshore wave conditions, as recorded by the Waverider buoy, included a 0.9 m swell with a peak period of 13 s coming from the 280°, and a 1.2 m wind-sea. The location of our measurements is well sheltered from the the swell, and swell heights increase as the buoys drift away from Chanel du Four. Figure 3.7 presents the mean current velocity estimated from the successive GPS positions, for all buoys and each of the 10-minute records over which wave spectra are estimated. After increasing from 1.3 to 1.4 m/s, the current drops to 0.9 m/s over the deeper region. As the waves travel against the

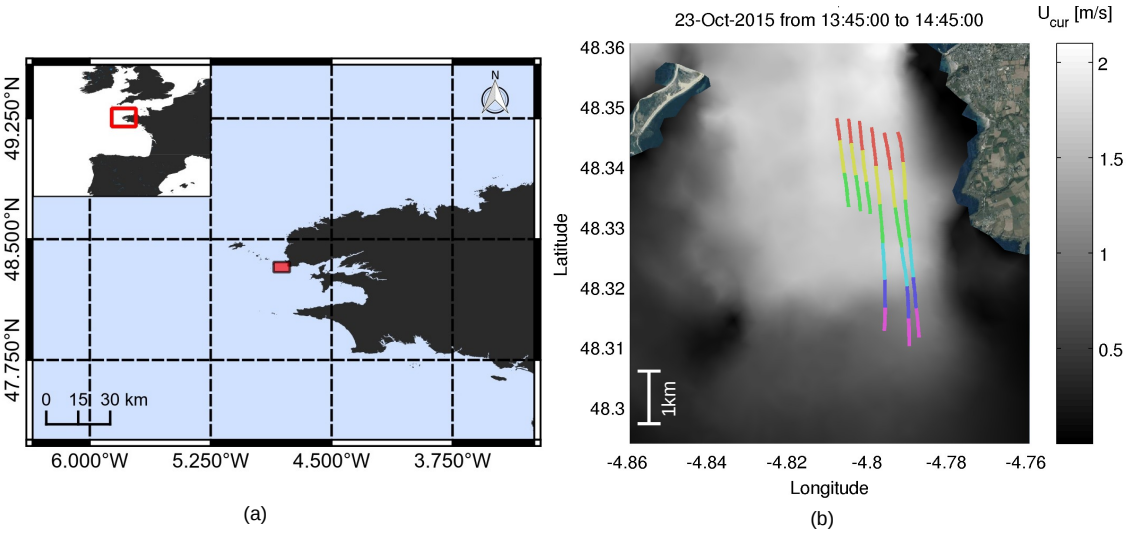

Figure 3.6: Study field location and local experimental conditions a) Four channel location b) Local current condition and drifters path. The current field shown here comes from a barotropic model simulation at 250 m resolution (Lazure and Dumas, 2008; Pineau-Guillou, 2013). Colored lines shows the 10-min SKIB displacement over current gradient at 23-October-2015 14:40 UTC.

current, they first experience the increase in the adverse current from 0.9 to 1.4 m/s.

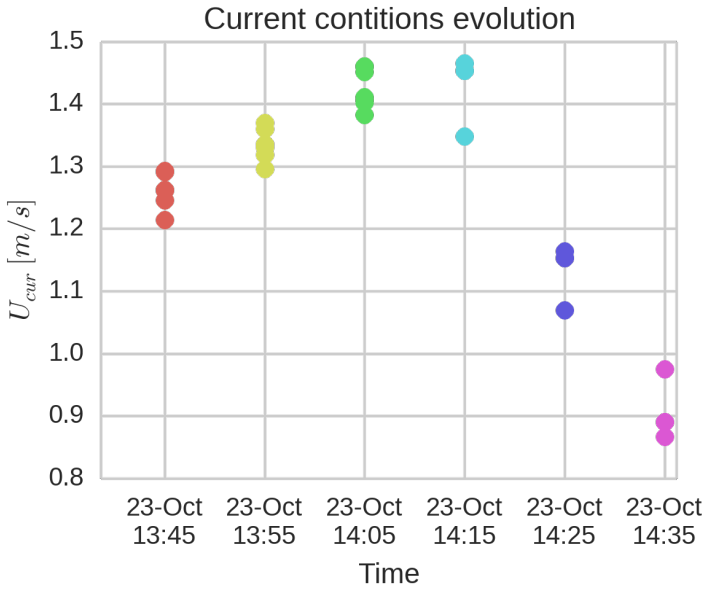

Figure 3.7: Evolution of the current velocity during the drift of the buoys. For each time segment each dot represents a single buoy.

The corresponding wave spectra are shown in Figure 3.8. There is little variation of the mean direction and directional spread (not shown).

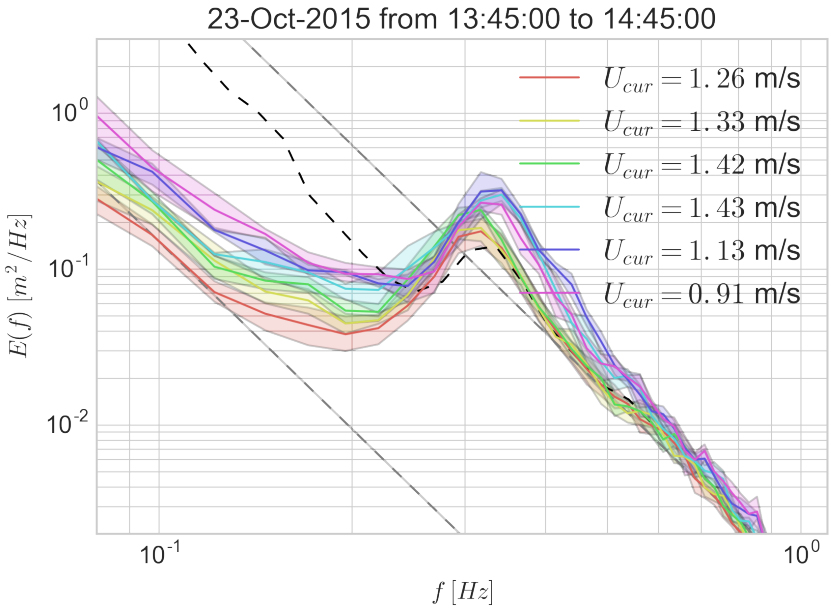

Figure 3.8: Variance spectral density evolution on time, 10 min Fourier transform from 23-October-2015 13:40 to 14:40 UTC. The gray dash lines shows the wind-sea saturation f^{-4} and noise floor limits for the first 10 minutes of acquisition. The colors lines follow the buoys displacement as on Figure 3.8. The solid lines shows the spatial mean of the spectral density measured during each 10 minutes acquisition. The lines shadow represent 99% confidence interval. The dash dark line is the spectral density measured by Pierre Noires Datawell buoy at an offshore location.

The effect of the current on the shape of the waves is analyzed using the non-dimensional saturation spectrum B, following Phillips (1984). With a velocity increase $\Delta_{U,1} = 0.6$m/s over a 1 km scale we measure an increase of the saturation level at frequencies from 0.35 to 0.5 Hz that does not exceed 50%. The following reduction in wave energy is more pronounced over the 3 km where the current slows down.

Figure 3.9 shows that the saturation level increases when waves face an accelerating and opposing current. This is similar to the cases studied in Zippel and Thomson (2017), from the Columbia River, in which opposing currents increase the steepness locally (without gradient analysis). In the final portion of the trajectories, the current speed decreases and the saturation relaxes to a lower value.

Given the complex interaction of wave generation by the wind, wave breaking and non-linear evolution, there are no simple theoretical results to interpret our observations. Starting from a dynamical balance in the absence of currents, Phillips (1984) provides an analysis of the the current effect as a deviation of the wave spectrum from a near-equilibrium state. Assuming that the wind forcing is proportional to B and a dissipation rate that is proportional to B^n with $n \simeq 3$. For a scale of current variation L,

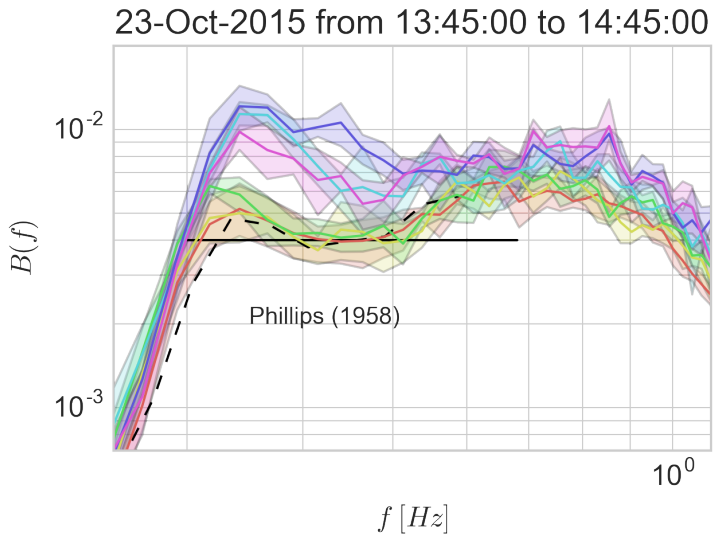

Figure 3.9: Saturation of the spectral density, time evolution over 10 min Fourier transform from 23-October-2015 13:40 to 14:40 UTC. The colors lines follow the buoys displacement as on Figure 3.8. The solid lines shows the spatial mean of the spectral density measured during each 10 minutes acquisition. The lines shadow represent 99% confidence interval. The dashed black line is the saturation measured at an offshore location by the "Pierre Noires" Datawell buoy.

he finds that the maximum value of B is

$$B_{\max} = B_0 \left[1 + 18\Delta_U/(cS)\right]^{[1/(n-1)]} \tag{3.10}$$

where B_0 is the equilibrium level of the saturation outside of the current gradient. S is scale of current variation normalized by the wind stress $L/(2\pi)C_d U_{10}^2/g \simeq 1$. For a relative frequency $f_r = 0.4$ Hz, $n = 3$ and $L = 1$ km giving $S = 1$, this gives $B_{\max} = 1.5B_0$. If n is reduced to 2, $B_{\max}/B_0$ is as large as 2.4, and diverges as n goes to 1. In other words, the dissipation rate must be a very steep function of B in order to absorb the wind forcing energy that converges into the small region of the current gradient. The limited increase in B in our data supports $n > 2$.

For example, a current speed of 1.6 m/s corresponds to blocking conditions for waves with periods shorter than 2 s, that have a group speed slower than 1.6 m/s, and these short waves should be strongly attenuated in a fixed reference frame. However, our measurements are in a reference frame moving with the current, in which the waves, even those with periods shorter than 2 s, are propagating past the drifting buoys. At frequencies above 0.5 Hz, the intrinsic group speed is less than 1.6 m/s and waves must be generated by the local wind and cannot propagate from the south. Our data

is consistent with $n = 3$, as used in Banner et al. (2000); Ardhuin et al. (2010). For $f_r = 0.6$ Hz, $n = 3$ gives $B_{\max} = 2.26B_0$,

3.5 Summary and conclusion

The Surface KInematics Buoy (SKIB) is a new low-cost drifter that has been designed for the investigation of wave-current interactions, including relatively short waves from 0.07 Hz and up to 1 Hz in frequency. Here we mostly used the heave data from the accelerometer that was first validated by comparing to reference Datawell waverider buoy up to 0.6 Hz. The shorter wave components were validated with stereo-video imagery.

The capabilities of the new drifter were illustrated by measuring the variation of wave properties across a current gradient that was relatively uniform and along the propagation direction. Such measurements are important for testing existing theories for wave dissipation, such as proposed by Phillips (1984) and now widely used in numerical wave models (e.g. Ardhuin et al., 2010).

4. Wind waves modulation by tidal currents

Tidal currents effect on wind-wave growth

Résumé

Que ce soit pour la formation de rides à la surface d'un lac ou le développement de vagues de tempête dans l'océan, la flux de quantité de mouvement entre l'air et l'eau est relié à l'état de la mer. La croissance des vagues dépend principalement du mécanisme de transfert de quantité de mouvement à partir des conditions de vent dans la couche limite de l'atmosphère océanique. Cependant, ce flux de quantité de mouvement de l'air vers l'océan est un processus complexe, couplé à l'état hydrodynamique local. Dans les domaines côtiers dominés par des effets de marée, les courants peuvent atteindre jusqu'à 4 m/s et ils modifient les propriétés du milieu et ainsi les ondes de surface qui s'y propagent. Par extension, donc leur interaction avec la criculation atmosphérique modifiant l'interaction avec les ondes de surface et la circulation de l'atmosphère inférieure.

Afin d'explorer les interactions complexes entre les courants, les vagues à différentes échelles et le vent, nous avons effectué une série de campagnes de mesures en mer d'Iroise (BBWAVES, Broad-Band WAVES) pour caractériser une large gamme de conditions d'états de mer. Les campagnes BBWAVES ont combiné plusieurs mesures simultanées du vent et des vagues cette zone de l'ouest de la France où la marée est connue pour son intensité. Grâce aux mesures effectuées, il a été possible de comparer la forme du spectre des ondes observées avec différentes conditions et paramétrages dans des modèles de numérique d'environnement côtier.

Les résultats préliminaires, dans des conditions de vent modérés et des courants forts, montrent une contribution énergétique significative et non attendue autour

des composants de la mer du vent. L'augmentation de l'énergie dans la mer du vent local n'a pas pu être expliquée par des expériences numériques ne considérant que le traditionnel effet Doppler sur la relation de dispersion, le vent relatif ou les conditions de résonance non linéaire.

Cependant, les mesures du vent à proximité de la surface en présence de forts courants, suggèrent une augmentation de l'ordre de O(50%) sur la vitesse du vent, et une augmentation d'un facteur jusqu'à de 5 à 10 de la variance de la densité spectrale. Cette variation est conforme à l'observation successive des vagues sous l'action d'un forçage similaire. Mais cela ne pouvait pas être expliqué par un effet de vent relatif, c'est-à-dire que la vitesse du vent pertinente pour la génération d'onde, est la vitesse dans le cadre de référentiel relatif qui se déplace avec le courant proche de la surface.

Par les observations dans ces campagnes BBWAVES, il a été possible de montrer qu'à petite échelle une interaction significative se produisait entre les systèmes atmosphérique et océanique ce qui, à notre connaissance n'a pas été observé par ailleurs dans la littérature. L'impact est alors significatif sur la propagation des ondes dans ce milieu où le vent entraînés par le courant vient modifier l'équilibre du système.

4.1 Introduction

When winds blow over the ocean, transfer momentum and energy to the ocean. A small portion of the wind momentum is directly transformed into current momentum, and the rest is responsible for wave generation and growth.

Small ripples at the surface are created primarily due the turbulence in the wind field. As these ripples develop and grow, their presence modifies the airflow over the sea and the pressure at the sea surface (Phillips, 1957). The feedback of the airflow on the waves is the main mechanism that explains wave growth.

From the preliminary ripple to the fully grown waves, the air-sea interface is characterized by nonlinear and dynamic processes that couple ocean and atmosphere. However, this coupling is usually partially neglected in forecast models, in which winds, currents and waves are usually computed separated. In particular, the ocean mixed layer with a depth of the order of 50 m, has a strong impact of momentum and turbulent kinetic energy exchange in the between ocean and atmosphere, with a clear impact in the atmospheric boundary layer (Sullivan and Mcwilliams, 2010). The works of Black et al. (2007) and Edson et al. (2007) attempts to connect coupled marine-atmospheric dynamic boundary layers over high and low wind speeds. Edson et al. (2007) results suggest that mesoscale ocean process can modulate the air-sea momentum and heat exchange, which may have important impact on mesoscale atmosphere forecast.

Waves are also sensitive to ocean conditions. Ocean currents, induce wave refraction and dissipation (Kudryavtsev et al., 1995; Waseda et al., 2009; Ardhuin et al., 2012; Rapizo et al., 2016). From observations and numerical experiments, Ardhuin et al. (2012) points out that in some macro-tidal environments the strong tidal current conditions can greatly influence the wave fields with induced variations up to 30% of the significant wave height.

In summary, the sea states conditions are the results of a subtle coupled balance between the atmospheric and oceanic boundary layers, and any dynamical process in one or the other can have a significant impact on wave properties. Because of that, the accuracy of numerical waves models rely on the accuracy of its forcing input fields, and on the parameterizations of the balance between its main source and sink terms that are the wind-wave generation, non-linear transfers, and dissipation (Komen et al., 1994; Janssen, 2008).

Numerical wave models used today for marine meteorology, rely on the action balance equation to solve the variance of the surface elevation across wavenumbers k and directions θ (Gelci et al., 1957; Janssen, 2008). The wave action density spectrum $N(k,\theta;\boldsymbol{x},t)$ evolves in five dimensions that are the two spectral dimensions (k and θ), two spatial dimensions (usually longitude and latitude) and time t (presented here as in the WAVEWATCH III model, equations 2.8 to 2.11 Tolman et al., 2014)

$$\frac{\partial N}{\partial t} + \nabla_x \cdot \dot{\boldsymbol{x}} N + \frac{\partial}{\partial k}\dot{k}N + \frac{\partial}{\partial \theta}\dot{\theta}N = \frac{S_{\text{tot}}}{\sigma} \tag{4.1}$$

$$\dot{\boldsymbol{x}} = \boldsymbol{c_g} + \boldsymbol{C}, \tag{4.2}$$

$$\dot{k} = -\frac{\partial \sigma}{\partial d}\frac{\partial d}{\partial s} - \boldsymbol{k} \cdot \frac{\partial \boldsymbol{C}}{\partial s}, \tag{4.3}$$

$$\dot{\theta} = -\frac{1}{k}\left[\frac{\partial \sigma}{\partial d}\frac{\partial d}{\partial m} + \boldsymbol{k} \cdot \frac{\partial \boldsymbol{C}}{\partial m}\right], \tag{4.4}$$

where $\boldsymbol{c_g}$ is the wave group velocity given by c_g, s is a coordinate in the θ direction and m is a coordinate perpendicular to s. The sum of the total source/sink functions are represented by S_{tot}, that act to locally enhance growth/decay of the waves. This includes input from the wind, dissipation and wave-wave non-linear interactions (S_{in},

S_{ds} and S_{nl} Tolman et al., 2014). $\sigma = \sqrt{gk\tanh kd}$ is the relative or intrinsic frequency, given by the dispersion relation condition, g is the gravity and d the water depth. For a fixed reference frame of over a mean surface current field C, the dispersion relation is modified by the Doppler shift to:

$$\omega = \sigma + \boldsymbol{k} \cdot \boldsymbol{C} \tag{4.5}$$

The Doppler shift on the dispersion relation of ocean waves influenced by currents is well documented for large-scale ocean currents (see for instance Mapp et al., 1985). A wide range of forcing conditions has indeed motivated the development of theoretical and numerical models of wave-current interactions (Leibovich, 1983; Thorpe, 2004). In fact, there is a very broad literature on theoretical effects of currents on wind wave propagation that leads to many developments in numerical wave modeling over the past two decades. Although, there are unfortunately very few validations of realistic numerical modeling of waves in currents, specially under strong current conditions (e.g., Masson, 1996; van der Westhuysen et al., 2012; Ardhuin et al., 2012).

Because of that, we aim to explore in this chapter the processes which interact with the free surface kinematics (waves, current and atmospheric interactions), their impacts on the shape of the waves spectrum and their numerical implications. For that, the theoretical current modulation on the short wave action is reviewed here. The performance of numerical stochastic wave model are tested under strong tidal current conditions, using different parameterizations for wind input and dissipation. The numerical results are compared with in situ experiments acquired under natural tidal current conditions in the North West of France.

4.2 Background

The balance between energy input and dissipation rates across the spectrum uses an empirical source function approach, distributing the total dissipation with a particular shape factor. Most wave forecast models today use empirical expressions for the dissipation rates that are adjusted to reproduce simple situations like fetch-limited growth and full develop sea state. Usually these parametrizations combine spontaneous dissipation rates limited by a steepness threshold, but they can present some strange behaviors in the presence of swells, in shallow water or in strong current conditions (Ardhuin and Filipot, 2016).

The evolution in time of wave source functions, such as the atmospheric input (S_{in}), the dissipation (S_{ds}) and the non-linear transfers (S_{nl}) are exemplified by Ardhuin and Filipot (2016, Section 5.3 and illustrated here at Fig.4.1) and briefly reviewed in this section.

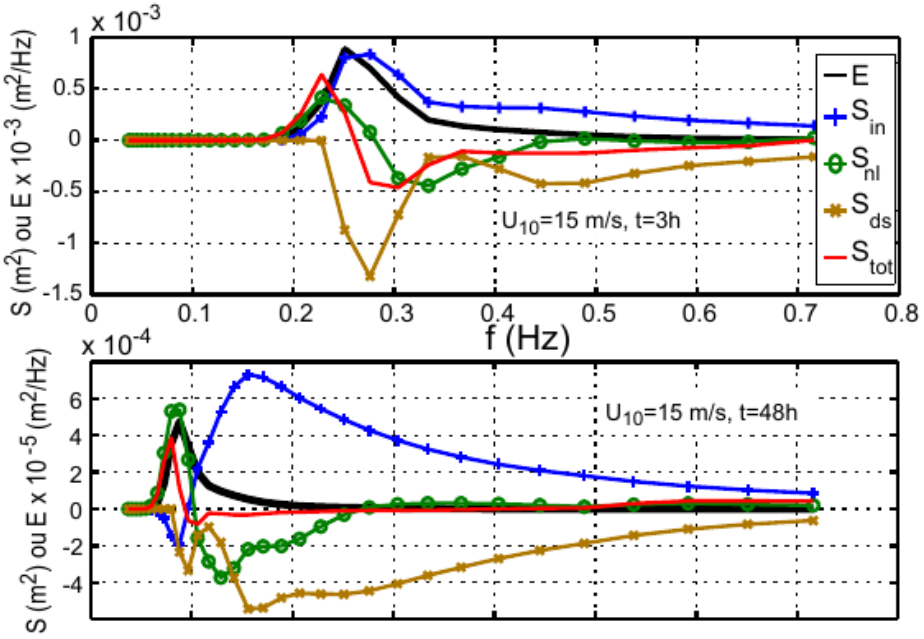

Figure 4.1: Source term balance for a wind speed of 15 m/s with a uniform sea starting from rest at $t = 0$. a) spectrum and source terms after 3 hours, b) after 2 days, (image from Ardhuin and Filipot, 2016).

In terms of wave and current interactions, the most traditional approach is to compute the Doppler shift of the dispersion relation and the relative wind effects (that is the wind speeds relevant for wave generation is the speed in the frame of reference moving with the surface current). The Doppler shift of the dispersion relation directly impacts the conservation of the waves action. It induces modification on the evolution of the wavenumber and apparent frequency (Eq.4.5 and 4.3). It consequently causes a

shortening or stretching in the wave steepness, modifying the breaking probability and the dissipation function.

4.2.1 Atmospheric input

Early developements by Jeffreys (1925, 1926) assumed that air flowing over the ocean surface was sheltered by the waves on their lee side. This would give a pressure difference, so the wind would work on the sea surface, pushing where the surface goes down and pulling on the lee side where it goes up. This work of the wind is the transfer of energy from wind to waves.

Later on, Ursell (1956) controlled laboratory experiments showed that this pressure difference was much too small to account for the observed growth rates and Jeffreys sheltering hypothesis was abandoned. Alternative theories were proposed by Phillips (1957) and Miles (1957). Miles theory considered the resonant interaction between the wave-induced pressure fluctuations and the free surface waves, giving a simple expression of the rate of growth of the waves as a function of the second derivative of the wind profile $U(z)$ at the height of the critical layer, $z = z_c$ where the wind speed matches the phase speed, namely $U(z_c) = C$. Miles theory did not consider the feedback of the waves on the wind profile, which was later introduced by Fabrikant (1976) and adapted by Janssen (1991).

Today it is expected that breaking waves also play a major role in wind-wave generation (Reul et al., 2008; Troitskaya et al., 2011), but that latter aspect will be neglected here and we start from the parameterization by Janssen (1991).

That parameterization was later adjusted by Bidlot et al. (2005, 2007) and Ardhuin et al. (2010) implementation in WAVEWATCH III model (Tolman et al., 2014) to arrive at a balance with semi-empirical dissipation terms. In this case, the full wind input source term reads:

$$S_{in}(k,\theta) = \frac{\rho_a}{\rho_w}\frac{\beta_{max}}{\kappa^2} e^Z Z^4 \left(\frac{u_\star}{c}\right)^2 \times \max[\cos(\theta-\theta_u),0]^p \sigma F(k,\theta) \tag{4.6}$$

where β_{max} is a non-dimensional growth parameter that comes from empirical adjustments, resulting either from measurements, or numerical simulations of air flow over waves, or from some observations of wave growth (e.g. Miles, 1959, 1996; Plant, 1982; Snyder et al., 1981; Donelan et al., 2005, 2006). $u_\star$ is the wind friction velocity, and $\kappa = 0.41$ is Von Kármán's constant. The Ardhuin et al. (2010) implementation consider (ρ_a/ρ_w) the air-water density ratio is constant, $p = 2$ and $Z = \log(kz_1) + \kappa/\left[\cos(\theta-\theta_u)(u_\star/c + z_\alpha)\right]$ is the effective wave age given by Janssen (1991), where z_α is a wave age tuning parameter, which was initially introduced to

represent the wind gustiness, and $(\theta - \theta_u)$ is the relative wind and wave direction.

The wind speed imposed in numerical wave models are usually defined at 10 m height (U_{10}), and the friction velocity $u_\star$ is estimated from inside the model. The wind stress is obtained from the wind speed and a surface roughness length z_0, assuming that the turbulent momentum flux $\langle \tau_h \tau_v \rangle$ is constant with height (which is not so true near the surface in the presence of waves) and that the mixing can be parameterized by an eddy viscosity of the form $\nu = l^2 \partial U = \partial z$, where the mixing length is given by $l = \kappa z$.

According to the Monin-Obukhov similarity theory (MOST), under these assumptions, the wind speed is assumed to follow a logarithmic profile as a function of height,

$$U(z) = \frac{u_\star}{\kappa} \log\left(\frac{z}{z_1}\right). \tag{4.7}$$

Whereas Miles had used a fixed z_1 which could be given by Charnock (1955), Fabrikant (1976); Janssen (1982) computed the feedback of the wave growth on the wind profile. This was later parameterized by Janssen (1991) as

$$z_1 = \frac{z_0}{\sqrt{1 - \tau_w/\tau}} \tag{4.8}$$

$$z_0 = \alpha_0 u_\star^2 / g \tag{4.9}$$

where z_1 is a roughness length modified by the wave-supported stress τ_w and (see Janssen, 1991; Ardhuin et al., 2010, for more details).

In fact, there are many discussions on the proper way to estimate z_0, a first reasonable guess was provided by the dimensional analysis of Charnock (1955), $z_0 \simeq 0.015 u_\star^2 / g$.

The wave-supported stress τ_w was an important part of Janssen (1991) parameterization, which includes the resolved part of the spectrum, as well as the growth of an assumed f^{-5} diagnostic tail beyond the highest frequency. This parameterization is highly sensitive to the high-frequency part of the spectrum since a high energy level there will lead to a larger value of z_1 and $u_\star$, which gives a positive feedback and reinforces the energy levels (e.g. Ardhuin et al., 2010).

To obtain a balance at high frequencies with the saturation-based dissipation, Banner and Morison (2006) and Ardhuin et al. (2010) included a sheltering condition

by replacing $u_\star$ by a wavenumber dependent $u'_\star(k)$ defined as

$$(u'_\star)^2 = u_\star^2(\cos\theta_u, \sin\theta_u) - |s_u| \int_0^k \int_0^{2\pi} \frac{S_{in}(k', \theta)}{c} (\cos\theta, \sin\theta) dk' d\theta \tag{4.10}$$

where $|s_u| \sim 1$ is the sheltering coefficient which can be used to tune the wind stresses for high winds, and c is the wave phase speed. This is in line with a saturation-based dissipation term allowing a better balance of the wind input at high frequency.

4.2.2 Dissipation

Many processes can contribute to the dissipation of the wave energy, but among them, wave breaking is generally the most important sink of energy for wind seas. One of the most traditional assumption made to characterize the hydrodynamic conditions at which waves start to break is related to the exceedance of the horizontal fluid particle velocity in the crest over the phase speed (Banner and Peregrine, 1993). The energy dissipation during a breaking event is the result of the conversion of mechanical wave energy into other forms of energy, in particular turbulence in the water and air (e.g., Melville, 1994), and it was measured in the laboratory for deep water waves by Duncan (1981) .

However, because the waves can randomly break at the sea surface, it is hard to predict where the breaking can occur and how much energy will be lost. So, one of the most traditional approach is to determine the dissipation rate associated to the breaking is based on the spectral dependence of the surface energy to an intensity of wave breaking. Phillips (1985) proposed a spectral dependence of the breaking strength parameter that were later observed by Banner et al. (2000); Babanin et al. (2001); Manasseh et al. (2006). In summary, these studies have led to the conclusion that the probability of breaking of dominant waves is a function of the steepness of these dominant waves. When generalized across the spectrum, this formulation gives a dissipation source term that links the breaking probability and the 'saturation' spectrum $B(k)$. This term turned out to be insufficient to explain the high probability of breaking for shorter waves. Hence, a cumulative breaking term $S_{bk,cu}$ was added. For completeness, one can also add the dissipation due to turbulence straining by the waves S_{turb} (Ardhuin and Jenkins, 2006). We thus have the saturation,

$$B(k) = \frac{k^5}{\omega^2} E(k) \tag{4.11}$$

and the saturation-based dissipation

$$\begin{aligned} S_{ds}(k,\theta) = \quad & \sigma \frac{C_{ds}^{sat}}{B_r^2} \left[\max\{B(k) - B_r, 0\}^2\right] E(k,\theta) \\ & + S_{bk,cu}(k,\theta) + S_{turb}(k,\theta) \end{aligned} \tag{4.12}$$

where the dissipation constant $C_{ds}^{sat} = 2.2 \times 10^{-4}$ (Ardhuin et al., 2007), $B_r = 0.0012$ in Babanin and Young (2005), $B_r = 0.0009$ and $B_r = 0.00084$ are tested in Ardhuin et al. (2010). Additionally, the $S_{bk,cu}(k,\theta)$ and $S_{turb}(k,\theta)$ constitutes the cumulative breaking source term and the dissipation by turbulence respectively (see Ardhuin et al., 2010, for more detailed explanation of this components). The formulation proposed by Ardhuin et al. (2010) also introduced a partial integration over directions for $B(k)$ in order to enhance the directional spreading of the resulting wave spectrum.

4.2.3 Non-linear spectral evolution

Because waves are not exactly linear, they can exchange energy between different spectral components, creating harmonics, bound waves, recurrence patterns and instabilities. The exchange of energy due to 4-wave interaction can be represented by a source term, first given by Hasselmann (1962), which takes the form of a Boltzmann integral, or collision integral, similar to the collision of molecules in a dense gas.

The Boltzmann integral describes the rate of change in the action density, for a particular wavenumber, due to resonant interactions between pairs of four wavenumbers. To interact, the wavenumbers and frequencies must satisfy a more general version of the resonant conditions

$$\begin{cases} \boldsymbol{k}_1 + \boldsymbol{k}_2 &= \boldsymbol{k}_3 + \boldsymbol{k}_4 \\ \sigma_1 + \sigma_2 &= \sigma_3 + \sigma_4 \end{cases} \tag{4.13}$$

The rate of change of action density E_1 at wave number k_1 due to all quadruplet interactions involving k_1 is given by

$$\frac{\partial N_1}{\partial t} = \int\int\int G(k_1,k_2,k_3,k_4)\delta(k_1+k_2-k_3-k_4)\delta(\sigma_1+\sigma_2-\sigma_3-\sigma_4) \tag{4.14}$$

$$\times [N_1 N_3 (N_4 - N_2) + N_2 N_4 (N_3 - N_1)] dk_2 dk_3 dk_4 \tag{4.15}$$

where G is the interaction coupling coefficient, for which expressions have been given by Herterich and Hasselmann (1980) (see, Van Vledder and Hurdle, 2002, for more information and numerical implementation).

This source term is generally very crudely approximated by the Discrete Interaction Approximation (DIA) proposed by Hasselmann et al. (1985). This parameteriza-

tion considers that a resonant nonlinear interaction occurs between four wave components (quadruplets) with wavenumber vector k_1 through k_4 as

$$\begin{cases} k_1 + k_2 &= k_3 + k_4 \\ \sigma_2 &= \sigma_1 \\ \sigma_3 &= (1+\lambda_{nl})\sigma_1 \\ \sigma_4 &= (1-\lambda_{nl})\sigma_1 \end{cases} \tag{4.16}$$

where $\lambda_{nl} = 0.25$ (WAMDI Group, 1988; Tolman and Chalikov, 1996). This method basically calculates the nonlinear interactions by considering a limited number of combinations of quadruplets (usually only one is used). For these quadruplets, the contribution δS_{nl} to the interaction for each discrete combination of the spectrum (f_r, θ) corresponding the spectrum of k_1, k_2, and so on.

The alternative is the exact Webb-Resio-Tracy method (WRT, from Webb, 1978; Tracy and Resio, 1982; Resio and Perrie, 1991), in which the 6-dimension integral of Hasselmann (1962) was reduced to 3-dimensions on the resonant manifold. Still the cost is about 300 times that of the DIA and is not yet applicable for operational weather forecasting at high resolution.

4.2.4 Interactions of waves and current

The spectral wave and current interactions are generally described using the quasi-uniform (linear) wave theory. The phase parameters (wavenumber vector $\boldsymbol{k}$) are modified by the Doppler-shift in the dispersion relation (Eq.4.5).

Considering a simple case, in the absence of dissipation in the wave action, an individual sinusoidal wave propagating, in deep water, with a constant absolute frequency (ω, Eq.4.5). For ω to be constant, the intrinsic frequency σ must adjust in the presence of the current. In this condition, the current modulates the wave phase speed along the propagation path, slowing down or accelerating the wave in the propagation direction, increasing or decreasing σ depending on the sign of $\boldsymbol{k} \cdot \boldsymbol{C}$.

For example, for waves opposing the current, $\boldsymbol{k} \cdot \boldsymbol{C} < 0$. In that case, as the magnitude of C increases, ω can be kept constant by an increase of σ and k, corresponding to shorter waves. In the absence of wave breaking, further consideration of wave action conservation leads to an increase of the wave spectral density $E(f)$. Most of this increase is due to the convergence in the flux of action and, in the limit of weak currents, 25% of the increase is energy transfered from the current to the wave (Ardhuin and Filipot, 2016, Chapter 6).

Current gradients introduce a spatial variation of the phase speed of ocean waves,

that induces refraction. Refraction usually plays a larger role than action conservation effects (Ardhuin et al., 2007).

Currents can dramatically increase the local density of wave energy, contributing to the appearance of extreme waves (Gutshabash and Lavrenov, 1986; White and Fornberg, 1998). This enhancement of wave heights is somewhat limited by wave breaking Phillips (1984); Ardhuin et al. (2012). Indeed, the changes in wave steepness can lead to a preferential breaking of waves in regions of strong current gradients. From that observation, Phillips (1984) pointed that in this situation the waves energy dissipation should be a nonlinear function of the wave steepness. These ideas have been included in spectral wave models following Banner et al. (2000); Banner and Morison (2006), with the dissipation $S_{ds}(k)$ parameterized from the spectral saturation $B(k)$.

In addition to the modification of the waves by the current, the wind over a moving sea surface can also be modified by the current, and the growth rate of waves is changed. Indeed, the generation of waves by the wind depends on the relative wind and current velocity. The continuity of velocities at the surface is

$$\boldsymbol{U}_{abs}(z=0) = \boldsymbol{C}. \tag{4.17}$$

Because the generation of waves by the wind is usually formulated in the frame of reference in which the surface current is zero, it is convenient to define a relative wind,

$$\boldsymbol{U}_{\mathrm{rel}}(z) = \boldsymbol{U}_{\mathrm{abs}}(z) - \boldsymbol{U}_c. \tag{4.18}$$

This relative wind not only comes into the parameterization of wind-wave growth, it is also the relevant wind velocity scale to formulate resistance law also known as Bulk Formula, that relate fluxes to mean quantities, for example the wind stress relation to the wind speed,

$$\tau/\rho_a = C_D \boldsymbol{U}^2_{10,\mathrm{rel}}, \tag{4.19}$$

where C_D is the surface drag coefficient (e.g. Edson et al., 2013).

Hersbach and Bidlot (2008) considered that the wind at an observed height z near or below the model 10 m height can be estimated using the interpolation method proposed by Geleyn (1988). The method of Geleyn (1988) is based on a Monin-Obukhov-type flux (for non-moving surface) and uses a simplified gradient functions Φ_M in Equation 4.7 to estimate U_{abs}, so

$$\frac{\partial \boldsymbol{U}_{\mathrm{abs}}}{\partial z} = \frac{\boldsymbol{u}_\star}{\kappa(z+z_0)} \Phi_M \left(\frac{z+z_0}{L} \right) \tag{4.20}$$

where Φ_M is a stability-dependent gradient function and L is the Obukhov length.

Given the constant stress approximation (no wind turning between U_{10} to $u_\star$) the wind vector is given by a simple reduction coefficient r_{wnd}, applied to the wind vector at the lowest model level. Since the method of Geleyn (1988) is based on a non-moving surface, this allows the estimation of the value r_{wnd} from an available model quantities U_L and U_c, plus a knowledge of roughness length z_0. So relative wind correction over a moving surface can be written as:

$$\boldsymbol{U}_{\text{rel}}(z_{\text{obs}}) = r_{\text{wnd}}\boldsymbol{U}_{\text{rel}}(z_L) = r_{\text{wnd}}(\boldsymbol{U}_L - \boldsymbol{U}_c) \tag{4.21}$$

where in the atmospheric wind model $\boldsymbol{U}_L$, at lowest level, is defined in the absolute frame.

To compare the model output with other sources of wind observations it is needed an adaptation of observation operator. Drifting buoy or ship data, for example, measure wind with respect to the relative frame. In opposite, moored buoys or scatterometers, measure wind with respect to an absolute frame. In those cases an adaptation of observation operator relative to $\boldsymbol{U}^{\text{mod}}$ modeled depends on the nature of the observation as (Hersbach and Bidlot, 2008):

$$\text{scatterometer}: \quad \boldsymbol{U}_{10}^{\text{mod}} = \boldsymbol{U}_{\text{rel}}(10) = r_{\text{wnd}}(\boldsymbol{U}_L - \boldsymbol{U}_c) \tag{4.22}$$

$$\text{buoy/ship}: \quad \boldsymbol{U}_{z_{\text{obs}}}^{\text{mod}} = \boldsymbol{U}_{\text{abs}}(z_{\text{obs}}) = r_{\text{wnd}}\boldsymbol{U}_L + (1 - r_{\text{wnd}})\boldsymbol{U}_c \tag{4.23}$$

where in absence of ocean currents $\boldsymbol{U}^{\text{mod}} = r_{\text{wnd}}\boldsymbol{U}_{\text{abs}}(z_L)$.

According to Hersbach and Bidlot (2008), at the lower wind model level, near 10 m, $r_{\text{wnd}} \sim 1$ and by comparing with many buoys measuring wind at a height of 4 or 5 m, $r_{\text{wnd}} < 1$. However, the same authors found that the effect on surface stress is smaller that what would have been intuitively obtained by subtracting the ocean current from the surface wind of a system ($r_{\text{wnd}} < 1$).

4.3 BBWAVES experiments

A few dedicated experiments in the laboratory and in the field have provided data on wave-current interactions, in particular at inlets or river mouths with a focus on wave blocking by the current (e.g. Masson, 1996; Chawla and Kirby, 2002; van der Westhuysen et al., 2012; Ardhuin et al., 2012; Dodet et al., 2013; Zippel and Thomson, 2017; Rapizo et al., 2017). Also several remote sensing observations have shown interesting features induced by currents on surface roughness (Kudryavtsev et al., 2005; Rascle et al., 2014, 2016, 2017), which is related to the properties of short gravity waves. In order to combine observation of dominant waves and shorter waves and understand the complex interaction of wind, waves and currents, a series of experiments designed to explore the a wide range of the wave spectrum was designed and carried out. These "Broad-Band WAVES" (BBWAVES) experiment were performed in 2014, 2015, 2016 and 2017, specifically to explore questions related to the interactions between long, intermediate and short gravity waves, in the presence of strong gradients of surface current in Northwest coast of France.

The experimental results obtained during the BBWAVES campaigns are used here and compared with results of the WAVEWATCH III model. The model is used to provide a context to point measurements and the data are also used to evaluate the model capabilities and performance in regions of strong current gradients.

After a feasibility study with drifting buoys in 2014, the 2015 BBWAVES experiment was carried out from 22 to 29 October in the region 5.16°W–4.76°W and 48.26°N–48.53°N (see, Fig.4.2). This area is a meso-tidal region with a typical spring tidal range of 6 m and currents exceeding 2 m/s around islands and headlands (Muller et al., 2007; Ardhuin et al., 2012).

This favors the definition of specific sea conditions to deploy the equipments, allowing to measure the sea state conditions under natural gradients of currents. A second BBWAVES campaign was conducted between 21st to 27th September 2016, under similar sea state conditions, aiming to validate and verify the observations on the previous one.

In order to measure the wave conditions along or across the current gradients in this area we used a ship-mounted stereo video wave system (Fig.4.3.a), six drifter buoys (Fig.4.3.d and 4.3.e) especially developed and tested to measure the waves under current conditions (see, Chapter 3) and for BBWAVES 2016 were also added a two SWIFT buoys developed by Thomson (2012, Fig.4.3.b). In addition, at several locations, a small trimaran (OCARINA, Bourras et al., 2014, see Fig.4.3.c) designed for the estimation of air-sea fluxes at the atmospheric surface boundary layer, were used to

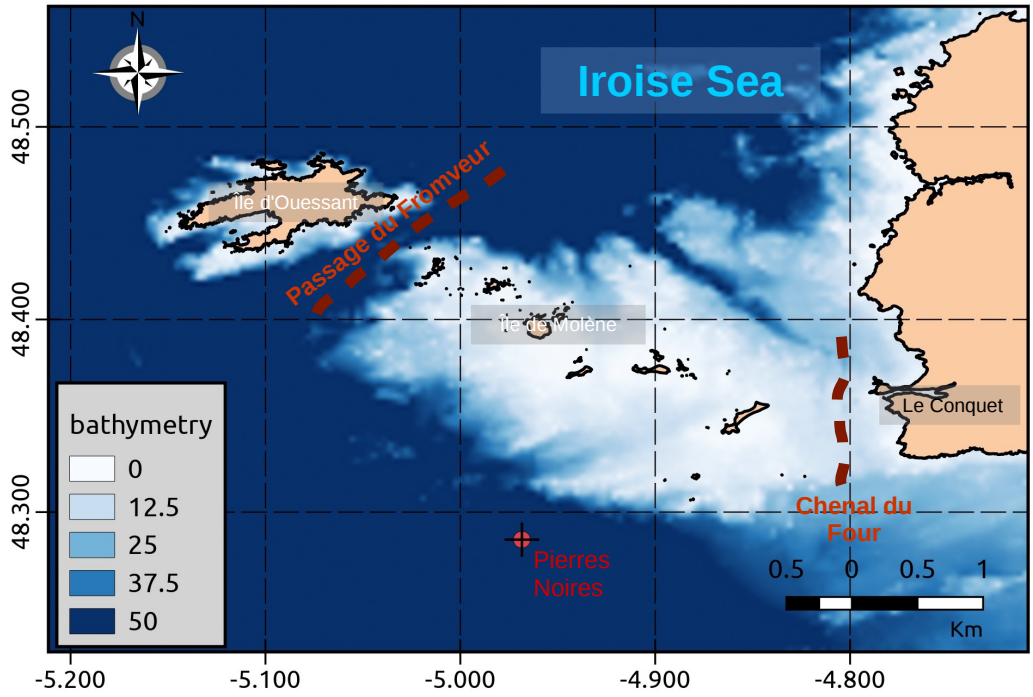

Figure 4.2: Study field at Iroise Sea. The red dash lines mark the position of the main current features analyzed in this study and the read dot mark the moored Datawell buoy, Pierres Noires, used to validate the equipments used here.

collecting data next to the wave sensors. Figure 4.3 shows the main equipments used during the experiments and the next sections are dedicated to briefly introduce those equipments and the main setup used.

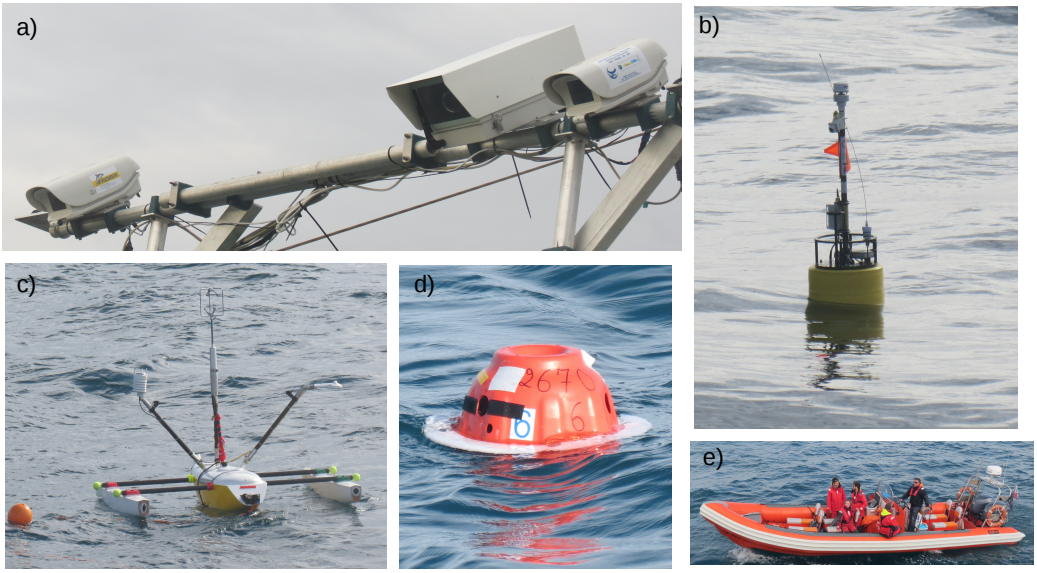

Figure 4.3: Main equipments and sensor used during the BBWAVES 2016 experiments: a) Stereo video system, b) SWIFT buoy, c) OCARINA, d) SKIB buoy, e) Zodiac boat

Drifting buoys

For BBWAVES 2015 and 2016 six buoys of a new kind were produced in the laboratory. These 'Surface KInematic Buoys' (SKIB) prototypes, were particularly optimized for the measurement of waves-current interactions, including relatively short wave components (relative frequency around 1 Hz). They combine a GNSS receiver with a motion-sensor package. These buoys drift with the surface current and provide unique measurements of wave-current interactions. A comparison with existing Datawell Directional Waverider and SWIFT buoys, as well as stereo-video imagery are presented in Chapter 3.

SWIFT

For the BBWAVES 2016 campaign, we also used two Surface Wave Instrument Float with Tracking (SWIFT) buoys developed by Thomson (2012, Fig.4.3.b). The SWIFT is a small spar buoy with a 0.3 m diameter and 2.15-m height, developed to measure and image wave breaking in a wave-following reference frame. This buoy is equipped with a GPS logger (QStarz BT-Q1000eX), an Aquadopp Doppler velocity profiler, an autonomous meteorological station, a digital video recorder system, a real time tracked radio frequency transmitter and an ultrasonic anemometer (AirMar PB200). The spectra for each 5-min burst are calculated as the ensemble average of the fast Fourier transform of 16 sub-windows with 50% overlap, which results in 32 degrees of freedom. The motion sensors included in the Aquadopp records the tilting and turning of the drifter during its deployment. In addition, the SWIFT horizontal velocity data from the phase-resolving GPS contain the wave orbital motions relative to the Earth reference frame.

Ship-mounted stereo-video system

The ship-mounted stereo video wave system consists in a pair of video cameras installed on the on the top of a proper boat ($\sim$ 7 to 11 m hight) synchronized with a Motion Unit to correct the ship movements and a GPS system to get the geographical cameras position. The stereo video system DIACAM (similar to WASS proposed by Benetazzo, 2006) consists in on two synchronized 5 Megapixel video cameras (2048 $\times$ 2456 pixels) BM-500GE JAI mounted with wide angle lenses. The distance between the cameras were 2 m and the acquisition interval were usually set at 12 to 15 Hz during $\sim$30 min. The maximum acquisition rate and duration were mainly limited by the writing speed and storage capacity of hard drive disks.

The general principle of 3D surface reconstruction can be found in Section 2.3

(also see Benetazzo, 2006; Leckler, 2013; Benetazzo et al., 2016, for more detailed informations). In the Lagrangian reference associated with the moving ship, the center point of field needs to be accounted. For that, a compact Inertial Navigation System with integrated Dual-antenna GNSS[1] receiver Ellipse2-D is then used for this purpose. It includes a MEMS-based Inertial Measurement Unit (IMU) and runs an enhanced Extended Kalman Filter (EKF) which fuses inertial and GNSS data. It provides Roll, Pitch, Heading, Heave, and Navigation data (see Section 2.4 for more details of the ship motion correction).

The 30 min stereo video results were gridded over 10 m $\times$ 10 m square surface with 0.1 m resolution, where x, y represent the longitude and latitude in UTM. The 3D spectrum $E(k_x, k_y, f)$ were obtained after applying a Hamming window in all three (x, y, t) dimensions to the elevation maps over time intervals of 85.33 seconds (1024 frames), with 50% overlapping (also see Section2.3.2 for more informations about the 3D spectrum reconstruction). As a result, the energy over frequency and waves number are acquired in a Lagrangian reference frame, and the Doppler shift in σ must be corrected by the mean boat velocity ($\boldsymbol{U_b}$) over the 1024 time window. So the apparent frequency is corrected by $\sigma_c = \sigma - \boldsymbol{k} \cdot \boldsymbol{U_b}$. Consequently, the heave frequency spectrum $E(f)$ is obtained by integration of the 3D spectrum and it is expressed in therms of the absolute frequency ($\omega = \sigma_c + \boldsymbol{k} \cdot \boldsymbol{U} = 2\pi f_a$).

OCARINA

The wind measurements near the surface were done by the OCARINA (Ocean Coupled to Atmosphere, Research at the Interface with a Novel Autonomous platform Bourras et al., 2014). This is a 2 m long trimaran floating platform specifically designed for the estimation of air-sea fluxes in the lower atmospheric boundary layer in order to investigate wind-wave interactions. The system was deployed from the research vessel and let freely drifting over the current fields analyzed here.

The equipments installed in the OCARINA uses a Vaisala WXT-520 meteorological station to measure the air temperature and humidity, static pressure, rain and wind, at 1 Hz. This meteorological instrument package was placed at a low elevation above the water line (1 m). An inertial motion unit (IMU) was placed at the horizontal center of OCARINA and at the level of the waterline. The inertial motion unit is an Xsens MTI-G device, which features three magnetometers, three accelerometers, three gyroscopes, a GPS, and a barometer. Winds were extrapolated to 10 m height, using the Charnock relation (U_{10}, Eq.4.7).

[1] Global Navigation Satellite System

4.3.1 Numerical experiment

Intending to evaluate how the spectral wave model WAVEWATCH III (WW3, version 4.18 from Tolman et al., 2014) performs under realistic current conditions, we did several numerical tests. The simulations for the tests use the advection schemes over an unstructured grids, implemented by Roland (2008), and most of the source functions for wave dissipation and generation follow the ones used in reference test case "TEST471" from Ardhuin et al. (2010). The nonlinear waves interactions were modeled using the Discrete Interaction Approximation (DIA, Hasselmann et al., 1985) and tests using the three-dimensional Boltzmann integral by Webb-Resio-Tracy method (WRT) will be presented in Section 4.5.

The simulations were done using a hight resolution triangular mesh over the Iroise Sea, with higher definition at high gradients of bathymetry areas and around the islands, where it is expected to observe stronger current conditions (Fig.4.4). The spatial resolution varies from $\sim$ 100 m close to the islands to $\sim$ 5 km close to the oceanic boundary. The spectral resolution considers 32 frequencies and 24 directions. The period studied correspond to the same time of BBWAVES experiments.

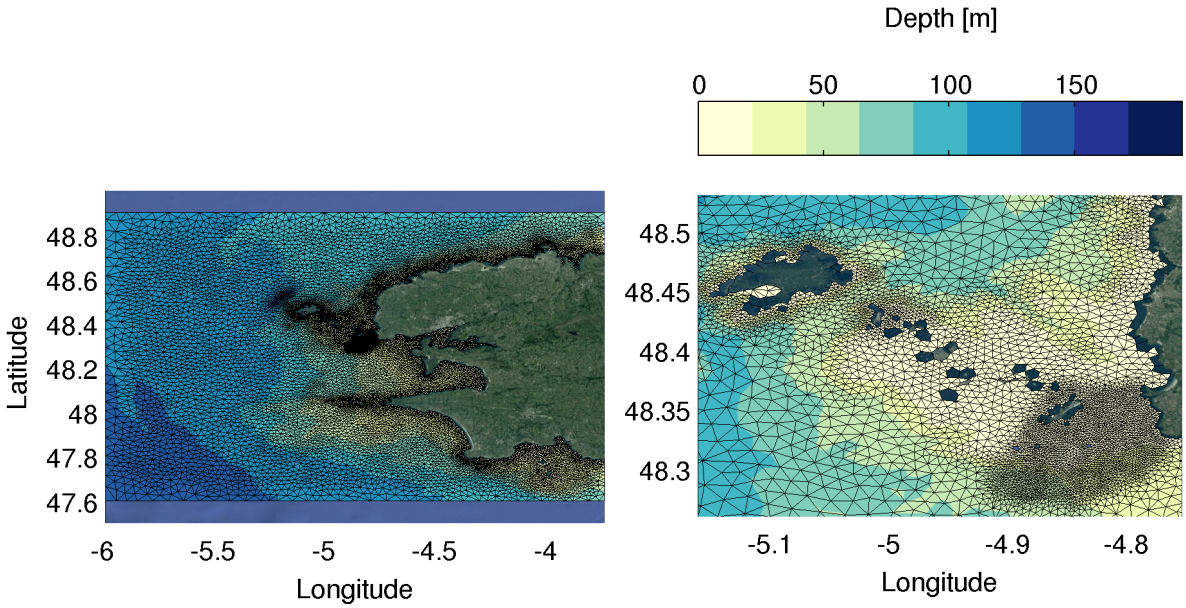

Figure 4.4: Bathymetry and mesh of the Iroise Sea area. Plot (a) present the whole area used for waves computation, while (b) is a zoom of the same mesh, refined in the areas of strong current observations.

Boundary conditions in the form of directional wave spectra are provided by hindcasts over the global ocean (Rascle and Ardhuin, 2013) and a nested mesh over the Bay of Biscay and English Channel (NORGASUG), that has been carefully vali-

dated against buoy and satellite altimeter data (Roland and Ardhuin, 2014). These are available at `ftp.ifremer.fr/ifremer/ww3/HINDCAST/NORGASUG/`). These model configurations are forced by European Center for Medium-Range Weather Forecasts (ECMWF) operational winds and tidal currents from a barotropic model (Ardhuin et al., 2012). The models use the parameterization by Ardhuin et al. (2010) as updated by Rascle and Ardhuin (2013) and the TEST471 settings for the input and dissipation (The WAVEWATCH III® Development Group, 2016). These offshore boundary conditions are generally accurate in terms of wave heights and mean periods, with normalized root mean square errors (NRMSEs) less than 10% for H_s offshore.

Our model grid is forced by the same current and water level model as the parent WAVEWATCH III grid, using a 250 m resolution implementation of MARS2D (Model for Application at Regional Scale, Lazure and Dumas, 2008). That implementation is described by Pineau-Guillou (2013).

For the wind forcing we again use ECMWF operational analyses and forecasts, giving a time resolution of 3 hours on a $0.125^\circ \times 0.125^\circ$ of spatial grid. An alternative wind source was tested over the same configuration using the Meteo-France small scale numerical prediction model (AROME, Ducrocq et al., 2005) with hourly output over a finer 2.5km grid.

4.4 Observations and numerical experiment results

4.4.1 Wave data

For the BBWAVES 2015 experiment, it was possible to compare the WW3 simulations with measurements of the SKIB buoys in areas of strong currents. The accuracy of a wave model like WW3 is usually assessed by comparisons to reference data of the standard integral parameters, like significant wave height, mean wave period, mean wave direction and directional spreading. However, because the Doppler shift in the dispersion relation, short waves are more influenced by the current than the swell components. So, in this work, we will mainly focus the wave analysis between the frequencies of 0.08 to 0.70 Hz where it is expected to observe the highest impact induced by the currents because the phase speed is closer to the current velocity. This frequency range is also where our drifting buoys are most accurate . For that purpose, we intend to compare the numerical observations with data from the drifter buoys on the spectral density of the surface elevation variance. The WW3 output of this variance $E(f)$ were used over the mesh grid points over the path of the buoys and at each 10 minutes intervals. We note that both the model and buoy data are relative frequencies, in the frame of reference moving with the current.

A spatial 10 min average between the six synchronized buoys was used to evaluate the space and time evolution of the wave field over the current structure. Figure 4.5 and 4.6 show the experimental and numerical results for SKIB buoys at BBWAVES 2015. The left panel presents the drift of the buoys over the current structure, the color lines represent the 10 minutes path used to compute the spectrum, starting in red. The wind velocity and field of current intensity are presented in those figures represent the WW3 forcing conditions at the beginning of SKIB acquisition. In the right panel is presented the spectral density of the variance of sea surface elevation and its evolution in time, from the model in dashed gray scale lines and from the buoys in solid colored lines. The model results presented here are mostly using the wind input and dissipation parameterizations from Ardhuin et al. (2010), with adjusted parameters "TEST471" described by The WAVEWATCH III® Development Group (2016).

The acquisitions presented here were carried mostly under moderate wind conditions, with speeds from 3 to 7 m/s. The current conditions pictured Figure 4.5 vary from 0.08 to 1.48 m/s, with a high variability depending on the buoys position over the current structure. Moreover, acquisitions presented at Figure 4.6 were collected under higher and more stable current structures, varying from 1.26 to 2.22 m/s.

A first comparison between the model results and SKIB buoys shows that the

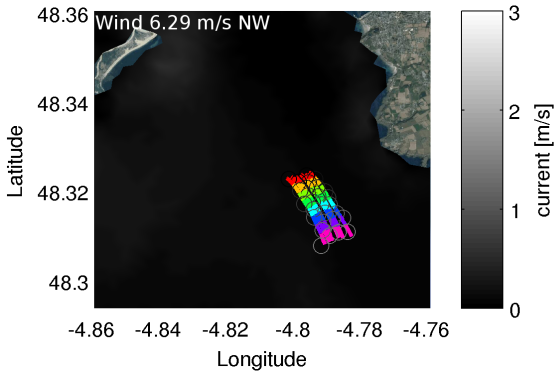

(a) SKIB 2015/10/22 11:00 to 12:20

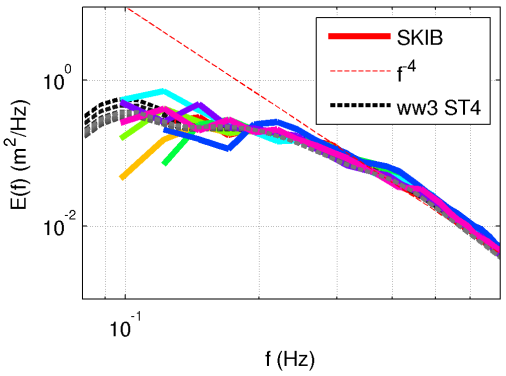

(b) SKIB 2015/10/22 11:00 to 12:20

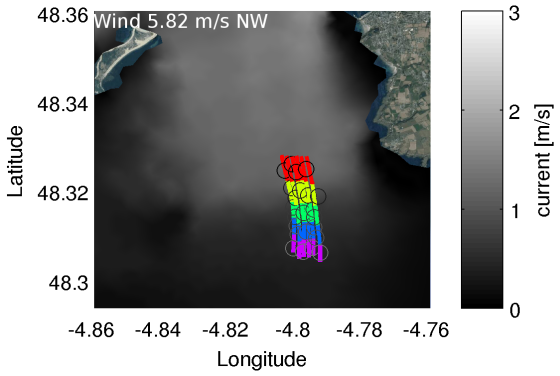

(c) SKIB 2015/10/22 13:00 to 13:50

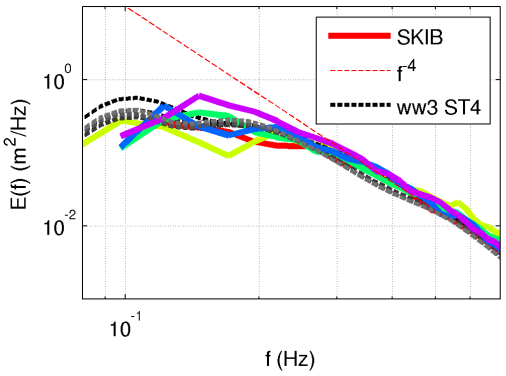

(d) SKIB 2015/10/22 13:00 to 13:50

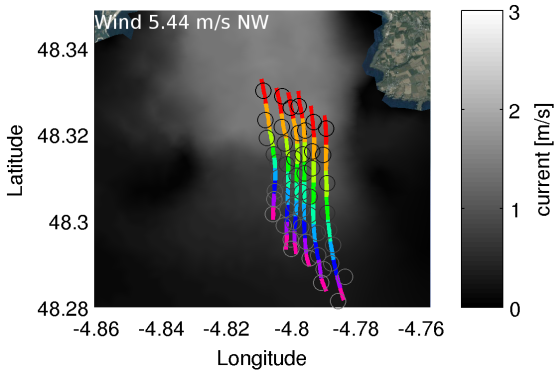

(e) SKIB 2015/10/22 14:30 to 16:00

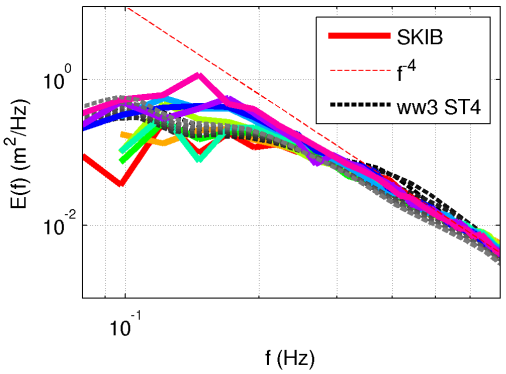

(f) SKIB 2015/10/22 14:30 to 16:00

Figure 4.5: Experimental conditions during BBWAVES 2015 SKIB acquisitions. The left panel shows the local current condition during the experiment, the 10 minutes drifting buoy segments of path are synchronized and marked by different colors, the gray circles represent the selected WW3 grid point output positions. The local wind conditions at 10 m considered in the model are labeled in white in the figures. The 10 minutes average spectral density of the variance and its evolution in time measured by SKIB buoys are presented in solid color lines, on the right panel, where the same quantity from the model is presented in dashed gray scale lines.

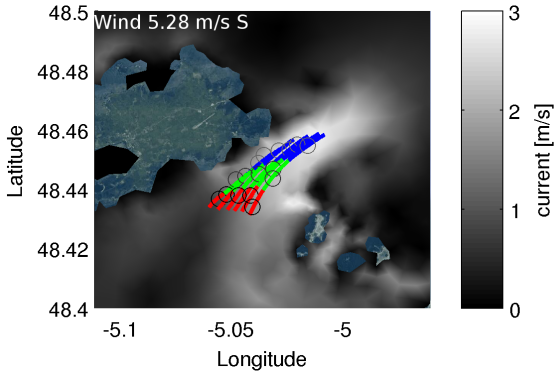

(a) SC1: SKIB 2015/10/23 08:30 to 09:00

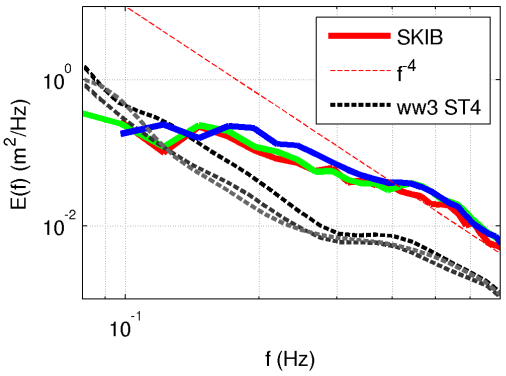

(b) SC1: SKIB 2015/10/23 08:30 to 09:00

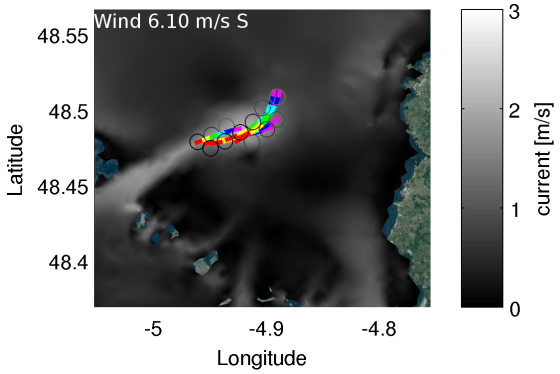

(c) SC2: SKIB 2015/10/23 10:30 to 11:30

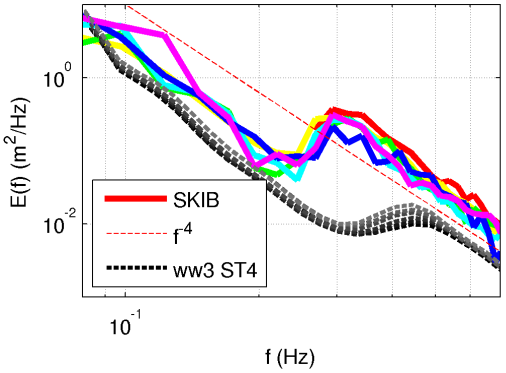

(d) SC2: SKIB 2015/10/23 10:30 to 11:30

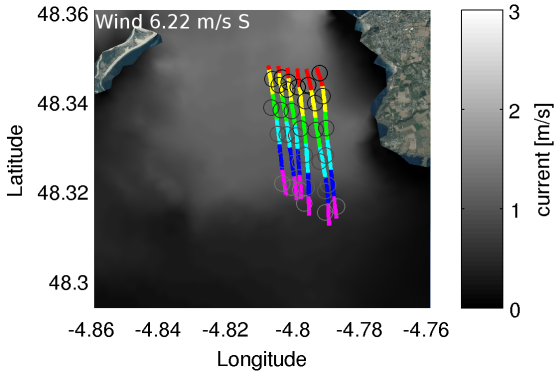

(e) SC3: SKIB 2015/10/23 13:40 to 14:40

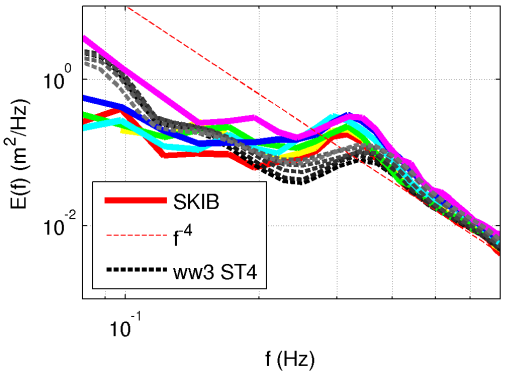

(f) SC3: SKIB 2015/10/23 13:40 to 14:40

Figure 4.6: Experimental conditions during BBWAVES 2015 SKIB acquisitions. The left panel shows the local current condition during the experiment, the 10 minutes drifting buoy segments of path are synchronized and marked by different colors, the gray circles represent the selected WW3 grid point output positions. The local wind conditions at 10 m considered in the model are labeled in white in the figures. The 10 minutes average spectral density of the variance and its evolution in time measured by SKIB buoys are presented in solid color lines, on the right panel, where the same quantity from the model is presented in dashed gray scale lines.

model can more or less represent the sea state conditions under low or moderate current conditions (Fig.4.5). However, errors strongly increase for currents over $\sim$1.2 m/s (see Figs. 4.5.f, 4.6.b,d and f). Those very general observations have led us to investigate these cases of stronger current conditions, where the WW3 model fails. From now, these observations presented in Figure 4.6 will be referenced as Study Cases (SC1, SC2 and SC3, respectively).

We note that the instruments used in this experiments were carefully tested and validated, as presented in Chapter 3. Nevertheless, to further verify the instrumental accuracy, the observed difference between the model output and the instruments were also obtained from the SWIFT buoys and ship-mounted stereo video system under similar conditions. Figure 4.7 exemplifies the oceanic and atmospheric conditions during a stereo video (SC4, Fig.4.7.a. and b.) and SWIFT buoy acquisition (SC5, Fig.4.7.c. and d.).

In selected case 1 (SC1, Fig.4.6.a) the SKIB were deployed in the Passage du Fromveur, with a light breeze from South, the relative wind and current direction is about 40^o. SC2 (Fig.4.6.c) presents similar atmospheric conditions to SC1, however, at SC2 the drifting buoys were placed at the edge of Passage du Fromveur, with a decreasing current speed from 1.73 to 1.05 m/s. Because in SC1 and SC2 the wind component has some alignment with the meridional buoys velocity, in these two cases we can considered that the short wave field are more or less following the current flow.

On the other hand, SC3 (Fig.4.6.e) is characterized by short wave and current propagating in an opposing direction. At SC3 the buoys were deployed in Chenal du Four, over an increasing current varying from 1.26 to 1.49 m/s. The wind waves were created by a 6.22 m/s South wind and propagating against this tidal current field. This is the same case already presented and discussed in Chapter 3 without the model comparison.

SC4 and SC5 (Fig.4.7) present a relative similar current conditions to the ones analyzed in SC1 and SC2, respectively. However, in these cases the relative wind and current suppose to be propagating in almost opposing direction (according to GFS U_{10} and buoys propagation direction). SC5 also present the strongest current condition analyzed here, where the drifting speeds varies from 1.4 to 3.6 m/s. These SC4 and SC5 cases are of particular interest because we also had measurements with the OCARINA and SWIFT.

4.4.2 Wind data

Here we use the data collected from the OCARINA and SWIFT instruments. The local wind, wave and current conditions appear in Figure 4.7.

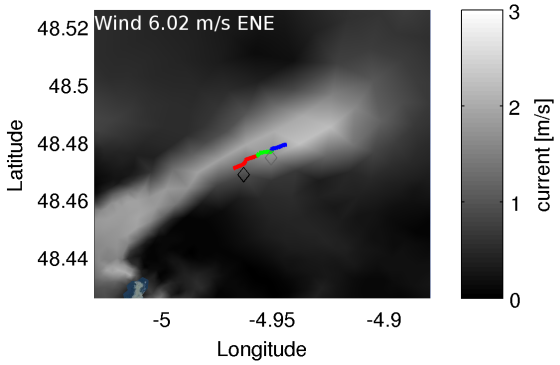

(a) SC4: Stereo video 2015/10/23 10:04 to 10:34

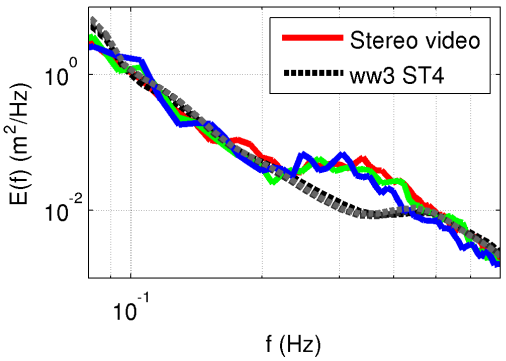

(b) SC4: Stereo video 2015/10/23 10:04 to 10:34

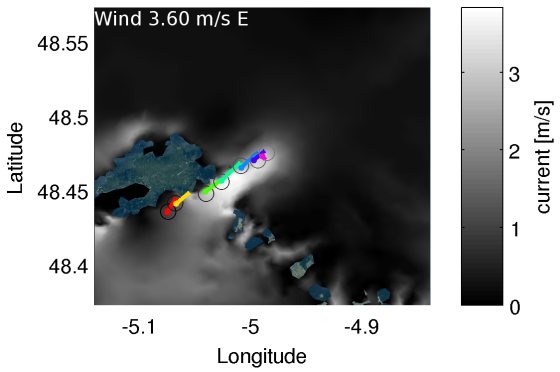

(c) SC5: SWIFT at 2016/09/21 15:08 to 16:32

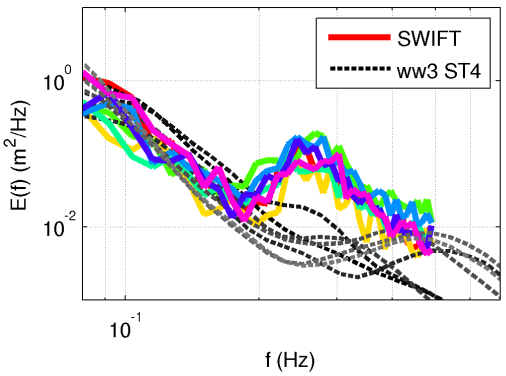

(d) SC5: SWIFT at 2016/09/21 15:08 to 16:32

Figure 4.7: Experimental conditions during stereo video and SWIFT acquisitions. The left panel shows the 10 minutes segments over the drifting buoy or stereo video path, superimposed on the estimated current condition from MARS simulations. The gray circles represent the positions of WW3 grid point output. The local wind condition at 10 m considered in the model is labeled in white in the figures. The evolution of the 10 minutes spectral density of the variance measured by stereo video and SWIFT buoy is presented in solid color lines, in the right panel where the same quantity from the model is presented in dashed gray scale lines.

Table 4.1: SC4 and SC5 wind and current conditions provided by the ECMWF operational model, compared with wind measurements from OCARINA and SWIFT, respectively. The MARS2D current C is also given for reference.

		SC4			SC5					
	Δt	34	12	12	12	12	12	12	12	min
Model	C	1.4	1.0	1.1	2.9	3.3	1.8	2.5	2.0	m/s
	U_{dir}	79	88	87	84	82	82	81	79	°
	U_{10}	6.0	3.6	3.6	3.6	3.6	3.6	3.6	3.7	m/s
Obs	U_{10}	5.4	4.7	4.4	4.9	3.7	3.2	5.7	5.1	m/s
	U_1	4.3	3.7	3.5	3.9	2.9	2.5	4.5	4.1	m/s
	U_{dir}	110	196	200	200	27	35	189	201	°

There are large differences in the wind directions between model and measurements, as indicated in Table 4.1. In case SC5 the wind direction difference is $\sim 120°$, and the measured velocity is 56% higher than the model. For all conditions the wind is on average 26% higher than the model.

4.5 Numerical tests

Numerical wave models are forced by winds, and the wind errors are generally expected to be the largest source of error (e.g. WISE Group, 2007; Rascle and Ardhuin, 2013). Given the large discrepancy between model and observations, we have thus investigated the accuracy of the wind forcing and tested a wide range of numerical model options. Table 4.2 shows the most important parameters tested and discussed in this section.

Table 4.2: Numerical tests, source term parameterizations, and adjustments of parameters and and wind forcing. The conditions in bold are the value, forcing or source function modified. ST4 is our controlled simulation with default values defined as TEST471 in The WAVEWATCH III® Development Group (2016). BJA is an abbreviation for the parameterization by Bidlot, Janssen and Abdallah (2005), which is activated by the ST3 switch in WW3, and mostly differs from ST4 by a global definition of wave steepness used for the dissipation parameterization. M2D is an abbreviation for the MARS2D hydrodynamic forcing field. WNDxR is an had hoc wind correction discussed in Section 4.5.1

	Source package				Breaking		Forcing		
Test	S_{in}	S_{ds}	S_{nl}	r_{wnd}	$C_{\mathrm{ds}}^{\mathrm{sat}}$	B_r	WND	WL	CUR
ST4	T471	T471	DIA	1.0	-2.2×10^{-5}	0.0009	ECMWF	M2D	M2D
AROME	T471	T471	DIA	1.0	-2.2×10^{-5}	0.0009	**AROME**	M2D	M2D
No current	T471	T471	DIA	1.0	-2.2×10^{-5}	0.0009	ECMWF	M2D	**0.0**
RWND=0	T471	T471	DIA	**0.0**	-2.2×10^{-5}	0.0009	ECMWF	M2D	M2D
WNDxR	T471	T471	DIA	1.0	-2.2×10^{-5}	0.0009	$U_{10}^{\mathrm{ECMWF}}\times\boldsymbol{R}$	M2D	M2D
ST3	**BJA**	**BJA**	DIA	1.0	–	–	ECMWF	M2D	M2D
SDSC2=0	T471	T471	DIA	1.0	**0.0**	0.0009	ECMWF	M2D	M2D
NL2	T471	T471	**WRT**	1.0	$\mathbf{-1.5\times10^{-5}}$	**0.0012**	ECMWF	M2D	M2D

To compare the differences between the observed and modeled at each frequency, for different time and positions, we use the mean space and time spectral density and of the variance spectral density for different model configurations and acquisitions.

Results are shown for the cases SC1–SC3 presented in Figures 4.6 and 4.7.

4.5.1 Alternative wind or current forcings

As explained in Section 4.2, phase-averaged spectral wave models are forced by the wind, which is usually specified as the direction and speed U_{10} at 10 m height. Following Plant (1982), the wave generation source term S_{in} is generally proportional to U_{10}^2. As a result, small errors in the wind forcing can have a large influence on short wave growth. In the present case, the 26% low bias revealed by the OCARINA and

SWIFT data suggest that the ECMWF wind error may be the main reason for the wave model underestimations in SC1 and SC2. Unfortunately, we have no in situ wind data for these three cases. We therefore tested another atmospheric model, the AROME system run by Meteo-France.

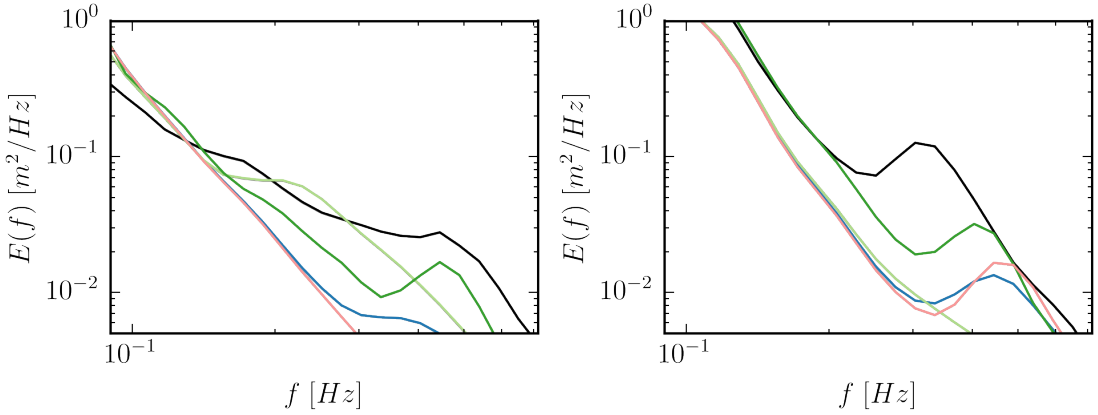

(a) SC1: SKIB 2015/10/23 08:30 to 09:00

(b) SC2: SKIB 2015/10/23 10:30 to 11:30

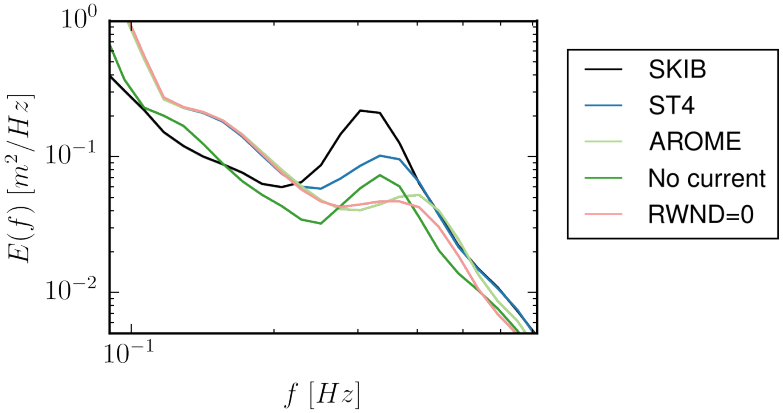

(c) SC3: SKIB 2015/10/23 13:40 to 14:40

Figure 4.8: Observation and numerical tests. The solid line represents a space and time average of the spectral density of the variance. The observation is shown in black and the color lines represent the different model setup, tested under strong current conditions presented in Figure 4.6. The differences are due to different parameterizations defined in Table 4.2.

Figure 4.8 shows that AROME winds are more accurate for SC1, but give worse results in SC2 and SC3. In general, the AROME wind speed was lower than that given by ECMWF, further reducing the short wave energy level.

Another important aspect of wave generation by the wind, is that it is the relative wind $\mathbf{U}_{10} - \mathbf{C}$ which drives the waves. Following Miles' theory we may also take $\mathbf{U}_c - \mathbf{C}$ where $\mathbf{U}_c$ is taken at the frequency-dependent critical layer height $z = z_c$, where the absolute phase speed $\mathbf{c}(f) + \mathbf{C}$ matches the wind speed $\mathbf{U}_{10}(z_c)$ (e.g. Hristov et al.,

2003). For $f = 0.25$ Hz, $z_c \simeq 3$ m, so that the effect of current is probably underestimated when using $\mathbf{U}_{10}$ instead of $\mathbf{U}_c$. In WW3, this correction on the wind speed that forces the wave growth is taken as a correction factor, with $\mathbf{U}_{\text{model}} = \mathbf{U}_{10} - r_{\text{wnd}}\mathbf{C}$. This effect was also found to be potentially important for tidal currents at coastal scales (Ardhuin et al., 2012). In our numerical tests, removing this relative wind effect, by taking $r_{\text{wnd}} = 0$, increased the error by 1 to 20% depending on the case and frequency. SC2 is an exception with better results obtained with the default value of $r_{\text{wnd}} = 1$. In general the importance of that effect should be tested with a coupled model combining ocean and atmosphere circulations, this is discussed below.

A sensitivity analysis on the current effect, running the model with or without current, shows that it has a significant impact. In SC3, with waves and current in opposing directions (Fig.4.6.e) the wave energy is lower without current, and the opposite is true for SC1 and SC2, when the waves follow the current.

Ad hoc correction of wind bias

From the near surface wind measurements, available only for SC4 and SC5, we observed that the ECMWF winds are biased. This bias may account for most of our wave model error in all cases. We present here a sensitivity analysis using a simple bias correction. Namely, the ECMWF forcing was multiplied by a constant factor R: $\boldsymbol{U}_{10}^{\text{ECMWF}} \times R$. For SC4 and SC5 the correction factor is calculated based on the near surface wind measurements from OCARINA and SWIFT, extrapolated to 10 m height (Tab. 4.1). For SC1, SC2 and SC3 we do not have the local wind information, so it was corrected by an a priori constant coefficient. These numerical tests follow ST4 parameterization with the only modification in the forcing fields (according to test WNDxR in Tab.4.2). The $\boldsymbol{R}$ coefficient used in each SCs is explicit in Table 4.3 and the results are presented in Figure 4.9.

Table 4.3: Constant correction factor $\boldsymbol{R}$ for used for each SCs theoretical wind sensitivity analysis.

	Test	$\boldsymbol{U}_{10}^{\text{ECMWF}} \times \boldsymbol{R}$	
SC1	WNDxR	$U \times \mathbf{1.5}$	$V \times \mathbf{1.5}$
SC2	WNDxR	$U \times \mathbf{1.5}$	$V \times \mathbf{1.5}$
SC3	WNDxR	$U \times \mathbf{1.1}$	$V \times \mathbf{1.1}$
SC4	WNDxR	$U \times \mathbf{-1.547}$	$V \times \mathbf{0.878}$
SC5	WNDxR	$U \times \mathbf{-5.864}$	$V \times \mathbf{-0.156}$

SC4 is the only case for which a wind correction was not able to give the main features of the measured wave spectra. In this case, the ship-mounted stereo video

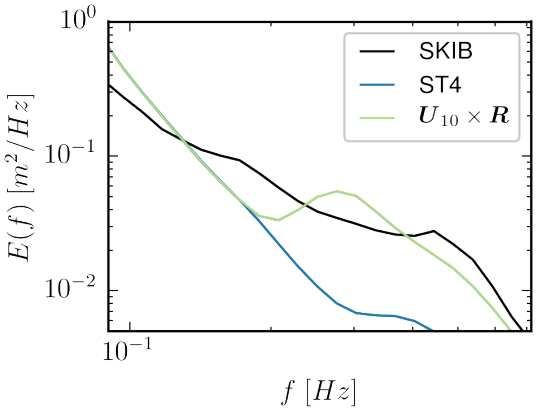

(a) SC1: from 2015/10/23 08:30 to 09:00

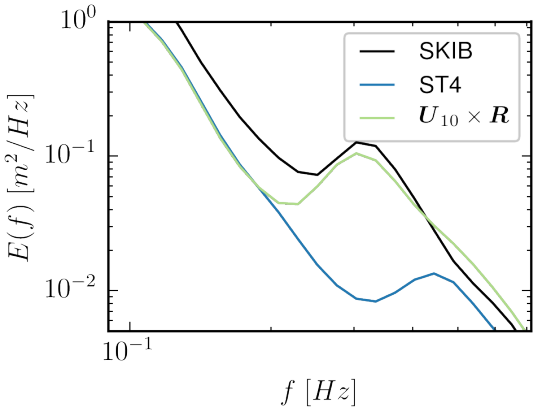

(b) SC2: from 2015/10/23 10:30 to 11:30

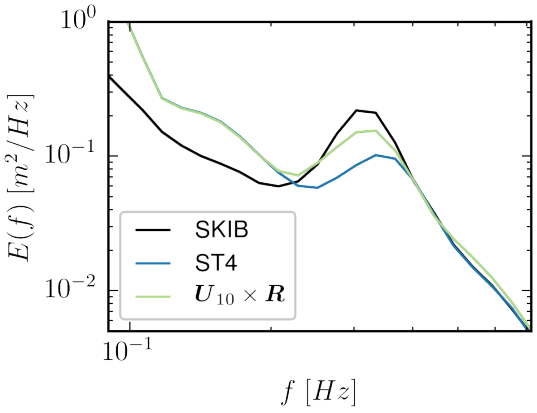

(c) SC3: from 2015/10/23 10:04 to 10:34

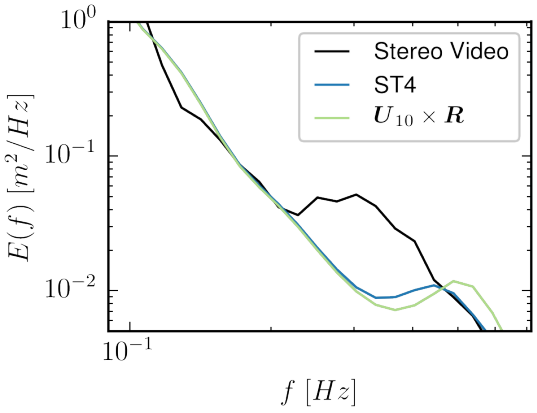

(d) SC4: from 2015/10/23 13:40 to 14:40

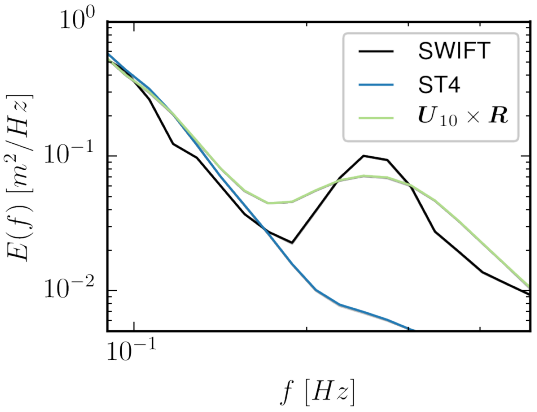

(e) SC5: from 2016/09/21 15:08 to 16:32

Figure 4.9: Observation and wind sensitivity tests. The solid line represents a space and time average of the spectral density of the variance. The observation is shown in black, the blue line uses the ECMWF wind forcing and the green line is a numerical test using the $\boldsymbol{U}_{10}^{\mathrm{ECMWF}} \times R$ correction.

and OCARINA were both collecting data, on the edge of the structure of the current field associated with Passage du Fromveur channel, at the same time (Fig.4.7.a). We speculate that in this case, this simplified wind forcing correction could not represent all the wave-current and air-sea interactions occurring all along the Passage du Fromveur channel.

As already discussed, if the wind forcing is biased this can be the most significant source of error in the model and cause a much stronger effect on the wind sea frequencies than the hydrodynamic current modulation. Given the errors on wind speeds and direction in SC4 and SC5 it appears that similarly weak corrections in all cases, except SC4, can explain most of the difference between model and observations.

In WW3 model, the wind stress is estimated from the wind speed at 10 m after the RWND correction, where the transfer of bulk momentum is used based on MOST theory to compute the wind input in the source function. The stress direction is typically assumed to be in the same direction as the wind U_{10}, although measurements have shown that this is generally incorrect, with differences that can exceed 30 degrees (e.g., Drennan and Shay, 2006; Potter et al., 2015). From the near surface measurements (expressed in Tab.4.1) we observed that the winds can turn and align with the tidal current, in SC5 for instance, even reversing the wind direction.

The wave energy observed at frequencies related to the wind sea spectrum was consistent with ad hoc wind corrections applied to U_{10}.

4.5.2 Wave dissipation parameterization

After forcing, the main source of error in wave models generally comes from parameterizations (Roland and Ardhuin, 2014). The parameterization by Bidlot et al. (2005), hereinafter called ST3, is a modification of the so-called WAM -Cycle 4 parameterization (Janssen, 1994). This uses a single mean steepness for the entire spectrum as a key parameter for the dissipation rate, compared to a steepness that varies across the spectrum in the case of ST4. As a result it was already showed by Ardhuin et al. (2012) that it tends to give larger waves in waves against current conditions because the short waves have a larger steepness that then mean steepness, and a dissipation based on the mean steepness tends to give a lower dissipation. Another difference between ST4 and ST3 is the ad hoc reduction of $u_\star$ at high frequency to balance the saturation-based dissipation, which gives a slower wave growth at short fetches.

When comparing model results in simulations with ST3 and ST4, SC3 is the most interesting case with realistic energy levels at high frequencies considering ST4, but with a strong underestimation at the wind sea peak. This difference is similar to the one reported by Ardhuin et al. (2007), with the presence of low frequency waves

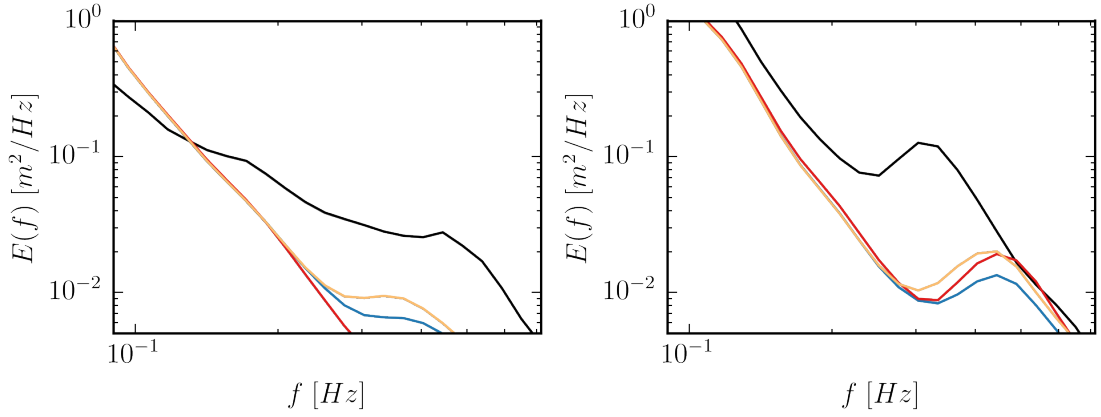

(a) SC1: SKIB 2015/10/23 08:30 to 09:00

(b) SC2: SKIB 2015/10/23 10:30 to 11:30

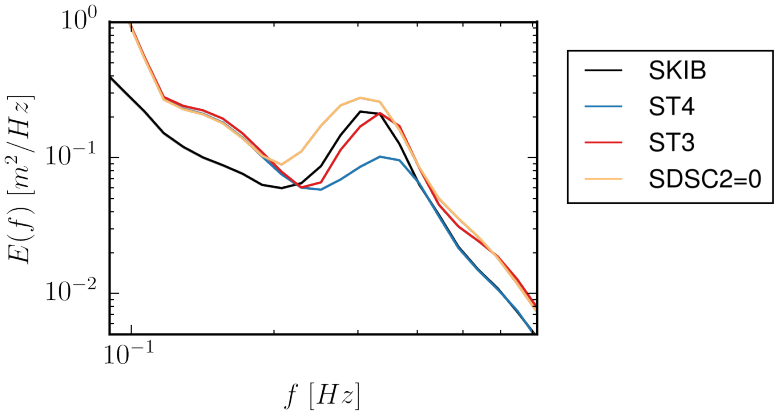

(c) SC3: SKIB 2015/10/23 13:40 to 14:40

Figure 4.10: Observation and model tests. The solid line represents a space and time average of the spectral density of the variance. The observation is shown in black and the color lines represent the different model setup, tested under strong current conditions presented in Figure 4.6. The difference between the parameters accounting of the physics in the model according to Table 4.2.

leading to a reduced value of the mean wavenumber and an artificial reduction in the short wave dissipation in ST3. At SC1 and SC2, the model generally has a wind sea peak ($f \simeq 0.25$ Hz) at too high a frequency. This bias can be related to the general bias at short fetch of ST4 simulations, or to an underestimation of the wind speed. For the other cases, we first note that the model errors are very large in SC1 and SC2 with a large negative bias of the modeled wave energy (Fig.4.6.a). In these two cases the difference between ST3 and ST4 is relatively minor. In fact, by setting the breaking dissipation to zero in ST4 ($C_{\text{ds}}^{\text{sat}} = 0$, Eq.4.12, numerical test SDSC2=0 at Fig.4.10) hardly reduced the negative bias, so that more than a dissipation problem it must be a problem of too low energy input, probably from the wind, possibly from the currents or the combination of wind and current.

4.5.3 Parameterization of nonlinear interactions

Another source term parameterization that is also the source of errors is the accounting of non-linear 4-wave interactions (NL2, Tab.4.2). The theory for these interactions is given by the Boltzmann integral formulation of Hasselmann (1962, 1963) that can be reduced to a 3-dimensional integral using the Webb-Resio-Tracy method, WRT for short (Webb, 1978; Tracy and Resio, 1982; Resio and Perrie, 1991). However, because of the large cost of computations, these interactions are usually approximated with the Discrete Interaction Approximation (DIA, proposed by Hasselmann et al., 1985). That approximation reduces the interaction to a very small sub-space of the possible interactions, which keeps the general shape of the S_{nl} source term but changes the magnitude of the different fluxes towards low and high frequencies and the resulting directional wave spectrum (Banner and Young, 1994; Polnikov and Farina, 2002; Resio et al., 2011; Ardhuin et al., 2007). Here we investigated the impact of the DIA parameterizations by switching to the accurate WRT method for computing S_{nl}, together with a minor reduction of wave dissipation following Banner and Young (1994), see parameters in Table 4.2. In order to limit the cost of this computation, we start from the DIA model result at noon on 23 October, and integrate the model for only 3 hours, corresponding to SC3. The results are detailed on Figure 4.11.

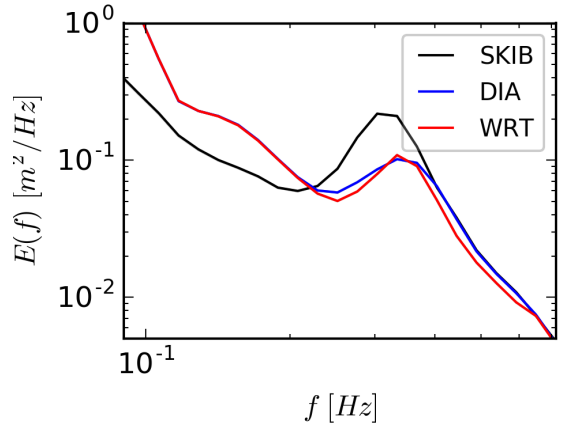

Figure 4.11: SC3: Average spectral density of the variance during SKIB buoy path, from 2015/10/23 13:40 to 14:40. The black line corresponds to the conditions observed by the drifting buoy and the color lines the numerical test with DIA and WRT methods for the computation of the non-linear source term S_{nl}.

As already found other simulations using WRT, (e.g. Banner and Young, 1994; Tolman et al., 2005; Gagnaire-Renou et al., 2010), the spectra computed with the exact method tends to have a narrower wind sea peak, closer to the shape of the observed spectra. However, the errors in the DIA cannot explain the strong underestimation of

the wave energy around the wind sea peak, which, as stated before are probably due to wind forcing errors.

4.5.4 Summary of model tests

In summary, in conditions of waves propagating in areas of strong current gradients, several processes may have a strong impact on the energy levels of the wind sea peak. In particular the wave generation by the wind in conditions where waves follow the current is very sensitive to wind speed errors. This is because the relative wind speed is further reduced when the current speed is subtracted, so that the errors on the wind speed are relatively more important for the relative wind.

In the conditions analyzed here, the errors due to parameterizations of the dissipation or non-linear source term may be important, but in the absence of more detailed wind measurements, they are difficult to isolate here.

4.6 Coupled models for winds and currents

One way to make progress on the wind forcing for wave growth is to have a more realistic atmosphere, coupled to the ocean. We have used the results from a coupled numerical simulation using Meso-NH and MARS3D. These model simulations were performed by Marie-Nöelle Bouin at LOPS, and the model set-up was developed by the LOPS team including Valérie Garnier and Jean-Luc Redelsperger. Meso-NH is an atmospheric circulation model (Lafore et al., 1998) and MARS3D is an ocean circulation model (Model for Application at Regional Scale, Lazure and Dumas, 2008). These two models are coupled by a standard coupling interface in the SURFEX surface model (Masson et al., 2013) based on the OASIS3-MCT coupling system. This coupling method follows the same implementation done by Voldoire et al. (2017). In this strategy, the sea surface moment flux and heat transfer between ocean and atmosphere is recomputed inside of each modeling timestep, constantly modifying the boundary conditions and consequently the near oceanic and atmospheric circulation.

Two Meso-NH simulations were done for BBWAVES 2015 experiment. One simulation was coupled with sea surface temperature and current (STC) from a 500x500 m MARS3D (Lazure and Dumas, 2008) and another simulation was forced with sea surface temperature from the OSTIA analysis (Donlon et al., 2012, Operational Sea Surface Temperature and Sea Ice Analysis,) and no current (NC). The atmospheric boundary condition for Meso-NH comes from the Meteo-France operational Arome winds every 3h. The Meso-NH was run on a 1.250×1.250 km horizontal grid resolution, 55 vertical levels, from 22/10/2015 00:00:00 to 24/10/2015 00:00:00 UTC corresponding to BBWAVES 2015 experiment.

According to Lafore et al. (1998) the Meso-NH bottom boundary is defined as an insulated rigid lid allowing for free slip tangential velocity. In the physical package of the model it is included the turbulent fluxes of heat, moisture and momentum normal to the surface are computed through bulk drag coefficients depending on wind and stability. These ocean and atmosphere exchanges depend on the wind speed and air-sea gradients of temperature, humidity and velocity. The fluxes at the air-sea interface take into account near-surface atmospheric and oceanic parameters, following a radiative scheme and a bulk parameterization of the sea surface turbulent flux.

$$\boldsymbol{\tau} = \rho_a C_D (\boldsymbol{C} - \boldsymbol{U}_a)^2 \tag{4.24}$$

where C_D is the drag coefficient calculated by a parameterization of the sea surface turbulent fluxes. U_a is the wind at the first atmospheric level ($\sim$ 10 m height). ρ_a is the air density and C it the horizontal current.

The atmospheric momentum flux varies in function of the sea state through the drag coefficient C_D depending on the roughness length z_0 such as:

$$C_D = \frac{\kappa}{\log\left[\left(\frac{z}{z_0}\right) - \Phi\left(\frac{z}{l}\right)\right]^2} \tag{4.25}$$

$$z_0 = \alpha\frac{u_\star}{g} + 0.11\frac{\nu}{u_\star} \tag{4.26}$$

where z is taken at the first atmospheric level, κ is the von Kàrmàn constant, Φ is an empirical stability function, and l the Monin-Obukhov length. The roughness length z_0 is related to the Charnock parameter α and to the friction velocity $u_\star$ through the Charnock's formulation (1955) with the smooth flow limit effect following Smith (1988).

This approach is very similar to the one used in WW3 for the relative wind correction, in the routine that computes the friction velocity $u_\star$, which is then used to compute S_{in}. However, here the coupling with the atmosphere allows to have all the atmospheric fields (U, τ, z_0 and others) influenced by the surface current, with a consistent boundary condition at the sea surface.

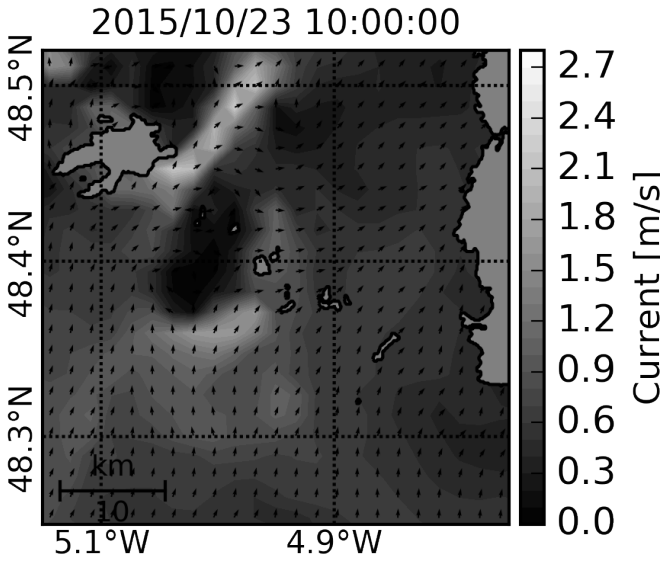

Figure 4.12: Meso-NH-MARS3D current conditions at 2015/10/23 10:00 UTC.

Figure 4.12 shows an example of the surface current from MARS3D that is passed to Meso-NH at October 23, 2015 10:00 UTC (time corresponding to SC4). The Meso-NH results for this time are presented on Figure 4.13. Figure 4.13 shows the Meso-NH wind speed at the lowest model level near to 10 m height (U_{10}) and air-sea moment flux at the ocean (τ_s) for STC and and NC simulations.

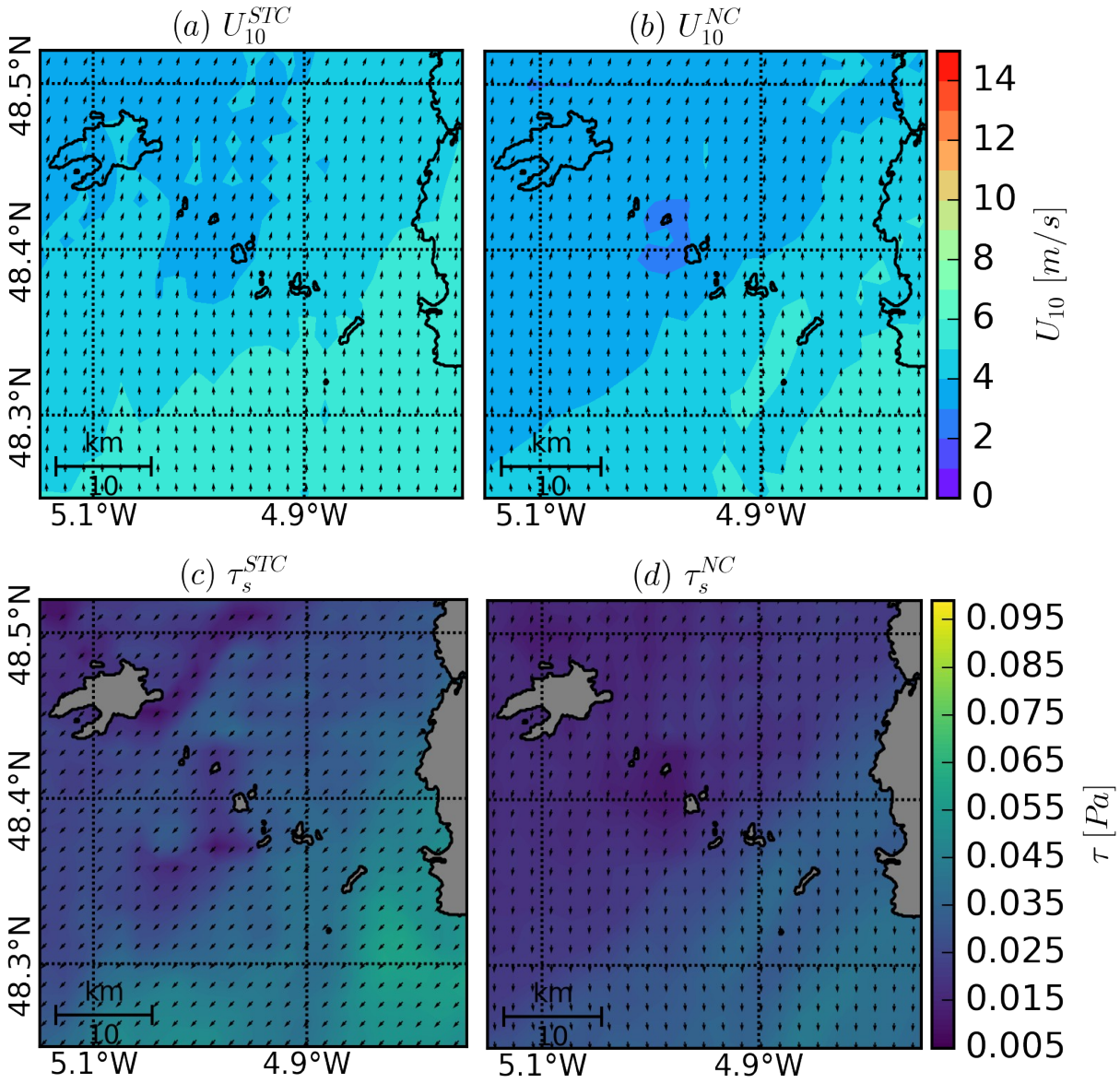

Figure 4.13: Meso-NH output for October 23, 2015 10:00 UTC. a) wind speed near a 10 m height (U_{10}) for the numerical simulation (STC) coupled with sea surface temperature and current from MARS3D; b) wind speed near a 10 m height (U_{10}) for the numerical simulation (NC) forced with OSTIA sea surface temperature and without current; c) Air-sea momentum flux at the ocean surface (τ_s) for STC numerical simulation, coupled with sea surface temperature and current from MARS3D; d) Air-sea momentum flux at the ocean surface (τ_s) for NC numerical simulation, without current.

Figure 4.13.a and b picture some differences between STC and NC simulations. A first analysis allows to observe that STC present higher speeds than NC, with a minor impact in the wind direction. To evaluate closer what is happening in the oceanic and atmospheric boundary layer, at Figure 4.13.c and d is possible to compare the air-sea moment flux τ_s for STC and NC. When comparing Figure 4.13.c with the current field (Fig.4.12) is possible to observe a significant reduction of τ_s over the tidal current structures.

In order to better quantify the differences between STC and NC, Figure 4.14 expresses the normalized difference between these two simulations.

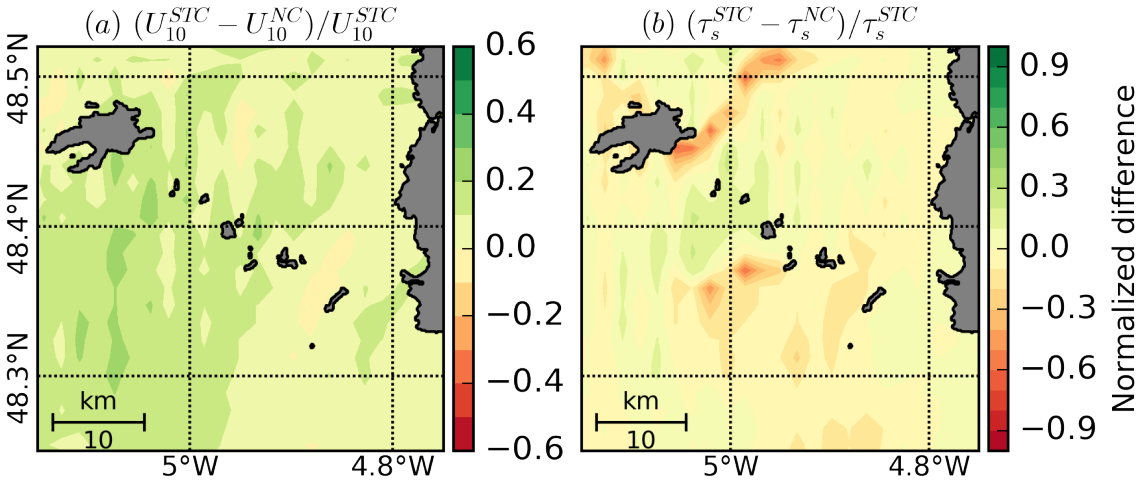

Figure 4.14: Comparison between STC and NC for Meso-NH output at October 23, 2015 10:00 UTC. a) shows the normalized difference for U_{10} and b) for τ_s.

When the models are coupled, U_{10} is intensified by about 20 to 40% around the Passage du Fromveur. This difference of 20 to 40% in the U_{10} is still much lower than the one expected from the observations data acquired during the BBWAVES 2015 campaign (Fig.4.15). This basically occurs because the AROME forcing field winds were much weaker than ECMWF, resulting in a weaker wind input.

The tidal current impact in the near surface circulation is more evident in the air-sea moment flux, where the coupled simulation with sea surface current has caused a reduction in the order of 90% in τ_s. This has a direct impact on the surface drag coefficient, wind shear and the roughness length, consequently modifying local wind speed and wave growth.

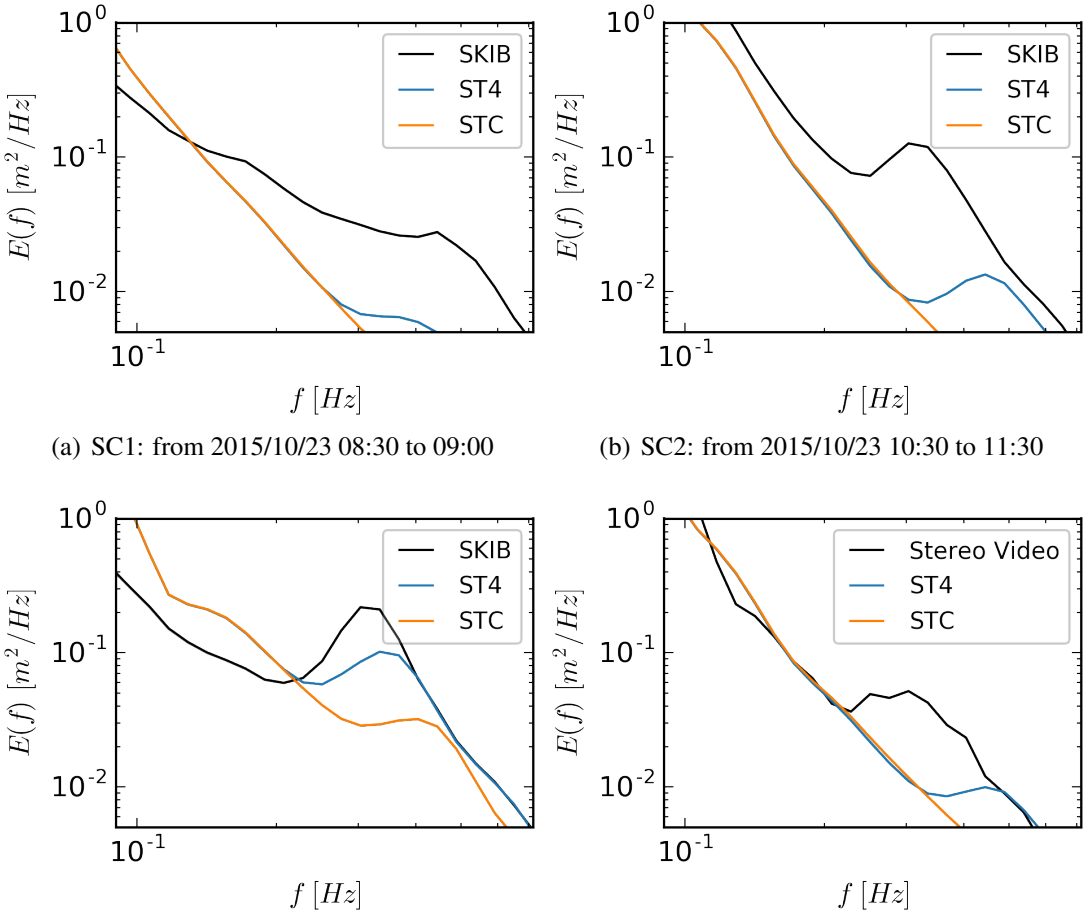

(a) SC1: from 2015/10/23 08:30 to 09:00

(b) SC2: from 2015/10/23 10:30 to 11:30

(c) SC3: from 2015/10/23 10:04 to 10:34

(d) SC4: from 2015/10/23 13:40 to 14:40

Figure 4.15: Spectral density of the variance for BBWAVES 2015 observations. ST4 in blue is our reference test, with ECMWF wind. STC (orange) corresponds to the same WW3 simulation, but with $r_{\text{wnd}} = 0.0$ and forced with U_{10}^{STC} from coupled Meso-NH-MARS3D simulation with sea surface temperature and current.

4.7 Summary and conclusion

In this chapter we used several drifting buoys in an environment with strong tidal currents to measure the wave transformations along their propagation path in various fields of coastal currents. These conditions have been difficult to reproduce numerically, presumably due to errors in the forcing wind fields leading to significant underestimation of the wind sea energy. These underestimations were systematic for all the sensors deployed and for both experiments, in 2015 and 2016.

By performing several numerical tests with different forcing fields we conclude that the main source of error was in the wind forcing. This wind bias could not be explained by the relative wind and current correction neither by different model parameterizations, accounting for dissipation, current and nonlinear processes.

With an artificial wind enhancement in the model, the estimation of the spectral density of the variance was able to reach the values measured by the buoys. This forced wind correction considered higher wind speeds, in the order of 10 to 50% increment in U_{10}.

A similar scale of variation of wind speed was also found by comparing two coupled Meso-NH and MARS3D simulations, the first accounting for fields of currents at the free surface and the second neglecting currents. However, the direct impact of currents in U_{10} was not so clear to observe in the coupled simulation results. A direct link between wind and current was more evident trough the air-sea moment flux. If compared with the simulation without current, the current have modified the air-sea moment flux in the scale of 90% around Passage du Fromveur area.

This possibility can be numerically solved by improving the parameterization of the empirical growth rate or by using a high-resolution coupled atmospheric, hydrodynamic and wave models, which is not investigated in this work. Nevertheless, from these observations and numerical experiments arises new focus on the interaction between fields of tidal currents and winds, probably not properly documented before. Complementary field observations and deeper investigation are thus required on this aspect.

5. Short waves modulation by longer waves

Stereo video observations of short waves breaking modulated by longer waves

Résumé

Les recherches sur le déferlement des vagues se sont d'abord intéressées à une prédiction déterministe de l'apparition du déferlement. Les travaux réalisés depuis Banner et all. (2000), ont étendu cette analyse à des relations statistiques entre la probabilité de déferlement et l'énergie moyenne dans une gamme fixe de fréquences. Cette approche est paticulièrement adaptée au paramétrage de la dissipation dans les modèles de prévision des vagues utilisant une représentation spectrale à phase moyennée. Les paramétrages anciennement proposés par Hasselmann (1974) et Komen et al. (1984) utilisaient un seul paramètre de pente pour l'ensemble du spectre des vagues, avec des effets artificiels d'interactions entre houle et mer du vent: typiquement l'ajout d'une houle provoquait une réduction de la dissipation pour la mer du vent (Ardhuin et al. 2007). L'analyse de la propagation de vagues dans des gradients de courant a amené Phillips (1984) à séparer les différentes composantes du spectre avec une taux de dissipation variant avec le cube de la densité spectrale. Cette approche est cohérente avec les observations de probabilité de déferlement, au moins pour les vagues dominantes. Elle est aujourd'hui largement utilisée dans les modèles opérationnels et produit généralement un meilleur accord avec les observations de hauteur significative et de forme du spectre (Ardhuin et al. 2010, Rascle et Ardhuin 2013, Stopa et al. 2016).

Cependant, il existe tout de même un lien entre les différentes componsantes du champ de vagues. En particulier, les ondes de plus grande longueur d'onde

provoquent une modulation des propriétés des vagues plus courte qui peut augmenter leur probabilité de déferlement. Dans ce chapitre nous utilisons une technique de stéréo-video qui permet d'observer en mer la forme des vagues courte et leur évolution, ainsi que les déferlement. Les données expériementales ont été acquises en septembre 2013, sur la plateforme de recherche océanographique de Katsiveli, située en mer, à 600 m de la côte sud de la Crimée, entre Sébastopol et Yalta. Deux traitements sont réalisés. Le premier est une reconstruction de l'évolution de la surface en trois dimensions, dont la méthode est décrite par Benetazzo (2006), Fedele et al. (2013), Leckler et al. (2015). Le second traitement est une analyse de l'écume et des évènements déferlants sur la base de la radiance de l'image. Ce deuxième traitement suit les travaux de Mironov et Dulov (2008). La combinaison des deux méthodes fournit une détection des déferlement en lien avec le champ d'élévation de surface $\zeta(x,y,t)$.

Nos résultats sont généralement compatibles avec la théorie de Longuet-Higgins. Ainsi, l'amplitude des modulations dépend de la direction relative des vagues longues par rapport au vent, et est plus importante pour des vents faibles. Une analyse de la distribution de l'énergie des vagues courtes en fonction des fréquences et des nombres d'onde montre un effet possible de la modulation. Enfin, nous proposons une prise en compte des modulations dans le paramétrage adapté de Banner et al. (2000), avec une saturation effective des vagues courtes modifiée par la présence des vagues longues.

5.1 Introduction

The breaking of surface gravity waves plays an important role in air-sea interactions (Melville, 1996). Wave breaking is the main source of waves energy dissipation and contributes to upper ocean mixing (Agrawal et al., 1992), while enhancing gas fluxes at the air-sea interface and producing spray in the atmosphere (Veron, 2015). Wave breaking also modifies many ocean parameters retrieved by remote sensing methods, from wind speed to surface salinity (e.g. Reul and Chapron, 2003; Mouche et al., 2017).

For random waves, the prediction of the breaking onset of a single wave is particularly difficult (Banner and Peirson, 2007). Another approach pioneered by Phillips (1984, 1985) looks at statistical properties of breaking wave fronts. Assuming a broad wave spectrum, Phillips (1984) hypothesized a non-linear relation between the breaking probability of waves with wavenumber k and the saturation spectrum $B(k)$, which is the non-dimensional surface elevation spectrum and thus a spectral measured of the wave steepness. This relation was needed to explain the strong enhancement of wave breaking in current gradients. This hypothesis was first verified by Banner et al. (2000) and other investigators including Romero et al. (2012b); Gemmrich et al. (2008); Thom-

son (2012); Sutherland and Melville (2013, 2015). This relation can be interpreted as a preferential breaking probability for steep waves, for which the orbital velocity approaches the phase speed, in a random wave height distribution that closely follows a Rayleigh distribution (Filipot et al., 2010).

The link between saturation and breaking probabilities has been used in numerical models, leading to successful parameterizations of related properties such as the dissipation rates for the wave energy. All this line of work has thus associated the dissipation rate of components with wavenumber k to the energy at the same wavenumber k, with no influence of other wave components. However, practical applications of numerical models suggest that it is not possible to reproduce the shape of wave spectra without some 'cumulative effect' of the long waves on the short waves. Many different parameterizations have been proposed to reproduce this behavior, with heuristic justifications that mentioned various processes such as the dissipation of short waves in the wake of breakers (Banner et al., 1989) or the enhanced steepness of short waves (SW) in the presence of longer waves (LW) (Donelan, 2001; Young and Babanin, 2006; Babanin and Young, 2005). One quantitative formulation by Ardhuin et al. (2010) computed the rate of passage of breaking waves and considered all shorter waves to be instantly dissipated. However this effect tends to produce a direction-integrated spectrum $E(k)$ that decays like $k^{-2.75}$ (Stopa et al., 2016) instead of the observed k^{-3} or steeper (Leckler et al., 2015). Also these parameterizations fail to reproduce both energy levels and directional distributions observed at wavelengths ranging from 1 to 10 m (Peureux et al., 2017).

Our focus in this chapter will be on the quantification of the enhancement of short waves (SW) steepness in the presence of longer waves (LW), and its consequences of wave breaking and energy dissipation. In practice our SW have wavelengths from 0.5 m to 10 m. Looking at such intermediate wavelengths, around 1 m, Dulov et al. (2002) found that dominant waves strongly influence their breaking probability. Dulov et al. (2002) study used digital video processing. Here we combine such video techniques for breaking detection (Mironov and Dulov, 2008; Thomson, 2012), using recent advances in stereo video (Benetazzo, 2006; Leckler, 2013; Bergamasco et al., 2016) that give a simultaneous measurement of the surface geometry. In particular we analyze data from a stereo-video experiment carried on a research platform off the coast of Crimea, in the Black Sea.

The first discussions on this subject starts with Longuet-Higgins and Stewart (1960). Their work explores the LW effects on SW is due to the excess momentum associated to the presence of short waves known as the radiation stress. This theory reproduces a shortening and steepening of the SW near the LW crest that is readily

observed. This model was refined by Longuet-Higgins and Stewart (1964) to include the modulation of the apparent gravity felt by the short waves. This forms the basis of the conservative model described below, which we will use to give solutions that extend the Longuet-Higgins and Stewart (1964) solution. This model is more readily formulated using the wave action $N = E_{\rm tot}/\sigma$ (Bretherton and Garrett, 1968; Andrews and McIntyre, 1978) in which $E_{\rm tot}$ is the density of short wave mechanical energy per unit surface, and σ is the intrinsic wave frequency. We recall that $E_{\rm tot} = \rho_w \widetilde{g} E$ where ρ_w is the water density, $\widetilde{g}$ is the apparent gravity felt by the short waves riding on the long waves, and E is the local short wave elevation variance, which is modulated along the LW profile. The conservation of N corresponds to an exchange of energy between the SW and LW that can also be interpreted as the work of the SW radiation stresses on the LW orbital velocities (Phillips, 1977).

Further extension of the modulation theory of the SW spectrum was done for shorter waves, with wavelengths typically 1 cm to 30 cm (Keller and Wright, 1975; Smith, 1986; Keller and Plant, 1990; Belcher and Hunt, 1993; Hara and Plant, 1994; Kudryavtsev et al., 2001; Kudryavtsev and Makin, 2002; Kudryavtsev and Chapron, 2016). The growth and decay of these SW is significant at the scale of a LW wavelength, due to the wind, dissipation and non-linear interactions. Hence the extension consisted of adding these non-conservative effects, and was used for remote sensing applications that use microwave scattering of the ocean surface. In particular this modulation is a central aspect of the Delta-K technique proposed to measure currents using Doppler radars (Alpers and Hasselmann, 1978), which is an alternative to the Doppler centroid method already used on Envisat (Chapron et al., 2005). Both methods will be considered for the Sea surface KInematics Multiscale monitoring (SKIM) mission (Ardhuin et al., 2017a).

Finally, to further develop this theory we intend to link our in situ observation to Phillips (1984, 1985) statistical approach and discuss the application of modulation theory in the context of wave dissipation parameterization based on the spectral saturation, following Ardhuin et al. (2010). The resulting parameterization presented here has some similarity to that of Donelan (2001), who proposed a parameterization of the dissipation in which the dissipation rate is proportional to $[1 + a\ {\rm mss}(k)^m]^n B(k)^p$, where ${\rm mss}(k)$ is the mean square slope of short waves modified by all wave components longer than k. According to Donelan (2001) observations $m = 1$, $n = 2$ and $a = 500$. However, we replace $m = 1$ by $m = 0.5$, to be consistent with modulation theory, and use values of a up to 20. These values of a will be later relate to the linear modulation transfer function (MTF), used in the non-conservative theories.

5.2 Theoretical background

5.2.1 Conservative theory

Based on the conservative theory, like proposed by Ramamonjiarisoa (1995), we will first consider the case of SW with an surface elevation variance $E(x,y,t)$ that varies on the scale of long waves. The LWs are assumed to be linear and their surface elevation ζ_l, orbital velocity U_l and downward vertical acceleration $\widetilde{g} = g - \partial^2\zeta/\partial t^2$ are given by a narrow-banded spectrum. Where the subscript $_l$ and $_s$ refers only to LW and SW properties.

Omitting the constant water density, the SW wave action

$$N = \widetilde{g}E/\sigma_s \tag{5.1}$$

where σ_s is the SW local intrinsic frequency. Since we consider only short wind-waves they are in deep water and their local wavenumber is $k = \sigma^2/g$ and the local intrinsic phase speed is $c = \sqrt{\widetilde{g}/k}$ and the group speed is $c_g = c/2$.

The determination of the local short wave elevation variance E reduces to the conservation of the number of waves and of the wave action. Without loss of generality we take the x axis along the propagation direction of the long waves, so that the SW propagate in direction θ_s[1]

$$\cos\theta_s \frac{\partial k}{\partial t} = -\frac{\partial}{\partial x}\left[(c\cos\theta_s + U_l)k\right] \tag{5.2}$$

$$\frac{\partial N}{\partial t} = -\frac{\partial}{\partial x}\left[(c/2\cos\theta_s + U_l)N\right] \tag{5.3}$$

$$E = \sqrt{\widetilde{g}k}N \tag{5.4}$$

The complexity in these equations comes from the right-hand side propagation and advection terms that are non-linear because both k or N and the velocity terms in brackets are modulated.

A similar form used by (Longuet-Higgins and Stewart, 1964, Section 8) is

$$\frac{\partial E}{\partial t} = -\frac{\partial}{\partial x}\left[(c/2 + 1.5U_l\cos\theta_l)E\right] \tag{5.5}$$

These authors introduced a very strong simplification, by assuming that the modulation of c and E on the right hand side could be neglected[2]. "*The horizontal variation of*

[1] These equations are only correct for $\theta_s = 0$ or $\theta_s = \pi$, otherwise an equation for $\partial\theta/\partial t$ should be added.

[2] In their case it is E and not N because they used radiation stresses and not wave action.

E and c arises only because of the interaction, and so is irrelevant to (Eq.5.5) if the equation is taken only to the lowest order." As we shall see below, this assumption is incorrect but it gave them a simple solution. For the case of LW and SW in the same direction, they considered a monochromatic long wave with

$$\zeta_l = A_l \cos(k_l x - \sigma_l t) \tag{5.6}$$

and they estimated

$$E = E_0 \left[1 + M_E \cos(k_l x - \sigma_l t)\right] \tag{5.7}$$

where M_E is the modulation transfer function (MTF) for the short wave elevation variance. They found that $M_E = 1.5$.

One reason why this solution is not correct is that the neglected terms are of the same order as the term that is kept. Their solution gives $\partial E/\partial x = 1.5 k_l E_0$ so that one of the neglected terms in the right hand side is $1.5 U_l \partial E/\partial x = 2.25 k_l U_l E$ which is actually larger than then $1.5 E \partial U_l/\partial x = 1.5 k_l U_l E$ term that they have kept, and the modulations of c also introduce terms of the same order.

The fact that the relative changes in energy, wavenumber are of the same order as the changes in U_l, is similar to the problem of waves going across a spatially varying but steady current gradient U_l. In that case the "modulating parameter" is a Froude number $\alpha = 2U_l/c_0$, ratio of the current speed and short wave group speed, with a solution is given by Phillips (1977) and Ardhuin and Filipot (2016, Chapter 7)

$$\widetilde{\sigma}_s = \sigma_s^0 \frac{1 - \sqrt{1 - 2\alpha}}{\alpha}. \tag{5.8}$$

Where $\sigma_{s,0} = 2\pi f = \sqrt{k_s/g}$ comes from the linear dispersion relation and $\omega_s = \sigma_{k_s}^0 + k_s U_l$ neglects the apparent gravity effect. In that case, for small values of α, we have $E = E_0(1+4\alpha)$, $\sigma_s = \sigma_{s,0}(1+\alpha)$, $k_s = k_{s,0}(1+2\alpha)$, and the short wave mean square slope is $B = B_0(1+8\alpha)$. We could thus expect a similar behavior, with a modulation parameter given by $\alpha = 2\cos\theta_s U_l/c_{s,0}$, instead of the $A_l k_l$ used by Longuet-Higgins and Stewart (1964, where $\alpha = 2c_l/c_{s,0}\cos\theta_s A_l k_l$).

In fact Equations 5.2 and 5.3 are very close to the system of equations investigated by Ardhuin et al. (2012). We use a numerical integration of Equations 5.2 and 5.3 in time starting from initial conditions $k = k_0$, $N = N_0$, and a boundary condition at $x = 0$. The values of k and N are discretized in a one-dimension domain with a resolution Δ_x, and this vector is updated in time with a time step Δ_t. The spatial derivatives are estimated using second order finite differences and the time integration corresponds

to an upwind scheme. The integration was performed in Matlab, using a second-order upwind scheme, following the work of Ardhuin et al. (2012) on wave modulation by tidal currents. The quality of the solution was verified by testing the convergence when both Δ_x and Δ_t are reduced. We thus start with periodic long waves, and our computation domain $10 \times L_1$ m over $10 \times T_1$, where L_1 and T_1 represent the LW length and peak period. The subscript $_1$ is used here to reference LW conditions at the peak of the spectrum.

Anticipating the conditions of the stereo video observations data presented below, we take a long wave amplitude varying from $A_1 = 0.01$m to $A_1 = 0.33$m, and a period $T_1 = 4.3$ s, and short waves with a period $T_s = 2.5$s. All integrations are performed with $\Delta_x = 0.01(2\pi/k_1) \simeq 0.5$ m horizontal resolution and a time step of $\Delta_t = 0.004$s.

In these first simulations we use the following LW orbital velocity, in which the tanh term is there to allow a smooth transition at the boundary condition,

$$U_l = U_{k_1}^{\mathrm{rms}} \cos(k_1 x - \omega_1 t) \times 0.5 \left\{1 + \tanh[(x - hdx)/10dx]\right\}. \tag{5.9}$$

Figure 5.1 shows the SW time evolution of H_s, wavenumber k_s and phase velocity c_s over the LW orbital velocity U_l at $x = 192$ m. Close to $x = 0$, the model behavior is nearly periodic, and we get a simple modulation with a generally larger wave energy and wavenumber at the crest of the LW.

So to explore deeper this relation in Figure 5.2 and 5.3 it is shown the oscillatory characteristic of the SW energy, modulated by a simple periodic LW forcing current. In this case it is presented N_0 and $\sigma_{s,0}$ initial conditions computed from several discrete intervals, considering realistic conditions measured from stereo video.

It is expected that both σ_s and ω_s oscillate around the linear deep water dispersion relation. Figures 5.2 and 5.3, a. and b., exemplify the SW wavenumber and apparent frequency dependency under a periodic LW orbital velocity.

Further away from $x = 0$ or using periodic boundary conditions in x, numerical solutions appear to be periodic in space but not in time. One may define MTFs from these, for example

$$M_E = \left(\max(E) - \overline{E}\right)/\overline{E}, \tag{5.10}$$

$$M_k = \left(\max(k) - \overline{k}\right)/\overline{k}, \tag{5.11}$$

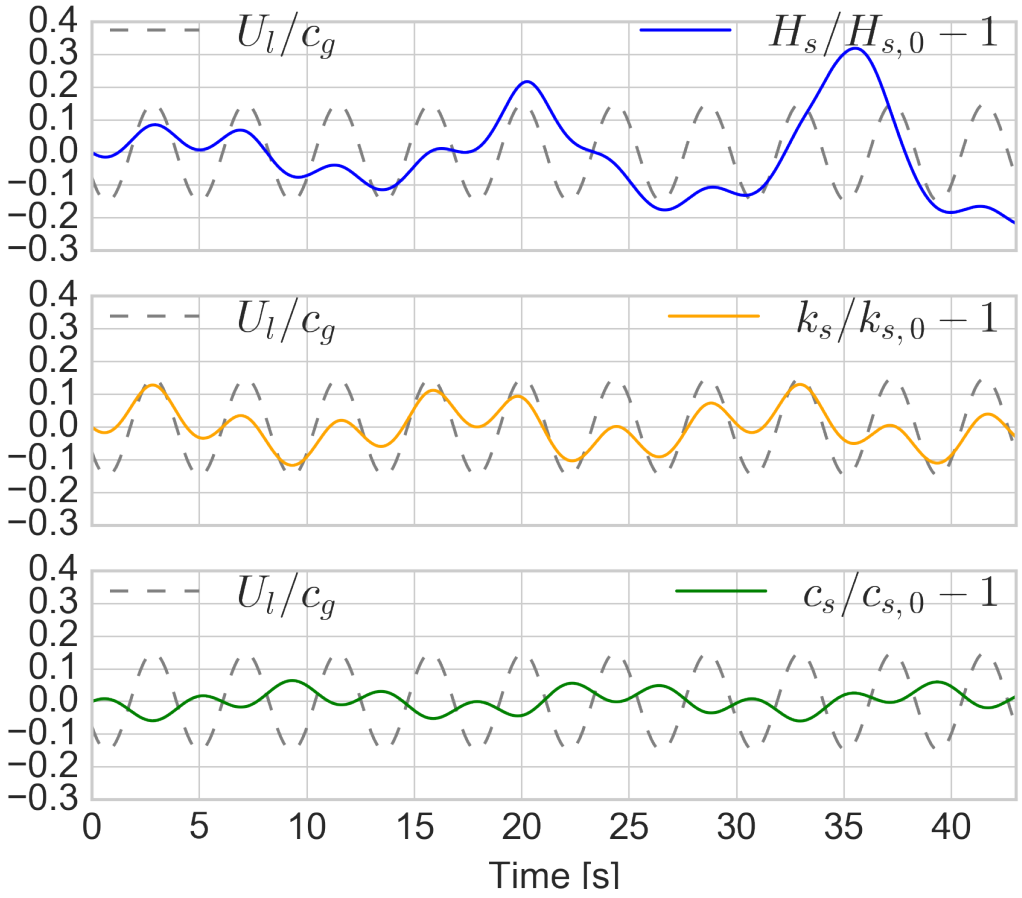

Figure 5.1: Example of time evolution of a SWs modulated by an oscillatory LW orbital velocity (U_l,Eq.5.9, with $T_1 = 4.3$ s and $A_1 = 0.33\text{m}^2/\text{Hz}$). The values of the wave action N, wavenumber k_s and phase velocity c_s are normalized by the SW its initial condition ($T_s = 2.5$ s and $A_{s,0} = 0.004$ m^2/Hz). The dash lines represent the oscillatory current field and the solid lines the modulated variables.

and

$$M_B = \left(\max(k^2E) - \overline{k^2E}\right)/\overline{k^2E}, \tag{5.12}$$

where the max and the average are taken over the x dimension. Integrations over $O(10)$ periods from a uniform short wave field rapidly develops variations with $M_E \simeq 4$, in the limit of small LW steepness and large differences between σ_l and σ. The full analysis of the complex behavior of these solutions is beyond the scope of the present work.

From our simulations we can say that M_E appears to be a growing function of k_1A_1, and also grows for σ decreasing towards σ_1. For $k_1A_1 < 0.001$ and $\sigma > 4\sigma_1$ the modulation oscillates at a period slightly larger than T_1 with a mean value around 2.5 for M_E and 5 for M_B during the first 10 oscillations, and there is a general increasing trend, when $c_1/c_{s,0}$ becomes smaller. For example, for the same long wave steepness

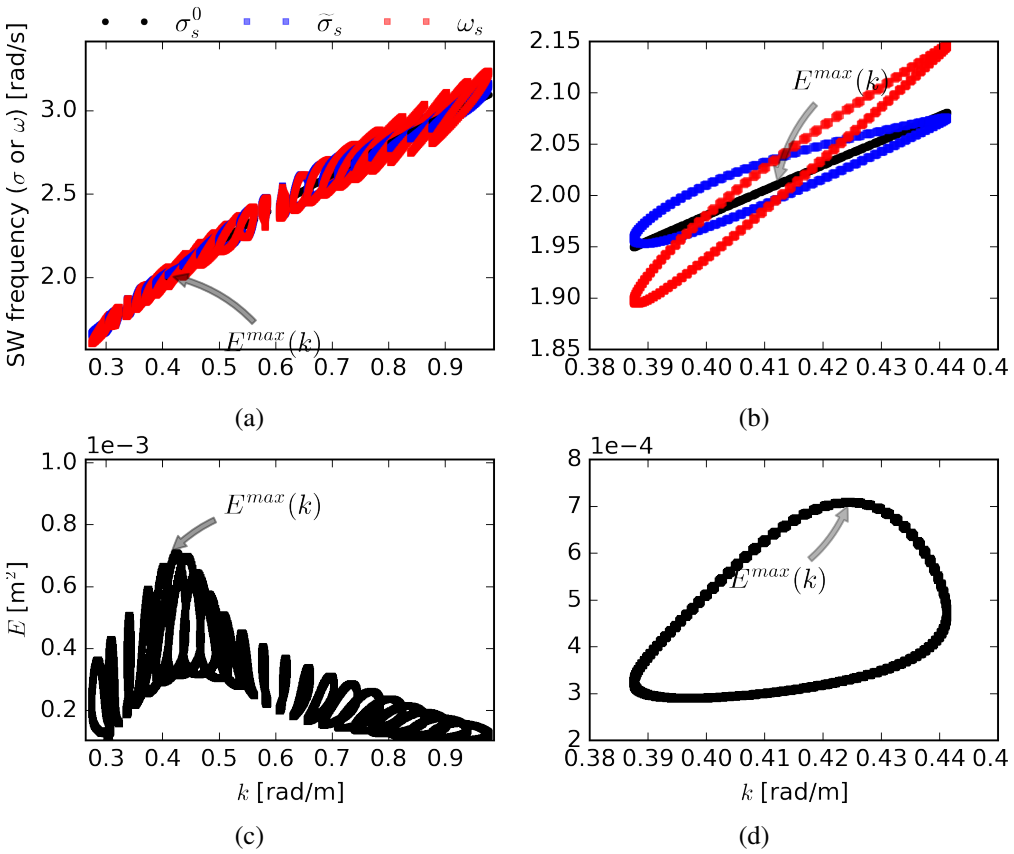

Figure 5.2: Wave energy modulated by an oscillatory LW orbital velocity obtained from the simplified model numerical solution considering several initial conditions from stereo video experiment (select case I, Sec.5.3). a) Modulated $\widetilde{\sigma}_s$ (blue), ω_s (red) and in black is the linear dispersion relation from several discrete initial conditions around the SW energy. b) Zoom in the modulated $\widetilde{\sigma}_s$ or ω_s at the peak of SW energy. c) Wave energy modulations by an oscillating current considering different initial waves action (N_0) and frequencies conditions (σ_s^0). d) Modulated wave energy at the peak of the waves action.

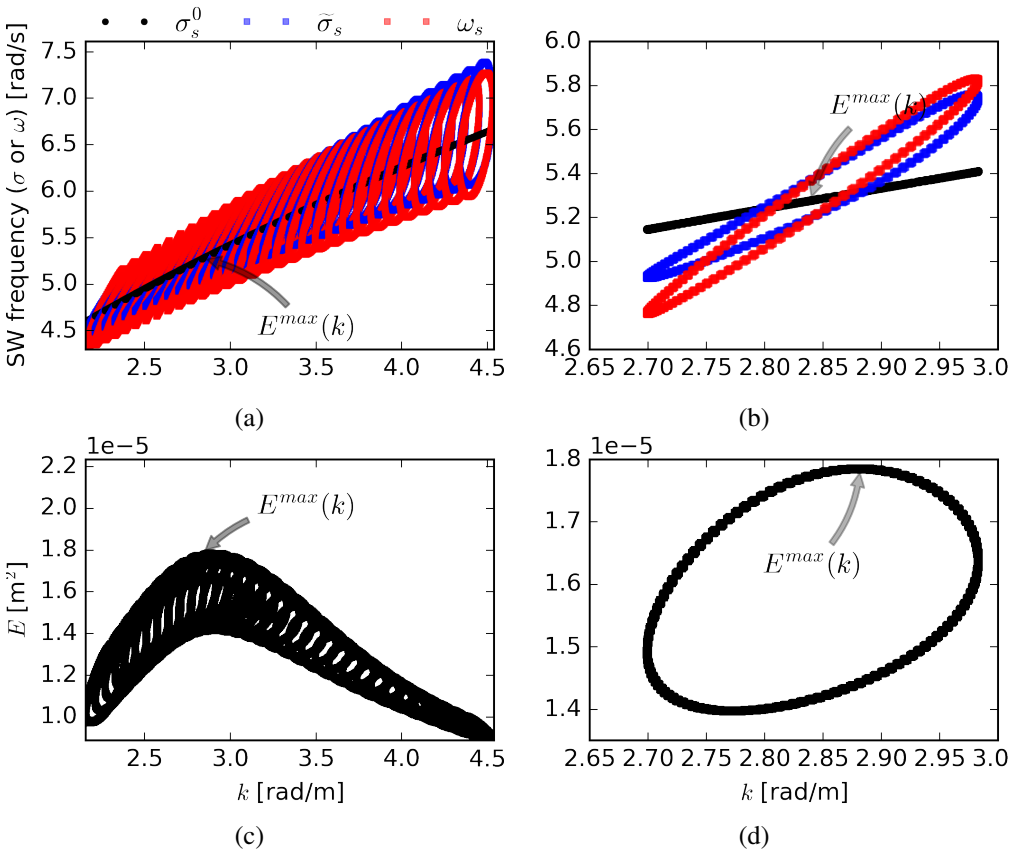

Figure 5.3: Wave energy modulated by an oscillatory LW orbital velocity obtained from the simplified model numerical solution considering several initial conditions from stereo video experiment (select case II, Sec.5.3). a) Modulated $\widetilde{\sigma}_s$ (blue), ω_s (red) and in black is the linear dispersion relation from several discrete initial conditions around the SW energy. b) Modulated σ_s or ω_s at the peak of SW energy. c) Wave energy modulations by an oscillating current considering different initial waves action (N_0) and frequencies conditions ($\sigma_{s,0}$). d) Modulated wave energy at the peak of the waves action.

$k_1A_1 < 2\times10^{-4}$, the mean values of M_E and M_B rise from 3.6 and 6.0 for $2c_1/c_{s,0} = 7$ to 7.4 and 9.4 for $2c_1/c_{s,0} = 3.4$, but they are independent of k_1A_1. For larger values of k_1A_1, this is not the case anymore, and the mean MTFs steeply increase with k_1A_1, rising to 14 and 16 for $2c_1/c_{s,0} = 3.4$ and $k_1A_1 = 0.04$, and 63 and 83 for $k_1A_1 = 0.064$, which corresponds to the significant waves in the case $H_{s,1} = 0.66$ m and $T_{p,1} = 4.3$ s, $T_s = 2.5$ s. In all cases, the MTF for k is much less variable, ranging from 1.3 to 2.5.

Clearly, such large values of M_B must lead to enhanced breaking of the short waves, and there is no wave action conservation in that case. The conservative nature of the model presented here (without growth nor dissipation of short waves) is its main limitation.

5.2.2 Modulation with growth and dissipation

A more complete model is thus necessary, adding at least dissipation. The theory has generally been formulated for short wave spectra, including generation by the wind and non-linear 4-wave interactions. The evolution of the short waves is thus given by the evolution of their action spectrum $N(\boldsymbol{k_s},\boldsymbol{x},t)$ (e.g. Phillips, 1977).

$$\frac{dN}{dt} = \frac{\partial N}{\partial t} + \dot{\boldsymbol{x}}\frac{\partial N}{\partial \boldsymbol{x}} + \dot{\boldsymbol{k_s}}\frac{\partial N}{\partial \boldsymbol{k_s}} = Q(\boldsymbol{k_s}) \tag{5.13}$$

where $Q(\boldsymbol{k_s})$ describes the sources and sinks of wave action. The surface elevation spectrum $E(\boldsymbol{k})$, and the wave action spectrum $N(\boldsymbol{k})$ are related by $N(\boldsymbol{k}) = E(\boldsymbol{k})/\sigma$, where σ is the intrinsic radian frequency, related to the wavenumber by the dispersion relation. The degree of the saturation spectrum is defined as $B(\boldsymbol{k}) = k^4E(\boldsymbol{k})$ (Phillips, 1985; Kudryavtsev and Makin, 2002).

In the absence of source terms (including wind energy input and dissipation), the local wave action $N(\boldsymbol{k},\boldsymbol{x},t)$ is conserved ($Q = 0$). The horizontal position of a short wave packet $\boldsymbol{x}$, and the short wavenumber, $\boldsymbol{k_s}$, vectors are independent of each other, but both are functions of the time variable (t). These vectors are in fact the position and momentum coordinates and satisfy the canonical equations also known as the Hamilton-Jacobi propagation equations, (e.g. Janssen, 2004, page 28)

$$\dot{\boldsymbol{x}} = \frac{\partial \boldsymbol{x}}{\partial t} = \frac{\partial \omega}{\partial \boldsymbol{k_s}} \tag{5.14}$$

$$\dot{\boldsymbol{k_s}} = -\frac{\partial \boldsymbol{k_s}}{\partial t} = -\frac{\partial \omega}{\partial \boldsymbol{x}}. \tag{5.15}$$

The absolute radian frequency of the waves (ω_s), as measured in a reference frame where the advection velocity is $\boldsymbol{U}$, is

$$\omega_s = \widetilde{\sigma}_s + \boldsymbol{k_s} \cdot \boldsymbol{U}. \tag{5.16}$$

Here $\boldsymbol{U} = \boldsymbol{U_l} + \boldsymbol{U_c}$ is the "advection velocity" for the short waves, that includes both long-wave orbital velocity $\boldsymbol{U_l}(\phi_l, t)$ and surface current $\boldsymbol{U_c}(\boldsymbol{x}, t)$. $\widetilde{\sigma}$ is the SW relative frequency.

According to Smith (1986) the LW orbital motion modifies the local acceleration. This creates an apparent gravity effect for SW propagation, given by,

$$\widetilde{\sigma}_s = \sqrt{\widetilde{\boldsymbol{g}} \cdot \boldsymbol{k_s} + \boldsymbol{T} \cdot \boldsymbol{k_s^3}} \tag{5.17}$$

where the traditional intrinsic frequency, σ_s, differs from $\widetilde{\sigma}_s$ as the effective gravity is also modulated by the long wave orbital velocity. The effective gravity is

$$\widetilde{\boldsymbol{g}} = |\boldsymbol{g} + \boldsymbol{D_t U}|, \tag{5.18}$$

where D_t is the Lagrangian derivative ($\partial/\partial t + \boldsymbol{U} \cdot \nabla$). Here $\boldsymbol{T}$ is the kinematic surface tension, normally scaled by the water density that can also be modulated because of distortion and compression of surface contaminants (Lange and Huhnerfuss, 1984; Henyey et al., 1987).

In this chapter we will not consider the modulation effect on the surface tension and our "short" waves will be intermediate waves with wavelengths around one meter. Neglecting the modulation effects on surface tension, Longuet-Higgins (1985, 1987b) arrived at the effective gravity

$$\widetilde{\boldsymbol{g}} = \boldsymbol{g} - \boldsymbol{a}, \tag{5.19}$$

where $\boldsymbol{g}$ is a constant gravity acceleration, and $\boldsymbol{a}$ is the Lagrangian acceleration due to the orbital motion of the long waves, with a vertical component a_z. The magnitude of $\widetilde{\boldsymbol{g}}$ is given by (e.g. Elfouhaily and Thompson, 2001)

$$\widetilde{g} = g\sqrt{1 - 2\frac{a_z}{g} + \frac{a^2}{g^2}} \approx g - a_z + \frac{a^2 - a_z^2}{2g} + \cdots \tag{5.20}$$

Assuming that a is defined as $D_l\boldsymbol{U}$ the total derivative of the long wave orbital velocity, $\boldsymbol{a} = dU_l/dt + dU_c/dt$. In conditions where the temporal and spatial current gradients are much larger than the LW length and period, the impact of a mean current

in the effective gravity can be negligible ($dU_c/dt \approx 0$). Thus,

$$a_z \approx \frac{\partial w}{\partial t} + \boldsymbol{U_l} \cdot \frac{\partial w}{\partial \boldsymbol{x}} \tag{5.21}$$

w is the vertical orbital velocity and the effective dispersion relation of short waves is

$$\begin{aligned} \widetilde{\sigma}_s(\boldsymbol{k_s}, \boldsymbol{x}, t) &= \sqrt{(gk_s - k_s a_z + \cdots) + T\boldsymbol{k_s}^3} \\ \widetilde{\sigma}_s^2(\boldsymbol{k_s}, \boldsymbol{x}, t) &= (gk_s + T\boldsymbol{k_s}^3) - k_s a_z + \cdots \end{aligned}$$

and the fist order approximation is

$$\widetilde{\sigma}_s^2(\boldsymbol{k_s}, \boldsymbol{x}, t) \approx \sigma_s^2 - k_s a_z \tag{5.22}$$

In the absence of currents, the apparent short wave frequency at Equation 5.16 is simplified

$$\omega_s = \widetilde{\sigma}_s + \boldsymbol{k_s} \cdot \boldsymbol{U_l} \tag{5.23}$$

and the first order ray Equations 5.14 and 5.15 become

$$\dot{\boldsymbol{x}} = \frac{\partial \omega_s}{\partial \boldsymbol{k_s}} = \frac{\partial \widetilde{\sigma}_s}{\partial \boldsymbol{k_s}} + \boldsymbol{U_l} \tag{5.24}$$

$$\dot{\boldsymbol{k_s}} = -\frac{\partial \omega_s}{\partial \boldsymbol{x}} = -\frac{\partial \widetilde{\sigma}_s}{\partial \boldsymbol{x}} - \frac{\partial}{\partial \boldsymbol{x}}(\boldsymbol{k_s} \cdot \boldsymbol{U_l}) \tag{5.25}$$

5.2.3 First order LW modulation amplitude

The first order modal representation of the wave orbital velocity can be derived from Hasselmann (1961), where the surface elevation and velocity potential can be write as:

$$\zeta(\boldsymbol{x}, t) = \sum_k A_k(t) \mathrm{e}^{\mathrm{i}\boldsymbol{k}\cdot\boldsymbol{x}} \tag{5.26}$$

$$\phi(\boldsymbol{x}, t) = \sum_k \phi_k(t) \mathrm{e}^{\mathrm{i}\boldsymbol{k}\cdot\boldsymbol{x}} \tag{5.27}$$

as A_k and ϕ_k represent the modal amplitude and the velocity potential, respectively, and using Hasselmann (1961) notation, it can be written as:

$$A_k(t) = A_k^- \mathrm{e}^{\mathrm{i}\omega_k t} + A_k^+ \mathrm{e}^{-\mathrm{i}\omega_k t} \tag{5.28}$$

$$\phi_k(t) = \phi_k^- \mathrm{e}^{\mathrm{i}\omega_k t} + \phi_k^+ \mathrm{e}^{-\mathrm{i}\omega_k t} \tag{5.29}$$

and they are related by:

$$A_k^{\pm} = \pm \mathrm{i} \frac{\omega_k}{g} \phi_k^{\pm} \tag{5.30}$$

with a modal amplitude $\phi_k^{\pm}$. The sign index refers to the direction of the propagation of the waves relative to the wave-number direction. In other terms, the velocity potential can also be written as $\phi_k = gA_k/i\omega_k$, where the non modulated dispersion relation is $\omega_k^2 = gk\tanh(kh)$. So the linear horizontal orbital velocity from Airy theory is defined as $U(k) = \omega A$

$$\begin{aligned} \boldsymbol{U}_k(\boldsymbol{x},t) &= \sum_k \mathrm{i} \frac{\omega_k^2}{g} \phi_k \mathrm{e}^{\mathrm{i}(\boldsymbol{k}\cdot\boldsymbol{x} - \omega_{k_1} t)} \\ &= \sum_k \mathrm{i} \frac{\omega_k^2}{g} \frac{gA_k}{\mathrm{i}\omega_k} \mathbf{e}^{\mathrm{i}(\boldsymbol{k}\cdot\boldsymbol{x} - \omega_{k_1} t)} \\ &= \sum_k \boldsymbol{U}_k \mathrm{e}^{\mathrm{i}(\boldsymbol{k}\cdot\boldsymbol{x} - \omega_k t)} \end{aligned} \tag{5.31}$$

for LW wavenumber the modal horizontal orbital velocity is given by $U_l = U_{\boldsymbol{k_1}} = \omega_{k_1} A_{k_1}$.

A similar approach can be used to derivate the local acceleration. According to Longuet-Higgins (1987b), the local acceleration is the first time derivative of the orbital velocity, as shown in Equations 5.20 and 5.22, given the first order simplification of the dispersion relation:

$$\widetilde{\sigma}_s = \sigma_s \sqrt{1 - \frac{k_s}{\sigma_s} a_z + \cdots} \tag{5.32}$$

as it is shown in Equation 5.21 the apparent gravity effect in the local acceleration can be write as the total derivative of the vertical LW orbital velocity. For a linear wave in deep water, the modal value of the vertical and horizontal orbital velocity are the same ($U_{z,k_1} = U_{k_l}$), with a $\pi/2$ phase shift.

$$\boldsymbol{U}_{z,k_l}(\boldsymbol{x},t) = \sum_{k_l} \boldsymbol{U}_{k_l} \mathrm{e}^{\mathrm{i}(\boldsymbol{k_1}\cdot\boldsymbol{x} - \omega_{k_l} t + \pi/2)} \tag{5.33}$$

$$\boldsymbol{a}_{z,k_l}(\boldsymbol{x},t) = \frac{d}{dt}\boldsymbol{U}_{z,k_l}(\boldsymbol{x},t)$$
$$\boldsymbol{a}_{z,k_l}(\boldsymbol{x},t) = \frac{\partial}{\partial t}\boldsymbol{U}_{z,k_l}(\boldsymbol{x},t) + \boldsymbol{U}_{k_l}\frac{\partial}{\partial \boldsymbol{x}}\boldsymbol{U}_{z,k_l}(\boldsymbol{x},t)$$
$$\boldsymbol{a}_{z,k_l}(\boldsymbol{x},t) = \sum_{k_l} U_{k_l}(\boldsymbol{U}_{k_l}\cdot\boldsymbol{k_l} - \omega_{k_l})\mathrm{e}^{\mathrm{i}(\boldsymbol{k_l}\cdot\boldsymbol{x}-\omega_{k_l}t)}$$

and this will simplify the first order modal modulation representation in Equation 5.23 to:

$$\omega_s = \sigma_s\sqrt{1-\frac{k_s}{\sigma_s}U_l(\boldsymbol{U}_l\cdot\boldsymbol{k_l}-\omega_l)} + \boldsymbol{k_s}\cdot\boldsymbol{U_l}. \tag{5.34}$$

We note that, for linear waves, the vertical and horizontal orbital velocities have the same modal amplitudes U_l but they are shifted by 90 degrees. Where orbital velocity and acceleration are also shifted by 90 degrees, a_z is maximum where the LW horizontal orbital velocity is maximized and vice versa. Also, the effect of LW orbital velocities varies with the relative direction of SW and LW whereas the acceleration modulation does not depend on the LW direction.

It is thus interesting to separate the effects of LW orbital velocity and relative acceleration. For that, we call ω_s^{ov} the modal LW orbital velocity modulation in ω_s, and ω_s^{ac} the acceleration-induced modulation. This is further discussed in Section 5.5. In the absence of current, our decomposition of $\omega_s = \omega_s^{ov} + \omega_s^{ac}$,

$$\omega_s^{ov} = \sigma_s + \boldsymbol{k_s}\cdot\boldsymbol{U_l} \tag{5.35}$$
$$\omega_s^{ac} = \sigma_s\sqrt{1-\frac{k_s}{\sigma_s}U_l(\boldsymbol{U}_l\cdot\boldsymbol{k_l}-\omega_l)} \tag{5.36}$$

5.2.4 LW modulation on SW growth

The generation of waves by the wind is not well known quantitatively and a number of heuristic models and parameterizations have been adjusted to measured wave growth or measured air-sea fluxes. The wind-wave growth term is generally expressed in the following form

$$Q(\boldsymbol{k}) = \beta(\boldsymbol{k})N(\boldsymbol{k}) \tag{5.37}$$

with a wide range of expressions given for the growth parameter β (e.g., Miles, 1959; Snyder et al., 1981; Mitsuyasu and Honda, 1982; Plant, 1982). For example Plant

(1982) gives

$$\beta(k,\varphi) = C_D \left(\frac{u_\star}{c}\right)^2 \cos\varphi|\cos\varphi| \tag{5.38}$$

where $u_\star$ is the friction velocity, C_D is the growth rate coefficient, and φ is the angle between the wind direction and the wave component.

In summary, the equations presented in this section are the basic system to prescribe the LW hydrodynamic perturbations in SWs wave dispersion relation. As consequence it is expected that this will impact the SW grow and dissipation process. We note that the modulation of the wind growth should also produce a growth of the long waves (Hasselmann, 1971). This effect will not be considered here.

5.2.5 Modulation Transfer Function (MTF)

The Ω parameter of Longuet-Higgins (1991)

Longuet-Higgins (1991) developed one of the first a theoretical investigation of simplified two-scale monochromatic wave model of a wind-ruffled surface including the modulation of LW orbital velocity on SWs, the dissipation of SW energy by breaking and its regeneration by wind. He defined the parameter

$$\Omega = \beta_s/(\gamma\sigma_l k_l A_{k_l}) \tag{5.39}$$

that gives the strength of the modulation. In this evaluation of Ω, he considered the form of β_s given by Plant (1982), and $\gamma = 2.08$ is a constant value.

When $\Omega < 1$ the SW breaks only over on specific region over the LW and when $\Omega \geqslant 1$ SW can break everywhere, as illustrated in Figure 5.4.

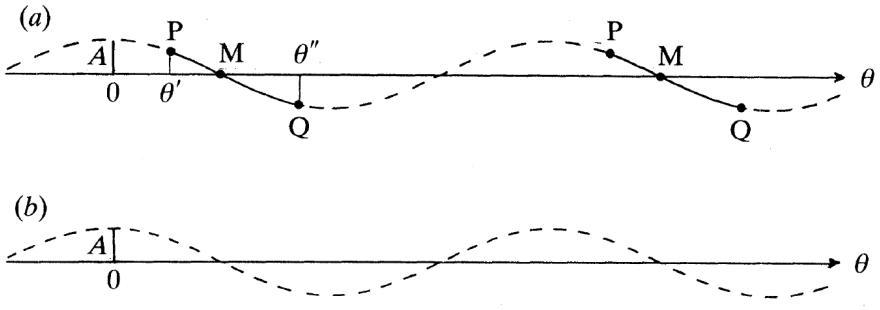

Figure 5.4: Time-history of SW on a uniform train of LW propagating in the same direction. The broken line indicates the interval where the SW are breaking a) $\Omega < 1$ b) $\Omega \geqslant 1$. Reproduced from Longuet-Higgins (1991)

According to Longuet-Higgins (1991), when the SWs are much shorter than the

LW, they can be considered as "surface roughness" with a local mean square slope (s^2). In the absence of current, Longuet-Higgins (1991) defined the short wave steepening relative to the orbital motion of the long waves as:

$$s \sim e^{\beta t + \gamma k_1 \eta} \tag{5.40}$$

where t and η can be used to define the SW relative position on LW. The SW steepness s grows over LW, and it is limited by a critical steepness $s_0 = a_0 k_0$. Longuet-Higgins (1987a) chose $s_0 = 0.22$ on the ground that the significant wave, with amplitude $2a_0$ could not exceed the breaking limit. This value is probably overestimated given the properties of random breaking waves revealed by Banner et al. (2000). Namely, breaking can occur even when the average steepness is far from the limiting steepness of monochromatic waves. This may lead to an underestimation of Ω where it can be much less than 1 and still approach the saturation with breaking events occurring everywhere.

For a group of SWs modulated by LW orbital velocity, as the LW moves forward, there may come a point P (Fig.5.4), on the windward face of LW, where where the straining of SWs overcome the wind input. The position where it occurs over the LW is defined by $\theta = \theta'$ and this should occur at certain θ'' position at the LW (see, Fig.5.4.a). At θ'', $s = s_0$ and between P and Q the waves are not breaking, so $s = s_0 \exp[\beta(t - t') + \gamma k_1(\eta - \eta')]$. This means that for $0 < \theta' < \pi/2$ and $0 < \theta'' < 2\pi$, the SW breaking tends to occurs mostly on the top of LW when $\theta'' - \theta'$ is maximized. As example, when $(\theta'' - \theta') \to 2\pi$ there are only on possible position for SW breakers and this should be in the crest of long wave (Longuet-Higgins, 1991, see, Fig.5.4).

θ' and θ'' are related to Ω (e.g. Longuet-Higgins, 1991, Eq. 2.7, 3.1 and 3.2) by assuming that the SW breaks where $s/s_0 \to 1$, and at this point $\partial s/\partial t = 0$, so Ω at a single wave train can be written as:

$$\frac{\partial s}{\partial t} = \left\{ \begin{array}{ll} (\beta + \gamma k_1 \partial \eta / \partial t) s, & s < s_0 \\ 0, & s = s_0 \end{array} \right\} \tag{5.41}$$

$$\beta - \gamma k_1 A_{k_1} \sigma_1 \sin\theta' = 0 \tag{5.42}$$

$$\Omega = \sin\theta' \text{ , and} \tag{5.43}$$

$$= -\frac{\cos\theta'' - \cos\theta'}{\theta'' - \theta'} \tag{5.44}$$

The simple model of Longuet-Higgins (1991) can be extended to conditions in which the long wave amplitudes are not constant and, appropriate for a narrow-band spectrum, follow a Rayleigh distribution. We thus redefine Ω for the root mean square amplitude of LW orbital velocity (U_l^{rms}) and also adapting for the conditions where the short and long wave are not necessarily propagating in the same direction, by adding a $(\theta_l - \theta_s)$ dependency in the SW and LW relative propagating direction. We will thus use

$$\Omega = \frac{1}{\gamma} \frac{\beta(\boldsymbol{k_s}, \varphi)}{\sigma_l k_l A_l^{rms} |\cos(\theta_l - \theta_s)|} \tag{5.45}$$

where

$$\sigma_1 A_{k_1}^{rms} = U_l^{rms} = \sqrt{2} \sqrt{\int E(f_l)(2\pi f_l)^2 df}, \tag{5.46}$$

in which $E(f_l)$ is restricted to the LW components of the wave spectrum.

We follow Longuet-Higgins (1991), in using the growth parameter from Plant (1982), that we further simplify as a function of the wind speed

$$\beta_{\text{Plant}} \simeq 3.2 \times 10^{-5} (U_{10}/c_s)^2 \sigma_s \tag{5.47}$$

as given by Eq.5.6 of Longuet-Higgins (1987a). Figure 5.5 shows how β evolves at different SW frequency f_s and wind speeds. An important remark here is that at low wind speed or lower frequencies $\beta \to 0$.

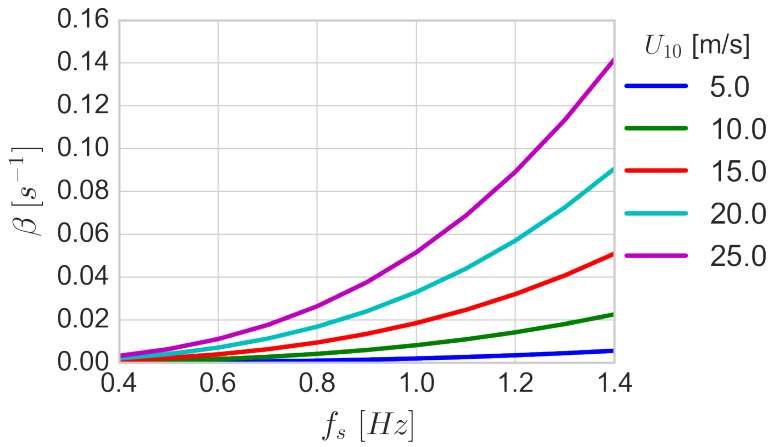

Figure 5.5: Longuet-Higgins (1987a, Eq.5.6) β function for different SW frequencies and wind speeds.

Statistically speaking, for linear waves the mean-square slope is

$$\overline{s^2} = \int (2\pi f)^4 / g^2 E(f) df. \tag{5.48}$$

When $\overline{s^2}/s_0^2 \to 1$, Ω should approach 1 and both θ' and θ'' tend to $\pi/2$. Under slow wind conditions, when $\Omega << 1$, then for a small θ', θ'' approaches 2π. This variable should be monotonically related with $k_l A_{k_l}$ and β/σ_l by Equations 5.41 and 5.42. In particular, when the LW steepness is held constant, but the wind generation factor is increased, so $\overline{s^2}/s_0$ grows because β increases.

First order MTF

An idea to determine quantitatively how much dominant waves can modulate SWs is originally introduced by Keller and Wright (1975) through the modulation transfer function (MTF). Namely, LW cause a small perturbation of all characteristics of the sea surface, airflow and short wave properties, which is a linear function of the LW amplitude. Taking Y to be any parameter like the wave action spectrum or the friction velocity, then variation $\widetilde{Y}$ induced by LW is

$$\widetilde{Y}(\boldsymbol{x},t) = \frac{1}{2}(\widehat{Y} e^{i(\boldsymbol{k_l}\cdot\boldsymbol{x}-\omega_l t)} + c.c) \tag{5.49}$$

where $\widehat{Y}$ is a complex amplitude. A negative imaginary part of $\widehat{Y}$ means that the maximum of the Y-variation is shifted to the forward slope of the LW. The MTF of Y, M_Y, is thus defined by

$$M_Y = \frac{\widehat{Y}}{A_{k_l} k_l \overline{Y}} \tag{5.50}$$

where $\overline{Y}$ is the mean value of Y.

The modulation of a SW by the LW can be described as a solution of the perturbed energy balance equation (Eq.5.13) (Caponi et al., 1988). Since the effect of the large-scale motion is small by assumption, we may apply a perturbation expansion of the Liouville operator as proposed in Alpers and Hasselmann (1978), where $\mathscr{L}[N] = dN/dt$.

$$\mathscr{L} = \overline{\mathscr{L}} + \delta\mathscr{L} \tag{5.51}$$

$$N = \overline{N} + \delta N \tag{5.52}$$

$$Q = \overline{Q} + \delta Q \tag{5.53}$$

The Taylor expansion of the source function Q is achieved through

$$\overline{Q} = Q(\overline{N}) = 0 \quad \text{and} \quad \delta Q = \frac{\partial Q}{\partial N}\Big|_{N=\overline{N}} \tag{5.54}$$

where $\partial Q/\partial N$ denotes the functional derivative of the source function Q.

According to Alpers and Hasselmann (1978), in the absence of large waves, the action spectrum satisfies the zeroth order radiation balance equation and the zero and first order can be written as:

$$\overline{\mathscr{L}}[\overline{N}] = \overline{Q} = 0 \tag{5.55}$$

$$\overline{\mathscr{L}}[\delta N] = \overline{\mathscr{L}}[\delta N] + \delta\mathscr{L}[\overline{N}] = \frac{\partial Q}{\partial N}\Big|_{N=\overline{N}}[\partial N]. \tag{5.56}$$

Following Keller and Wright (1975) and Alpers and Hasselmann (1978), we assume that Q can be linearized as

$$\frac{\partial Q}{\partial N}\Big|_{N=\overline{N}}[\delta N] = -\mu(\boldsymbol{k},\boldsymbol{x})\delta N \tag{5.57}$$

$1/\mu$ is a characteristic relaxation time of the system which is empirically determined from experimental data considering the input from the wind, the damping processes and the conservative transfer processes within the wave field (Alpers and Hasselmann, 1978).

So, from Equation 5.57, the Fourier representation of δN can be represented by the kernel that multiplies the linear harmonics of the surface elevation of an ambient current to produce a relative modulation of the wave action, where the first order perturbed wave action is then expressed as a function of the equilibrium action ($\overline{N}$) and a sum over the hydrodynamic MTF $M(\boldsymbol{k})$ as:

$$\delta N = \widetilde{N} = \overline{N} \sum_{k_l, s=\pm} M(k_l, s) k_l A_{k_l} e^{i(\boldsymbol{k_1}\cdot\boldsymbol{x} - s\omega_{k_l} t)} \tag{5.58}$$

it is implied that $M(\boldsymbol{k}, s)$ is independent of the Fourier transform of the long-wave field amplitude (A_{k_l}), such that M, is a linear transfer function between the relative change in spectral energy of the SWs and the LW amplitude. We note that this MTF differs from the one in the previous section because here the wavenumber is fixed, it is Eulerian in spectral space, while in the conservative model we followed wave packets in spectral space.

When the wavenumber k_s of the modulating SW is much larger than k_l, the SW group velocity is much smaller than the LW phase velocity, and the linearized wave action conservation Equation 5.13 for a small disturbance $\widetilde{N}$ (i.e., $\widetilde{N}/\overline{N} \ll 1$) is reduced

to (e.g., Alpers and Hasselmann, 1978).

$$\frac{\partial \widetilde{\overline{N}}}{\partial t} - \boldsymbol{k_s}\frac{\partial \boldsymbol{u}}{\partial \boldsymbol{x}}\frac{\partial \overline{N}}{\partial \boldsymbol{k_s}} = \frac{\widetilde{Q}}{\omega_s} \tag{5.59}$$

where $\widetilde{Q}$ is the variation of the energy source and is a small perturbation of the energy source (Eq.5.37). Thus, the disturbance in Q can be caused by the surface wind stress variation via the growth rate parameter β which enters the energy wind input and in the energy losses described by the first and second terms in Equation 5.37, respectively.

A simple expression for the small disturbance of the energy source Q can be easily found by combining modal $\widetilde{N}$ amplitude Equations 5.59 and 5.58.

$$-i\omega\frac{M}{k_1}\overline{N} + \dot{\boldsymbol{k}}_{\boldsymbol{s}}\frac{\partial \overline{N}}{\partial \boldsymbol{k_s}} = \widetilde{Q}\omega\frac{M}{k_l}\overline{N} \tag{5.60}$$

From Equation 5.57 we can rewrite this expression as:

$$(\omega + i\mu)\frac{M}{k_l} = -i\frac{\dot{\boldsymbol{k}}_{\boldsymbol{s}}}{\overline{N}}\frac{\partial \overline{N}}{\partial \boldsymbol{k_s}} \tag{5.61}$$

With these derivatives of the source functional, the hydrodynamic MTF is described by Elfouhaily et al. (2001)[3] as:

$$M_N = -\frac{\omega_l - i\mu_s}{\omega_l^2 + \mu_s^2}\frac{\omega_l}{k_l^2}(\boldsymbol{k_l}\cdot\boldsymbol{k_s})\frac{\boldsymbol{k_l}}{\overline{N}}\frac{\partial \overline{N}}{\partial \boldsymbol{k_s}} \tag{5.62}$$

This expressions for the hydrodynamic MTF is simplified by Elfouhaily et al. (2001) by assuming a given form for the directional wave spectrum and the wind growth rate. By combining the unidirectional wave spectrum from Elfouhaily et al. (1997) with the growth rate proposed by Plant (1982), Elfouhaily et al. (2001) obtain the linear MTF

$$\begin{aligned} M_N \;=\; & -\frac{\omega_l - i\mu_s}{\omega_l^2 + \mu_s^2}\omega_l\cos(\theta_s - \theta_1) \\ & \times\left[-4\cos(\theta_s - \theta_l) - \left(\frac{2}{ln(2)}\tanh^{-1}\Delta_{k_s} + 1\right)\tan 0.5\varphi\sin(\theta_s - \theta_l)\right] \end{aligned} \tag{5.63}$$

where $\theta_s - \theta_l$ defines the relative direction between long and short waves. In Equation 5.63, Δ_{k_s} represents a spreading function defined by Elfouhaily et al. (1997) that describes the conditions where SW and the wind are not in the same direction. This

[3]Note, here M is different of $R^{s_l}_{k_l}$ from Elfouhaily et al. (2001, Eq.9.2) because it is divided by the modulating LW wavenumber ($M \equiv R^{s_l}_{k_l}/k_l$) to get a correct modulation amplitude, as discussed in Elfouhaily et al. (2001, Section 10).

MTF can be even more simplified in conditions of short waves aligned to the wind ($\tan 0.5\varphi = 0$) and this equation is reduced to (e.g. from Elfouhaily et al., 2001):

$$M_N = 4\frac{\omega_l - i\mu_{s_0}}{\omega_l^2 + \mu_{s_0}^2}\omega_l \cos^2(\theta_s - \theta_l) \tag{5.64}$$

where $\mu_{s_0} = p\beta(k_s)$ is the relaxation rate where the short waves are aligned to the wind and p is a ratio, function of the wind friction velocity, as expressed in Elfouhaily and Thompson (2001). The most likely value of this ratio is 2, as defined by Phillips (1985).

It is clear that the phase of the modulation is dictated entirely by the ratio of μ_s to ω_s. This means that in the linear MTF, neither the local acceleration nor the orbital velocity influence the phase of the modulation. Another important point is that the phase of the modulation of this linear MTF is independent of the relative propagation direction between modulated and modulating waves. Considering Plant (1982) as the growth rate, this approximation also neglects any LW effect on the modulations of the wind forcing that might be important according to Kudryavtsev and Makin (2002), Kudryavtsev and Chapron (2016).

In conditions of low wind speed $\mu \to 0$ (see Fig.5.5) and the MTF $\to 4$. Also, with this first order simplified solution (Eq.5.64) it is expected to have a very low variation in the MTF amplitude, in conditions where SW and LW are aligned (see Fig.5.6).

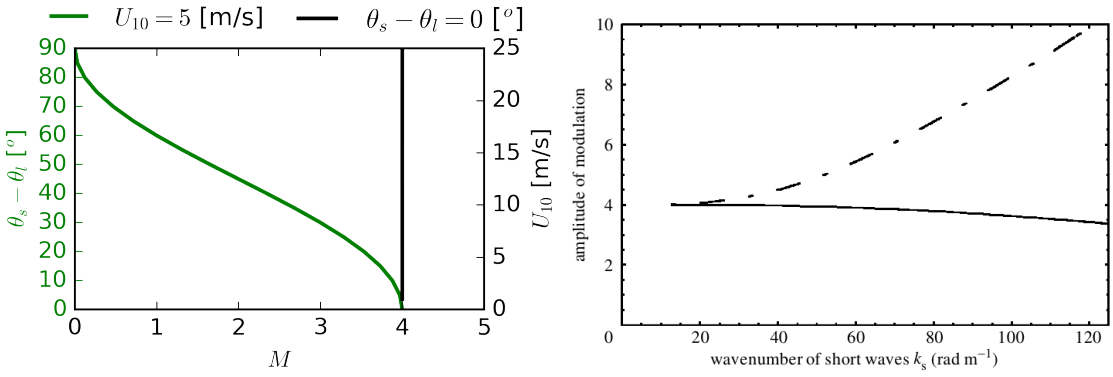

(a) (b)

Figure 5.6: Modulus of the MTF for the wave action spectral density, a) $|M_N|$ according to Elfouhaily et al. (2001), in the case of $T_s = 2.5$ s and $T_l = 10$ s. The green line shows the MTF modulus as a function of the relative SW–LW direction $\theta_s - \theta_l$ and a constant wind speed of 5 m/s. In black, MTF for $\theta_s - \theta_l = 0$ and different wind speeds (U_{10}). b) Elfouhaily et al. (2001, Figure 3) Comparison between the normalized amplitudes of the first-order (solid curve) and second-order (dash-dotted curve) MTFs for various short waves. The wavelength of the modulating wave is 31 m and $u_\star = 0.23$ m/s.

5.3 Stereo video experiments and selected conditions.

Following these theoretical developments we explore the modulation of short waves in the ocean. For this, we turn to video techniques for mapping the evolving sea surface (Benetazzo, 2006; Leckler, 2013) and analyzing the occurrence of breaking waves (Mironov and Dulov, 2008; Leckler, 2013). Video processing methods used here are described in Section 2.3.

The data we analyze was acquired between 16 September and 5 October 2013 at the research platform of the Marine Hydrophysical Institute (Fig.5.7.a and b). This experiment was part of the IOWAGA project, funded by the European Research Council, with the support of the Marine Hydrophysics Institute of Sebastopol. It followed the 2011 experiment reported by Leckler et al. (2015), using a similar instrumentation. Many other experiments on wind-waves and marine meteorology have been performed on this platform (e.g. Babanin and Soloviev, 1998a,b; Dulov et al., 2002; Kosnik and Dulov, 2011; Yurovskaya et al., 2013; Yurovsky et al., 2017).

The instrumented platform is located 500 meters off the coast next to Katsiveli in the Black Sea, near the southern tip of Crimea. The water depth in the cameras footprint is about 30 m. The wind speed and direction are measured at the center of the platform, 23 m above sea level. The stereo system used consists in a synchronized pair of video cameras of 5 Megapixel (2048×2456 pixels) BM-500GE, with wide angle lens and the acquisition rate was set at 12 and 15 Hz (depending on the acquisition. The system was mounted approximately 12.25 m above the ocean surface and the distance between the cameras was 1.86 m. The cameras were installed on the eastern corner of the deck of the platform, point to a direction 82^o clockwise of North.

The sea state conditions in Katsiveli are dominated by wind seas with a wide range of possible fetches, from 1000 km across the Black sea, to 500 m for northerly winds. During the 12 days of the experiment, wind speed and direction were highly variable. The mean wind speed ($\overline{U_{10}}$) between September 21 to October 02 was 7.35 m/s and the highest measured wind speed was 22.79 m/s. We particularly thank Mickael Accensi for staying two nights on the platform during the storm and operating the video system in good morning light conditions.

The typical wind directions during the experiment were from West and East. Strong wind conditions (over 10.8 m/s) usually comes from East, North and West. The mean significant wave height ($\overline{H_s}$) measured by the wave gauge was 0.67 m and the highest value of H_s observed was 1.96 m. In all of the selected observations presented here, wave breaking is dominated by SW, with directions following the the wind direction.

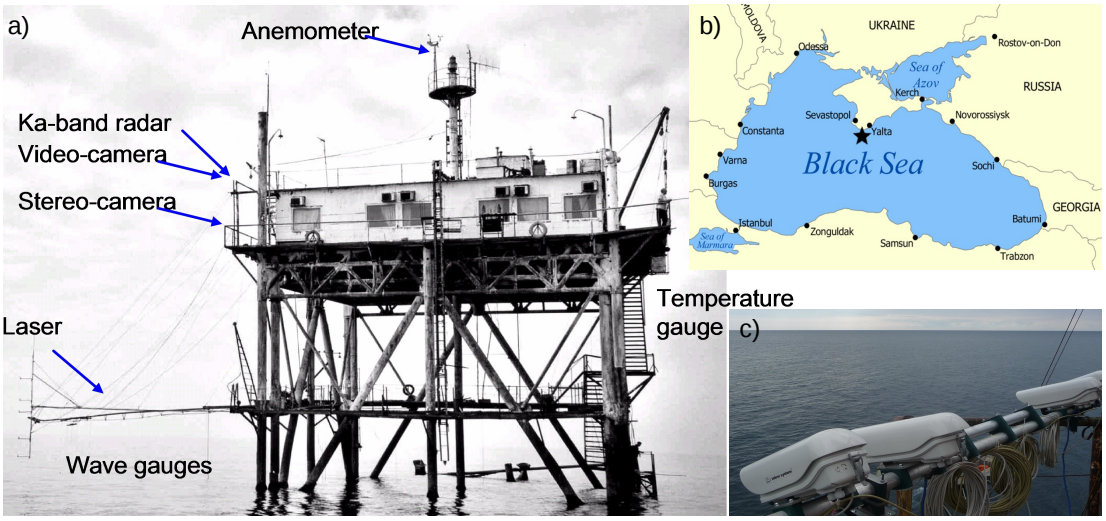

Figure 5.7: a) Research platform of the Marine Hydrophysical Institute; b) Position of the research platform; c) WASS and DIACAM stereo video system

Typically, each stereo video acquisition have the duration of approximately 30 min video record, at 12 frames per second and cover an area about $19 \times 19\ m^2$ of the sea surface, but it can vary some times. After processing all the stereo data, I have chosen to present here three representative records. There are characterized by : I) Wind sea and swell propagating in the same direction, II) wind sea and swell propagating in orthogonal direction and III) wind sea and swell propagating in opposite direction with strong winds.

Table 5.1 gives the main wind and sea state parameters for the selected cases. The sea state condition for each selected case are represented by a snapshot of a rectified image from the right stereo video camera. A quantitative information for the 30 minutes video acquisition is represented by the energy spectrum $E(f,\theta)$. The spectrum is shown in the image coordinate system, and the nautical orientation is labeled in the figure.

The wave spectrum is partitioned following Kerbiriou et al. (2007), with partition heights and periods listed below the figures, (H_{s1}, T_{p1}) for the first (longer wave) partition and (H_{s2}, T_{p2}) for the second (short wave) partition. The positions of the two spectral peaks are marked by black triangles in the spectra. Wind speed and direction were collected at 23 m height and corrected to 10 m using a constant roughness length ($z_0 = 0.0002$), this results are represented here by U_{10} and U_{dir}.

Figure 5.8 shows the surface elevation spectra for the three selected records (I,II,III), the partitions of the spectrum (following Kerbiriou et al., 2007) are used to compute H_{s1}, T_{p1}, D_{p1}, H_{s2}, T_{p2} and D_{p2}. The solid black line represents the three dimensional spectrum integrated along k_x and k_y, while the solid color lines represent

Table 5.1: Selected measurement records during the 2013 Katsiveli experiment. The date and time of the start of the video acquisition is given to the left. A snapshot of the sea surface is at the center, and the right plot shows the directional spectrum derived from the stereo. The main wave and wind components are presented below the figures, where each spectral partition is represented by the subscript $_1$ and $_2$.

I) 2013-09-30 10:20:01

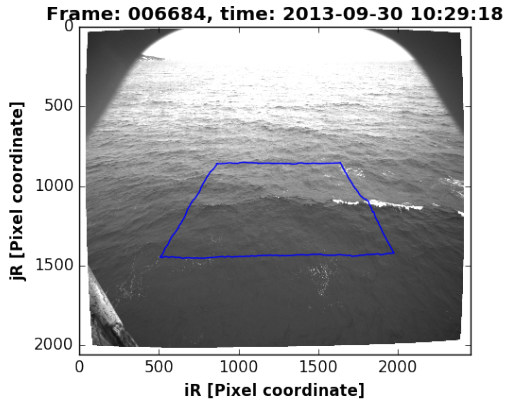

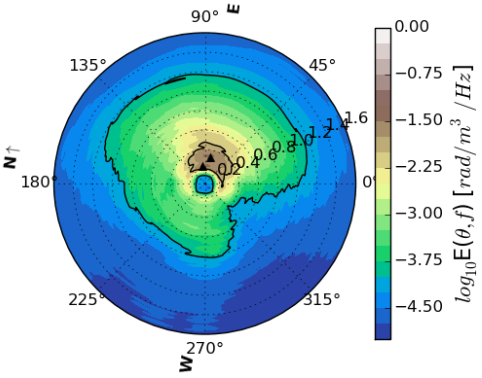

H_{s1} = 0.66 m T_{p1} = 4.3 s U_{10} = 8.7 m/s U_{dir}= E H_{s2} = 0.35 m T_{p2} = 3.0 s

II) 2013-09-22 13:00:01

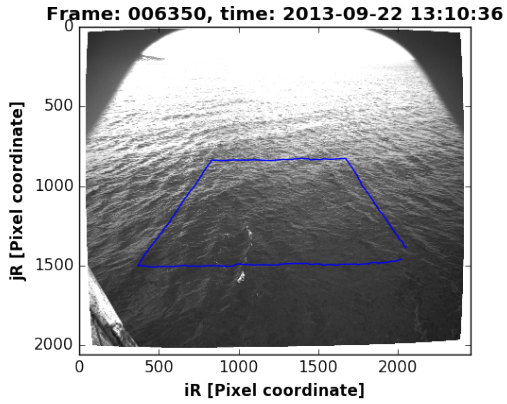

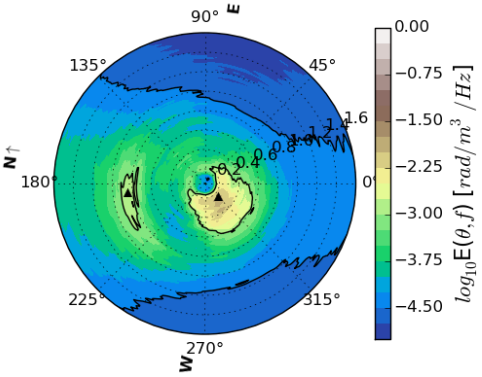

H_{s1} = 0.41 m T_{p1} = 4.1 s U_{10} = 6.1 m/s U_{dir}= N H_{s2} = 0.11 m T_{p2} = 1.2 s

III) 2013-09-25 12:15:01

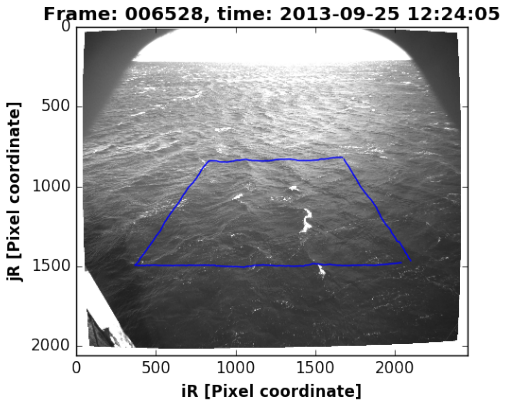

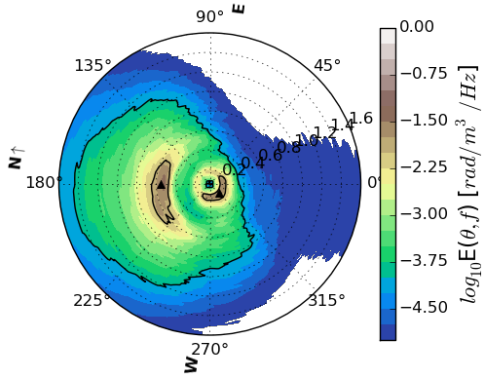

H_{s1} = 0.65 m T_{p1} = 5.7 s U_{10} = 15.2 m/s U_{dir}= N H_{s2} = 0.32 m T_{p2} = 1.8 s

the first and second partition of the directional spectrum.

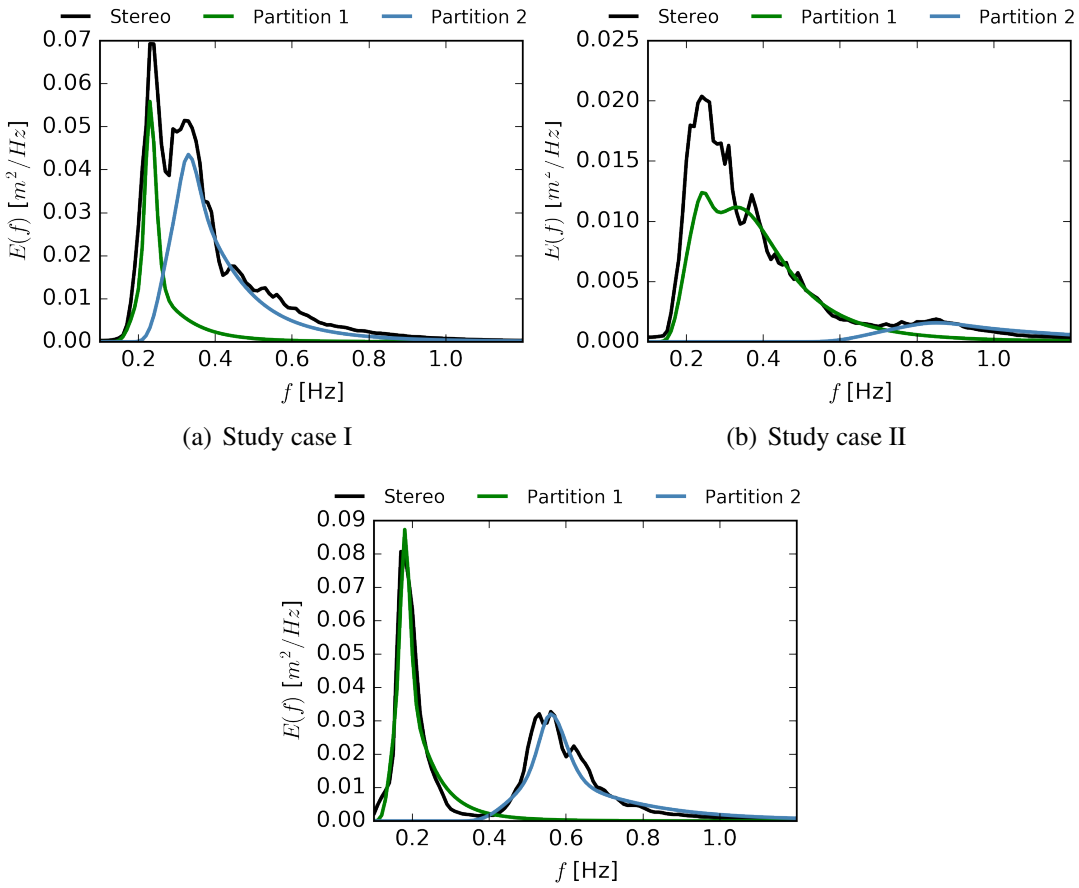

(a) Study case I

(b) Study case II

(c) Study case III

Figure 5.8: Frequency energy spectrum and spectrum partition for each selected case. The solid black line shows the integration of the 3 dimensional wavenumber and frequencies spectrum while the color lines shows the first and second partition of the waves spectrum (LW and SW). The partition method follows (Kerbiriou et al., 2007) for a JONSWAP spectrum.

During record I, the easterly wind has a speed between 8 and 10 m/s. The sea state has two partitions, one is the LW with a peak the spectrum at 4.25 s, the LW significant wave height is about 0.4 m from East, while the local SW system is dominated by 3 s waves from East and modal amplitude around 10 cm.

The second selected record (II) is characterized by average wind speeds of 6 to 10 m/s, with a very short fetch due to the North-Northwest direction. The sea state condition is well defined by LW and SW conditions propagating in approximated orthogonal direction, the LW conditions are dominated by former 4 s and 0.4 m swell from Southwest, while very short SW are driven by the local wind, with a peak period of 1.8 s and 10 cm amplitude. From the breaking detection method, all of the breaking waves in record II were clearly at SW frequency and direction.

The third selected record (III) occurs under strong northerly wind conditions (around 15 m/s), opposing a swell from the south-west, 135° from the wind direction. This LW system has a significant wave height of 0.65 m with a peak period of 5.6 s, while the SW has a 0.32 m wave height and 1.8 s peak period from North. Breaking waves are mostly associated with these SW.

5.4 LW modulation on SW wavenumber and frequency spectrum

If LW are modulating the SW dynamic in these selected records, the modulation effect might be observed in the SW spectrum. As described by Leckler et al. (2015), the three-dimensional spectrum $E(k_x, k_y, f)$ preserves a high level of directional distribution informations and are a key for understanding the energy balance in the wind-wave spectrum between wind-wave generation, non-linear interactions and dissipation. Usually it is expected that the wave energy is mostly located around the linear dispersion relation (Eq.5.16) where non-linear shifts in the dispersion relation have been interpreted as a Doppler shift by the Stokes drift or the underwater current velocity (as example, Ardhuin et al., 2009; Leckler et al., 2015). Here we will consider only the modal amplitude of the apparent gravity effect (Eq.5.36) and orbital velocity (Eq.5.35) impact on the dispersion relation and in the three-dimensional spectrum. Figure 5.9 present the 3 dimensional slices in the spectrum cube, the left panel shows a cut of $E(k_x = 0, ky, f)$ and $E(k_x, ky = 0, f)$ while the right panel cuts the $E(k_x, ky, f_c)$ in several frequencies as $f_c = [0.45, 0.60, 0.75, 0.90, 1.05, 1.20, 1.35, 1.50]$ Hz.

The results presented on Figures 5.9–5.11 suggest a significant change in the apparent frequency and wavenumber caused by the oscillatory LW orbital velocities. In opposite, the vertical acceleration has only slightly impact on the dispersion relation. The SW wavenumbers are shifted from the linear dispersion relation, like a Doppler shift induced by currents.

Here, on Figures 5.9–5.11 we are only considering a monochromatic LW direction acting over a generic SW direction. A proper simulation of the impact on the spectrum should also consider the change in spectral density. On Figure 5.10 in the (k_x, f)-plane, shows a significant shift around $f = 0.8Hz$, because of LW contribution along the y axis.

The relative impacts of ω_s^{ov} in the dispersion relation are significantly bigger than ω_s^{ac}. On the one hand, ω_s^{ac} the effect is weak and not dependent of the relative long and short wave direction. On the other hand, the strength of ω_s^{ov} depends on the SW and LW relative direction ($\boldsymbol{k_s} \cdot \boldsymbol{U_l}$).

The modified dispersion relation by ω_s^{ov} is still much smaller than the shifts caused by local current, or second order bound waves as described by Leckler et al. (2015) and Peureux et al. (2017). Under certain low and moderate sea state conditions, this nonlinear contributions to the spectrum appear to be an important source of deviations from the usual superposition of linear waves.

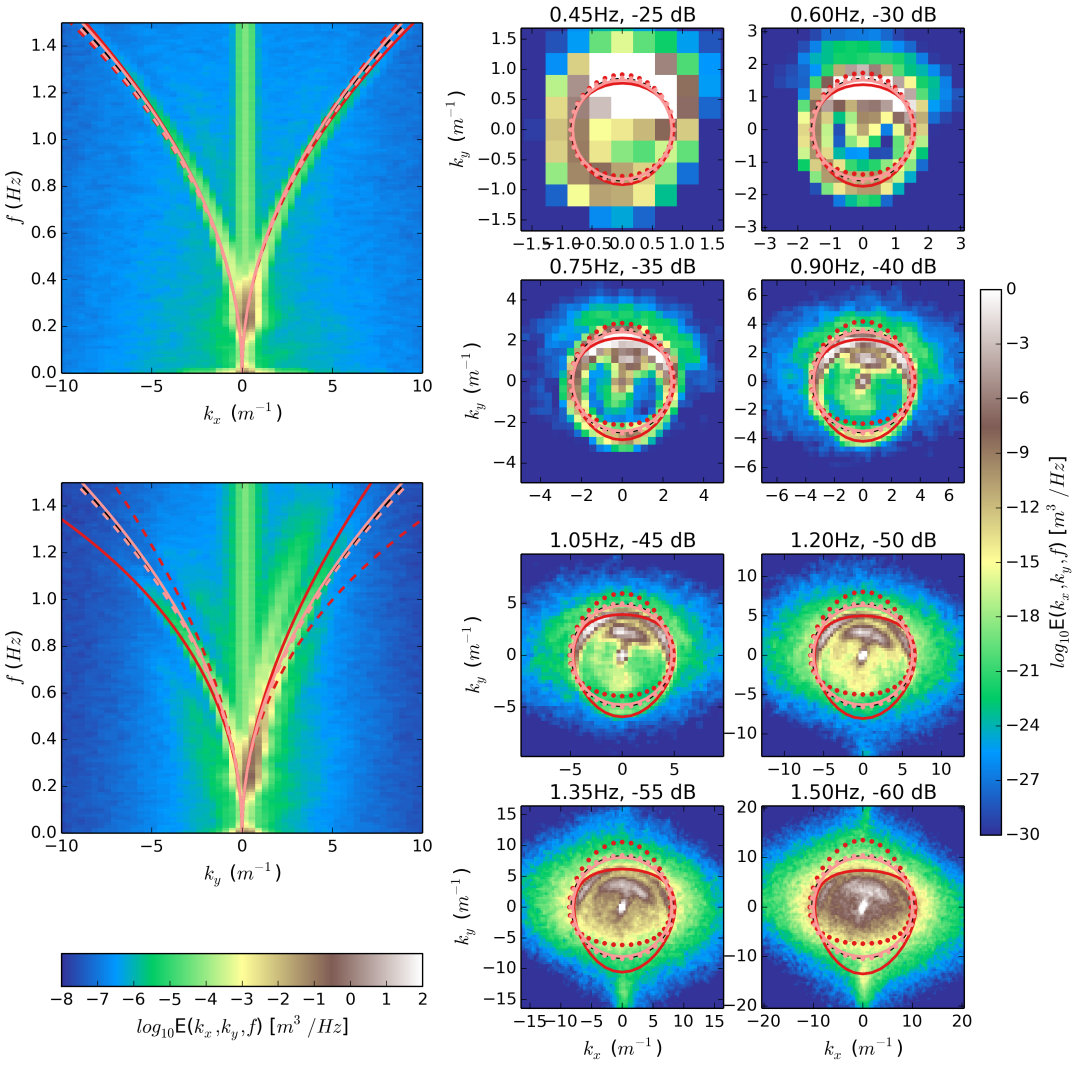

Figure 5.9: Three dimensional cuts in the spectrum cube for record I. The dashed black line represent the linear dispersion relation ($2\pi f\sqrt{gk\tanh(kh)}$) without current. The red lines indicate the expected modulation effect of the LW orbital velocity the U_l^{rms}, given by Eq.5.35. The pink lines represent the modulation due to the vertical acceleration a_z as given by Eq.5.36. The left panel shows slices in the $k_y = 0$ and $k_x = 0$ planes, while the right panel shows slices at constant frequencies 0.45, 0.60, 0.75, 0.90, 1.05, 1.20, 1.35 and 1.50 Hz. Our convention is that the energy appears in the direction from where it is coming. The solid and dash correspond to a '+' or '-' sign replacing $\pm$ in Eqs.5.35 and 5.36.

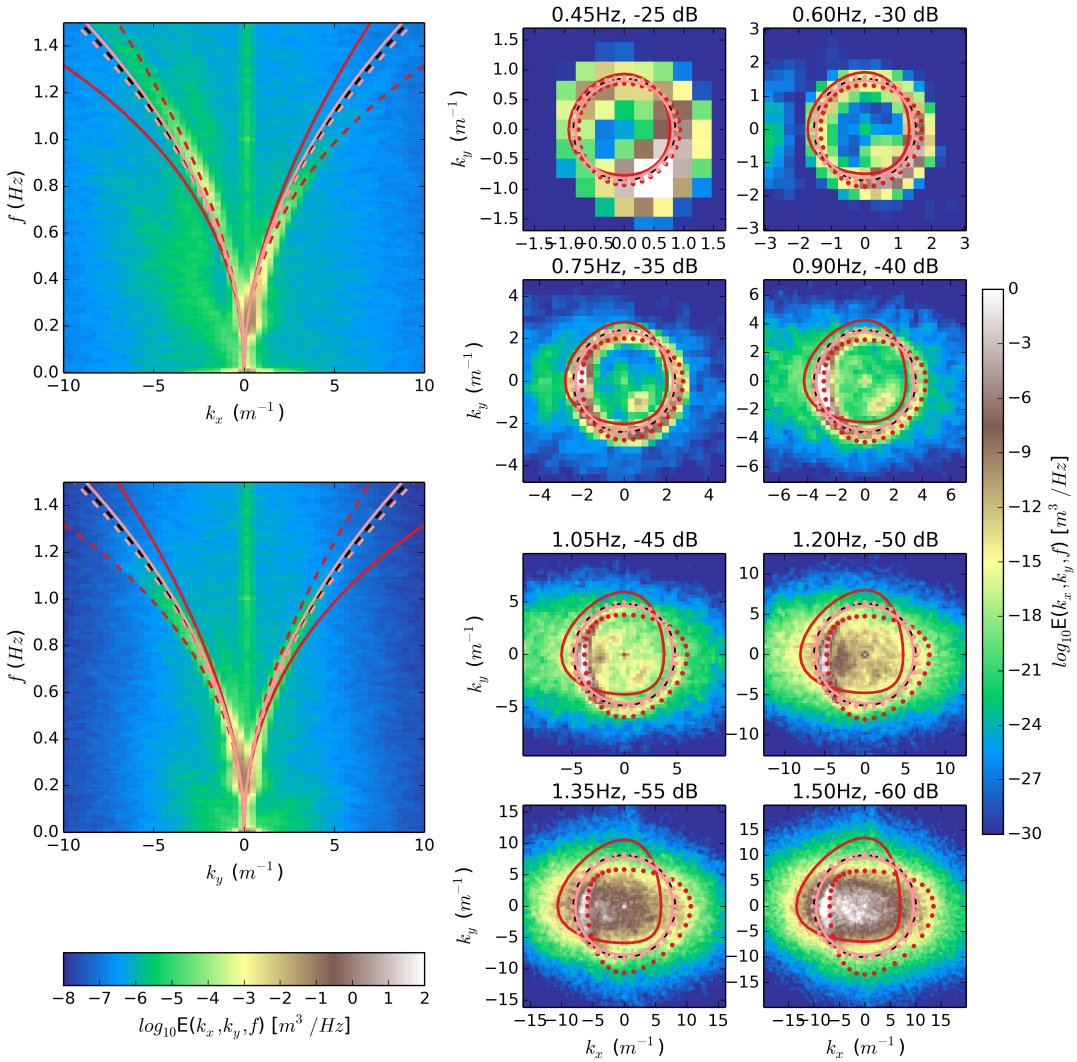

Figure 5.10: Same as Figure 5.9, for record II.

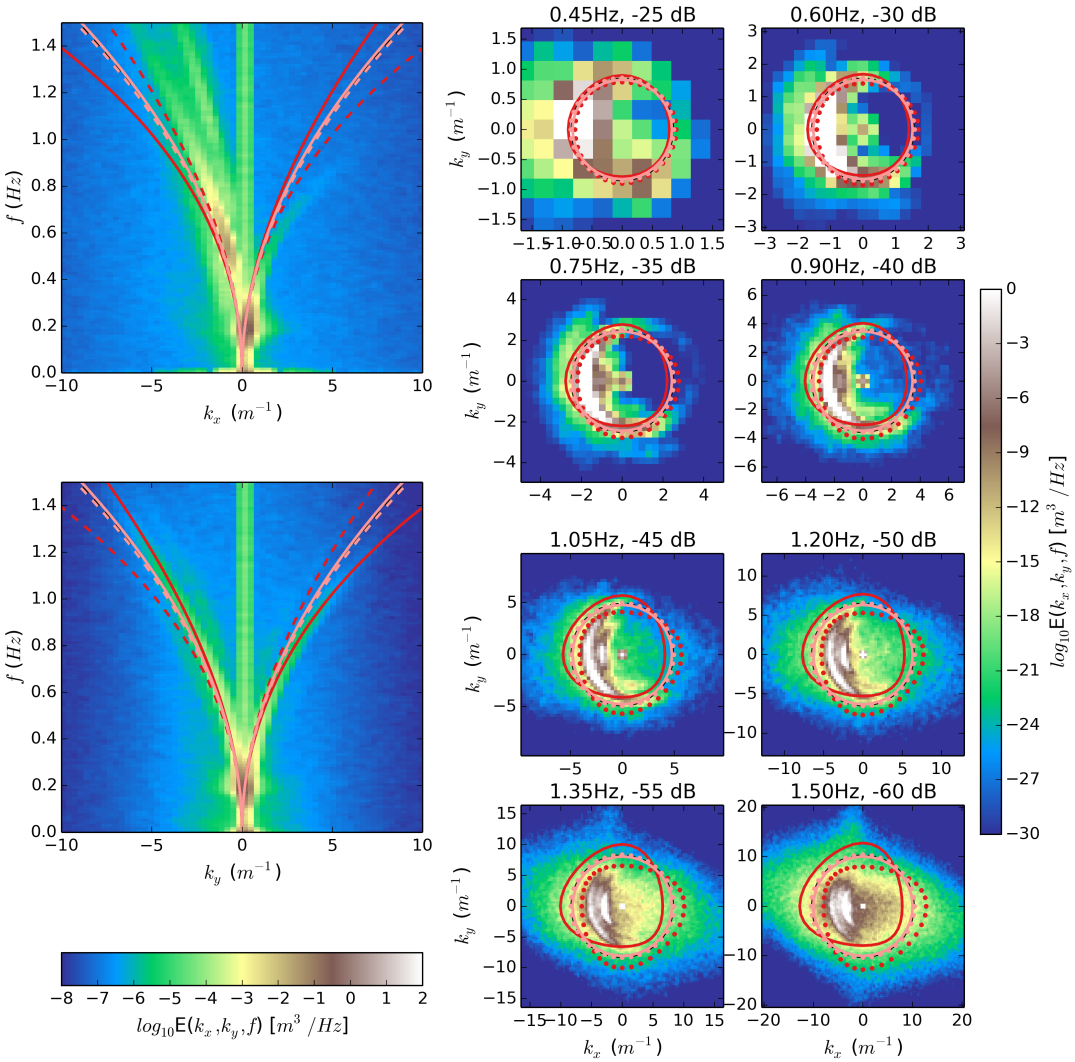

Figure 5.11: Same as Figure 5.9, for record III.

5.5 Observation of LW modulation on SW breaking

The three selected stereo video acquisitions have in common that they are characterized by a bimodal sea state conditions. So in these conditions, the SW can be modulated by the presence of LW. Figures 5.12–5.14 show the time evolution of the surface elevation at the location of breaking events $\zeta(t, x_b, y_b)$. The time interval for each breaking time series correspond to one LW peak wave period (T_p), in a way that the breaking events always occur at $t/T_p = 0.5$. The surface elevation time series for each breaking event is shown with a solid blue line. There are 411 breaking events for record I (Fig.5.12), 572 and 4342 for II and III respectively (Figs.5.13 and 5.14). The average of all these time series gives the solid black. The standard deviation is represented by the shaded area in Figs.5.12.b, 5.13.b and 5.14.b. The same treatment of the surface vertical velocity ($\partial\zeta/\partial t$) is presented in green (Figs.5.12.b, 5.13.b and 5.14.b), with a rapid evolution characterizing the breaking events.

In record I, with moderate wind speeds and SW propagating in the same direction as LW (Fig.5.12) SW break mostly at the crest of LW, where LW orbital velocity is maximum and the local vertical acceleration and LW sheltering are minimum.

In contrast, record II has most of LW components propagating perpendicular to the wind and SW (Fig.5.13). In that case, the SW breaking events occur at all phases of the surrounding LW profile.

Finally, our record III (Fig.5.14) corresponds to higher wind speeds. In this case, there is a moderate modulation of the SW properties. This relatively weak effect is probably mostly due to the oblique LW direction, intermediate between records I and II. In that record, there is a weak preference for SW breaking to occur at the crest of LWs, but breaking events are also found in the troughs.

The preferential breaking of SW near the crest of the LW can also be analyzed with the the probability density function (PDF) of breaking elevation. By selecting the mean foam surface elevation at the beginning of each active breaking event $\zeta_b(t_0)$ we can determine the elevation where the SWs starts to breaks. Figure 5.15 presents the normalized histogram of the elevations $\zeta_b(t_0)$ at the onset of breaking events, and the red dashed line represent a normal PDF fitted to this distribution. To compare the SWs breaking elevation with the surface elevation during the stereo video acquisitions, a Normalized PDF (N PDF) of the surface elevation $\zeta(x, y, z, t)$ is plotted in blue at the same figure.

The offset between the PDF of surface elevations at breaking onsets and the full elevation space-time series indicates a preferential breaking of SWs at the crest of LWs. This offset is largest for record I, consistent with a stronger SW modulation.

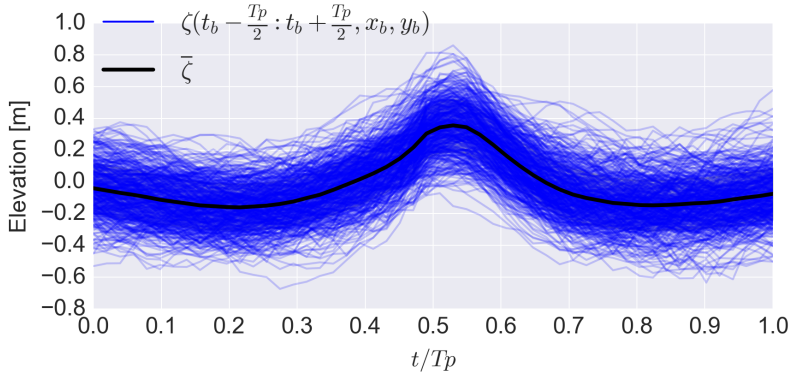

(a) Sea surface elevation

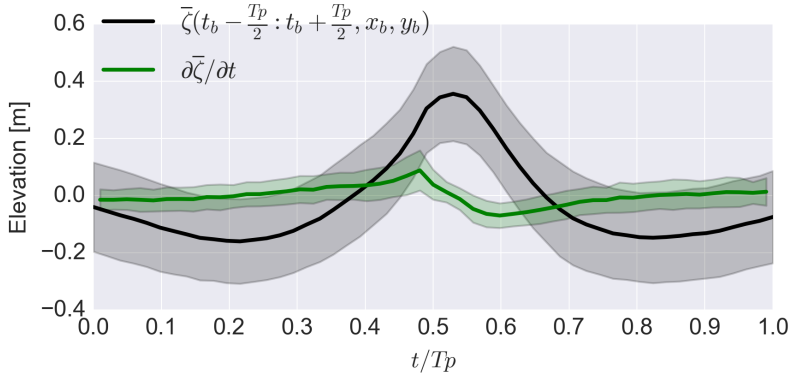

(b) Mean profile and standard deviation

Figure 5.12: Time series of sea surface elevation ζ around the wave breaking events for selected case I, with all breaking events starting at $t/Tp = 0.5$. a) the blue lines show the raw surface elevation $\zeta(t, x_b, y_b)$ while the black line represents the average of all time series. b) Average surface elevation $\overline{\zeta}$ (black) during breaking events, and time derivative $\partial\overline{\zeta}/\partial t$ (green). The standard deviation of the trend lines are represented by the shadowed areas.

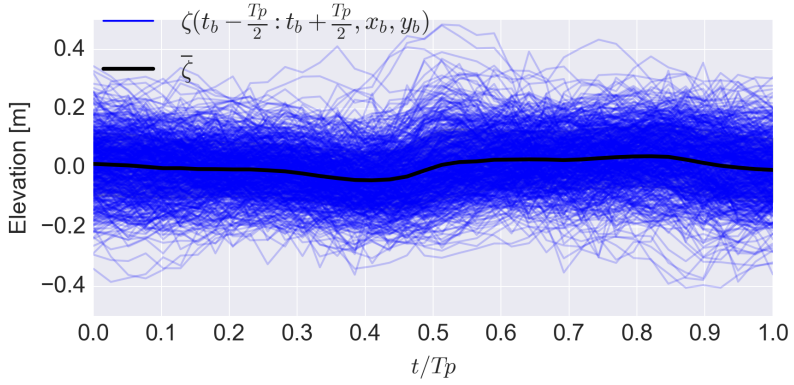

(a) Sea surface elevation

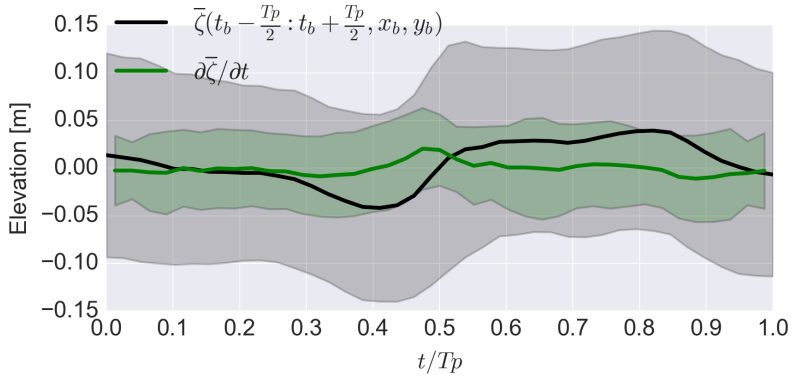

(b) Mean profile and standard deviation

Figure 5.13: Same as Figure 5.12, for record II.

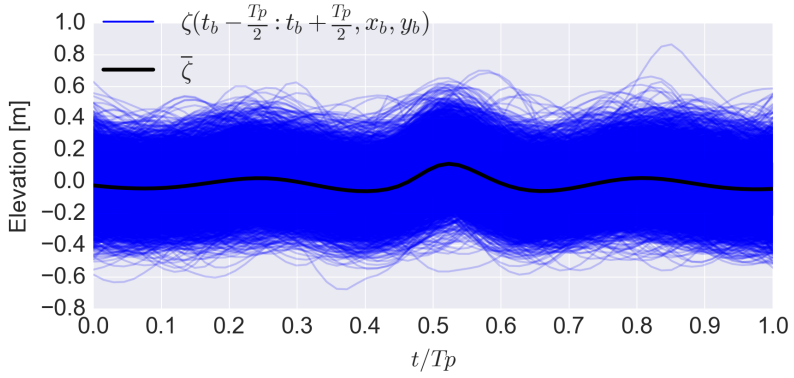

(a) Sea surface elevation

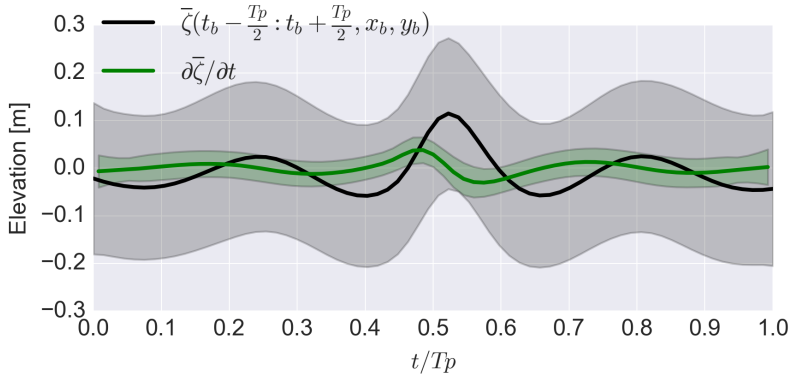

(b) Mean profile and standard deviation

Figure 5.14: Same as Figure 5.12, for record III.

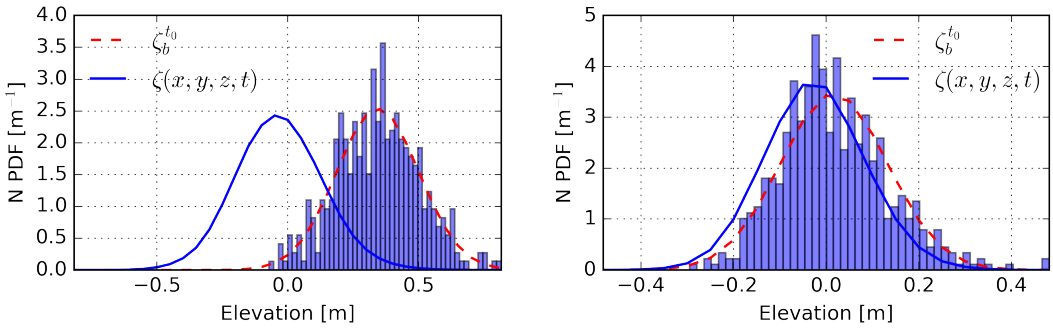

(a) Study case I

(b) Study case II

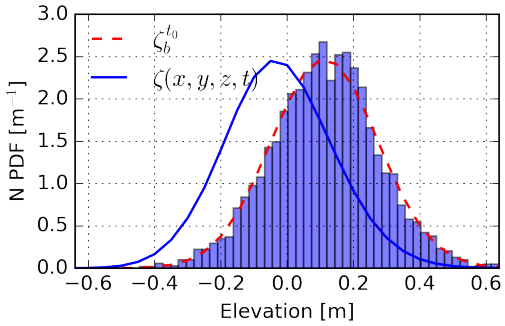

(c) Study case III

Figure 5.15: Normalized probability density functions (N PDF) of the surface elevation ζ (blue line), and of the elevation at the initial breaking positions (blue bars). The dash red lines shows the Gaussian N PDF fitted to the blue bars.

Under unfavorable LW modulation, like record III and II, the breaking can randomly occur at the sea surface and $\overline{\zeta_b}$ tends to zero.

According to Longuet-Higgins (1991), both the LW orbital velocity and the SW growth rate can be characterized by a single parameter Ω (Eq.5.45). More recently Elfouhaily et al. (2001) defined a first order MTF function (M, Eq.5.64) to characterize to LW hydrodynamic modulation on the SWs. So from the wind and waves observations acquired in the research platform we computed the Longuet-Higgins (1991) Ω and Elfouhaily et al. (2001) M functions (Tab.5.2).

Table 5.2: Observation data conditions compared with Longuet-Higgins (1991) Ω and Elfouhaily et al. (2001) M functions

	k_1 [m]	k_s [m]	U_l [m/s]	Ω	M
I	0.21	0.44	0.148	0.0019	3.77
II	0.23	2.9	0.229	0.0208	1.67
III	0.13	1.26	0.164	0.0598	1.98

Now we recall that when $\Omega < 1$, SW breaking only occurs around the crests of

LW, and for $\Omega > 1$ SW breaking is distributed uniformly along the LW profile. So, the first remarkable fact is that $\Omega \ll 1$ for all selected cases, meaning that our short waves are not very short and the expected effect of wind growth on the time scale of the LW period is negligible. According to Longuet-Higgins (1991), if SW breaking occurs, it should occur only close to the wave crest.

Even for the higher wind speeds $\Omega \ll 1$. The fact that we observe breaking for all elevations may be explained by a difference in the orientation of the two wave trains, and also the general probabilistic (Banner et al., 2000) and not deterministic nature of wave breaking. Indeed, Banner et al. (2000) clearly showed that waves break when the mean steepness is much less than the 0.22 used by Longuet-Higgins (1991). Also, the short waves have a broad spectrum and β, and thus Ω rapidly increase towards high frequencies.

A logical correction would thus be to extend the Longuet-Higgins (1991) modulation theory by considering breaking probabilities, for example those given by Banner et al. (2000). However, Ω still an interesting function to be investigated as it is an inverse function of M, where smalls values of Ω should represent bigger modulation amplitudes.

5.6 Modulations on the saturation spectrum

Following the work of Banner et al. (2000) and Filipot et al. (2010) we can take a probabilistic approach and express the breaking probability in terms of the saturation, which is now modulated with a MTF M_B.

Here we will consider the MTF of the conservative model, which follows a wave packet. In particular we consider the maximum value of B reached during the modulation by a monochromatic wave of amplitude $A_{k_1} = H_{s,1}/2$. for a narrow long wave spectrum this is

$$B^+(k_s,\theta_s) = \overline{B}(k_s)\,(1+2M_B\sqrt{\mathrm{mss}_1}) \tag{5.65}$$

and the lowest value

$$B^-(k_s,\theta_s) = \overline{B}(k_s)\,(1-2M_B\sqrt{\mathrm{mss}_1}) \tag{5.66}$$

with the long wave mean square slope given by

$$\mathrm{mss}_1 = 2\sum_{k_1} k_1^2 A_{k_1}^2. \tag{5.67}$$

based on our calculations, we can anticipate that the first order M_B tends to 4.5 when the short and longer wave are propagating in the same direction and $M_B \to 0.5$ when the waves are propagating in orthogonal direction. In this last conditions, the 0.5 corresponds just to the apparent gravity effect contribution on SW modulation. So we expect that M_B should actually be larger when $c_1 - c_s\cos(\theta_s - \theta_1)$ is small.

We recall that the saturation is the spectral equivalent of the mean square slope integrated over a spectral bandwidth $\Delta_k = k$. Most authors have used the following definition,

$$B = k^3E(k) = \frac{(2\pi f)^5}{4\pi g^2}E(f) \tag{5.68}$$

It should be noted that Ardhuin et al. (2010) restricted the integration in direction and Filipot et al. (2010) used an integration in wavenumber in order to keep only waves that contribute to the same wave groups and that have the time to evolve together towards breaking.

Figure 5.16 shows the observed saturation spectrum $\overline{B}(f)$ from the approximate 30 min stereo video record and our estimate of B^+ and B^-. The gray lines represent the maximum and minimum saturation amplitude ($B^{\pm}(f)$) for SW modulated by a sig-

nificant LW correspondent to f_{p1}. The Ardhuin et al. (2010) constant is derived from the Banner et al. (2000) threshold above which breaking of random waves start to occur. The Phillips (1958) constant is the upper limit reached by the spectral density, a limitation that is caused by wave breaking. It is actually lower by 30 to 50% compared to the saturation level in most observations (Banner et al., 1989; Leckler et al., 2015).

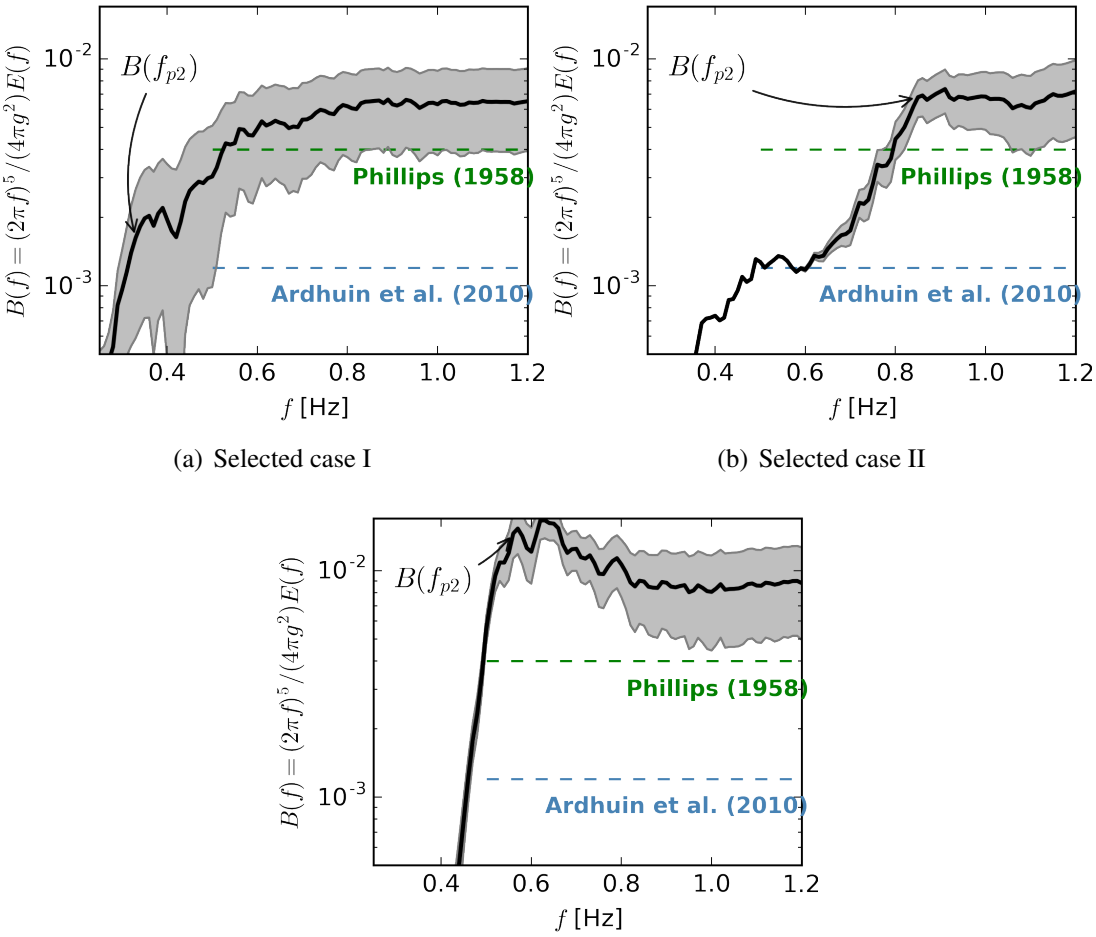

(a) Selected case I

(b) Selected case II

(c) Selected case III

Figure 5.16: Spectral saturation $B(f)$. The solid black line represent observed $\overline{B}(f)$ by stereo video while the shadow area in gray represent a theoretical maximum and minimum saturation amplitude $B^{\pm}(f)$ if is consider a stationary and uniform modulation condition. A dash color line mark the constant saturation threshold by Ardhuin et al. (2010) and Phillips (1958). The arrow indicate the saturation at the wind sea peaks $B(f_{p2})$.

In practice, because of the random characteristic of the sea surface, we can consider $\overline{B}(f)$ as the given by the average spectrum, and $B^{\pm}(f)$ represents typical maximum and minimum values of B over a modulation cycle.

We thus expect that the LW peak causes a fluctuation of the SW saturation in

the shaded grey area indicated in Figure 5.16. When considering shorter and shorter waves, the modulating LW should be expanded to cover a wider range of frequency, probably increasing the modulation towards the higher frequencies. For case I, the fact that our MTF is enough to have B^- fall below the saturation threshold for waves breaking proposed by Ardhuin et al. (2010), in the trough of the LW is consistent with out observed breaking probabilities that show no breaking at trough level.

From observational data, the value of B^+ cannot be compared directly to the measured spectra (B) because it may be above the true saturation that is in practice limited by breaking. But in therms of numerical application, in favorable modulation conditions, B^+ is more interesting to investigate breaking events. Where B^+ could suggest that the SW can actually start to break much before B reach the saturation threshold.

5.7 Conclusions and perspectives

Based on stereo video observations and breaking detection methods this chapter investigates bimodal sea states conditions for which long waves (LW) may have a modulating effect on short wave (SW) steepness, and thus an impact on SW breaking. Three different sea state conditions were selected to be represented here, where (I) wind sea and swell propagating in the same direction, (II) wind sea and swell propagating almost in orthogonal direction and (III) a condition with the wind sea and swell propagating in opposite direction with strong winds.

Several stereo video observations of the sea surface elevation during SW breaking events have revealed that under favorable LW modulation conditions (like selected case I), the SW breaking tends to occur near the crest of LW. On the other hand, conditions with SW and LW propagating on orthogonal direction or under strong winds, like selected case II and III, the waves tend to break almost everywhere over the LW. When SW breaking are modulated by LW, the probability density function of the breaking elevation is also shifted updwards.

We considered SW waves of intermediate frequency, around 0.4 Hz, so that the influence of wave growth only plays a minor role at the scale of one LW period, as quantified by the Ω parameter introduced by Longuet-Higgins (1991). For our intermediate waves $\Omega \ll 1$ and we may consider a conservative modulation theory in which action is conserved, and look at plausible enhancement of SW steepness due to LW modulation alone.

This is the first time that the full nonlinear equations based on the conservation of wave action and number of crests are applied to the problem of short wave modulation by long waves. These equations produce solutions that are not periodic in time and appear to be a function of the long wave steepness $k_l A_l$ and the ratio of long to short wave phase speeds c_l/c_s. In these solutions, the relative modulation of the saturation $M_B = B_{\max}/\overline{B} - 1$ is close to $5k_l A_l$ when $k_l A_l < 0.001$ and $c_l/c_s > 6$. This value of M_B rises sharply when $c_l/c_s < 3$ is below 3 and for realistic values of $k_l A_l$. With M_B exceeding 10 in realistic conditions.

Already using a variation of the wave saturation level with $M_B = 4$ gives strong changes in the saturation level that can explain the absence of wave breaking at the LW trough level in the case I observed with stereo video.

We have made preliminary efforts, not discussed in this chapter, to parameterize this effect in the WAVEWATCH III model (Fig.5.17). The results suggest that using values of $M_B \simeq 10$ are sufficient to reproduce strongly bimodal spectra and a f^{-5} decay of the wave spectrum $E(f)$ at a level consistent with observations. This modulation

of SW by LW may thus be the key "cumulative" dissipation effect that contributes to the shape of spectrum for $f > 2f_p$. A detailed validation of both the amplitude modulation and breaking occurrence is thus a central question for the future development of numerical models like WAVEWATCH III. It is thus necessary to better quantify the modulation effect in models that resolve the LW phase, and the conservative model presented here could be modified to include a breaking parameterization that would avoid unrealistic SW steepnesses. There is certainly the need to work with models that resolve both LW and SW phases such as High Order Spectral models (e.g. Ducrozet et al., 2016).

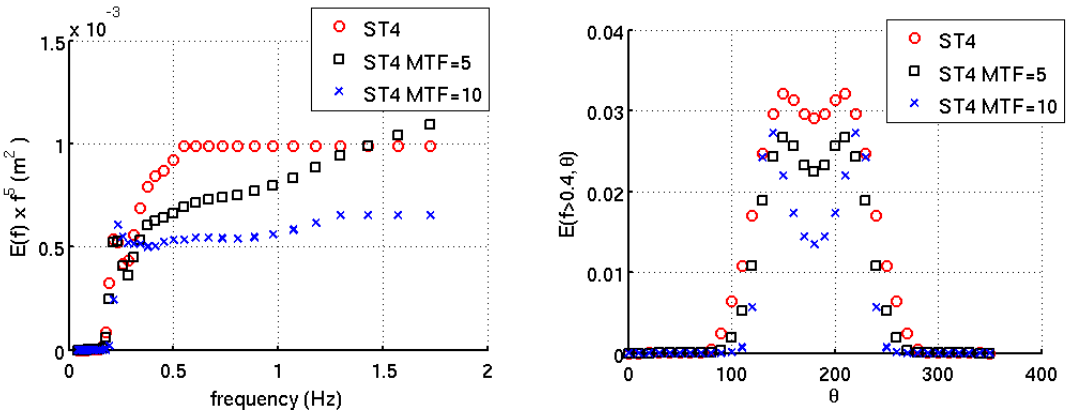

(a) (b)

Figure 5.17: Preliminary results of a WAVEWATCH III numerical simulation considering the Test 471 from Ardhuin et al. (2010) and ST4 source package (red curve) and considering a constant MTF, $M_B = 5$ (black) and $M_B = 10$ (blue). a) Impact in the saturation spectrum and b) in the directional distribution.

In summary, the combination of stereo video observations and breaking detection provide new insights on the SWs dynamics and dissipation, and a unique dataset for further development and validation of parameterizations in phase-averaged models. The physical findings and discusses on this chapter still preliminary but with promising application on waves modeling, and remote sensing for which the shape of wave spectra at present is still unsatisfactory.

6. Final considerations

Despite wind waves are being studied for more than 60 years now, the lack of field observation in a broad range of sea surface conditions still blind the understanding of many physical processes. In this work we try to apply some modern sensing techniques to investigate old ocean wave problems. The observations were compared against the some present and ancient theoretical framework. The results have revealed important insights where the stochastic numerical model parameterizations could fail and can be improved.

To access that, firstly we develop and tested the The Surface KInematics Buoy (SKIB), a new low-cost drifter that has been designed for the investigation of wave-current interactions. The equipment performed well in representing the directional variance spectral density between 0.045 to 0.800 Hz. The devices were able to measure wave properties varied across a current gradient that is relatively uniform and along the propagation direction. Such measurements were important for testing existing theories for wave dissipation and current interaction widely used in numerical wave models.

When compared against spectral waves model, the observations, over strong current gradients, always present a significant increment of energy in the wind sea components. Same observations were systematic verified by other drifting buoys and stereo video observation. After performing several numerical tests, we conclude that the main source of error was in the atmospheric forcing. By considering different physical assumption and parameterization, the present model parameterization for waves and currents interactions and dissipation were only able to impact in the order of O(10%) of the numerical error while by forcing a correction on the wind the results start to get more consistent with varying spectral density measured by the buoys.

These observations suggest that in a strong tidal current areas the wind is fre-

quently biased and it has a much more significant impact on the short-fetch wave growth than the wave-current interaction by itself. Nevertheless, this observation and numerical experiments rises a special tidal current and wind interaction that could not be solved by the relative wind and current effect and more field observations and deeper investigation are required.

From stereo video observations and breaking detection methods it was investigated several bimodal sea states conditions where longer waves can modulate short-scale waves breaking. The stereo video breaking observations have revealed that under favorable long wave modulation conditions the short wave tends to break near the crest of the long wave and this can modify the breaking elevation probability density function. Despite this phenomenon is investigated since the 80s, this is possibly the first direct field observation of long wave modulation on short waves breaking.

This observations have a direct impact on short waves dynamic. In a favorable modulation scenario, long waves can modify the breaking velocity and the energy dissipated. This effect is usually neglected by breaking parametrization used on stochastic models, with a direct impact the short waves action.

From the three dimensional wavenumber and frequency spectrum and a controlled simplified numerical simulations without breaking it was possible to investigate how the long wave orbital velocity modulation the short wave action around the dispersion dispersion relation. This result suggests that the energy spread around the dispersion relation is not a direct function of the wavenumber and apparent frequency modulation amplitude, but also depends on the short wave action around those frequencies.

This modulation of SW by LW may thus be the key "cumulative" dissipation effect that contributes to the shape of spectrum for $f > 2f_p$. However, more detailed investigation is needed to quantify how much the modulation amplitude influence the breaking probabilities. This is needed to adjust the parameterization of that effect in phase-averaged models like WAVEWATCH III, that do not resolve these variations in SW amplitude along the LW phase.

In summary, the numerical simulation combined with the Lagrangian sensing techniques under tidal current environment revealed important characteristics of wind-waves-current dynamics not properly observed and discussed before. Nevertheless, the combination of stereo video observations and breaking detection also have provide new insights on the short waves dynamics and dissipation. The physical findings and discussed on this thesis still preliminary, but this results have promising application on stochastic waves modeling, remote scening and waves energy assessment.

Our future developments in those topics aim to improve the SKIB buoys capabil-

ity to lower frequencies and try to reduce even further the equipment costs. We also intend to test the equipment to other applications like extreme sea measurements and ice and sea interaction.

In strong current and low wind conditions, our numerical tests prove to be inefficient in representing the sea state conditions. So we need to investigate further the wind, wave and current interaction by doing more coupled numerical test and field experiments in this kind of complex environment.

In favorable modulation conditions, our preliminary numerical tests, including the longer wave modulation effect on the saturation based parameterization looks very promising and already revealed important aspects of short wave dynamics. However, we still have to find a more precise way to calculate the modulation amplitude for the difference spectrum components and at different environmental conditions. After that we can start to investigate more realistic scenarios and generalize this theory.

Appendices

A. Surf zone stereo video experiment

There is a very long history of use the visible range of remote sensing technique for shallow waters and surf zone applications. An example is the work of Holland et al. (2001), whom applied particle image velocimetry (PIV) methods to the swash zone. In 2007, Holman and Stanley proposed the Argus program, used to monitor beach morphologic behavior and coastal zones. Holland et al. (1997) used a video system to propose a simplified wave model to link the breaking dissipation to bathymetry.

Inspired in those works, many other authors have explored the visible range of the beach monitoring system. However, after a decade of stereo video wave measurements apparently only a few authors have tried to explore its applicability in the surf zone. The work of Vries et al. (2011) is a pioneer in exploring the potential application of this methodology in a large scale surf zone domain (103–104m^2). According to their experiment, the reconstructed surface elevation has a good agreement with the estimation of the wave heights and periods compared with an available buoy data.

In this context, we developed the Porsmilin beach stereo video experiment. The initial ultimate goal was to test if this system can measure waves in shallow water and breaking with good spatial and temporal resolution. This first field experiments were carried out on the Porsmilin beach (Fig.A.1), at Locmaria-Plouzané, northwest coast of the France, 48.35^{o}N, 4.68^{o}W, on 04 May, 2015. This beach was selected because it is part of the French NSO DYNALIT (National Service of Observation) with a constant survey and research monitoring. This portion of the beach also has some practical advantages, like a near parking loft and accessible power connection.

In this experiment, the two video cameras were installed in front of the beach, at the top of an Ifremer van (Fig.A.1). The stereo video system and methodology used in this experiment follow the Leckler (2013) toolbox as presented in Chapter 2.

Figure A.1: Surf zone stereo video experiment at Porsmilin beach 4th of May, 2015.

The underwater topography was acquired during the low tide using a LIDAR scanner by the lab "Domaines Océaniques" and the "Pôle Image" of IUEM. This was possible because this is a macro-tidal area, with ∼6 m of tidal amplitude. The stereo video experiments were done during the high tide, when most of the beach is flooded.

Figures A.2.a and A.2.b exemplify a snapshot of the Porsmilin stereo video experiment. A first look at the results (Fig.A.2.a) suggest a good coherence between the visual and the surface elevation map. However, when the surface elevation is plotted over x and y axis (Fig.A.2.b), the results presented some unexpected elevation gradients, probably creating unrealistic topologies.

These errors tend to be observed in shadowed areas from the cameras view, behind the wave crest, or around the broken crest. This basically occurs because the cameras were not high enough to measure the waves from the beach. So the wave crest creates some blind spots for the stereo video reconstruction. The lack of information in some particular regions introduces some bias in the linear grid interpolation, creating a severe error in the interpolated 3D surface elevation field. To avoid that, in the next beach experiment the cameras were placed higher, in the top of the cliff ($\sim$ 20 m height), recording the sea surface almost orthogonal to the wave propagation direction.

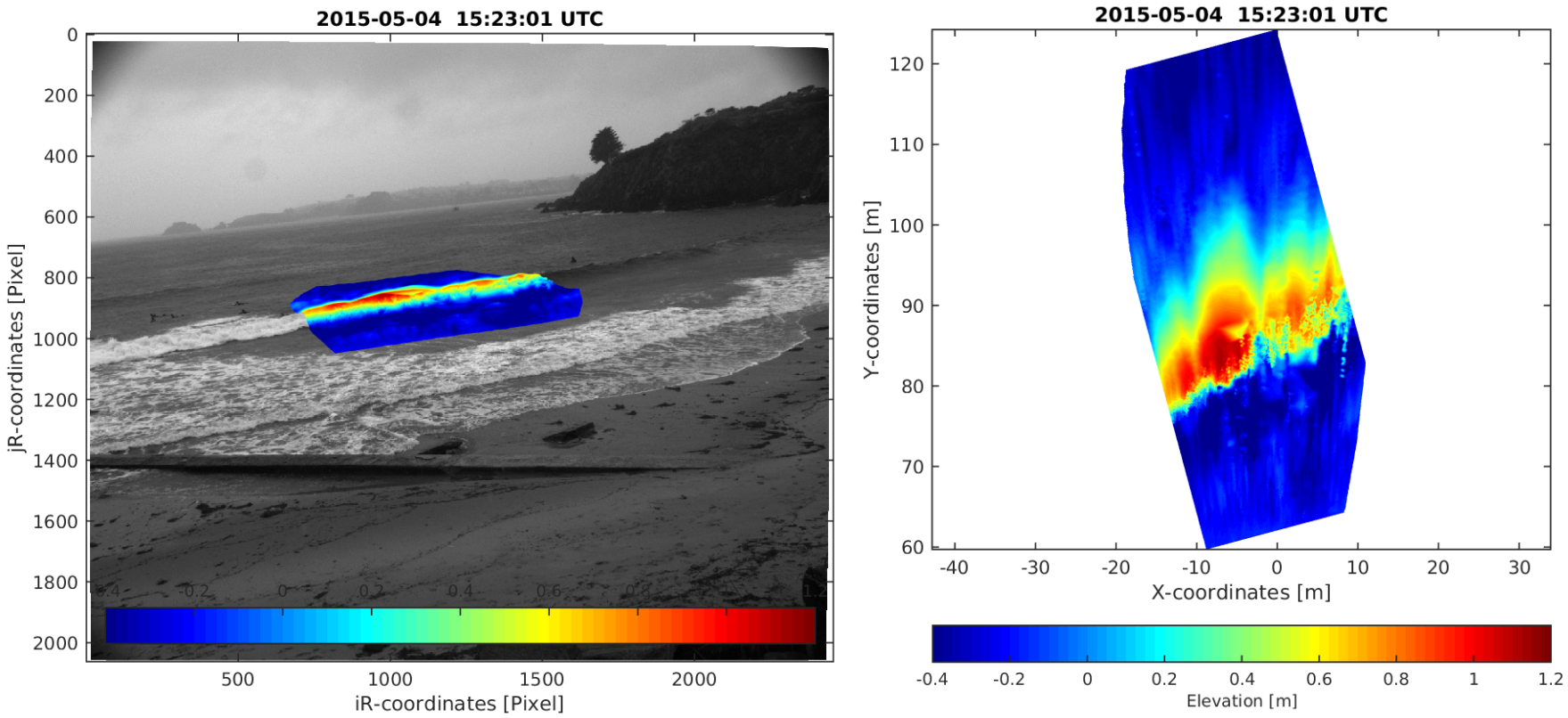

(a) (b)

Figure A.2: Porsmilin beach stereo video experiment (48.35^{o}N, 4.68^{o}W, 04 of May, 2015). a) Right camera bitmap image and the colored map over shows the surface elevation (in meters) from the reconstructed and gridded stereo video processing. b) Gridded Surface elevation in x, y, z coordinate system for the same stereo video footage presented in (a).

This second stereo video acquisition was carried out on the same beach, from October 2016 from 19th of October to 3rd of November as part of the Dynatrez II experiment. The data processing for this experiment is still ongoing. But a preliminary result is presented in Figure A.3.

In this condition, the stereo video processing was also modified for Bergamasco et al. (2017) open source WASS pipeline. This new stereo video code is particularly valuable for this experiment because it allowed to reconstruct all the pixels in the sea surface footage, without severely increase the computational cost. Because of that it is now possible to improve the spatial stereo video resolution and also the covered area.

As already demonstrated by Vries et al. (2011), the stereo imaging of the surf zone is a qualified method for obtaining surface elevation and shallow water wave data. This method can provide a highly resolved (both in time and space) data on the water surface elevation over large areas. However, a proper field validation of this method, including limitation and usability in the surf zone still pending for future works. Future field campaigns should seek to obtain and validate measurements over a wide range of environments and conditions.

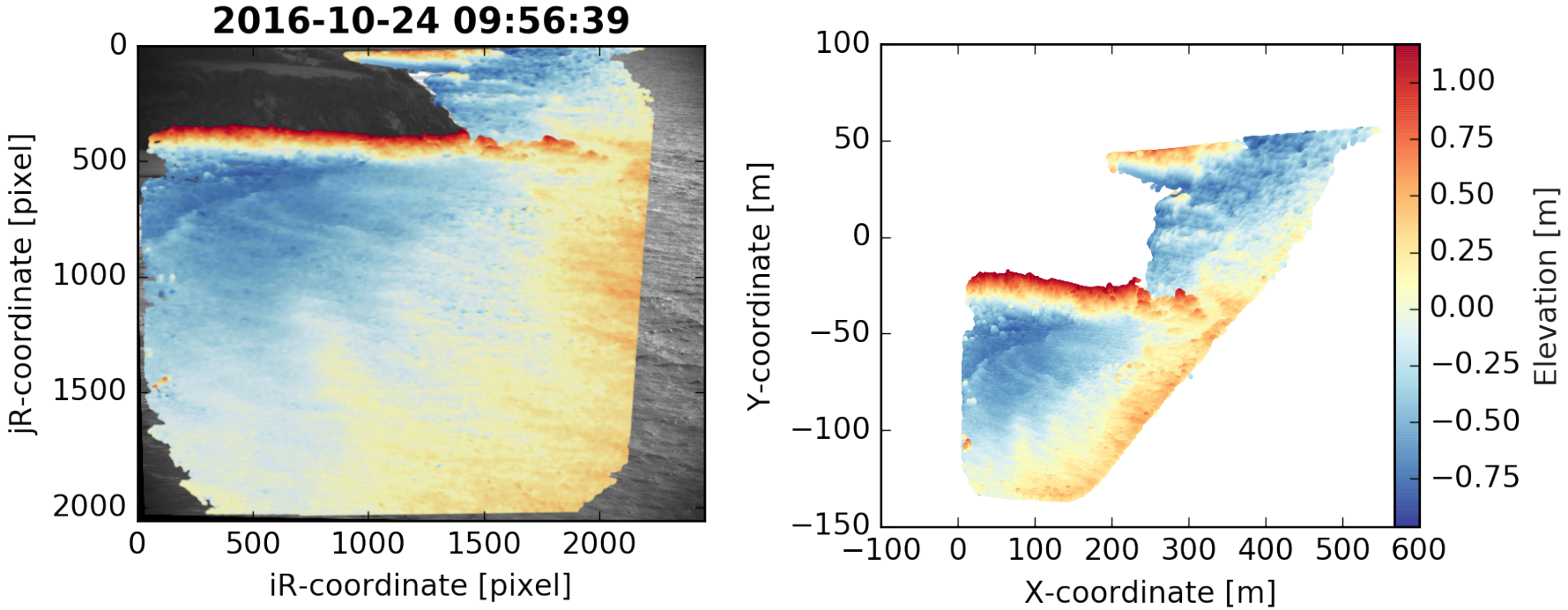

(a) (b)

Figure A.3: Example of stereo video surface reconstruction for Dynatrez II experiment. a) Sea surface elevation over the right camera footage. b) Sea surface elevation in the world coordinates system.

Bibliography

Agrawal, Y. C., Terray, E. a., Donelan, M. a., Hwang, P. a., Williams, a. J., Drennan, W. M., Kahma, K. K., and Kitaigorodskii, S. a. (1992). Enhanced dissipation of kinetic energy beneath surface waves. *Nature*, 359:219–220.

Alpers, W. and Hasselmann, K. (1978). The two-frequency microwave technique for measuring ocean-wave spectra from an airplane or satellite. *Boundary-Layer Meteorology*, 13(1-4):215–230.

Andrews, D. G. and McIntyre, M. E. (1978). On wave action and its relatives. *J. Fluid Mech.*, 89:647–664. Corrigendum: vol. 95, p. 796.

Ardhuin, F., Aksenov, Y., Benetazzo, A., Bertino, L., Brandt, P., Caubet, E., Chapron, B., Collard, F., Cravatte, S., Dias, F., Dibarboure, G., Gaultier, L., Johannessen, J., Korosov, A., Manucharyan, G., Menemenlis, D., Menendez, M., Monnier, G., Mouche, A., Nouguier, F., Nurser, G., Rampal, P., Reniers, A., Rodriguez, E., Stopa, J., Tison, C., Tissier, M., Ubelmann, C., van Sebille, E., Vialard, J., and Xie, J. (2017a). Measuring currents, ice drift, and waves from space: the sea surface kinematics multiscale monitoring (skim) concept. *Ocean Sci. Discuss.*

Ardhuin, F., Chapron, B., and Collard, F. (2009). Observation of swell dissipation across oceans. *Geophysical Research Letters*, 36(6):1–5.

Ardhuin, F. and Filipot, J. F. (2016). *Ocean waves in geosciences*.

Ardhuin, F., Herbers, T. H. C., Watts, K. P., van Vledder, G. P., Jensen, R., and Graber, H. C. (2007). Swell and slanting-fetch effects on wind wave growth. *Journal of Physical Oceanography*, 37(4):908–931.

Ardhuin, F. and Jenkins, A. D. (2006). On the interaction of surface waves and upper ocean turbulence. *J. Phys. Oceanogr.*, 36(3):551–557.

Ardhuin, F., Rascle, N., Chapron, B., Gula, J., Molemaker, J., Gille, S. T., Menemenlis, D., and Rocha, C. (2017b). Small scale currents have large effects on wind wave heights. *J. Geophys. Res.*, 122:4500–4517.

Ardhuin, F., Rogers, E., Babanin, A. V., Filipot, J.-F., Magne, R., Roland, A., van der Westhuysen, A., Queffeulou, P., Lefevre, J.-M., Aouf, L., and Collard, F. (2010). Semiempirical dissipation source functions for ocean waves. Part I: definition, calibration, and validation. *Journal of Physical Oceanography*, 40(9):1917–1941.

Ardhuin, F., Roland, A., Dumas, F., Bennis, A.-C., Sentchev, A., Forget, P., Wolf, J., Girard, F., Osuna, P., and Benoit, M. (2012). Numerical wave modelling in conditions with strong currents: dissipation, refraction and relative wind. *Journal of Physical Oceanography*, (1996):120723054131002.

Babanin, A. V. and Soloviev, Y. P. (1998a). Field investigation of transformation of the wind wave frequency spectrum with fetch and the stage of development. *J. Phys. Oceanogr.*, 28:563–576.

Babanin, A. V. and Soloviev, Y. P. (1998b). Variability of directional spectra of wind-generated waves, studied by means of wave staff arrays. *Mar. Freshwater Res.*, 49:89–101.

Babanin, A. V. and Young, I. R. (2005). Two-phase behaviour of the spectral dissipation of wind waves. In *Ocean Waves Measurement and Analysis, Fifth International Symposium WAVE*, pages 1–11, Madrid.

Babanin, A. V., Young, I. R., and Banner, M. L. (2001). Breaking probabilities for dominant surface waves on water of finite constant depth. *Journal of Geophysical Research*, 106(C6):659—-676.

Baldock, T. E., Manoonvoravong, P., and Pham, K. S. (2010). Sediment transport and beach morphodynamics induced by free long waves, bound long waves and wave groups. *Coastal Engineering*, 57(10):898–916.

Banner, M., Jones, I., and Trinders, J. (1989). Wavenumber spectra of short gravity waves. *Journal of Fluid Mechanics*, 198(1989):321–344.

Banner, M. L., Babanin, A. V., and Young, I. R. (2000). Breaking Probability for Dominant Waves on the Sea Surface. *Journal of Physical Oceanography*, 30(12):3145–3160.

Banner, M. L., Barthelemy, X., Fedele, F., Allis, M., Benetazzo, A., Dias, F., and Peirson, W. L. (2014). Linking reduced breaking crest speeds to unsteady nonlinear water wave group behavior. *Physical Review Letters*, 112(11):1–5.

Banner, M. L. and Morison, R. P. (2006). On modeling spectral dissipation due to wave breaking for ocean wind waves. In *Proceedings of the 9th International workshop on wave hindcasting and forecasting, Victoria, Canada*.

Banner, M. L. and Peirson, W. L. (2007). Wave breaking onset and strength for two-dimensional deep-water wave groups. *J. Fluid Mech.*, 585:93–115.

Banner, M. L. and Peregrine, D. H. (1993). Wave breaking in deep water. *Annual Reviews in Fluid Mechanics*, 25(1991):373–397.

Banner, M. L. and Young, I. R. (1994). Modeling spectral dissipation in the evolution of wind waves. part I: assessment of existing model performance. *J. Phys. Oceanogr.*, 24(7):1550–1570.

Beers, L. M. and Tran, C. (2016). Sydney's wild weather: Worst storm in 40 years swallows pools, up to 1000 evacuated from their homes and the city's transport system in chaos.

Belcher, S. E. and Hunt, J. C. R. (1993). Turbulent shear flow over slowly moving waves. *Journal of Fluid Mechanics*, 251:109–148.

Benetazzo, A. (2006). Measurements of short water waves using stereo matched image sequences. *Coastal Engineering*, 53(12):1013–1032.

Benetazzo, A., Ardhuin, F., Bergamasco, F., Cavaleri, L., Guimarães, P. V., Schwendeman, M., Sclavo, M., Thomson, J., and Torsello, A. (2017). On the shape and likelihood of oceanic rogue waves. *Scientific Reports*, 7(1):8276.

Benetazzo, A., Barbariol, F., Bergamasco, F., Torsello, A., Carniel, S., and Sclavo, M. (2016). Stereo wave imaging from moving vessels: Practical use and applications. *Coastal Engineering*, 109:114–127.

Benetazzo, A., Fedele, F., Gallego, G., Shih, P. C., and Yezzi, A. (2012). Offshore stereo measurements of gravity waves. *Coastal Engineering*, 64:127–138.

Benoit, M., Frigaard, P., and Schäffer, H. A. (1997). Analysing multidirectional wave spectra: A tentative classification of available methods. In *IAHR-Seminar: Multidirectional Waves and their Interaction with Structures*, pages 131—-158.

Bergamasco, F., Benetazzo, A., Barbariol, F., Carniel, S., and Sclavo, M. (2016). Multi-view horizon-driven sea plane estimation for stereo wave imaging on moving vessels. *Computers and Geosciences*, 95:105–117.

Bergamasco, F., Torsello, A., Sclavo, M., Barbariol, F., and Benetazzo, A. (2017). WASS: An open-source pipeline for 3D stereo reconstruction of ocean waves. *Computers and Geosciences*, (August):1–9.

Bertin, X., Bruneau, N., Breilh, J. F., Fortunato, A. B., and Karpytchev, M. (2012). Importance of wave age and resonance in storm surges: The case Xynthia, Bay of Biscay. *Ocean Modelling*, 42:16–30.

Bidlot, J., Janssen, P., and Abdalla, S. (2005). Memorandum research department, A revised formulation for ocean wave dissipation in CY29R1. Technical Report 1.

Bidlot, J.-R., Janssen, P. A. E. M., and Abdalla, S. (2007). A revised formulation of ocean wave dissipation and its model impact. *ECMWF Technical Memorandum*, 509(January).

Black, P. G., D'asaro, E., Drennan, W. M., French, J. R., Niiler, P. P., Sandord, T. B., Terrill, E. J., Walsh, E. J., and Zhang, J. A. (2007). Air–sea exchange in hurricanes synthesis of observations from the coupled boundary layer air–sea transfer experiment. *Bulletin of the American Meteorological Society*, 88(March):357–374.

Blenkinsopp, C. E., Turner, I. L., Allis, M. J., Peirson, W. L., and Garden, L. E. (2012). Application of lidar technology for measurement of time-varying free-surface profiles in a laboratory wave flume. *Coastal Engineering*, 68:1 – 5.

Bourras, D., Branger, H., Reverdin, G., Marié, L., R., C., Baggio, L., Caudoux, C., Morrisset, S., Geyskens, N., Weill, A., and Hauser, D. (2014). A new platform for the determination of air–sea fluxes (OCARINA): overview and first Results. *Journal of Atmospheric and Oceanic Technology*, 31(1):1043–1062.

Bretherton, F. P. and Garrett, C. J. R. (1968). Wavetrains in inhomogeneous moving media. *Proc. Roy. Soc. of London*, A302:529–554.

Campbell, A. J., Bechle, A. J., and Wu, C. H. (2014). Observations of surface waves interacting with ice using stereo imaging. *Journal of Geophysical Research: Oceans*, 119(6):3266–3284.

Caponi, E. A., Crawford, D. R., and Yuen, H. C. (1988). Modulation of radar backscatter from the ocean by a variable surface current. *Journal of Geophysical Research*, 93(C10):12,249–12,263.

Caudal, G., Hauser, D., Gac, C. L., Valentin, R., Lapauw, L., Delaye, L., Pauwels, N., and Tison, C. (2014). Kuros: A new airborne ku-band doppler radar for observation of the ocean surface. In *2014 International Radar Conference*, pages 1–6.

Cavaleri, L., Curiotto, S., Porta, G. D., and Mazzoldi, A. (1981). Directional wave recording in the northern Adriatic sea. *Nuovo Cimento*, 4C(5):519–534.

Chapron, B., Collard, F., and Ardhuin, F. (2005). Direct measurements of ocean surface velocity from space: interpretation and validation. *J. Geophys. Res.*, 110(C07008).

Chapron, B., Johnsen, H., and Garello, R. (2001). Wave and wind retrieval from SAR images of the ocean. *Ann. Telecommun.*, 56:682–699.

Charnock, H. (1955). Wind stress on a water surface. *Quarterly Journal of the Royal Meteorological Society*, 81(350):639–640.

Chase, J., Cote, l. J., Marks, W., Mehr, E., Pierson, W. J., Ronne, F. C., Stephenso, G., Vetter, R. C., and Walden, R. (1957). The directional spectrum of a wind generated sea as determined from data obtained by the Stereo Wave Observation Project.

Chawla, A. and Kirby, J. T. (2002). Monochromatic and random wave breaking at blocking points. *J. Geophys. Res.*, 107(C7):3067.

COST Action 714 Working Group 3, W. G. (2005). *Measuring and analysing the directional spectra of ocean waves*. Office for Official Publications of the European Communities, Luxembourg.

de Vries, J. and Haarlem, B. (2007). Designing a GPS-based mini wave buoy. *International Ocean Systems*, (Buoys):20–23.

Dodet, G., Bertin, X., Bruneau, N., Fortunato, A. B., Nahon, A., and Roland, A. (2013). Wave-current interactions in a wave-dominated tidal inlet. *Journal of Geophysical Research: Oceans*, 118(3):1587–1605.

Donelan, M. A. (2001). A nonlinear dissipation function due to wave breaking. In *Proceedings of ECMWF workshop on ocean wave forecasting, 2–4 July*, pages 87–94.

Donelan, M. a., Babanin, A. V., Young, I. R., and Banner, M. L. (2006). Wave-Follower Field Measurements of the Wind-Input Spectral Function. Part II: Parameterization of the Wind Input. *Journal of Physical Oceanography*, 36(8):1672–1689.

Donelan, M. A., Babanin, A. V., Young, I. R., Banner, M. L., and McCormick, C. (2005). Wave-follower field measurements of the wind-input spectral function. Part I: Measurements and calibrations. *Journal of Atmospheric and Oceanic Technology*, 22(7):799–813.

Donelan, M. A., Hamilton, J., and Hui, W. H. (1985). Directional spectra of wind-generated waves. *Phil. Trans. Roy. Soc. London A*, 315:509–562.

Donlon, C. J., Martin, M., Stark, J., Roberts-Jones, J., Fiedler, E., and Wimmer, W. (2012). The Operational Sea Surface Temperature and Sea Ice Analysis (OSTIA) system. *Remote Sensing of Environment*, 116:140–158.

Drennan, W. M. and Shay, L. K. (2006). On the variability of the fluxes of momentum and sensible heat. *Boundary-Layer Meteorology*, 119(1):81–107.

Ducrocq, V., Bouttier, F., Malardel, S., Montmerle, T., and Seity, Y. (2005). The Arome project, Mediterranean floods: scientific and technical answers from the (French) state. *La Houille Blanche*, 2:39—-44.

Ducrozet, G., Bonnefoy, F., Touzé, D. L., and Ferrant, P. (2016). HOS-ocean: Open-source solver for nonlinear waves in open ocean based on high-order spectral method. *Computer Phys. Comm.*, 203(Supplement C):245–254.

Dugan, J. P., Piotrowsky, C. C., Williams, J. Z., Piotrowski, C. C., and Williams, J. Z. (2001). Water depth and surface current retrievals from airborne optical measurements of surface gravity wave dispersion. *Journal of Geophysical Research*, 106(C8):16903–16915.

Dulov, V. A., Kudryavtsev, V., and Bolshakov, A. N. (2002). A field study of whitecap coverage and its modulations by energy containing surface waves. *Gas Transfer at Water Surface*, 127(Geophysical Monograph):187–192.

Duncan, J. H. (1981). An experimental investigation of breaking waves produced by a towed hydrofoil. *Proc. Roy. Soc. Lond. A*, 377:331–348.

Edson, J., Crawford, T., Crescenti, J., Farrar, T., Frew, N., Gerbi, G., Helmis, C., Hristov, T., Khelif, D., Jessup, A., Jonsson, H., Li, M., Mahrt, L., McGillis, W., Plueddemann, A., Shen, L., Skyllingstad, E., Stanton, T., Sullivan, P., Sun, J., Trowbrudge, J., Vickers, D., Wang, S., Wang, Q., Weller, R., WILKIN, J., Williams, A., Yue, D. K. P., and Zappa, C. (2007). The coupled boundary layers and air-sea transfer experiment in low winds. *Bulletin of the American Meteorological Society*, 88(March):341–356.

Edson, J. B., Jampana, V., Weller, R. A., Bigorre, S. P., Plueddemann, A. J., Fairall, C. W., Miller, S. D., Mahrt, L., Vickers, D., and Hersbach, H. (2013). On the exchange of momentum over the open ocean. *J. Phys. Oceanogr.*, 43:1589–1610.

Elfouhaily, T., Chapron, B., Katsaros, K., and Vandemark, D. (1997). A unified directional spectrum for long and short wind-driven waves. *Journal of Geophysical Research*, 102(C7):15781–15796.

Elfouhaily, T. and Thompson, D. (2001). Higher-order hydrodynamic modulation : theory and applications for ocean waves. *The Royal Society*, 457(2015):2585–2608.

Elfouhaily, T., Thompson, D., Chapron, B., and Vandemark, D. (2001). Improved electromagnetic bias theory: Inclusion of hydrodynamic modulations. *Journal of Geophysical Research*, 106(C3):4655–4664.

Fabrikant, A. L. (1976). Quasilinear theory of wind-wave generation. *Izv. Atmos. Ocean. Phys.*, 12:524–526.

Fedele, F. (2012). Space-time extremes in short-crested storm seas. *Journal of Physical Oceanography*, 42(9):1601–1615.

Fedele, F., Benetazzo, A., Gallego, G., Shih, P. C., Yezzi, A., Barbariol, F., and Ardhuin, F. (2013). Space-time measurements of oceanic sea states. *Ocean Modelling*, 70:103–115.

Filipot, J.-F., Ardhuin, F., and Babanin, A. (2010). A unified deep-to-shallow-water wave-breaking probability parameterization. *J. Geophys. Res.*, 115:C04022.

Gagnaire-Renou, E., Benoit, M., and Forget, P. (2010). Ocean wave spectrum properties as derived from quasi-exact computations of nonlinear wave-wave interactions. *J. Geophys. Res.*, 115:C12058.

Gallego, G., Benetazzo, A., Yezzi, A., and Fedele, F. (2008). Waves statistics and spectra via a variational wave acquisition stereo system. In *OMAE 2008-57160*, pages 1–8, Estoril, Portugal.

Gelci, R., Cazalé, H., and Vassal, J. (1957). Prévision de la houle. La méthode des densités spectroangulaires. 9:416–435.

Geleyn, J. F. (1988). Interpolation of wind, temperature and humidity values from model levels to the height of measurement. *Tellus A*, 40(A):347–351.

Gemmrich, J. R., Banner, M. L., and Garrett, C. (2008). Spectrally resolved energy dissipation rate and momentum flux of breaking waves. *Journal of Physical Oceanography*, 38(6):1296–1312.

Gerritzen, P. L. (1993). The calibration of wave buoys. *The Hydrographic Society*, (31):1–5.

Gower, J. F. R. (1979). The computation of ocean wave heights from GEOS-3 satellite radar altimeter. *Remote sensing of Environment*, 8:97–114.

Graber, H. C., Terray, E. A., Donelan, M. A., Drennan, W. M., Van Leer, J. C., and Peters, D. B. (2000). ASIS-a new Air-Sea interaction spar buoy: Design and performance at sea. *Journal of Atmospheric and Oceanic Technology*, 17(5):708–720.

Guimarães, P. V., Farina, L., Toldo, E., Diaz-Hernandez, G., and Akhmatskaya, E. (2015). Numerical simulation of extreme wave runup during storm events in Tramandaí Beach, Rio Grande do Sul, Brazil. *Coastal Engineering*, 95:171–180.

Gutshabash, Y. S. and Lavrenov, I. V. (1986). Swell transformation in the cape Agulhas current. *Izv. Atmos. Ocean. Phys.*, 22(6):494–497.

Hara, T. and Plant, W. J. (1994). Hydrodynamic modulation of short wind-wave spectra by long waves and its measurement using microwave backscatter. *Journal of Geophysical Research*, 99(C5):9767–9784.

Hasselmann, K. (1961). On the non-linear energy transfer in a gravity wave spectrum Part 1. General theory. *Journal of Fluid Mechanics*, 12(4):481–500.

Hasselmann, K. (1962). On the non-linear energy transfer in a gravity-wave spectrum. *J. Fluid Mech*, 12(1960):15.

Hasselmann, K. (1963). On the non-linear energy transfer in a gravity wave spectrum, Part 2. *Fluid Mechanics*, 15:273–281.

Hasselmann, K. (1971). On the mass and momentum transfer between short gravity waves and larger-scale motions. *J. Fluid Mech.*, 4:189–205.

Hasselmann, K. and Hasselmann, S. (1991). On the nonlinear mapping of an ocean wave spectrum into a synthetic aperture radar image spectrum and its inversion. *J. Geophys. Res.*, 96(C6):10713–10729.

Hasselmann, S., Hasselmann, K., Allender, J. H., and Barnett, T. (1985). Computations and parameterizations of nonlinear energy transfer in a gravity-wave spectrum, Part II. *Journal of Physical Oceanography*, 15:1378–1391.

Hauser, D., Caudal, G., Rijckenberg, G. J., Vidal-Madjar, D., Laurent, G., and Lancelin, P. (1992). Ressac: a new airborne fm/cw radar ocean wave spectrometer. *IEEE Transactions on Geoscience and Remote Sensing*, 30(5):981–995.

Hauser, D., Tison, C., Amiot, T., Delaye, L., Corcoral, N., and Castillan, P. (2017). SWIM: The first spaceborne wave scatterometer. *IEEE Trans. on Geosci. and Remote Sensing*, 55(5):3000–3014.

Henyey, F. S., Creamer, D. B., Dysthe, K. B., Schult, R. L., and Wright, J. A. (1987). The energy and action of small waves riding on large waves. *Journal of Fluid Mechanics*, 189(1):443–462.

Herbers, T. H. C., Jessen, P. F., Janssen, T. T., Colbert, D. B., and MacMahan, J. H. (2012). Observing ocean surface waves with GPS-tracked buoys. *Journal of Atmospheric and Oceanic Technology*, 29(7):944–959.

Herbers, T. H. C. and Lentz, S. J. (2010). Observing directional properties of ocean swell with an acoustic doppler current profiler (ADCP). *Journal of Atmospheric and Oceanic Technology*, 27(1):210–225.

Hersbach, H. and Bidlot, J.-r. (2008). The relevance of ocean surface current in the ECMWF analysis and forecast system. In *ECMWF Workshop on Ocean-atmosphere interactions,*, pages 61–73.

Herterich, K. and Hasselmann, K. (1980). A similarity relation for the nonlinear energy transfer in a fhite-depth gravity-wave spectrum. *Journal of Fluid Mechanics*, 97:215–224.

Holland, K. T., Holman, R., Lippmann, T. C., Stanley, J., and Plant, N. (1997). Practical use of video imagery in nearshore oceanographic field studies. *IEEE Journal of Oceanic Engineering*, 22(1):81–92.

Holland, K. T., Puleo, J. A., and Kooney, T. N. (2001). Quantification of swash flows using video-based particle image velocimetry. *Coastal Engineering*, 44(2):65–77.

Holman, R. and Stanley, J. (2007). The history and technical capabilities of Argus. *Coastal Engineering*, 54(6-7):477–491.

Holthuijsen, L. H. (1983). Observations of the directional distribution of ocean-wave energy in fetch-limited conditions. *Journal of Physical Oceanography*, 13(2):191–207.

Hristov, T. S., Miller, S. D., and Friehe, C. A. (2003). Dynamical coupling of wind and ocean waves through wave-induced air flow. *Nature*, 422:55–58.

Hwang, P. a., Wang, D. W., Walsh, E. J., Krabill, W. B., and Swift, R. N. (2000). Airborne Measurements of the Wavenumber Spectra of Ocean Surface Waves. Part I: Spectral Slope and Dimensionless Spectral Coefficient. *Journal of Physical Oceanography*, 30(11):2753–2767.

Jackson, F. C., Walton, W. T., and Baker, P. L. (1985). Aircraft and satellite measurement of ocean wave directional spectra using scanning-beam microwave radars. *J. Geophys. Res.*, 90:987–1004.

Jahne, B. (2004). *Practical handbook on image processing for scientific and technical applications*. CRC Press, 2 edition.

Janssen, P. (2004). *The interaction of ocean waves and wind*. Cambridge University Press.

Janssen, P. A. E. M. (1982). Quasilinear approximation for the spectrum of wind-generated water waves. *J. Fluid Mech.*, 117:493–506.

Janssen, P. A. E. M. (1991). Quasi-linear theory of wind-wave generation applied to wave forecasting. *Journal of Physical Oceanography*, 21(1):1631—-1642.

Janssen, P. A. E. M. (1994). Technical report No. 71: Results with a coupled wind wave model. Technical report, ECMWF.

Janssen, P. A. E. M. (2008). Progress in ocean wave forecasting. *Journal of Computational Physics*, 227(1):3572–3594.

Jeans, G., Primrose, C., Descusse, N., Strong, B., and van Weert, P. (2003). A comparison between directional wave measurements from the RDI Workhorse with waves and the Datawell directional Waverider. *Proceedings of the IEEE/OES Seventh Working Conference on Current Measurement Technology*, 1:148–151.

Jeffreys, H. (1925). On the formation of water waves by wind. *Proceedings of the Royal Society of London*, 107(742):189–206.

Jeffreys, H. (1926). On the formation of water waves by wind. *Proceedings of the Royal Society of London*, 110(754):241–247.

Keller, W. C. and Plant, W. J. (1990). Cross section and modulation transfer function at L and Ku bands measured during the tower ocean wave and radar dependence experiment. *Journal of Geophysical Research*, 95(16):277–289.

Keller, W. C. and Wright, J. W. (1975). Microwave scattering and the straining of wind–generated waves. *Radio Science*, 10(2):139–147.

Kerbiriou, M.-a., Prevosto, M., Maisondieu, C., Clement, A., and Babarit, A. (2007). Influence of sea-states description on wave energy production assessment. In *Proceedings of the 7th European Wave and Tidal Energy Conference*, volume 1, pages 1–10.

Klette, R., Schluns, K., and Koschan, A. (1998). *Computer Vision: Three-Dimensional Data from Images*. Springer Singapore, 1 edition.

Komen, G. J., Cavaleri, L., Donelan, M., Hasselmann, K., Hasselmann, S., and M., J. a. P. A. E. (1994). *Dynamics and modelling of ocean waves*. Cambridge University Press.

Kosnik, M. V. and Dulov, V. A. (2011). Extraction of short wind wave spectra from stereo images of the sea surface. *Meas. Sci. Tech.*, 22:015504.

Kudryavtsev, V. (2005). On radar imaging of current features: 1. Model and comparison with observations. *Journal of Geophysical Research*, 110(C7):1–27.

Kudryavtsev, V., Akimov, D., Johannessen, J., and Chapron, B. (2005). On radar imaging of current features: 1. model and comparison with observations. *J. Geophys. Res.*, 110:C07016.

Kudryavtsev, V. and Chapron, B. (2016). On growth rate of wind waves: impact of short-scale breaking modulations. *Journal of Physical Oceanography*, 46(1):349–360.

Kudryavtsev, V., Grodsky, V. V., Dulov, V. A., and Bolshakov, A. N. (1995). Observations of wind in Golf Stream frontal zone. *Journal of Geophysical Research*, 100(20):715—-727.

Kudryavtsev, V., Yurovskaya, M., Chapron, B., Collard, F., and Donlon, C. (2017a). Sun glitter imagery of surface waves. part 1: Directional spectrum retrieval and validation. *J. Geophys. Res.*, 122.

Kudryavtsev, V., Yurovskaya, M., Chapron, B., Collard, F., and Donlon, C. (2017b). Sun glitter imagery of surface waves. part 2: Waves transformation on ocean currents. *J. Geophys. Res.*, 122.

Kudryavtsev, V. N. and Makin, V. K. (2002). Coupled dynamics of short waves and the airflow over long surface waves. *J. Geophys. Res.*, 107(C12):3209.

Kudryavtsev, V. N., Makin, V. K., and Meirink, J. F. (2001). Simplified model of the air flow above waves. *Boundary-Layer Meteorology*, 100(1):63–90.

Kuik, A. J., van Vledder, G. P., and Holthuijsen, L. H. (1988). A method for the routine analysis of pitch-and-roll buoy wave data. *J. Phys. Oceanogr.*, 18:1020–1034.

Lafore, J. P., Stein, J., Asencio, N., Bougeault, P., Ducrocq, V., Duron, J., Fischer, C., Héreil, P., Mascart, P., Masson, V., Pinty, J. P., Redelsperger, J. L., Richard, E., and Vilà-Guerau De Arellano, J. (1998). The Meso-NH atmospheric simulation system. Part I: Adiabatic formulation and control simulations. *Annales Geophysicae*, 16(1):90–109.

Lange, P. A. and Huhnerfuss, H. (1984). Horizontal surface tension gradients induced in monolayers by gravity water wave action. *Journal of Physical Oceanography*, 14:1620–1628.

Laxague, N. J. M., Haus, B. K., Bogucki, D., and Özgökmen, T. (2015). Spectral characterization of fine-scale wind waves using shipboard optical polarimetry. *J. Geophys. Res.*, 120:3140–3156.

Lazure, P. and Dumas, F. (2008). An external-internal mode coupling for a 3D hydrodynamical model for applications at regional scale (MARS). *Advances in Water Resources*, 31(2):233–250.

Leckler, F. (2013). *Observation et modélisation du déferlement des vagues*. PhD thesis, Université de Bretagne Occidentale.

Leckler, F., Ardhuin, F., Peureux, C., Benetazzo, A., Bergamasco, F., and Dulov, V. (2015). Analysis and interpretation of frequency-wavenumber spectra of young wind waves. *Journal of Physical Oceanography*, 45:2484–2496.

Leibovich, S. (1983). The form and dynamics of Langmuir circulations. *Annual Review of Fluid Mechanics*, 15(1):391–427.

Long, C. E. and Resio, D. T. (2007). Wind wave spectral observations in Currituck Sound, North Carolina. *J. Geophys. Res.*, 112:C05001.

Longuet-Higgins, M. S. (1985). Accelerations in steep gravity waves. *Journal of Physical Oceanography*, 15(11):1570–1579.

Longuet-Higgins, M. S. (1986). Eulerian and Lagrangian aspects of surface waves. *J. Fluid Mech.*, 173:683.

Longuet-Higgins, M. S. (1987a). A stochastic model of sea-surface roughness I. Wave crests. *Proceedings of the Royal Society of London*, 410:19–34.

Longuet-Higgins, M. S. (1987b). The propagation of short surface waves on longer gravity waves. *Journal of Fluid Mechanics*, 177:293–306.

Longuet-Higgins, M. S. (1991). A stochastic model of sea-surface roughness. II. *Proceedings of the Royal Society of London*, 435:405–422.

Longuet-Higgins, M. S., Cartwright, D., and Smith, N. D. (1963). Observations of the directional spectrum of sea waves using the motions of a floating buoy. *Ocean wave spectra*, pages 111–136.

Longuet-Higgins, M. S. and Stewart, R. W. (1960). Changes in the form of short gravity waves on long waves and tidal currents. *Journal of Fluid Mechanics*, 8(1):565–583.

Longuet-Higgins, M. S. and Stewart, R. W. (1964). Radiation stress in water waves, a physical discussion with applications. *Deep Sea Research*, 11:529–563.

Lygre, A. and Krogstad, H. E. (1986). Maximum entropy estimation of the directional distribution in ocean wave spectra. *J. Phys. Oceanogr.*, 16:2,052–2,060.

Ma, Y., Soatto, S., Kosecka, J., and Sastry, S. (2004). *An invitation to 3-D vision from images to geometric models*. Springer-Verlag New York, 1 edition.

Manasseh, R., Babanin, A. V., Forbes, C., Rickards, K., Bobevski, I., and Ooi, A. (2006). Passive acoustic determination of wave-breaking events and their severity across the spectrum. *Journal of Atmospheric and Oceanic Technology*, 23(1):599–618.

Mapp, G. R., Welch, C. S., and Munday, J. C. (1985). Wave refraction by warm core rings. *Journal of Geophysical Research*, 90(C4):7153–7162.

Martins, K., Blenkinsopp, C., Power, H., Bruder, B., Puleo, J., and Bergsma, E. (2017). High-resolution monitoring of wave transformation in the surf zone using a lidar scanner array. *Coastal Engineering*, 128:37 – 43.

Masson, D. (1996). A case study of wave-current interaction in a strong tidal current. *J. Phys. Oceanogr.*, 26:359–372.

Masson, V., Le Moigne, P., Martin, E., Faroux, S., Alias, A., Alkama, R., Belamari, S., Barbu, A., Boone, A., Bouyssel, F., Brousseau, P., Brun, E., Calvet, J.-C., Carrer, D., Decharme, B., Delire, C., Donier, S., Essaouini, K., Gibelin, A.-L., Giordani,

H., Habets, F., Jidane, M., Kerdraon, G., Kourzeneva, E., Lafaysse, M., Lafont, S., Lebeaupin Brossier, C., Lemonsu, A., Mahfouf, J.-F., Marguinaud, P., Mokhtari, M., Morin, S., Pigeon, G., Salgado, R., Seity, Y., Taillefer, F., Tanguy, G., Tulet, P., Vincendon, B., Vionnet, V., and Voldoire, A. (2013). The SURFEXv7.2 land and ocean surface platform for coupled or offline simulation of Earth surface variables and fluxes. *Geoscientific Model Development*, 6:929–960.

Mastenbroek, C., Burgers, G., and Janssen, P. A. E. M. (1993). The dynamical coupling of a wave model and a storm surge model through the atmospheric boundary layer.

Melville, W. K. (1994). Energy dissipation by breaking waves. *Journal of Physical Oceanography Oceanography*, 24(1):2041—-2049.

Melville, W. K. (1996). The role of surface wave breaking in air-sea interaction. *Annu. Rev. Fluid Mech.*, 28:279–321.

Melville, W. K. and Matusov, P. (2002). Distribution of breaking waves at the ocean surface. *Letters to Nature*, 417:58—-63.

Miles, J. W. (1957). On the generation of surface waves by shear flows. Part 4. *Journal of Fluid Mechanics*, 13(1):185–204.

Miles, J. W. (1959). On the generation of surface waves by shear flows. Part 2. *Journal of Fluid Mechanics*, 6(4):568–582.

Miles, J. W. (1996). Surface-wave generation: a viscoelastic model. *Journal of Fluid Mechanics*, 1(1):131–145.

Minster, F., Jourdan, D., Boissier, C., and Midol-Monnet, P. (1991). Estimation of the sea-state bias in radar altimeter Geosat data from examination of frontal systems. *Journal of Atmospheric and Oceanic Technology*, 9:174—-187.

Mironov, A. S. and Dulov, V. A. (2008). Detection of wave breaking using sea surface video records. *Measurement Science and Technology*, 19(1):1–10.

Mitsuyasu, H. and Honda, T. (1982). Wind-induced growth of water waves. *Journal of Fluid Mechanics*, 123(1):425–442.

Mouche, A. A., Chapron, B., Zhang, B., and Husson, R. (2017). Combined co- and cross-polarized SAR measurements under extreme wind conditions. *IEEE Trans. on Geosci. and Remote Sensing*, 120(99):1–10.

Muller, H., Dumas, F., Blanke, B., and Mariette, V. (2007). High-resolution atmospheric forcing for regional oceanic model: The Iroise Sea. *Ocean Dynamics*, 57(4-5):375–400.

Nouguier, F., Chapron, B., Collard, F., Mouche, A., Rascle, N., Ardhuin, F., and Wu, X. (2017). Sea surface kinematics from near-nadir radar measurements. *IEEE Trans. on Geosci. and Remote Sensing*, submitted.

O'Reilly, W. C., Herbers, T. H. C., Seymour, R. J., and Guza, R. T. (1996). A comparison of directional buoy and fixed platform measurements of Pacific swell. *J. Atmos. Ocean Technol.*, 13:231–238.

Pearman, D. W., Herbers, T. H. C., Janssen, T. T., van Ettinger, H. D., McIntyre, S. A., and Jessen, P. F. (2014). Drifter observations of the effects of shoals and tidal-currents on wave evolution in San Francisco bight. *Continental Shelf Research*, 91:109–119.

Peureux, C., Benetazzo, A., and Ardhuin, F. (2017). Note on the directional properties of meter- scale gravity waves. *Ocean Science Discussions*, 1(1):1–18.

Phillips, M. (1957). On the generation of waves by turbulent wind. *Journal of Fluid Mechanics*, 2:417—-445.

Phillips, O. M. (1958). The Equilibrium Range in the Spectrum of Wind Generated Waves. *Journal of Fluid Mechanics*, 4:426 – 434.

Phillips, O. M. (1977). *The dynamics of the upper ocean*. Cambridge University Press, 2 edition.

Phillips, O. M. (1984). On the response of short ocean wave components at a fixed wavenumber to ocean current variations. *J. Phys. Oceanogr.*, 14:1425–1433.

Phillips, O. M. (1985). Spectral and statistical properties of the equilibrium range in wind-generated gravity waves. *Journal of Fluid Mechanics*, 156(1):505–531.

Pineau-Guillou, L. (2013). Validation des modèles hydrodynamiques 2D des côtes de la Manche et de l'Atlantique. Technical report, Ifremer, Brest.

Plant, W. J. (1982). A relationship between wind stress and wave slope. *Journal of Geophysical Research-Oceans*, 87(C3):1961–1967.

Polnikov, V. G. and Farina, L. (2002). On the problem of optimal approximation of the four-wave kinetic integral. *Nonl. Proc. Geophys.*, 9:497–512.

Potter, H., Collins, III, C. O., Drennan, W. M., and Graber, H. C. (2015). Observations of wind stress direction during typhoon Chaba (2010). *Geophys. Res. Lett.*, 42:9898–9905.

Queffeulou, P. (2004). Long term validation of wave height measurements from altimeters. *Marine Geodesy*, 27:495–510. DOI: 10.1080/01490410490883478.

Rademakers, P. (1993). Technical Note: Waverider-wavestaff comparison. *Ocean Engineering*, 20(2):187–193.

Ramamonjiarisoa, A. (1995). On the kinematics of short waves in the presence of surface flows of larger scales. *Journal of Fluid Mechanics*, 298:249–269.

Rapizo, H., Babanin, A. V., Provis, D., and Rogers, W. E. (2017). Current-induced dissipation in spectral wave models. *J. Geophys. Res.*, 122:2205–2225.

Rapizo, H., Waseda, T., Babanin, A. V., and Toffoli, A. (2016). Laboratory experiments on the effects of a variable current field on the spectral geometry of water waves. *Journal of Physical Oceanography*, 46:2695—-2717.

Rascle, N. and Ardhuin, F. (2013). A global wave parameter database for geophysical applications. part 2: model validation with improved source term parameterization. *Ocean Modelling*, 70:174–188.

Rascle, N., Chapron, B., Ponte, A., Ardhuin, F., and Klein, P. (2014). Surface roughness imaging of currents shows divergence and strain in the wind direction. *Journal of Physical Oceanography*, 44(8):140509140828004.

Rascle, N., Molemaker, J., Marié, L., Nouguier, F., Chapron, B., Lund, B., and Mouche, A. (2017). Intense deformation field at oceanic front inferred from directional sea surface roughness observations. *Geophys. Res. Lett.*, 48:5599–5608.

Rascle, N., Nouguier, F., Chapron, B., Mouche, A., and Ponte, A. (2016). Surface roughness changes by fine scale current gradients: Properties at multiple azimuth view angles. *J. Phys. Oceanogr.*, 46:3681–3694.

Resio, D. and Perrie, W. (1991). A numerical study of nonlinear energy fluxes due to wave-wave interactions Part 1. Methodology and basic results. *Journal of Fluid Mechanics*, 237:603—-629.

Resio, D. T., Long, C. E., and Perrie, W. (2011). The role of nonlinear momentum fluxes on the evolution of directional wind-wave spectra. *J. Phys. Oceanogr.*, 41(4):781–801.

Retzler, C. (2006). Measurements of the slow drift dynamics of a model Pelamis wave energy converter. *Renewable Energy*, 31(2):257–269.

Reul, N., Branger, H., and Giovanangeli, J.-P. (2008). Air flow structure over short-gravity breaking water waves. *Boundary-Layer Meteorol.*, 126:477–705.

Reul, N. and Chapron, B. (2003). A model of sea-foam thickness distribution for passive microwave remote sensing applications. *J. Geophys. Res.*, 108(C10):3321.

Reverdin, G., Morisset, S., D.Bourras, Martin, N., Lourenço, A., Boutin, J., Caudoux, C., Font, J., and Salvador, J. (2013). Surpact A SMOS Surface Wave Rider for Air-Sea Interaction. *Oceanography*, 26(1):48–57.

Roland, A. (2008). *Spectral Wave Modelling on Unstructured Meshes*. PhD thesis, Institut fur Wasserbau und Wasserwirtschaft.

Roland, A. and Ardhuin, F. (2014). On the developments of spectral wave models: numerics and parameterizations for the coastal ocean. 64(6):833–846.

Romero, L., Melville, W. K., and Kleiss, J. M. (2012a). Spectral Energy Dissipation due to Surface Wave Breaking. *Journal of Physical Oceanography*, 42(9):1421–1444.

Romero, L., Melville, W. K., and Kleiss, J. M. (2012b). Spectral energy dissipation due to surface wave breaking. *J. Phys. Oceanogr.*, 42(9):1421–1444.

Sepulveda, H. H., Queffeulou, P., and Ardhuin, F. (2015). Assessment of SARAL AltiKa wave height measurements relative to buoy, Jason-2 and Cryosat-2 data. *Marine Geodesy*, 38(S1):449–465.

Shemdin, O. H., Tran, H. M., and Wu, S. C. (1988). Directional measurement of short ocean waves with stereophotography. *Journal of Geophysical Research: Oceans (1978–2012)*, 93(C11):13891–13901.

Smith, J. (1986). Short surface waves with growth and dissipation. *Journal of Geophysical Research*, 91(C2):2616–2632.

Smith, S. D. (1988). Coefficients for sea surface wind stress, heat flux, and wind profiles as a function of wind speed and temperature. *Journal of Geophysical Research: Oceans*, 93(C12):15467–15472.

Snyder, R. L., Dobson, F. W., Elliott, J. A., and Long, R. B. (1981). Array measurements of atmospheric pressure fluctuations above surface gravity waves. *Journal of Fluid Mechanics*, 102(-1):59.

Stopa, J. E., Ardhuin, F., Bababin, A., and Zieger, S. (2016). Comparison and validation of physical wave parameterizations in spectral wave models. *Ocean Modelling*, 103:2–17.

Sugimori, Y. (1975). A study of the application of the holographic method to the determination of the directional spectrum of ocean waves. *Deep-Sea Research and Oceanographic Abstracts*, 22(5).

Sullivan, P. P. and Mcwilliams, J. C. (2010). Dynamics of winds and currents coupled to surface waves. *Annual Reviews in Fluid Mechanics*, 42:19—-42.

Sutherland, P. and Melville, W. K. (2013). Field measurements and scaling of ocean surface wave-breaking statistics. *Geophysical Research Letters*, 40(12):3074–3079.

Sutherland, P. and Melville, W. K. (2015). Field measurements of surface and near-surface turbulence in the presence of breaking waves. *Journal of Physical Oceanography*, 45(4):943–965.

Terray, E. A., hole oceanographic institution ma Dept. of applied ocean physics, W., Engineering, Drennan, W. M., and Donelan, M. A. (1999). *The Vertical Structure of Shear and Dissipation in the Ocean Surface Layer*. AD-a365 369. Woods hole oceanographic institution ma Department of applied ocean physics and engineering.

The WAVEWATCH III ® Development Group (2016). User manual and system documentation of WAVEWATCH III ® version 5.16. Tech. Note 329, NOAA/NWS/NCEP/MMAB, College Park, MD, USA. 326 pp. + Appendices.

Thomas, P. (2015). *Developpement d'une bouee derivante pour mesures de vagues*. PhD thesis, ENSTA Bretagne.

Thomson, J. (2012). Wave breaking dissipation observed with "SWIFT" drifters. *Journal of Atmospheric and Oceanic Technology*, 29(12):1866–1882.

Thomson, J., Schwendeman, M. S., Zippel, S. F., Moghimi, S., Gemmrich, J., and Rogers, W. E. (2016). Wave-Breaking turbulence in the ocean surface layer. *Journal of Physical Oceanography*, 46(6):1857–1870.

Thorpe, S. (2004). Langmuir Circulation. *Annual Review of Fluid Mechanics*, 36(1):55–79.

Tolman, H. L., Accensi, M., Alves, H., Ardhuin, F., Bidlot, J., Booij, N., Bennis, A.-C., Campbell, T., Chalikov, D. V., Chawla, A., Filipot, J.-F., Foreman, M., Janssen, P.,

Leckler, F., Li, J.-G., Lind, K., Orzech, M., Padilla–Hernández, R., Rogers, W. E., Rawat, A., Roland, A., Sikiric, M. D., Szyszka, M., Tracy, B., van Vledder, G. P., van der Westhuysen, A., and Zieger, S. (2014). User manual and system documentation of WAVEWATCH III. *National Oceanic and Atmospheric Administration, National Weather Service Center for Environmental Prediction*, 1:311.

Tolman, H. L. and Chalikov, D. (1996). Source terms in a third-generation wind wave model. *Journal of Geophysical Research*, 26(1):2497—-2518.

Tolman, H. L., Krasnopolsky, V. M., and Chalikov, D. V. (2005). Neural network approximations for nonlinear interactions in wind wave spectra: direct mapping for wind seas in deep water. *Ocean Modelling*, 8:253–278.

Tracy, B. a. and Resio, D. T. (1982). Theory and calculation of the nonlinear energy transfer between sea waves in deep water. Technical report, Wave Information Studies of U.S. Coastlines.

Troitskaya, Y., Sergeev, D., Ermakova, O., and Balandina, G. (2011). Statistical parameters of the air turbulent boundary layer over steep water waves measured by the piv technique. *J. Phys. Oceanogr.*, 41:1422–1454.

Ursell, F. (1956). Wave generation by wind. *Surveys in mechanics*, 1:216–249.

van der Westhuysen, A. J., van Dongeren, A. R., Groeneweg, J., van Vledder, G. P., Peters, H., Gautier, C., and van Nieuwkoop, J. C. C. (2012). Improvements in spectral wave modeling in tidal inlet seas. *Journal of Geophysical Research: Oceans*, 117(8):1–23.

Van Vledder, G. and Hurdle, D. P. (2002). Performance of formulations for whitecapping in wave prediction models. In *OMAE'02, 21st International Conference on Offshore Mechanics and Artic Engineering*, pages 1–9, Osolo.

van Weeren, D., Joosten, H., and Scrivens, R. (2005). Hybrid power: the buoy has it. *International Ocean Systems*, (Power Sources):1—-3.

Veron, F. (2015). Sea spray. *Annu. Rev. Fluid Mech.*, 47:507–538.

Visser, P. J. (1991). Laboratory measurements of uniform longshore currents. *Coastal Engineering*, 15(5-6):563–593.

Voldoire, A., Decharme, B., Pianezze, J., Lebeaupin Brossier, C., Sevault, F., Seyfried, L., Garnier, V., Bielli, S., Valcke, S., Alias, A., Accensi, M., Ardhuin, F., Bouin, M.-

N., Ducrocq, V., Faroux, S., Giordani, H., Léger, F., Marsaleix, P., Raynaud, R., Redelsperger, J.-L., Richard, E., and Riette, S. (2017). The seamless and multi-model coupling between atmosphere, land, hydrology, ocean, waves and sea-ice models based on SURFEX surface model using OASIS3-MCT. *Geoscientific Model Development Discussions*, (May):1–39.

Vries, J. J., Waldron, J., and Cunningham, V. (2003). Field tests of the new datawell DWR-G GPS wave buoy. *Sea Technology*, 44(December 2003):50–55.

Vries, S., Hill, D., de Schipper, M., and Stive, M. (2011). Remote sensing of surf zone waves using stereo imaging. *Coastal Engineering*, 58(3):239–250.

Walsh, E. J., III, D. W. H., Hines, D. E., Swift, R. N., and Scott, J. F. (1985). Directional wave spectra measured with the surface contour radar. *Journal of Physical Oceanography*, 15(5):566–592.

WAMDI Group, T. (1988). The WAM model - A third generation ocean wave prediction model. *Journal of Physical Oceanography*, 18(12):1775–1810.

Waseda, T., Kinoshita, T., and Tamura, H. (2009). Evolution of a random directional wave and freak wave occurrence. *Journal of Physical Oceanography*, 39(1):621–639.

Webb, D. J. (1978). Non-linear transfers between sea waves. *Deep-Sea Research*, 25(3):279–298.

Welch, P. D. (1967). The use of fast Fourier transform for the estimation of power spectra: a method based on time averaging over short, modified periodograms. *IEEE Trans. Audio and Electroacoustics*, 15(2):70–73.

White, B. S. and Fornberg, B. (1998). On the chance of freak waves at sea. *J. Fluid Mech.*, 355:113–138.

WISE Group (2007). Wave modelling - the state of the art. *Progress in Oceanography*, 75:603–674.

Young, I. (1995). The determination of confidence limits associated with estimates of the spectral peak frequency. *Ocean Eng.*, 22:669–686.

Young, I. (1999). *Wind generated ocean waves*. Elsevier, 1 edition.

Young, I. R. and Babanin, A. V. (2006). Spectral distribution of energy dissipation of wind-generated waves due to dominant wave breaking. *Journal of Physical Oceanography*, 36:376–394.

Yurovskaya, M. V., Dulov, V. A., Chapron, B., and Kudryavtsev, V. N. (2013). Directional short wind wave spectra derived from the sea surface photography. *J. Geophys. Res.*, 113:C12024.

Yurovsky, Y. Y., Kudryavtsev, V. N., Grodsky, S. A., and Chapron, B. (2017). Ka-band dual copolarized empirical model for the sea surface radar cross section. *IEEE Trans. on Geosci. and Remote Sensing*, 55(3):1629–1647.

Zappa, C. J., Banner, M. L., Schultz, H., Corrada-Emmanuel, A., Wolff, L. B., and Yalcin, J. (2008). Retrieval of short ocean wave slope using polarimetric imaging. *Meas. Sci. Technol.*, 19:055503.

Zhang, Z. (2000). A flexible new technique for camera calibration (Technical Report). Technical Report 11.

Zippel, S. and Thomson, J. (2017). Surface wave breaking over sheared currents: Observations from the mouth of the Columbia river. *J. Geophys. Res.*, 122:3311–3328.

UNIVERSITE BRETAGNE LOIRE

CENTRALE NANTES

Thèse de Doctorat

Pedro Veras Guimarães

Titre ligne 1: Surfaces de mer et dissipation d'énergie

Title of thesis: Sea surface and energy dissipation

Résumé

Les formulations et modèles de vagues stochastiques sont les outils les plus traditionnels pour l'évaluation et la prévision des états de mer. Cependant, la prise en compte de nombreux processus physiques essentiels à l'évolution des vagues reste souvent lacunaire dans ces types d'approches. Une des raisons possible est notamment que peu d'observations viennent documenter ces processus. La dissipation des ondes est ainsi mal quantifiée par les méthodes d'observation traditionnelles dans tout l'éventail des conditions océaniques. Dans ce contexte, le travail présenté dans cette thèse explore plus avant les conditions menant au déferlement à travers la modulation de l'énergie des ondes courtes par de fort courants de marée et par des ondes plus longues. Dans cette étude, nous avons profité des campagnes de mesure BBWAVES, spécialement conçues pour acquérir de la donnée dans des zones d'interactions vagues-courants. Ces campagnes ont notamment permis de tester une nouvelle bouée dérivante conçue pour la mesure des vagues dans des zones à forts courants de marées. Grâce à des mesures simultanées en zones de forts courants, il a été possible de mettre en évidence des lacunes dans la modélisation des états de mer, et l'influence vraisemblable des erreurs dans la modélisation atmosphérique pour ces conditions. Cette thèse a également tiré parti d'une campagne de mesure stéréo-vidéo d'états de mer en Mer Noire afin d'étudier différents aspects du déferlement des vagues dans une grande variété de conditions d'état de mer bimodales. Ces mesures ont permis de mettre en évidence une modulation des ondes courtes par des longues et une incidence sur les propriétés de déferlement.

Mots clés
Vagues; stéréo-vidéo; bouée dérivante; modélisation; interaction vague-courant; modulation; déferlement

Abstract

Stochastic wave formulations and models are the most common tools for the assessment and forecast of sea surface conditions. Their ability to account for some of the processes encountered by waves during their evolution remains however a central question. Among other processes, the wave dissipation is for instance still poorly quantified and traditional methods for wave measurements fail to proper insight into its physics in a wide range of conditions. In this context, the work presented in this PhD aims to explore available observation techniques for their application to several quantitative aspects of the dissipation of wave energy, and particularly for short wave modulated by strong tidal currents, for short wave modulated by longer waves. This work takes advantage of the BBWAVES oceanic campaigns, especially planned to explore questions related to wave and current interactions. Data from a large variety of sensors are analyzed. The campaign provides the ground for the test of a new design of drifting buoy aimed at measuring waves in areas of strong tidal current. Its performances are verified and the description it provides of the area is explored. From simultaneous measurements, it was possible to highlight the actual inaccuracies in wave model capabilities as well as the contribution of the error contained in the atmospheric modeling over strong tidal currents to the misevaluation of sea states. This work also used an extensive dataset from a stereo video experiment in the Black Sea to investigate wave breaking in bimodal sea state conditions. These measurements have revealed the influence of long wave modulation over short wave breaking.

Key Words
Ocean waves; stereo video; drifting buoy; wave modeling; wave-current interaction; modulation; breaking